Noninvasive Temperature Estimation Technique for HIFU Therapy Monitoring Using Backscattered Ultrasound

Ajay Anand

A dissertation submitted in partial fulfillment of the
requirements for the degree of

Doctor of Philosophy

University of Washington

2005

Program Authorized to Offer Degree: Department of Electrical Engineering

University of Washington
Graduate School

This is to certify that I have examined this copy of a doctoral dissertation by

Ajay Anand

and have found that it is complete and satisfactory in all respects,
and that any and all revisions required by the final
examining committee have been made.

Chair of Supervisory Committee:

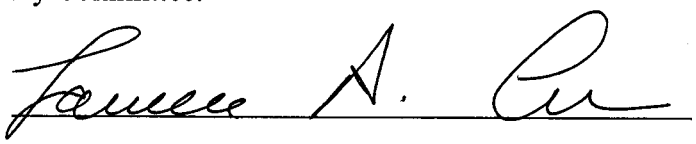

Lawrence A. Crum

Reading Committee:

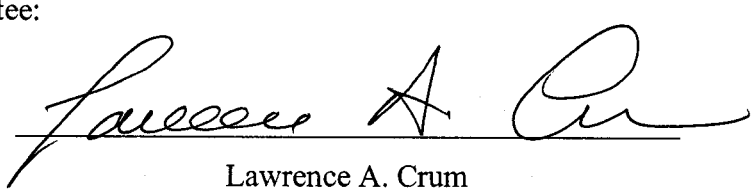

Lawrence A. Crum

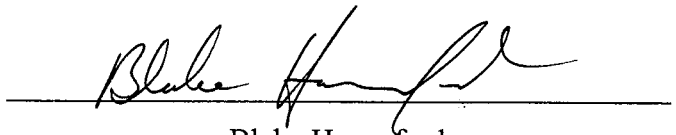

Blake Hannaford

Peter J. Kaczkowski

Date: 06/02/05

In presenting this dissertation in partial fulfillment of the requirements for the doctoral degree at the University of Washington, I agree that the Library shall make its copies freely available for inspection. I further agree that extensive copying of the dissertation is allowable only for scholarly purposes, consistent with "fair use" as prescribed in the U.S. Copyright Law. Requests for copying or reproduction of this dissertation may be referred to Proquest Information and Learning, 300 North Zeeb Road, Ann Arbor, MI 48106-1346, to whom the author has granted "the right to reproduce and sell (a) copies of the manuscript in microform and/or (b) printed copies of the manuscript made from microform."

Signature 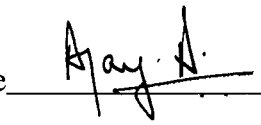

Date 06/02/05

University of Washington

Abstract

Noninvasive Temperature Estimation Technique for HIFU Therapy Monitoring Using Backscattered Ultrasound

Ajay Anand

Chair of the Supervisory Committee:
Professor Lawrence A. Crum
Department of Bioengineering

High Intensity Focused Ultrasound (HIFU) has potential applications in a variety of medical fields that benefit from selective destruction of tissue volumes. Being a noninvasive technique, HIFU provides the ability to ablate localized tissue volumes without damaging intervening tissue, thus eliminating the need for incisions. However, the lack of real-time feedback during the various stages of therapy has been a major hindrance to its widespread clinical acceptance. The ability to accurately track and monitor the therapy progress is therefore important for the success of HIFU treatment protocols.

This work consists of three specific goals. First, an integrated software-based experimental data acquisition system was built, using a commercially available ultrasound scanner, to collect the raw ultrasound backscatter (RF) during HIFU therapy. Second, signal processing approaches were developed to visualize the temporal evolution of lesion formation by analysis of the RF data. Temperature change related information throughout HIFU therapy delivery and post-treatment cool-down was obtained by tracking echo shifts in the RF using cross-correlation techniques. Characteristic changes in the spectral content of RF echoes, due to changes in the scattering properties of the

heated region, were observed well before the appearance of hyper-echogenic regions on B-mode images in the focal zone. Third, a bioheat transfer equation model-based non-invasive quantitative temperature estimation technique for HIFU therapy monitoring was developed and validated in tissue mimicking phantoms and excised animal tissue. In this approach, initial estimates of local thermal and acoustic parameters are first obtained prior to therapy through "calibration" exposures performed in the treatment region. Tissue heterogeneity over a larger targeted region of interest is modeled as a change in the magnitude of the heating rate. During therapy, this magnitude is updated using an optimization technique that minimizes the difference between the model predicted and measured echo shift values. Ultrasound derived temperature estimates were validated against independent thermocouple measurements, close to but not at the HIFU focus. This model-based technique permits noninvasive temperature estimation over the entire therapeutic range, and is thus a departure from previously reported ultrasound-based temperature estimation techniques. These results demonstrate potential for applicability of the techniques in image-guided HIFU therapy.

TABLE OF CONTENTS

LIST OF FIGURES v

LIST OF TABLES xii

1. INTRODUCTION 1

1.1. High Intensity Focused Ultrasound 1
1.2. Image Guided Therapy 2
1.2.1. X-ray 3
1.2.2. Magnetic Resonance Imaging 3
1.2.3. Ultrasound 4
1.2.3.1. Monitoring changes in the elastic modulus 5
1.2.3.2. Monitoring changes in Sound speed, Attenuation and Backscatter 7
1.2.3.3. Monitoring change in Temperature 9
1.3. Key limitations of current ultrasound-based temperature estimation methods 12
1.4. Contributions of this dissertation 13
1.5. Organization of this dissertation 14

2. SOFTWARE-BASED RF DATA ACQUISITION SYSTEM FOR HIFU THERAPY MONITORING 16

2.1. Introduction 16
2.2. System Description 17
2.3. External System Control 19
2.4. Custom Acquisition Modes 22
2.5. Application in HIFU therapy monitoring 26
2.5.1. Experiment setup 27
2.5.2. Timing Analysis - Latency and Jitter Measurements 29
2.6. Application in Elastography 32
2.7. Discussion 35
2.8. Conclusion 36

3. MONITORING HIFU LESION FORMATION USING BACKSCATTERED ULTRASOUND 38

3.1. Introduction 38
3.2. Effect of temperature on ultrasound backscatter 38

3.3. Mathematical model describing effect of temperature on ultrasound backscatter 41
3.4. Inter-tissue variability of relationship between strain and temperature 45
3.5. Estimation of temperature induced strain from ultrasound backscatter – Algorithm description 47
3.6. *In vitro* experiments 51
3.6.1. Experimental Therapy Protocols 51
3.6.2. Point HIFU lesions in excised bovine liver tissue 52
3.6.2.1. Experiment Setup 52
3.6.2.2. Results 53
3.6.3. Scanned HIFU lesion in a tissue mimicking phantom 55
3.6.3.1. Experiment setup 56
3.6.3.2. Results 57
3.7. Quantitative Temperature Monitoring using Backscattered Ultrasound ("Hotwire" Experiment) 60
3.7.1. Experiment Setup 61
3.7.1.1. Independent measurement of c(T) curve 62
3.8. Tracking Changes in Tissue Scattering Properties during HIFU lesion formation 67
3.8.1. Description of Algorithm 68
3.8.2. Results 69
3.9. Summary and Discussion 72
3.10. Motivation for bioheat transfer model-based quantitative temperature estimation approach for HIFU therapy monitoring 73

4. MODEL-BASED TEMPERATURE ESTIMATION TECHNIQUE FOR HIFU THERAPY MONITORING: PART I 76

4.1. Introduction 76
4.2. Bioheat Transfer Equation (BHTE) 76
4.3. Overview of BHTE model-based temperature estimation approach 78
4.4. Calibration experiments 81
4.4.1. Estimation of K 81
4.4.1.1. Theory 81
4.4.1.2. Methodology for estimation of K from ultrasound backscatter 83
4.4.1.3. Experiments 85
4.4.1.4. Experimental results 90
4.4.1.5. Simulations 94
4.4.2. Estimation of Q 97
4.4.2.1. Methodology 97
4.4.2.2. Experiments 99
4.4.2.3. Results 103

4.5. Summary and Discussion 106
4.6. Conclusions 109

5. MODEL-BASED TEMPERATURE ESTIMATION TECHNIQUE FOR HIFU THERAPY MONITORING: PART II 111

5.1. Introduction 111
5.2. *In situ* Estimation of $\varepsilon(T)$ 111
5.2.1. Estimation methodology 111
5.2.2. Experimental data acquisition and analysis 114
5.2.3. Invasive measurement of $\varepsilon(T)$—ground truth measurements 115
5.2.4. Comparison between invasive and noninvasive ε(T) results 118
5.3. Noninvasive Temperature estimation 119
5.3.1. Description of noninvasive temperature estimation technique 119
5.3.2. In vitro experiments for noninvasive temperature estimation 121
5.3.3. Results 124
5.4. Discussion 127
5.5. Conclusions 129

6. *IN VITRO* TISSUE EXPERIMENTS 130

6.1. Introduction 130
6.2. Tissue preparation 130
6.3. Experiment setup 132
6.4. Results and Discussion 133
6.4.1. Estimation of thermal diffusivity (K) 133
6.4.2. Noninvasive detection of boiling onset and in situ heating rate 134
6.4.3. Estimation of $\varepsilon(T)$ 137
6.4.4. Noninvasive temperature estimation 139
6.5. Temperature dependence of thermal diffusivity 141
6.6. Conclusion 143

7. CONCLUSIONS AND FUTURE WORK 144

7.1. Conclusions 144
7.2. Suggestions for future work 147
7.2.1. Applicability in *in vivo* conditions 147
7.2.2. Two dimensional estimation algorithm 148
7.2.3. Estimation of $\varepsilon(T)$ parameters over the entire therapeutic range 149
7.2.4. Motion compensation 149
7.2.5. Homogeneity of thermal and acoustic parameters 150
7.2.6. Optimization of therapy and real-time dosimetry control 150
7.2.7. Validation studies with MRI thermometry 151

REFERENCES **152**

APPENDIX A: GENERATION OF SIMULATED RF DATA **165**

APPENDIX B: RELATION BETWEEN TEMPERATURE INDUCED STRAIN *(ε)* AND TEMPERATURE *(T)* **171**

APPENDIX C: RF DATA ANALYSIS PROGRAMS AND GRAPHICAL USER INTERFACES **175**

C.1. HDI 1000 RF data analysis GUI 175
C.2. Heat Source Estimation GUI 177
C.3. Boiling Onset Detection GUI 178

LIST OF FIGURES

Figure 1.1 Principle of HIFU 2

Figure 2.1 Block diagram representation of data flow in a commercial ultrasound scanner 16

Figure 2.2 Block diagram representation of ATL HDI 1000 ultrasound scanner system architecture (receiver section) showing the internal data path in the default mode and in the custom-developed RF data access mode. 18

Figure 2.3 Flowchart for software master control program developed using LabVIEW™ to control RF data acquisition on HDI 1000. 21

Figure 2.4(a) B-mode image of the carotid artery reconstructed from the RF signals collected for a full lateral width of 2.5 cm (default) (b) B-mode image reconstructed from the RF signals with system in reduced scanline mode [lateral width set to 0.6 cm (32 scan lines)] 24

Figure 2.5 Plot of acquisition frame rate (frames per second) versus lateral width using CL 10-5 probe for axial depth settings of 2.2 cm, 4.5 cm and 8.2 cm with the system in *reduced sector width* mode. 24

Figure 2.6(a) B-mode image of the carotid artery reconstructed from the RF signals collected for a full lateral width of 2.5 cm (default) (b) B-mode image reconstructed from the RF signals with system in sparse scanline mode [inter scanline spacing=4 linewidths] 25

Figure 2.7 Plot of acquisition frame rate (frames per second) versus lateral width for axial depth settings of 2.2 cm, 4.5 cm and 8.2 cm with the system in *sparse scanline* mode. 25

Figure 2.8 B-mode image showing interference due to HIFU beam 26

Figure 2.9 Experiment setup for synchronized RF data acquisition during HIFU therapy. 28

Figure 2.10 Timing diagram showing the synchronization between HIFU therapy delivery and HDI 1000 RF data acquisition. 28

Figure 2.11 Sequence of fundamental B-mode images reconstructed from the acquired ultrasound RF backscatter during and shortly after HIFU therapy. 29

Figure 2.12 Experimental setup for latency measurement 30

Figure 2.13 Screenshot of oscilloscope output illustrating latency between control signal output from the master control program and initiation of RF frame acquisition measured using a hydrophone....31

Figure 2.14 Plot showing measured frame interval (-o) and user specified frame interval (--) sent out from software program between consecutive frames (in seconds)....32

Figure 2.15 Schematic representation of the experimental setup used for the elastography application. 33

Figure 2.16 (a) B-mode image (c) Strain elastogram of the acrylamide gel phantom subject to 0.1 mm axial compression per step from the top using an external compressor. 34

Figure 3.1 Illustration of the shift in the backscattered ultrasound echo locations due to temperature induced sound speed change and thermal expansion along the propagation path of the imaging pulse....39

Figure 3.2 Sound speed versus Temperature measured in Ex-vivo Pork Liver. The data is fitted with a second order polynomial (Bloch, S. MS Degree Thesis, University of Washington, Seattle)....40

Figure 3.3 (a) Local Sound speed change profiles (b) Cumulative echo shift profiles corresponding to the sound speed change profiles in (a). 43

Figure 3.4 Temperature dependence of strain for (a) normal human liver (b) liver with an intermediate fat content (c) marked fatty liver [72]. 45

Figure 3.5 Measured temperature dependence of sound speed for different mammalian tissues. 46

Figure 3.4(a) Orientation of imaging transducer and image acquisition plane (b) Organization of the RF data set. 48

Figure 3.5 Block diagram representation of temperature induced strain estimation algorithm for a pair of RF frames i and i+1 collected at experiment time (slow time) t and $t+\Delta T$....48

Figure 3.6 Graphical illustration of the various processing parameters used in the algorithm to estimate temperature induced strain....49

Figure 3.7 Travel time change maps ($\delta t_{adjacent}$) expressed as apparent displacement in microns (middle row) and temperature induced strain maps (bottom row) for in vitro bovine liver experiment. 54

Figure 3.8 Relative orientation of the HIFU transducer, imaging probe and plane of HIFU lesion formation for the scanned lesion formation experiment....56

Figure 3.9 Maps of changes in local travel time (bottom row) and corresponding B-mode images (top row) during and shortly after therapy for a circular scanned HIFU therapy protocol in a phantom. 58

Figure 3.10 1-D lateral strain profiles along *R* in figure Figure 3.9 at time t=2, 4, 6,8 and 10 seconds after HIFU therapy commences (-o-) and the corresponding Gaussian fits (—) to each curve. 59

Figure 3.11 Gaussian radius at various times during HIFU heating relative to value at *t= 2* s for 1-D strain profiles along R in Figure 3.9. 59

Figure 3.12 Strain amplitude at various times during HIFU heating relative to value at t= 2 s for 1-D strain profiles along R in Figure 3.9 60

Figure 3.13 (a) Schematic representation of the hotwire experiment setup for quantitative temperature estimation. 62

Figure 3.14 Schematic of experiment setup for *c(T)* measurements (*Picture courtesy of Lafon et.al., [101]*) 63

Figure 3.15 Illustration of typical waveforms acquired at the receiver transducer that are used to compute the sound speed of the gel phantom sample. 65

Figure 3.16 Sound speed versus temperature curve for polyacrylamide gel phantom used to invert ultrasound echo shift estimates to temperature 65

Figure 3.17 (a) A screenshot of the HDI 1000 ultrasound scanner B-mode image showing locations of thermocouples and heating wire (b) Temperatures estimated from sound speed change by processing the RF data incorporating the information from the independently measured c(T) curve at t= 19 seconds. 66

Figure 3.18 Comparison of time profiles of temperature at location of thermocouple 1 in Figure 3.17. 67

Figure 3.19 Block diagram illustration of algorithm to monitor change in scattering properties. 68

Figure 3.20(a) Illustration of typical parameters used in the algorithm. (b) Spectrum of typical RF line segment from bovine liver tissue. 70

Figure 3.21(a) Standard M-mode display for a scanline passing through the HIFU focal zone (b) Spectral color M-mode display for the same line. 71

Figure 4.1 Block diagram illustrating model-based temperature estimation approach for monitoring thermal therapy. 78

Figure 4.2 Schematics illustrating the experimental protocol for the BHTE model-based noninvasive temperature estimation approach for HIFU therapy monitoring. 80

Figure 4.3 Schematic diagram showing the relative orientation of the HIFU transducer, imaging probe and HIFU beam geometric focus 81

Figure 4.4 Flowchart of iterative minimization based technique to estimate A_{max} and R based on equation (4.8) 83

Figure 4.5 Schematic of experimental setup for noninvasive K estimation. The setup is similar to that shown in Figure 2.8. 86

Figure 4.6 Schematic of experimental setup for transient hot-wire technique....88

Figure 4.7 B-mode image along a cross-section illustrating the experimental setup for the transient hotwire method. 89

Figure 4.8(a) $s(r,t)$ and (b) $\varepsilon(r,t)$ at times t=1 s through 15 s (after HIFU heating pulse was turned off) at intervals of 2 seconds for an A-line passing through center of HIFU focal region. 91

Figure 4.9 Zero-lag cross-correlation σ_i versus depth at iteration 0 (o) and at final convergence (□) of the BHTE model-based strain estimation algorithm....91

Figure 4.10 Plot of Gaussian radius $R(t)^2$ versus time t estimated from a RF data set acquired in the alginate phantom....92

Figure 4.11(a) Temperature profiles measured using thermocouples placed around the nichrome heating wire in the *transient hotwire experiment*....93

Figure 4.12 Plot of the ratio between *estimated* thermal diffusivity and *true* value input into the simulation over 50 iterations. 97

Figure 4.13 Simulated temperature profile at the geometric focus of a HIFU transducer during heating. 98

Figure 4.14 Photograph of diaphragm of stethoscope and microphone assembly used for boiling detection. 100

Figure 4.15 Normalized experimentally measured 2-D acoustic pressure profile of HIFU transducer. 102

Figure 4.16 Normalized 1-D transverse profile of acoustic pressure distribution for the HIFU transducer. 102

Figure 4.17 Plot showing relation between input electrical power and output acoustic power for the HIFU transducer used in the experiments for noninvasive estimation of Q. 103

Figure 4.18 Time domain output of stethoscope recorded during a HIFU exposure lasting 50 seconds. 103

Figure 4.19(a) Typical time domain output of stethoscope recorded during a HIFU exposure lasting approximately 50 seconds as in Figure 4.18. (b) Spectrogram of the time domain signal shown in (a) computed using the Short Time Fourier Transform (STFT). 104

Figure 4.20 Noninvasively detected boiling times for five exposures at two HIFU intensities in the alginate phantom 105

Figure 5.1 Flowchart illustrating the iterative optimization technique for noninvasive estimation of $\varepsilon(T)$. 112

Figure 5.2(a) Finite element mesh (b) Normalized acoustic intensity profile in dB scale and (c) Spatial temperature distribution obtained using the multiphysics finite element modeling tool—FEMLAB™. 115

Figure 5.3 Photograph of experimental setup for invasive measurement of $\varepsilon(T)$ using waterbath setup 116

Figure 5.4 (a) B-mode image of sample immersed in water tank during heating. (b) RF echoes over the axial distance represented by the rectangular segment (A-B) in (a) for the scanline shown by the dotted line. 117

Figure 5.5 Plot of experimentally measured temperature induced strain ε as a function of temperature and polynomial fits to the data 118

Figure 5.6 Comparison between noninvasive and invasive (waterbath) estimates of $\varepsilon(T)$ 119

Figure 5.7 Block diagram representation of iterative optimization based technique for noninvasive temperature estimation 120

Figure 5.8 Schematic diagram of thermocouple holder used to position thermocouples around the geometric focus of the HIFU transducer. *Drawing courtesy of Andy Proctor* 122

Figure 5.9 Photograph of experimental setup for noninvasive temperature estimation and validation using thermocouples. 123

Figure 5.10 B-mode image showing the location of the three thermocouples, HIFU transducer and imaging probe 124

Figure 5.11 Illustration of the technique for noninvasive temperature estimation at iterations 1, 3, 5 and 10. 126

Figure 5.12 Comparison between noninvasive temperature estimates and readings from in situ thermocouples placed at transverse distances of 1, 3 and 4 mm from the HIFU focus. 127

Figure 5.13 Spatial profiles showing the temperature evolution around the HIFU focus at times t=1, 2, 4, 7 and 8 s after the HIFU therapy delivery started. 127

Figure 6.1 Photograph of turkey breast muscle tissue sample placed in the degassing chamber 131

Figure 6.2 (a) Tissue sample suspended by a sewing thread from a clamp and held in place near the center of the sample holder (b) Alginate gel is poured to encase the tissue 132

Figure 6.3 Plot of square of Gaussian radius $R(t)$ versus time after the HIFU heating pulse was turned off. 134

Figure 6.4(a) Plot showing output of stethoscope during HIFU therapy delivery (b) Spectrogram of stethoscope output shown in (a) 135

Figure 6.5 Plot illustrating detected boiling onset times for four different turkey breast muscle samples 136

Figure 6.6 Plot of temperature induced strain (ε) versus temperature (T) measured using the waterbath experiment setup. 137

Figure 6.7 Linear least squares fit to $\varepsilon(T)$ mapping in the temperature range between 22 to 40 degrees. 138

Figure 6.8 Comparison between noninvasively estimated $\varepsilon(T)$ slope values and ground truth measurements obtained using the waterbath setup 139

Figure 6.9 B-mode image showing thermocouples inserted in the turkey breast tissue sample. 140

Figure 6.10 Comparison between thermocouple readings and noninvasive temperature estimates at 1, 3 and 4 mm radial distances away from the axis of the HIFU transducer. 140

Figure 6.11 Spatial maps illustrating the temperature evolution around the HIFU focus at various times during and after HIFU therapy delivery 141

Figure 6.12 Comparison between BHTE computed temperature profiles and measured thermocouple profiles for a 45 second HIFU exposure. 143

Figure A.1 Flowchart of simulated RF data generation scheme 165

Figure A.2 (a) Simulation geometry with axisymmetry along the HIFU beam propagation axis (b) Finite element mesh with higher mesh element density near the focal zone of the HIFU transducer. 166

Figure A.3 Temperature profile computed using the finite element implementation of the BHTE 167

Figure A.4 Scatterer distribution along a RF A-line. 168

Figure A.5 (a) Ultrasound transmit pulse used in the simulations with center frequency of 5MHz and bandwidth of 50%. (b) Frequency spectrum for the pulse shown in (a). 168

Figure A.6 Scatterer shift along the depth direction 169

Figure A.7 Simulated RF signals generated before therapy commenced and during heating. 170

Figure B.1(a) B-mode image showing the location of the HIFU focus. The HIFU transducer is placed at the left of the image. (b) Temperature distribution in and around the HIFU focus in degrees Celsius along the *red* vertical line in (a) 172

Figure B.2 Linear and quadratic $\varepsilon(T)$ profiles 172

Figure B.3 Simulated strain (ε) profiles for (a) Linear and (b) Quadratic $\varepsilon(T)$ relationship 173

Figure B.4 Scatterer location shift profiles for the (a) Linear and (b) Quadratic $\varepsilon(T)$ relationship corresponding to the strain profiles in Figure B.3 174

Figure C.1 Screen shot of graphical user interface developed for analysis of RF data acquired from the HDI 1000 ultrasound scanner. 176

Figure C.2 Screen shot of graphic user interface designed to implement the noninvasive heat source estimation technique 177

Figure C.3 Screen shot of the graphical user interface developed to implement the noninvasive boiling onset detection technique. 178

LIST OF TABLES

Table 4.1 Acoustic and Thermal parameters used to generate simulated RF lines for validation of ultrasound-based thermal diffusivity K estimation algorithm 96

Table 4.2 Comparison between noninvasively estimated *in situ* heat source (Q_s) and calculated heat source (Q_{cal}) 106

Table 6.1 Comparison between estimated heat source and calculated heat source.....136

ACKNOWLEDGEMENTS

I am grateful to my advisor Dr. Peter Kaczkowski for his valuable guidance and encouragement throughout my doctoral studies. I thank Dr. Lawrence Crum for his support, encouragement and helping me stay focused. I am grateful to Dr. Kirk Beach for his valuable feedback on the various aspects of this research project. My sincere thanks are due to Dr. Blake Hannaford and Dr. John Zahorjan for serving on my dissertation supervisory committee.

I thank my parents and sister for their constant encouragement and patience during this long journey through graduate school in pursuit of the doctoral degree. I gratefully acknowledge the assistance and support of my colleagues and friends in the Center for Industrial and Medical Ultrasound (CIMU) and Department of Electrical Engineering at the University of Washington.

DEDICATION

To my late grandparents

1. INTRODUCTION

1.1. High Intensity Focused Ultrasound

High intensity ultrasound fields can be focused on deep seated regions within the human body. If sufficient sound energy is concentrated within the focal volume, the temperature in that region is raised to levels at which the constituent cells are killed. Figure 1.1 shows a schematic diagram of the principle of this technique, which is referred to as High Intensity Focused Ultrasound (HIFU) [1-3] or Focused Ultrasound Surgery (FUS) [4-7]. The focusing of ultrasound can result in high acoustic intensities (measured as power density in W/cm^2) at the focus. An intensity gain of 100 to 1000 times can be achieved in the cross-sectional area of the beam at the focus, resulting in intensities upward of 1000 W/cm^2, 4-5 orders of magnitude greater than that of diagnostic ultrasound systems. The technique has potential applications in any medical field that may benefit from the selective destruction of tissue volumes. Recent clinical interest has concentrated on treating soft-tissue cancers [8-10], debulking enlarged prostates (benign prostatic hyperplasia) [10] and acoustic homeostasis [11-13]. HIFU provides the ability to ablate localized tissue volumes without damaging intervening and surrounding tissue, thus eliminating the need for incisions – a feature that distinguishes it from other widely used ablative therapies such as Radio Frequency ablation [14-16].

HIFU has a different philosophy from conventional hyperthermia in which the temperature is raised a few degrees above body temperature and maintained for a relatively lengthy time, typically on the order of minutes [17-19]. In HIFU, the temperature typically rises by more than 40-50°C in a few seconds with increases up to 70°C in one second having been reported [20]. Therapeutic temperatures exceeding 50°C lead to irreversible cell destruction and above 80-90°C ("thermonecrosis"), cystic cavities due to boiling or cavitation can be induced [21]. The rapid deposition of thermal energy leads to a peak temperature rise that is independent of advective cooling by blood flow—an important consideration for tissues in which the vascular pattern is not completely known or predictable [1]. One consequence of the rapid heating to cytotoxic temperatures

is that there is a very narrow boundary between live cells and dead cells at the edges of the focal volume. The volume of dead cells is referred to as a *lesion*. This method of cell killing is commonly called *thermal ablation*.

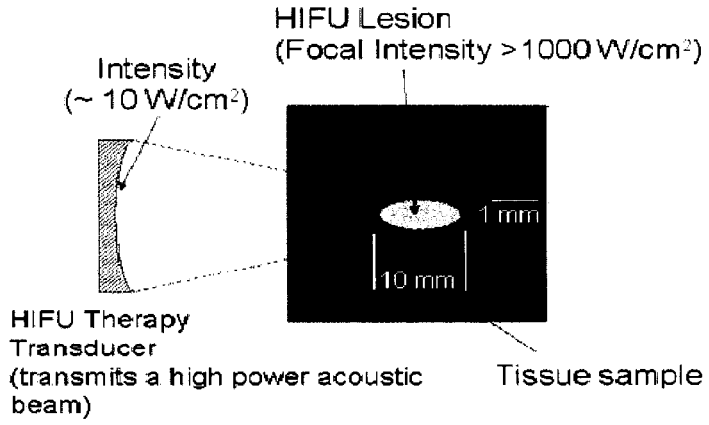

Figure 1.1 Principle of HIFU

At the high acoustic pressures employed in HIFU, the possibility of the presence of cavitation effects in addition to the thermal mechanism is significant. Acoustic cavitation is defined as the phenomenon in which the pressure wave, during its negative swing, can draw gas out of solution, and the bubbles thus formed may be set into oscillation [22]. A purely thermal technique of inducing the lesion during HIFU therapy has the advantage that the shape and position of the lesion can be accurately predicted while cavitation renders the tissue destruction less predictable [1, 23, 24].

1.2. Image Guided Therapy

As important as the therapy delivery components used in HIFU therapy is the adjunct imaging component. Since HIFU is a noninvasive modality, providing an imaging capability concurrent with treatment is a necessity in a clinical setting. Noninvasive imaging methods are preferable since the ability to use invasive devices in deep seated tissue regions (which are typically regions of interest for HIFU) is severely restricted. The potential role of noninvasive imaging methods in facilitating HIFU can be described as:

a) *Planning,* to identify and target the exact location of the abnormal tissue to be treated,
b) *Guidance,* that includes imaging of the treatment site at pre-ablative intensities to determine the location of the therapy beam and provide feedback on local beam geometry,
c) *Monitoring,* which includes the ability to provide feedback on treatment progress and ensure optimal therapeutic dose control, and,
d) *Post-therapy follow-up* imaging to assess treatment efficacy

A number of imaging modalities have been proposed to achieve some or all of the above objectives in a noninvasive manner. These include X-ray, Magnetic Resonance Imaging (MRI) and a number of variants of ultrasound based methods [25, 26]. A brief overview of the applicability of each of the methods for imaging HIFU therapy is given below.

1.2.1. X-ray

X-ray imaging was the earliest imaging modality employed for guidance of HIFU therapy. X-ray images were used both to map the area of treatment and to subsequently monitor the HIFU lesion formation for treatment of Parkinson's disease [3]. Currently, several ultrasonic thrombolysis approaches that use catheter systems to deliver the ultrasound energy are performed under fluoroscopy and X-ray guidance [27]. *However, X-ray is an ionizing imaging modality and can deliver high doses to both patient and clinician in a real-time setting.*

1.2.2. Magnetic Resonance Imaging

Magnetic Resonance Imaging (MRI) is a relatively new method of guidance for HIFU therapy and offers several advantages. Unlike X-ray based methods, MRI produces no ionizing radiation. MRI can provide information on functional and physiological parameters of tissues, including diffusion, perfusion, flow, and temperature. This latter capability is particularly useful in HIFU therapy because it can be used to detect tissue damage induced by thermal ablation. Correct targeting is established using a verification

test pulse of low-energy dose that does not cause permanent tissue damage [28]. Tissue temperatures in the therapeutic ultrasound field are available within approximately 5 s after treatment completion, with a resolution of approximately 1°C [29]. Follow-up evaluation of HIFU-induced lesions can also be done by MRI. The high correlation of lesion formation with temperature provides a means to measure the treatment volume and quantify tissue damage.

However, high costs are associated with MRI; it also requires a special environment that can hinder patient accessibility; and minimal use of metal parts in the HIFU assembly is necessary to prevent distortion of the MRI images [3]. In addition, the temporal resolution is limited in MRI due to the slow image acquisition frame rate [30-32]. Hence, MRI is inherently not real-time, resulting in temporal misinterpretation of temperature profiles and lengthened treatment times. *These limitations are currently an impediment in the widespread adoption of MRI guided HIFU therapy systems.*

1.2.3. Ultrasound

Ultrasound based methods offer significant advantages in guiding acoustic therapy compared to other options. These include:

1. Imaging can be done in real time,
2. Being a non-ionizing modality, the side effects can be kept to a minimum,
3. It is relatively inexpensive,
4. By employing ultrasound imaging methods, the therapy and imaging hardware can be easily integrated into the same assembly,
5. The effects of path distortion can be minimized because both the therapy beam and imaging beam would be affected similarly and hence remain registered with respect to each other.

Several methods of ultrasound based imaging techniques to monitor HIFU therapy have been proposed and investigated. These methods can be broadly classified based on the properties of tissue whose changes are tracked to provide the image guidance.

1.2.3.1. Monitoring changes in the elastic modulus

Necrosis of tissues and cells as a result of coagulation of proteins is seen to be the main mechanism responsible for histological changes observed in regions treated with HIFU [3, 33-36]. Protein denaturation due to ablation elevates the elastic modulus of treated soft tissue [37-39]. HIFU lesions induced in liver are approximately six to twelve times stiffer than normal tissue [40]. Several ultrasound-imaging techniques such as Sonoelasticity, Elastography [41], Vibro-acoustography [42] and Acoustic Radiation Force Imaging (ARFI) [44] recently developed to differentiate between normal soft tissues and hard lesions have been proposed as a method of visualizing the region treated by HIFU. Shi et.al. [40] describe a technique, based on sonoelasticity [134], where a low-frequency vibration (< or = 5 Hz) was applied to porcine liver samples in which HIFU lesions had been induced and the resulting velocity pattern within the sample was measured using Doppler spectral analysis to map the treated region. The spatial extent of treated regions using this technique compared favorably with independent geometric measurements of the gross pathology. Righetti et. al. [37] showed a high correlation *(r=0.92)* between the damaged areas in maps obtained by employing elastographic processing methods and the corresponding areas as measured from the gross pathology photographs. However, these noninvasive measurements were only made before and some time after an HIFU lesion was created, permitting detection of permanent changes in tissue properties. They do not address the problem of monitoring the formation of the lesion during therapy. Ultrasound-stimulated acoustic emission (USAE), similar in principle to vibro-acoustography is a relatively new method for the estimation of mechanical properties using a localized, remote harmonic excitation [42]. It relies on the principle that two focused beams overlapping at a remote region inside the tissue and oscillating at slightly different frequencies can generate a mechanical force (or, radiation force) that excites the tissue locally and causes it to vibrate at the difference frequency. The feasibility of using a frequency shift of the resonant peaks of the USAE signal for monitoring the tissue stiffness variation with temperature has been recently reported [43]. However, the authors report that the sensitivity of the resonance frequency shift to

stiffness change is considerably reduced in certain temperature ranges encountered in HIFU. Furthermore, to map a 2-D spatial region using this technique, the entire dual transducer assembly is mechanically translated in a raster format and a measurement is made at each motion step along the path. This significantly increases the treatment time and limits the applicability of this technique in a real-time scheme which is desirable for HIFU lesion monitoring. Acoustic radiation force impulse (ARFI) imaging is a radiation force-based imaging method that provides information about the local mechanical properties of tissue [44]. ARFI imaging uses short-duration acoustic radiation forces to generate localized displacements in tissue, and these displacements are tracked using ultrasonic correlation-based methods. The tissue response to these forces can be monitored both spatially and temporally. Displacement magnitude is inversely proportional to local tissue stiffness and is typically on the order of 10 μm. A novel method of detecting subdermal lesions through the use of ARFI was recently proposed [45]. For the results reported in their paper, ARFI-induced displacements were about two to three times greater in normal healthy tissue compared to within the necrosed tissue region. The ability of ARFI imaging to clearly distinguish lesions from surrounding healthy tissues arises from the large increase in elastic modulus in the lesion. However, this ARFI-based approach was also focused on detecting permanent changes in tissue mechanical properties before and after the therapy. They do not address the problem of monitoring the formation of the lesion during therapy. Lizzi et. al. [46] also developed an acoustic radiation force based monitoring technique and demonstrated that radiation force induced displacements in normal untreated tissue were about 50% greater than that in the treated region. They suggest that "push" pulses that deliver the radiation force and associated imaging pulses used to track the displacements could be interspersed at regular intervals during therapy exposures, and therapy could be continued until it results in a predetermined alteration in the magnitude and spatial extent of tissue motion characteristics indicative of the desired lesion.

1.2.3.2. Monitoring changes in Sound speed, Attenuation and Backscatter

Changes in *attenuation* [47], *backscatter coefficient* [48] and *speed of sound* [49] in biological tissue with temperature rise have been reported. In a recent study, comparison of images of all of these properties with optical photographs for the same tissue sample treated with HIFU provided a qualitative demonstration that attenuation coefficient was the most useful and backscattering coefficient was the least useful acoustic parameter for visualizing the lesions [50]. Quantitatively, the data demonstrated significant increases in attenuation coefficient (approximately 300%) and sound speed in lesioned liver relative to normal, whereas backscattering was shown not to change in a significant manner except when undissolved gas is the mechanism for increased acoustic scattering.

In order to be able to detect changes in these acoustic tissue properties noninvasively, several approaches have been proposed. The most obvious solution entails the use of B-mode imaging, which is a commercially available ultrasound imaging modality that can show changes in backscatter. This method is unfortunately not optimal for visualizing thermal damage since the acoustic backscatter from ablated volumes created primarily by a thermal mechanism does not change significantly [1]. However, if gas bubbles have been produced either by acoustic cavitation or by the boiling of tissue water, then they will be highly reflective and the region will be visible on B-mode imaging. Vaezy et. al. [51] developed a real-time ultrasound B-mode based imaging technique to visualize the treated region during HIFU based remote acoustic homeostasis procedures. Their approach also relies on the ability to visualize a hyperechoic spot on the B-mode image appearing possibly due to bubbles to target and monitor the progress of therapy. It was shown that the time for the hyperecho to appear was inversely proportional to the applied HIFU intensity. The changes on B-mode images, however, are typically short lived, invariably appear sometime after therapy commences and are almost always associated with the lesion having already been formed. It has also been shown that there is no correlation between the degree of backscattering and degree of tissue damage [52]. B-mode imaging by itself therefore does not effectively provide

quantitative or parametric information that can be used to reliably track changes in the different stages of therapy.

A noninvasive technique for making local measurements of attenuation variations by tracking changes in the spectral content of the raw ultrasound backscatter (commonly referred to as "Radio Frequency (RF)") has been reported for imaging HIFU lesions [53]. It was shown that changes in the mean attenuation in the 4-7 MHz range varied significantly (in the region of 86% of the initial level) in comparison to measurements performed without forming lesions. However, the comparison was only made on data acquired prior to and after treatment. Hence, only permanent changes in attenuation were tracked using this technique. Bloch et. al. [49] developed a system to measure sound speed and attenuation changes as a function of temperature. Experiments were performed in freshly excised porcine liver samples. Their results demonstrate that the sound speed increases monotonically as the tissue is heated to 50°C and then decreases with continued heating. The results were consistent with previously reported results in the literature [54]. The maximum change in the sound speed was on the order of 1%. However, these measurements were made in transmission mode and were invasive in nature. Attempts to measure changes in speed of sound with temperature noninvasively have been made early on [55]. To measure the speed of sound, it is necessary to measure both distance and time of flight. Although this can be achieved relatively easily in transmission mode, it is difficult to do reliably using reflection ultrasound commonly used in a clinical setting [56].

All of the above methods seek to image changes in tissue properties affected by the temperature rise induced by HIFU. In order to use the extensive literature relating treatment outcomes to measured thermal dose (which have been reliably used to predict the outcome of therapy) [57], extensive calibration would be required to relate the properties discussed above to temperature so that the thermal dose can be computed based on such measurements.

1.2.3.3. Monitoring change in Temperature

There exists considerable motivation for the development of techniques for directly estimating the temperature through noninvasive methods for monitoring therapy progress. As is well known, the toxic effect at high temperatures on cells depends both on the temperature achieved and the time for which these temperatures are maintained [58]. It has been shown for many tissue types that it is the *temperature history* that determines therapy effectiveness and not the temperature value by itself [59]. This can be quantified using the quantity known as the *thermal dose* which was first introduced in the hyperthermia treatment literature. The thermal dose for cases where the temperature varies during the treatment time can be mathematically computed using the formulation proposed by Sapareto and Dewey [60], as,

$$\begin{aligned} TD_{43}(x, t_{end} - t_0) &= \sum_{t=t_o}^{t_{end}} 2^{T(t,x)-43} \Delta t, \ \mathrm{T} >= 43 \\ TD_{43}(x, t_{end} - t_0) &= \sum_{t=t_o}^{t_{end}} 0.5^{T(t,x)-43} \Delta t, \ \mathrm{T} < 43 \end{aligned} \tag{1.1}$$

where, T is the temperature at time t, Δt represents the time interval between consecutive temperature measurements, TD_{43} is the thermal dose referenced to 43° C, x is the spatial location in tissue where the thermal dose is computed, t_o and t_{end} represent the start time and end time of treatment respectively. In words, the thermal dose can be stated as follows: Given a temperature versus time profile at the treatment site that results in a thermal dose TD_{ref} (referenced to temperature T_{ref}) and a certain therapeutic outcome, the same outcome can be achieved by maintaining the tissue at the temperature T_{ref}.

Equation (1.1) has typically been used in hyperthermia treatments where the treatment times are on the order of a few minutes and stays near 43° C. Some authors have extended the use of this definition to HIFU treatments and have reported that TD_{43} = 240 minutes is a suitable threshold for tissue necrosis in HIFU therapy [59, 61]. It may be noted, however, that TD_{43} = 240 minutes is equivalent to a time at 56° C of 1.7 s. It

would seem more rational to use 56° C as the reference temperature for HIFU since treatment times are typically on the order of a few seconds [58].

From equation (1.1), it can be seen that estimating the temporal and spatial profile of temperature rise during treatment is essential for computing the thermal dose. This motivates the development of noninvasive temperature estimation methods. Temperature measurements obtained during therapy can then be used to dynamically update the treatment parameters by employing a feedback mechanism to optimize the applied dose [62]. With the recent advent of multi-element heating devices such as therapeutic phased array based systems [63, 64], it is possible to dynamically change the therapeutic power applied and spatial distribution of the intensity profile to ensure optimal thermal dose delivery to the target tissue region. These phased array systems typically have a number of transducer elements whose pulse amplitude and duration can be independently varied to achieve the optimal dose distribution in tissue. Dose optimization methods have been extensively investigated for applications in hyperthermia using temperature measurements from a limited number of fixed invasive sensors [65]. This however provides less information than is necessary to produce satisfactory temperature distributions to assess thermal dosimetry properly. The performance of feedback based therapy delivery systems would be greatly improved if temperature distributions over the entire treatment volume were made available to the therapy controller [66]. These optimization schemes can be extended to HIFU applications if parameters such as temperature can be reliably tracked and used for feedback, possibly enabling real-time control of the applied thermal dose.

Using equation (1.1) to compute thermal dose, MRI thermometry studies for HIFU imaging have reported that the estimated size of the necrotic area, based on the thermal dose calculated from MRI temperature maps, corresponded well with the actual lesion size determined by histology and conventional MRI images obtained 5 days post-treatment [57]. Clinical applications of MRI guided temperature imaging recently reported include treatment of breast tumors [67], uterine fibroids tumors [68] and prostate cancers [69].

Ultrasound imaging being a convenient, cost-effective, real-time imaging modality is an attractive option for the development of temperature monitoring and guidance systems and has the potential to overcome many of the limitations encountered in MRI, microwave radiometry and impedance tomography based methods [70]. A number of approaches to estimate temperature from backscattered ultrasound have been reported in the literature. Simon et. al. [70] reported a technique based on detection of shifts in echo location of backscattered ultrasound from a region of tissue undergoing thermal therapy. The echo shifts are due to the combination of the local temperature dependence of speed of sound and thermal expansion in the heated region. The echo shifts are estimated from the correlation of successive backscattered ultrasound frames, and the axial derivative of the accumulated echo shifts was shown to be proportional to the temperature rise. The estimated temperature maps were overlaid on the gray-scale ultrasound images to illustrate the applicability of this technique for image guidance of focused ultrasound thermal therapy. Another approach from the same research group [71] was based on the discrete scattering model and the observation that most biological tissues are semi-regular scattering lattices. The spectrum of the backscattered RF signal collected with a diagnostic ultrasound transducer from a semi-regular tissue sample exhibits harmonically related resonances at frequencies determined by the average spacing between scatterers along a segment of the A-line. It was shown that these resonances change with changes in the tissue temperature within the processing window. Changes in the resonances were linearly proportional to temperature with the proportionality constant being determined by changes in the speed of sound with temperature and the linear coefficient of thermal expansion of the tissue. Miller et. al. [72] performed detailed simulation studies to verify if the echo shifts in the RF signals caused by low temperature rises can be accurately determined and whether such a technique can be used to locate the focal spot of the therapy beam. Their experimental results [73] further confirmed that imaging the echo shift information was a feasible method of visualizing the location of the HIFU focus. These authors conclude that the techniques are most suitable for treatment planning and assessment of the acoustic beam at the focal spot. Hyperthermia treatment, where the

maximum temperature rise expected is less than 10°C above body temperature, or assessment of the geometry of the therapeutic ultrasound beam in a HIFU application where sub-ablative intensities are employed, are potential target clinical applications for the methods proposed in this set of papers.

Another ultrasound based method for noninvasively estimating the temperature rise was based on tracking the changes in backscattered energy [66]. These results were also reported for the temperature range 37-50° C, which is below the temperature range encountered during HIFU exposures at ablative intensities. The paper asserted that changes in ultrasound backscatter energy can be correlated to temperature change. To obtain quantitative temperature information from this technique, a set of calibration experiments would have to be performed to obtain the relationship between temperature and the backscatter energy and this process is complicated since significant variability amongst tissue types exist.

Two recent papers [74, 75] have applied the approach proposed by Simon et. al. [70] for monitoring temperatures in the therapeutic range during Radio Frequency Ablation [76]. They however assumed that the local echo location shifts were linearly proportional to temperature over the entire temperature range and computed the proportionality constant in a set of independent calibration experiments. The temperatures measured on thermocouples attached to the RF probe were in agreement with noninvasive ultrasound-based temperature estimates. They hypothesized that for the particular geometry used in the experiment and the boundary conditions, the effects of thermal expansion must have reduced the impact of the non-monotonic nature of the sound speed versus temperature curve and a monotonic linear relation was therefore adequate. However, this assumption was not verified explicitly in the papers and may not be applicable in all experimental scenarios.

1.3. Key limitations of current ultrasound-based temperature estimation methods

All the temperature estimation techniques described in section 1.2.3.3 were used to obtain temperature maps in phantoms and animal tissue, where the temperature rise was

limited to a maximum of about 10-15° C above body temperature. In each of the techniques, an invasive calibration experiment was first performed to determine the relation between temperature and echo location shifts measured from the ultrasound backscatter. The *low sensitivity* of the sound speed change to temperature beyond 50°C (sound speed versus temperature relationship flattens out for most soft tissues near this temperature) makes direct mapping of RF echo location shifts to temperature *difficult and is a fundamental limitation of these methods*. Hence, these methods are not *directly applicable* for temperature monitoring during ablative thermal therapy applications such as HIFU.

1.4. Contributions of this dissertation

The goal of this research is to *develop and implement a noninvasive quantitative ultrasound-based temperature estimation technique, applicable over the entire therapeutic temperature range, for monitoring HIFU therapy.* The specific contributions of this dissertation are:

a. *Bioheat transfer model-based technique for temperature estimation*

   A model based approach for temperature estimation is employed that combines spatio-temporal constraints imposed by the underlying physical model for heat diffusion (Bioheat Transfer equation [77]) with the noninvasively acquired ultrasound backscatter data. This approach *addresses the problem arising from the lack of sensitivity of echo shift data to temperature over regions of the therapeutic temperature range* that limits the direct extension of earlier ultrasound-based temperature estimation methods for ablative therapy applications.

b. *Noninvasive estimation of mapping between ultrasound echo shift and temperature*

   The mapping relating the echo shift information to temperature is *noninvasively* estimated during a set of pre-therapy "calibration" HIFU exposures performed in the treatment region before therapy commences. This mapping can then be used to interpret measured echo shifts and estimate temperature in and near the

treated zone. This is a departure from previously reported temperature estimation techniques developed primarily for therapy guidance, wherein *a priori* knowledge of the mapping was assumed or invasively measured in an independent experiment.

c. *Noninvasive estimation of local tissue thermal properties using acoustic techniques*

Acoustic techniques for noninvasive estimation of local tissue thermal properties, namely, thermal diffusivity and heating rate have been developed in this dissertation. Although developed and presented herein as an integral component of the temperature estimation technique, these techniques can be independently employed in therapy planning and dosimetry, which is an important step required to accurately predict the applied thermal dose and plan the therapy protocol.

d. *Improved visualization of HIFU lesion formation*

Novel signal processing-based techniques were developed as part of the preliminary feasibility analysis to visualize the temporal evolution of the ultrasound backscatter acquired during and after HIFU therapy delivery. The results obtained demonstrate improved visualization of the treatment region compared to standard fundamental B-mode images, which is a standard imaging mode on all modern ultrasound scanners.

In addition, experimental data acquisition tools and numerical modeling capabilities to implement and evaluate the performance of the techniques described above were designed. Mostly notably, the ATL HDI 1000, a commercial ultrasound scanner, was modified by adding system software that permitted customized acquisition modes and access to the RF data (in demodulated and decimated form as I/Q). These details are provided throughout the dissertation.

1.5. Organization of this dissertation

In Chapter 2, a detailed description of the experimental software-based data acquisition system developed to acquire the raw ultrasound backscatter during HIFU

therapy is presented. The operation of the system is discussed along with a description of the custom developed operating modes and measured performance specifications. This system is used in all the experiments described in the subsequent chapters. In Chapter 3, a mathematical model describing the effect of temperature on ultrasound backscatter is presented first. Two signal processing-based algorithms designed to extract information from the ultrasound backscatter that are related to changes in tissue properties induced by HIFU are described. Results obtained by applying these noninvasive techniques in *in vitro* tissue mimicking phantoms and animal tissue experiments are presented.

The model-based noninvasive quantitative temperature estimation approach developed for HIFU therapy monitoring is introduced in Chapter 4. A description of the methodology is presented first. The calibration procedure designed to noninvasively estimate the local thermal parameters, namely, thermal diffusivity and heating rate *in situ* during HIFU exposures is then presented, followed by results from validation experiments performed in tissue mimicking phantom experiments. In Chapter 5, the model-based temperature estimation approach is described and the technique is validated in tissue mimicking phantoms. Chapter 6 is devoted to validating the temperature estimation algorithm developed in Chapters 4 and 5 in *in vitro* excised animal tissue samples. Conclusions and suggestions for future work are provided in Chapter 7.

2. SOFTWARE-BASED RF DATA ACQUISITION SYSTEM FOR HIFU THERAPY MONITORING

2.1. Introduction

As described in Section 1.2.3, several ultrasound-based techniques to noninvasively guide, monitor and assess the efficacy of HIFU therapy have been reported in the literature [30, 40, 47, 49, 53, 70, 72, 78, 79]. All of these signal processing based imaging methods greatly benefit from the ability to apply processing algorithms directly to the beamformed but otherwise unprocessed ultrasound backscatter data (commonly referred to as the "RF") that contains the amplitude as well as phase information. Figure 2.1 shows a block diagram representation of the signal flow in the receiver section of an ultrasound scanner for generation of B-mode image data. From the figure, it can be seen that B-mode (envelope detected) images preserve only the amplitude but discard the instantaneous phase of the signal. The loss of phase information adversely limits the ability to accurately track small ultrasound echo shifts that are typically fractions of a wavelength and commonly encountered in ultrasound temperature estimation applications. For the application of differential processing techniques between a pair of RF frames, it is desirable that the frames being compared are acquired with a minimal possible inter-frame delay to minimize de-correlation artifacts, and greater flexibility and control of data acquisition frame rate is desirable.

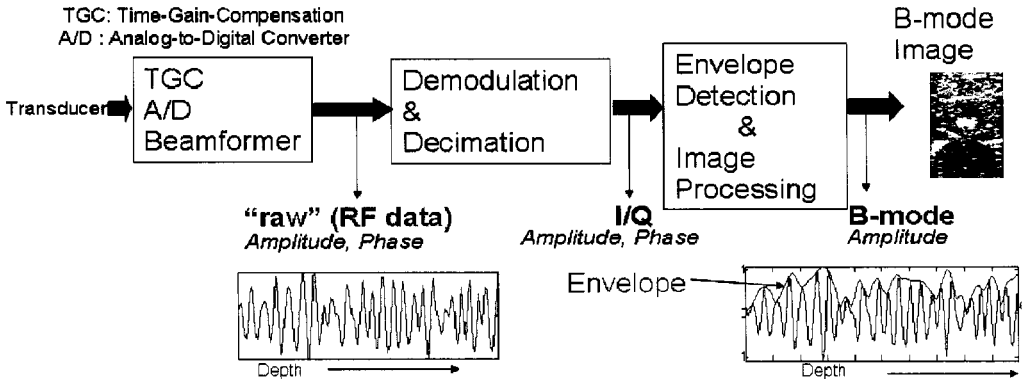

Figure 2.1 Block diagram representation of data flow in a commercial ultrasound scanner

In this chapter, an ultrasound RF data acquisition system developed in-house using a software-modified ATL HDI 1000 commercial ultrasound scanner (Philips Medical

Systems, Bothell, WA) for use in HIFU imaging applications is described. This system allows demodulated RF data access at relatively high frame rates useful for tracking the rapid yet subtle changes in tissue during HIFU treatment. A detailed description of the system features is presented in Section 2.2. The specialized software developed to control the system operation is described in Section 2.3. Custom modes of operation developed in-house that provide the ability to trade-off acquisition frame rate and lateral image widths are described in Section 2.4. The application of this data acquisition system for HIFU therapy monitoring is presented in Section 2.5. This flexibility is demonstrated in Section 2.6 through an application in the field of elastography [41]. All of the experiments on HIFU therapy monitoring described in subsequent chapters were performed using this system.

2.2. System Description

The ATL HDI 1000 diagnostic ultrasound scanner system [80] was introduced commercially in 1997 as the first such system with a dominantly software-based architecture; system development was halted in 1999, and production was discontinued by early 2000. Figure 2.2 shows a block diagram representation of the receiver section of the system architecture. The system beamformer consists of 64 transmit and 32 physical receive channels which can be multiplexed to provide 64/64 transmit/receive synthetic aperture acquisitions; the system can be used in synthetic aperture mode (64 channels) or in physical aperture mode (32 channels only). An analog TGC is applied to each receive channel. The A/D converter samples the input on each channel at 4 times the nominal center frequency (f_0). f_0 is typically set to be close to the center frequency of the received echo signal, taking into account the effects of attenuation occurring along the imaging beam path.

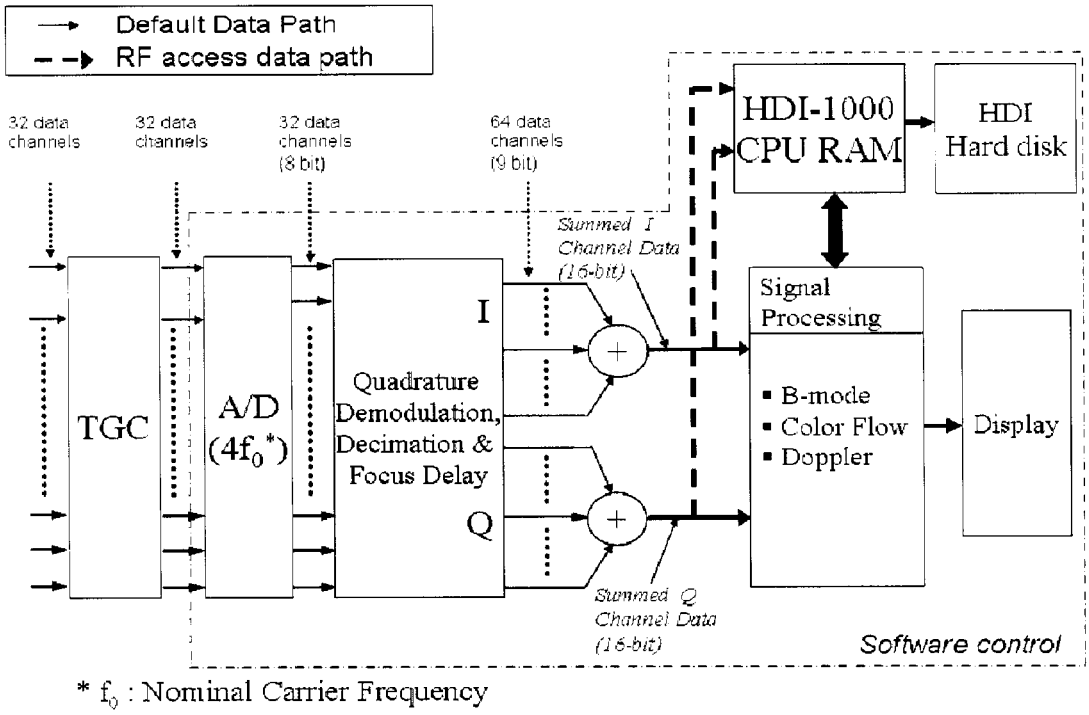

Figure 2.2 Block diagram representation of ATL HDI 1000 ultrasound scanner system architecture (receiver section) showing the internal data path in the default mode and in the custom-developed RF data access mode. Analog Time Gain Control (TGC) is applied to each of the 32 input channels followed by digitization at $4f_0$ with 8-bit precision. The data is quadrature demodulated and decimated, and focusing delays are applied to generate 32 channels each of I and Q data (each with 9-bit precision). Individual I and Q data channels are then summed to obtain 16-bit beamformed quadrature demodulated data, and routed either to HDI CPU RAM and HDI Hard disk, or to signal processing and display functions.

The digitized signal on each channel is then quadrature demodulated and decimated with a simple averaging algorithm to obtain baseband in-phase (I) and quadrature (Q) data. The I and Q data on the individual channels are delayed for dynamic focus and summed to obtain baseband summed quadrature data, beamformed along a particular scanline. In the default mode of operation, I and Q channels are processed by the signal processing block to obtain B-mode, Color flow or Doppler data, depending on the acquisition mode selected by the user. When RF data access is desired, the summed quadrature baseband data follows the path indicated by the heavy dotted line in Figure 2.2. The data are temporarily stored in a pre-allocated memory block within volatile RAM on the system computer (HDI 1000 CPU RAM in Figure 2.2). After the desired number of frames have been acquired and stored, the frames are copied to the hard-disk

as a binary file with additional fields containing information about the acquisition parameters necessary to interpret the RF data during offline processing. Since most of the system operation is controlled by software (dotted box in Figure 2.2), modifications to meet data acquisition requirements for research purposes can be made relatively easily. In our current setup, RF data access is supported for standard echo imaging (same transmitter configuration as for B-mode) but modifications of the software to store RF data for Doppler and M-mode can be achieved with modest additional effort.

The maximum size of the memory block reserved in the HDI 1000 CPU RAM for storing the acquired frames temporarily is 75 MB. It is based on a circular addressing scheme. Hence once the entire memory block is full after a series of sequential frame writes, the address counter is reset causing the buffer to wrap around and frames acquired thereon replace those stored earlier starting from the first in the current acquisition sequence. For a given set of acquisition parameters, the total number of frames that can be stored in the allocated memory block can be approximately calculated using the following formula that takes into account the dependence of acquisition depth and frequency on frame size,

$$\text{Total number of frames } (N_{max}) = \frac{M \times k}{D \times f}$$

where M = Allocated memory block (Maximum 75 MB), D = Acquisition depth, f = Center Frequency of transducer, k= scaling constant to be determined through a calibration test.

For an acquisition depth of 4.5 cm with the ATL CL 10-5 (Philips Medical Systems, Bothell, WA) linear scanhead, approximately 300 frames can be temporarily stored in HDI 1000 CPU RAM.

2.3. External System Control

The HDI 1000 system is based on a computer running a UNIX-like operating system (Amiga operating system). The software-dominant architecture on which the HDI 1000 is built allows for extensive external control of its operation, including front panel controlled acquisition parameters (imaging depth, focus positions, number of foci, TGC,

etc). In addition, the start of RF frame acquisition can be initiated from an external source with latency and jitter times on the order of a few milliseconds. Thus, RF data acquisition can be well synchronized with other instruments that are part of an experimental setup. Control commands from another computer are issued via Telnet, and acquired RF data can be transferred to that computer for off-line processing via FTP. A software master control program using LabVIEW™ (National Instruments, Austin, Texas) was developed to control the HDI 1000 system as well as other devices and instruments. Figure 2.3 shows the flow chart for the master control program which can be configured to interleave HDI frame acquisitions with a variety of external events such as robotic motion, therapeutic energy delivery, or other actuation and sensing functions.

The HDI 1000 system configuration is selected at power-up time, using the floppy disk controller to modify the boot sequence. Normal imaging operation defined by the manufacturer is the default startup mode (no floppy disk), but insertion of a "research mode" floppy disk prior to startup forces a customized initialization using special scripts residing on the floppy.

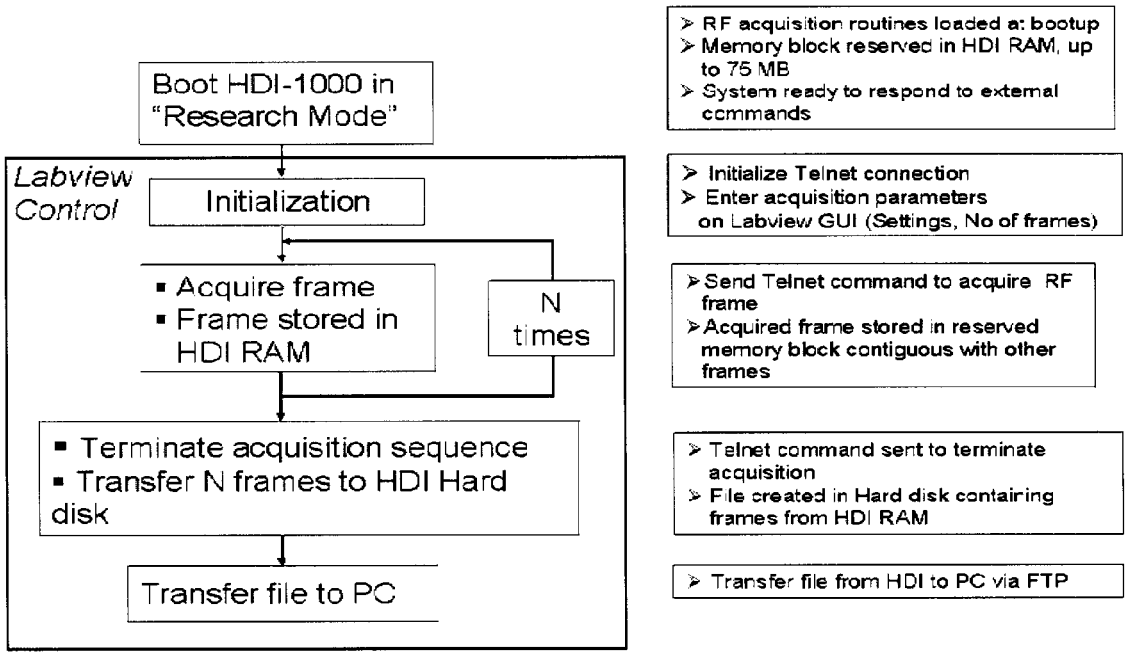

Figure 2.3 Flowchart for software master control program developed using LabVIEW™ to control RF data acquisition on HDI 1000. The bulleted list on the right summarizes the action of each block.

This flexibility allows the system to function both as a clinically approved ultrasound imaging scanner and as a RF data acquisition system for research use. These scripts allocate a buffer in the HDI 1000 RAM (see Figure 2.2) where acquired RF data frames are first stored, initialize directory paths and other acquisition control scripts for the research mode, and launch the Telnet communications program. The master control program, running on an external Windows® PC that is connected to the HDI 1000 via ethernet, then takes over imaging system operation. Specific acquisition settings for the current experiment are sent to the HDI 1000. In the simplest data acquisition mode, the control program periodically sends very brief commands to initiate each frame acquisition, based on user-specified settings for total number of frames to be acquired (N) and the desired frame rate. Each acquired frame is stored in contiguous blocks in the HDI 1000 RAM. Once the entire frame acquisition sequence is complete, in response to a final control command the set of frames residing in RAM are transferred to the HDI computer's hard disk and stored as a binary data file. Then, the data file is transferred to

the PC via FTP over the ethernet connection. The master control sequence used to simultaneously control the HIFU signal generation circuitry is described in Section 2.5.

2.4. Custom Acquisition Modes

The performance of algorithms used for motion and velocity estimation is greatly improved by acquiring data at high frame rates. In addition, high frame rate data acquisition allows speckle noise to be reduced by employing temporal averaging [81, 82] without compromising on temporal resolution. Typically, there is a trade-off between the number of scan lines per frame (the default is the maximum value of 128 scan lines corresponding to a lateral width of 2.5 cm for the intra-operative compact linear probe [CL10-5, Philips Medical Systems, Bothell, WA]) and the frame rate (the latter also depends on the maximum depth of the image). Two data acquisition schemes for increasing the frame rate using a reduced number of scan lines per frame have been implemented in this work. In this paper, they are referred to as 1) *reduced sector width* and 2) *sparse scanline* mode. Considerable improvements in frame rate are achieved in both these modes by controlling the beamformer firing sequence to capture only the desired number of lines and thus reducing the amount of data processing within the system.

In *reduced sector width* mode, a contiguous subset of the 128 lines making up the complete image is used to form a narrower 2-D image. Figure 2.2 shows B-mode images of the carotid artery reconstructed from the RF signals collected for a full lateral width of 2.5 cm (default). The system was then switched to the *reduced sector width* mode with lateral width set to 0.6 cm (32 scan lines) and another image was acquired with the scanhead placed at close to the same location. Figure 2.4(b) shows the B-mode image reconstructed from the RF signals for this acquisition. Both images were acquired using the compact linear probe (CL10-5). For this probe, the nominal center frequency (f_0) is 6.15 MHz and the sampling rate is 24.6 MHz ($4f_0$). The plot in Figure 2.5 shows the frame rates obtained in the default mode with full sector width (128 scan lines) and in the *reduced sector width* mode [lateral width of 0.6 and 1.25 cm] for an acquisition depth of 2.2, 4.5 and 8.2 cm using the CL10-5 scanhead. Corresponding to the axial depths of 2.2

cm, 4.5 cm and 8.2 cm, there are 176, 360 and 656 I/Q data points per scanline respectively. The frame rate is essentially inversely proportional to the lateral image width. This mode of operation is useful when data acquisition at high frame rates is desired and the lateral field of view can be compromised.

In the *sparse scanline* mode, the total lateral field of view is the same as for the default mode. However, a sparse subset of the total 128 scanlines is used to acquire the frame with inter-scanline spacing set to 2, 4, or 8 line widths. Figure 2.6(a) shows the B-mode image of the carotid artery [same region as Figure 2.4(a)] with a default scanline spacing of 1 (all 128 scanlines active). Figure 2.6(b) shows the reconstructed B-mode with the system setup for *sparse scanline* acquisition with an inter-scanline spacing of 4. This *sparse scanline* mode is well-suited for applications in which high frame rates are desired with full sector width, and a decrease in lateral resolution is acceptable. Figure 2.7 presents the frame rates obtained in the default mode (128 scan lines) and the *sparse scanline* mode for an acquisition depth of 2.2, 4.5, and 8.2 cm.

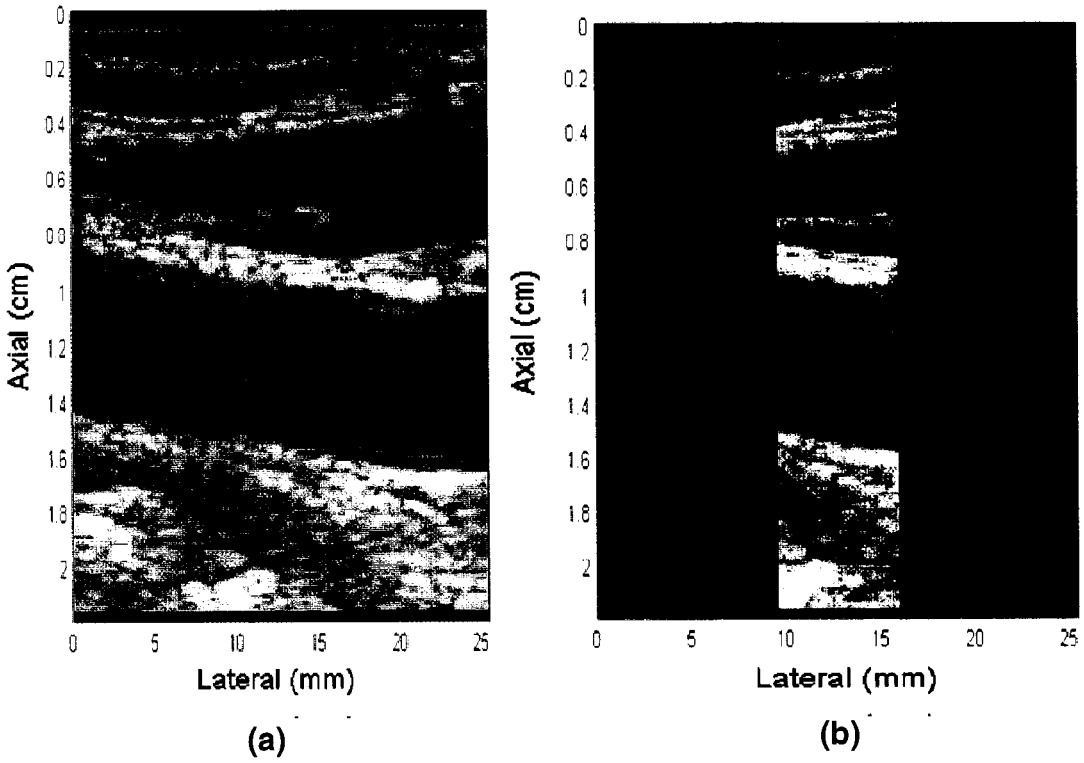

Figure 2.4(a) B-mode image of the carotid artery reconstructed from the RF signals collected for a full lateral width of 2.5 cm (default) (b) B-mode image reconstructed from the RF signals with system in reduced scanline mode [lateral width set to 0.6 cm (32 scan lines)]. Image was acquired with the scanhead placed close to the same location as for Figure 2.4(a)

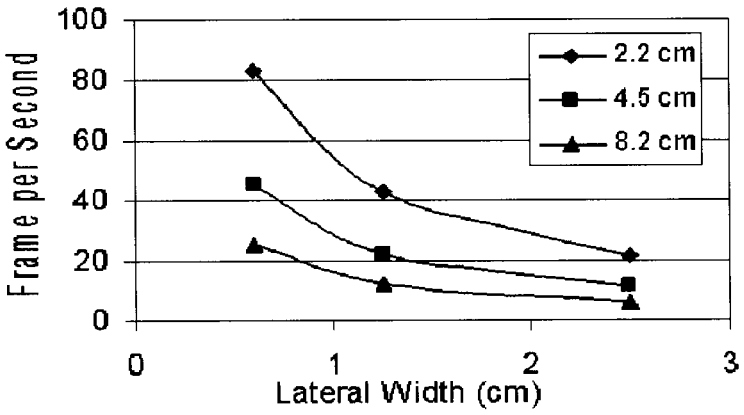

Figure 2.5 Plot of acquisition frame rate (frames per second) versus lateral width using CL 10-5 probe for axial depth settings of 2.2 cm, 4.5 cm and 8.2 cm with the system in *reduced sector width* mode. The lateral widths of 0.6, 1.25 and 2.5 cm correspond to 32, 64, and 128 contiguous scanlines, respectively

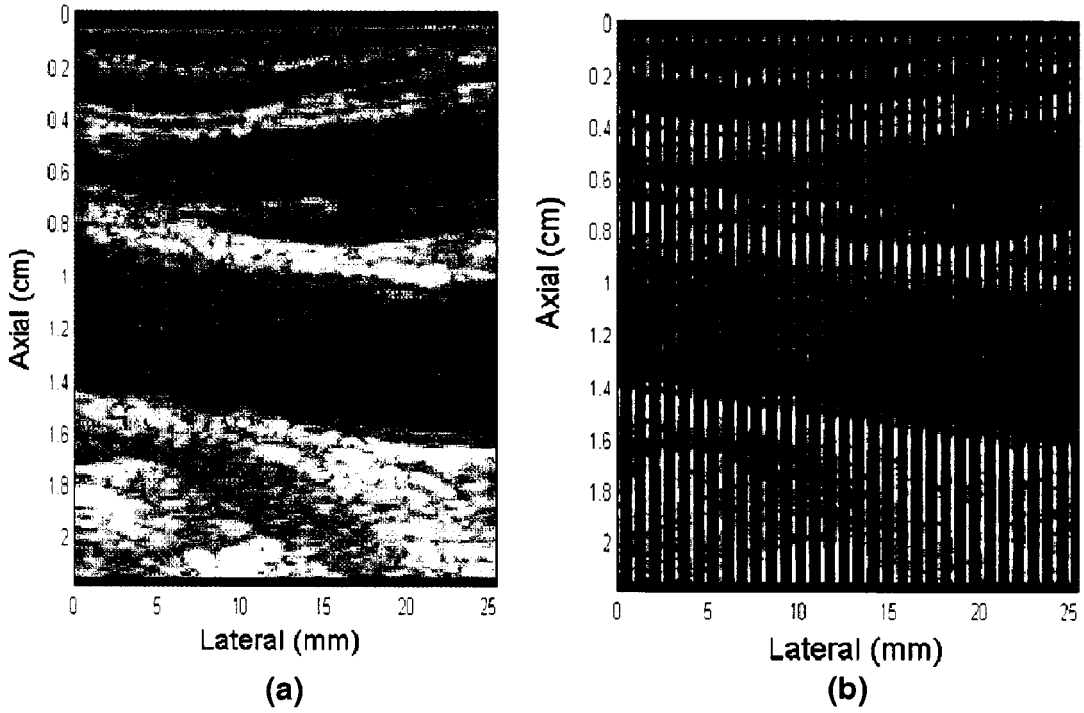

Figure 2.6(a) B-mode image of the carotid artery reconstructed from the RF signals collected for a full lateral width of 2.5 cm (default) (b) B-mode image reconstructed from the RF signals with system in sparse scanline mode [inter scanline spacing=4 linewidths]. Image was acquired with the scanhead placed close to the same location as for Figure 2.6(a)

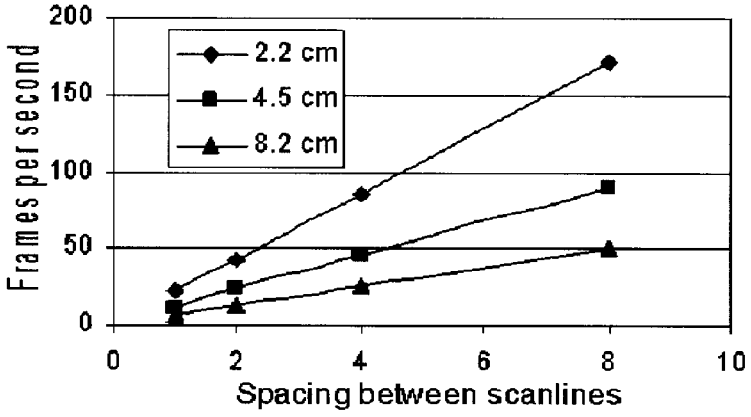

Figure 2.7 Plot of acquisition frame rate (frames per second) versus lateral width for axial depth settings of 2.2 cm, 4.5 cm and 8.2 cm with the system in *sparse scanline* mode. Line spacing of 1 represents the default acquisition mode with 128 scanlines. The inter-scanline spacing of 2, 4, and 8 correspond to 64, 32, and 16 scanlines of data, respectively.

2.5. Application in HIFU therapy monitoring

One of the important requirements of an ultrasound RF data acquisition system for use in HIFU therapy monitoring is proper synchronization between HIFU therapy ON times and RF data acquisition since interference between the HIFU beam and the imaging system would otherwise degrade the RF data quality significantly. A B-mode image reconstructed from the RF data acquired during HIFU is shown in Figure 2.8.

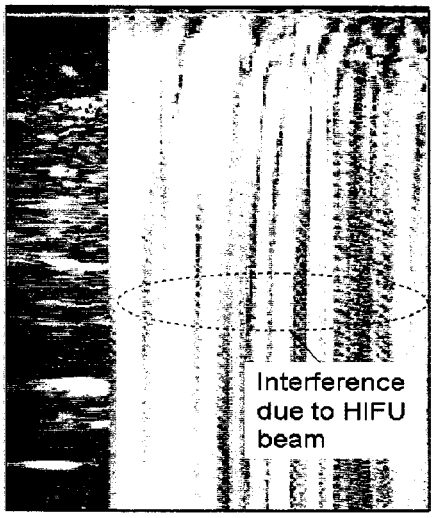

Figure 2.8 B-mode image showing interference due to HIFU beam

This interference is reported to occur due to saturation of the receiver electronics in the front end of the imaging scanner by the HIFU [51]. This problem was partially solved in Vaezy et. al [51] by triggering a gate signal on the HIFU therapy control unit with the excitation pulse of one of the elements of the imaging probe. As a result, the HIFU interference pattern is relegated to a section of the image frame outside the zone of lesion formation. However, this setup does not support simultaneous RF data acquisition desirable for off-line algorithm development. The software system reported in this work developed around the HDI 1000 ultrasound scanner, and the master control program written in LabVIEW™, makes interleaved RF data acquisition with HIFU therapy delivery straightforward. Moreover, integrated control of therapy delivery and imaging from the same master controller (PC) ensures proper synchronization which is essential

for quantitative imaging applications. A detailed description of such an application is presented in this section.

2.5.1. Experiment setup

The RF data acquisition system was first tested during an *in vitro* experiment to study the formation of HIFU-induced lesions in bovine liver tissue. The schematic diagram for the *in vitro* experiments is presented in Figure 2.9. A PC running the master control software program (Section 2.3) sends control signals to the HIFU signal generation circuitry (HP-33120 function generator, Hewlett Packard, Palo Alto, CA) via GPIB, and to the HDI 1000 via Telnet. The control sequence begins with a software command sent by the program to turn on the HIFU source. After a programmable ON-time has elapsed (50-200 ms) the HIFU is turned off (via GPIB) and a command dispatched to the HDI 1000 to acquire a RF frame while the HIFU is off. The software program then waits for 100 ms (programmable) for the HDI 1000 to complete acquisition (transmit-receive-store) before turning the HIFU on again for another exposure-image cycle. The above sequence is repeated with the master program alternately interleaving HIFU pulses with RF data frame acquisitions. The timing diagram representing this synchronization scheme is presented in Figure 2.10. The total therapy delivery time (excluding the brief 100 ms intervals when therapy is momentarily turned off for imaging) was 2 s while post-therapy acquisition of RF data frames continued for an additional 40 seconds.

A compact linear scanhead (CL 10-5, Philips Medical Systems, Bothell, WA) was used for imaging along with a single PZT element HIFU transducer (SU107; Sonic Concepts, Woodinville, WA), nominally operating at 3.5 MHz with an aperture diameter of 33 mm, and a focal depth (radius of curvature) of 35 mm. The HDI 1000 was set to acquire the full lateral width of 2.5 cm (128 scanlines). As shown in Figure 2.9, the HIFU transducer was driven by a power amplifier (A150, ENI, Rochester, NY) connected to a signal generator emitting a gated sine wave. In this arrangement, the frame rate of the HDI 1000 is about 10 fps, but the HIFU duty cycle was chosen to be 66% (200 ms ON, 100 ms OFF) and the HDI 1000 is in a frozen state between frame acquisitions. No HIFU

interference is observed in the RF data; indeed, the actual ultrasound acquisition time is significantly shorter than the 100 ms allotted.

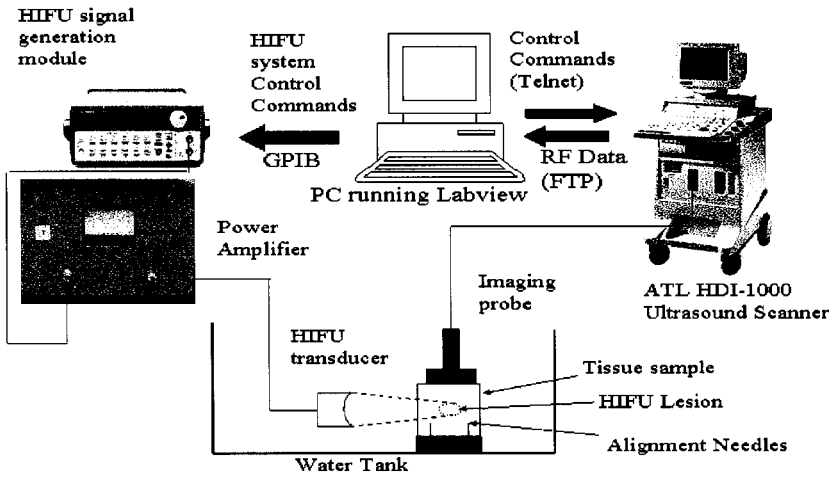

Figure 2.9 Experiment setup for synchronized RF data acquisition during HIFU therapy. The PC running Labview™ alternately sends control commands to the HIFU generation module (via GPIB) and the HDI 1000 ultrasound scanner (via Telnet). The imaging probe is aligned such that it scans along the longitudinal axis of the therapy beam in plane with the HIFU lesion.

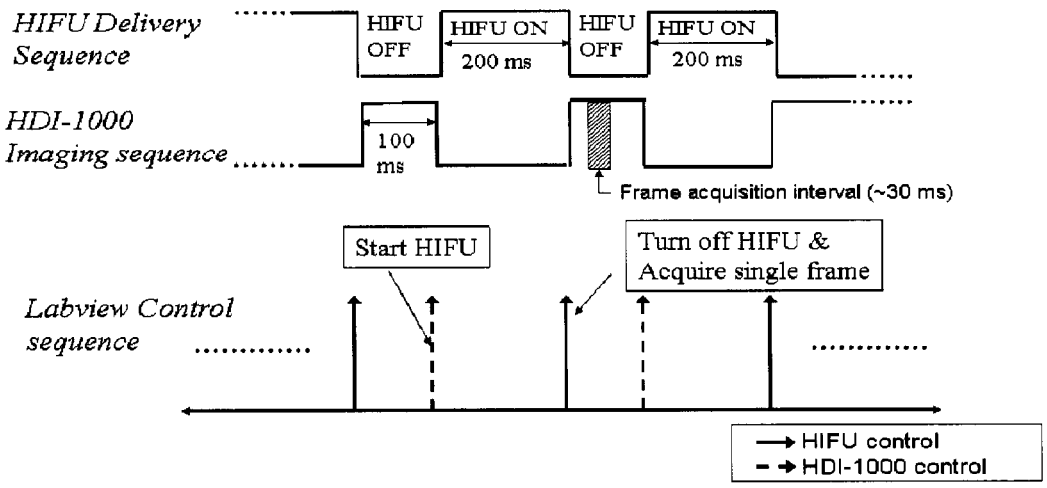

Figure 2.10 Timing diagram showing the synchronization between HIFU therapy delivery and HDI 1000 RF data acquisition. The timing parameters shown on the diagram were used for an *in vitro* HIFU experiment (HIFU ON: 200 ms, RF acquisition: 100 ms). Note that although actual frame acquisition lasts only about 30 ms, additional delay is incorporated to account for internal data transfer and system latencies.

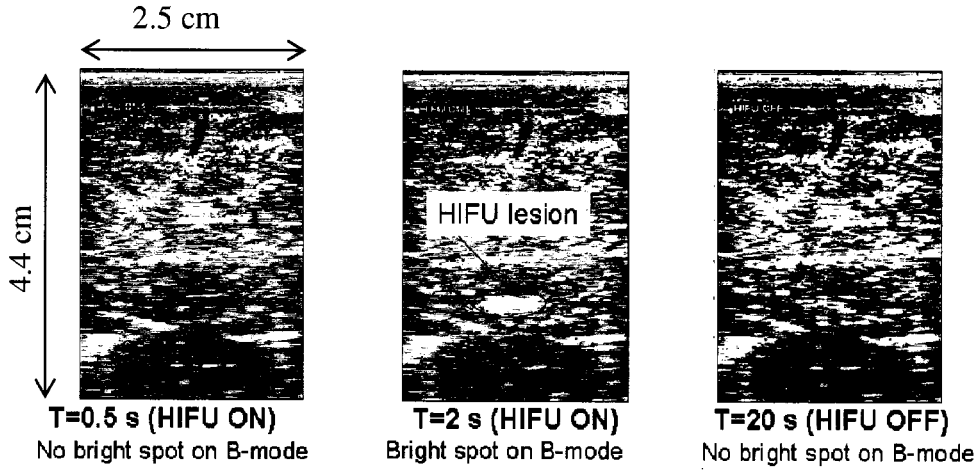

Figure 2.11 Sequence of fundamental B-mode images reconstructed from the acquired ultrasound RF backscatter during and shortly after HIFU therapy. The total therapy ON time was 2 s. Note that synchronization between therapy delivery and the ultrasound imager provides HIFU interference free B-mode images. A visible hyperechogenic spot is observed on the B-mode image quite sometime after HIFU therapy commenced (2 s) and they disappear shortly after therapy was turned off. Aside from subtle scintillation of the speckle pattern in the focal zone prior to the hyperechogenicity, little change in the image is visible.

The results of these initial HIFU experiments, shown in the B-mode images of Figure 2.11, indicate that hyperechogenic regions forming in the neighborhood of the HIFU beam focal zone can appear (and disappear) very rapidly, and aside from subtle scintillation of the speckle pattern in the focal zone prior to the echogenicity, little change to the image is visible. Conversely, processing of the full wave signal (RF) indicate that progressive changes in the sound speed of the medium, and in scattering characteristics of the tissue, are almost immediately detectable upon initiation of HIFU exposure and well before a lesion is formed. Differential processing of backscattered RF ultrasound can provide quantitative measures of lesion evolution and is the subject of the subsequent chapters in this dissertation.

2.5.2. Timing Analysis - Latency and Jitter Measurements

As may be noted from the system description presented in Section 2.2, to synchronize the RF data acquisition with the HIFU therapy delivery, a software-based approach was employed to control the instrumentation components. To quantify the

software timing latency between issuing a control command from the master control program and observing the instrument response, a timing analysis was performed. Specifically, the latency in the frame acquisition after a control command has been issued from the PC was experimentally measured. A schematic of the experimental setup is shown in Figure 2.12. The HDI 1000 ultrasound scanner is controlled over the Telnet port from the master-controller PC. At the same instant that a software control command to initiate RF frame acquisition is sent to the ultrasound scanner, a TTL high signal (+ 5V) is sent out on the parallel port of the PC and recorded on the oscilloscope on Channel 1. After a brief delay (5 ms), the TTL pulse is set low. The transmit pulse recorded by a needle hydrophone placed at the focus of the imaging transducer (indicated by the focus markers on the B-mode image) along the edge of the first scanline is recorded on Channel 2. The time delay between the signals recorded on Channel 1 and 2 is measured and is an estimate of the system latency.

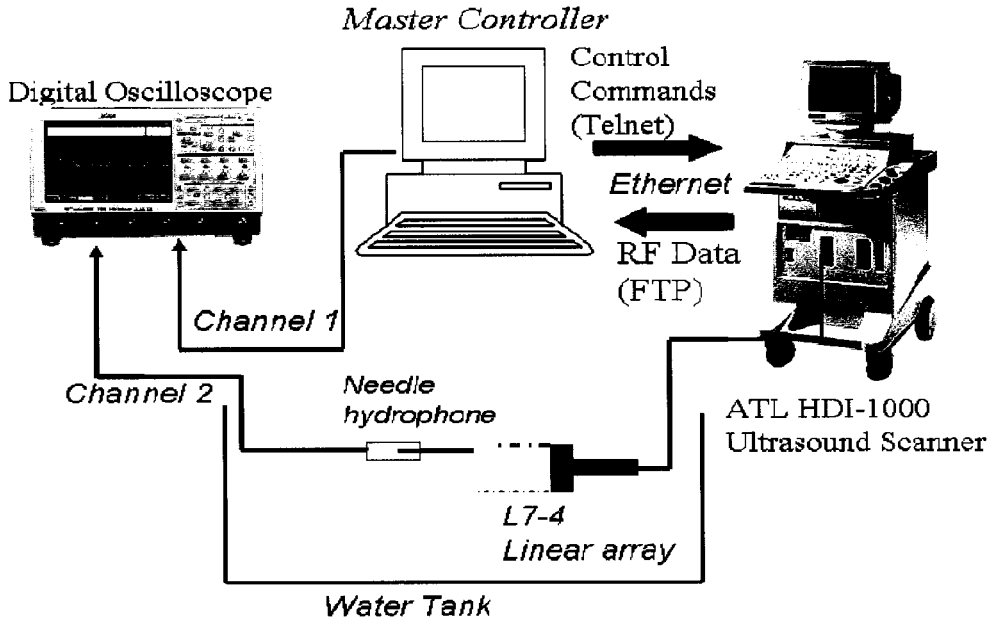

Figure 2.12 Experimental setup for latency measurement

A screenshot of the oscilloscope screen is shown in Figure 2.13. The figure shows that the latency is approximately 17 ms. This value includes the internal PC latency in

sending the control command over the Telnet port, delays along the Telnet link and the system delay internally within in the HDI 1000 associated with parsing the Telnet command, activating the beamformer and starting the frame acquisition.

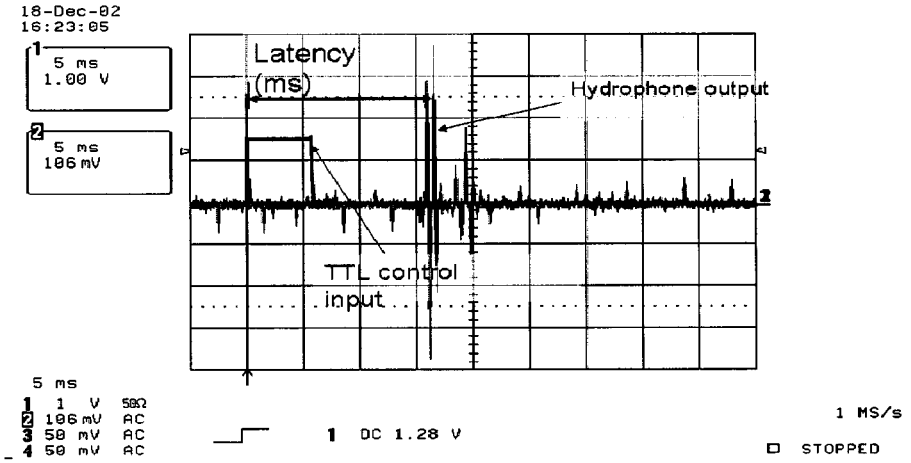

Figure 2.13 Screenshot of oscilloscope output illustrating latency between control signal output from the master control program and initiation of RF frame acquisition measured using a hydrophone

To quantify the jitter in the latency measurement, the internal clock count of the HDI 1000 was recorded at the start of each frame acquisition. The variability in the difference between clock counts (reported in ms) for consecutive frames was a measure of the jitter. The plot in Figure 2.14 shows the time interval between consecutive frame acquisitions in response to software control commands that initiate frame acquisition from the PC. Note the fine scale along the vertical axis. A total of 50 frames were acquired with a programmed interframe acquisition interval of 0.6 s. The deviation from the red dotted line is a measure of the jitter in the frame acquisition interval. The mean inter-frame interval over the 50 readings was 0.5999 s with a standard deviation of 6.97×10^{-4} s.

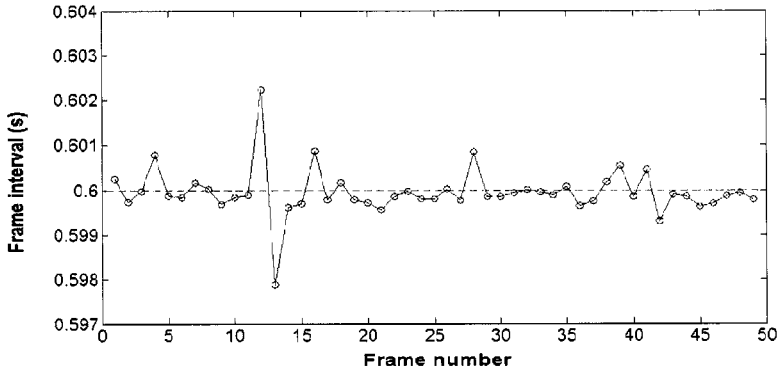

Figure 2.14 Plot showing measured frame interval (-o) and user specified frame interval (--) sent out from software program between consecutive frames (in seconds)

2.6. Application in Elastography

Although the primary application for this system in our research is in acquisition of RF data during HIFU experiments, the system can be easily adapted to meet the data acquisition needs for other emerging ultrasound imaging modalities requiring access to RF data such as elastography [41, 83, 84], new Doppler-based imaging techniques for measuring vascular and physiologic function [85], and radiation force imaging [42, 44]. This flexibility is demonstrated in this section through an application in the field of elastography [41] — a recently developed quantitative technique to image tissue strain under external compression, and to infer the elastic modulus.

A tissue-mimicking phantom with an inclusion (7% polyacrylamide was used for the background and 15% for the inclusion making it stiffer) loaded with scatterers was subject to external compression in the axial direction in steps of 0.1 mm using a mechanical fixture holding the imaging probe (L11-5, Philips Medical Systems) attached to a 1-D motion stage. The Young's modulus of the background and inclusion measured using a mechanical indenter was 16.3 kN/m^2 and 33.4 kN/m^2 respectively. A schematic representation of the experimental setup is shown in Figure 2.15.

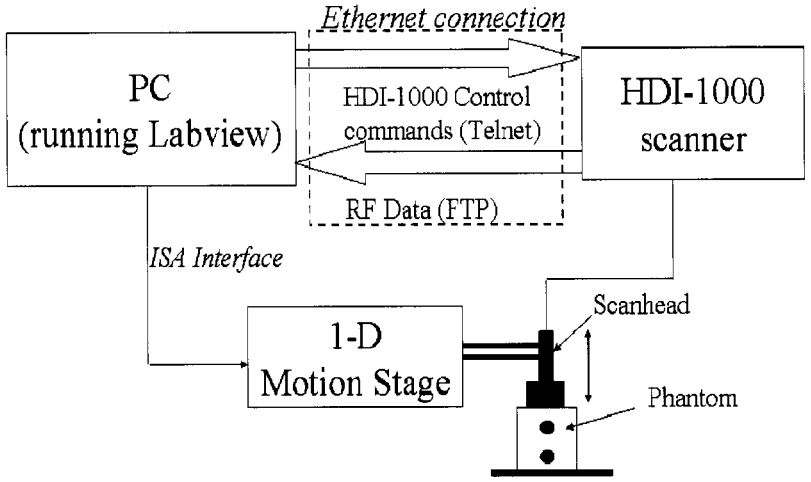

Figure 2.15 Schematic representation of the experimental setup used for the elastography application. An external compression is applied in the axial direction using a mechanical fixture mounted on a 1-D motion stage. Motion of the phantom is limited to the axial and lateral direction with constraints applied to prevent motion in the elevation direction. Movement of the motion stage and RF data acquisition using the HDI 1000 is controlled from the PC running the LabVIEW based master control program.

The software program (described in Section 2.3) was modified for use in this application to control the movement of the motion stage and to initiate acquisition of RF data frames, essentially replacing the HIFU system with the mechanical compression system. The acquisition sequence begins with a command sent to the HDI 1000 to acquire a RF data frame (via Telnet). After the frame has been acquired, a command is dispatched to the motion stage (via ISA interface) to move the transducer to compress the phantom by 0.1 mm (out of a total phantom height of about 9 cm). The above sequence was repeated until the phantom was compressed by the desired total displacement of 10 mm, with RF data frames collected between each displacement step resulting in a total of 100 RF frames. This data set permitted exploration of various algorithms and parameter choices for determining strain, and assessing the noise in the system.

Figure 2.16 illustrates typical results of this test. The RF lines were divided into overlapping segments and the axial displacement between segments at the same lateral position selected from frames ten time steps apart was computed using a 1-D cross-correlation algorithm. A least-squares strain estimator was used to compute the axial strain from the displacement estimates. Figure 2.16(a) shows the B-mode image of the

phantom with the external compression applied at the top of the image; by design, there is little echo contrast between the background and the inclusion. The axial displacement map is shown in Figure 2.16(b) and the strain elastogram appears in Figure 2.16(c). The region surrounding the inclusion is delineated with a dotted line on the B-mode image. Visible contrast between the background and the inclusion is seen on the strain elastogram.

An estimate of the error in the displacement estimates was also obtained using a "sham" measurement in which no external motion was applied. A set of 10 RF frames were acquired with no external compression and the 1-D displacement tracking algorithm was used to estimate the axial displacement. The mean displacement error (averaged over the entire frame) was 0.4 μm. The theoretical lower bound on the error in the displacement, calculated using the expression derived in [86], was 0.25 μm. Additional sources of error not included in the theoretical calculation but which could affect the experimental result are building vibrations that could have propagated to the sample holder, jitter in the position of the ultrasound probe and inhomogeneities within the sample that could have locally affected the SNR and the displacement estimate.

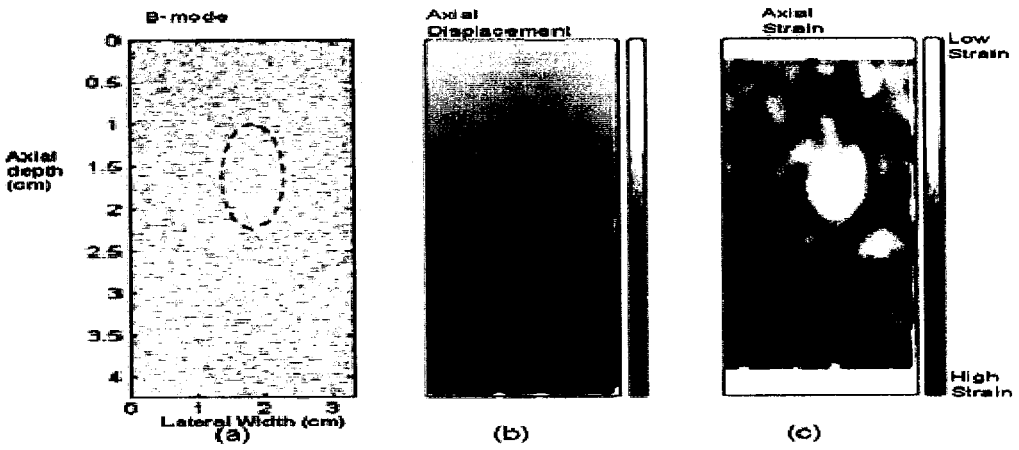

Figure 2.16 (a) B-mode image (c) Strain elastogram of the acrylamide gel phantom subject to 0.1 mm axial compression per step from the top using an external compressor. Lighter colors (towards white) on the color scale represent low relative strain while colors towards black (bottom) represent higher relative strain. The total displacement resulting from the external compression was 10 mm. The axial displacement is shown in (b). The dotted line on the B-mode image indicates the boundary of the inclusion.

To determine the suitability of the HDI 1000 for freehand elastography, we assume that choosing a minimum displacement (external compression) of five times the displacement error would provide a reasonable signal-to-noise ratio; thus, at least 2 μm compression between frames would be desirable. Assuming a freehand acquisition frame rate of 10 frames per second, a compression rate of at least 20 μm/s would be adequate. However, to avoid speckle de-correlation as a result of large external strains, it would be desirable to limit the maximum applied external compression rate to less than 10 mm/s. Consequently, freehand elasticity imaging for externally applied compressions in the range 20 μm/s to 10 mm/s on simple objects should be feasible using this system. *In vivo* elasticity imaging is typically much more difficult, but the results of the phantom test indicate that the HDI 1000 system is a promising tool for freehand elastographic data acquisition.

The system is also being used as the primary data acquisition instrument in research efforts currently underway in our facility to develop imaging techniques to characterize tissues based on a difference in pulsatile motion induced by internal cardiac contractions [87]. This technique relies on the ability to measure displacements much smaller than a wavelength along the ultrasound beam. The custom acquisition modes (described in Section 2.4) are employed to provide the high frame rates (at least 50 fps) required for this application, in order to properly sample the full bandwidth of the cardiac pulsatile waveform.

2.7. Discussion

An in-house developed ultrasound RF data acquisition system using a commercially available ultrasound scanner for HIFU lesion monitoring has been presented in this chapter. The software-based architecture of the system provides the capability to develop additional custom acquisition modes allowing the user to select optimum acquisition settings for parameters such as frame rate, scanline density etc. for a given application. As illustrated in Figure 2.5 and Figure 2.7, the newly developed *reduced sector width* and *sparse scanline* modes significantly improves the RF data acquisition frame rate. For the *reduced sector width* mode Figure 2.5 (a), at each of the selected imaging depths, the

frame rate increases by almost a factor of 4 when the sector width is reduced from the default setting of 2.5 cm to 0.6 cm. For the *sparse scanline mode (*Figure 2.7*)*, the acquisition frame rate increases linearly with the scanline spacing. Moreover, since the transmit pulse sequences and the beamforming parameters are programmed in software via re-configurable application program interfaces (APIs), the system can support the future development and implementation of custom transmit pulse sequences and beamforming algorithms, required for applications such as coded excitation imaging [88] and harmonic imaging. This will extend the scope of applications potentially possible with the system.

The ability to externally control the operation of the HDI 1000 ultrasound scanner provides the capability to synchronize the RF data acquisition with additional devices and instruments that are part of the experiment setup. For example, in the application on HIFU lesion monitoring using backscattered ultrasound (Section 2.5), ensuring that RF data is only acquired during therapy OFF times is essential to avoid interference that would otherwise render parts of the RF data frames unusable for post processing.

Although the primary application for this system in our research is acquisition of RF data during HIFU experiments, the system can be easily adapted to meet the data acquisition needs for other emerging ultrasound-based imaging modalities requiring access to RF data such as elasticity imaging [84], new Doppler-based imaging techniques for measuring vascular and physiologic function [85, 89] and radiation force imaging [44]. All of these imaging modalities rely on the ability to track small displacements on the order of microns which are better resolved by analyzing the RF data compared to the envelope detected B-mode data. The results from the "sham" experiment show that the expected error in the RF echo shift estimates is below the micron sized displacements typically encountered in these modalities.

2.8. Conclusion

The HDI 1000 ultrasound scanner is recognized as one of the first commercial scanners to be built on software dominant system architecture. Compared to the high-end systems available today that typically employ 128 channel beamformers with advanced

post-processing algorithms such as spatial and temporal compounding [90], the HDI 1000 system with a 32 channel beamformer is a low to mid range system. Nevertheless, it provides the opportunity to implement and validate novel RF data processing algorithms in a research environment. The subsequent chapters in this dissertation further demonstrate the ability of the software-based acquisition system to acquire temporally synchronized HIFU interference free ultrasound backscatter data along with data from other acoustic and thermal sensors. Parts of the material presented in this chapter have been previously reported in a conference proceedings paper [91].

3. MONITORING HIFU LESION FORMATION USING BACKSCATTERED ULTRASOUND

3.1. Introduction

The goal of this chapter is to demonstrate that tracking changes in the raw ultrasound backscatter (commonly referred to as "ultrasound RF") provides improved visualization of lesion formation induced by HIFU compared to standard fundamental ultrasound B-mode images. Two signal processing approaches to track changes in the ultrasound backscatter were applied, one designed to track temperature related information and the other designed to detect changes in local tissue scattering properties. The chapter begins with a brief description of the effect of temperature on ultrasound backscatter in Section 3.2. The mathematical model explaining this effect is summarized in Section 3.3. In section 3.5, a signal processing based algorithm to estimate temperature induced strain from ultrasound backscatter is described. *In vitro* experiments performed in tissue mimicking phantoms and excised bovine liver to validate this algorithm is presented in section 3.6. A preliminary experiment on quantitative temperature estimation is presented in section 3.7. The technique developed to detect local changes in tissue scattering properties related to HIFU lesion formation by tracking changes in the spectral content of the backscattered signals is described in section 3.8. The chapter concludes with a discussion motivating the need for a thermal diffusion model-based temperature estimation algorithm for HIFU therapy monitoring that is then further developed and presented in Chapter 4 and 5.

3.2. Effect of temperature on ultrasound backscatter

When a region of tissue is heated, the backscattered ultrasound signal experiences echo location shifts [70]. These shifts are due to changes in the *local sound speed* and *thermal expansion*. The change in sound speed causes an apparent shift in the scatterer location while the thermal expansion effect causes a physical shift. Figure 3.1 shows an illustration of the change in the echo locations caused by local changes in temperature along the ultrasound pulse propagation path. The scatterers shown are all initially at

temperature T_0 (*panel (a)*). The corresponding backscattered signal is simulated in panel (c).

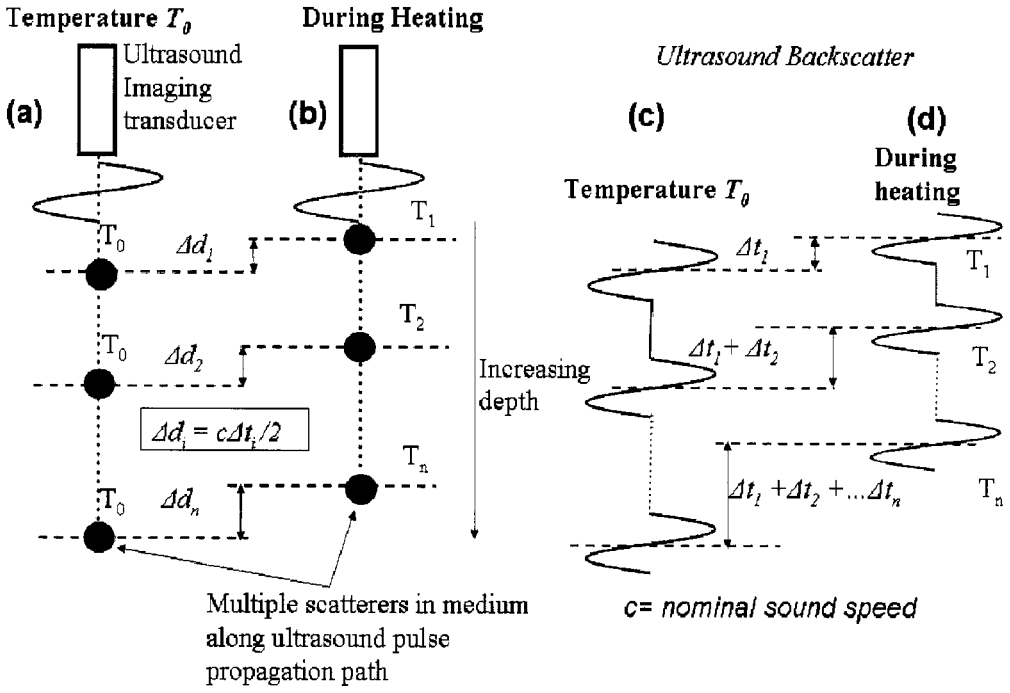

Figure 3.1 Illustration of the shift in the backscattered ultrasound echo locations due to temperature induced sound speed change and thermal expansion along the propagation path of the imaging pulse. c is the nominal sound speed assumed in the imaging system. The total shift in the echo at a particular depth is the cumulative sum of the local travel time change occurring at depths shallower to it. Panel (a) represents the scatterer locations along the pulse propagation path at temperature T_0. (b) illustrates the scatterer locations when the local temperature changes to T_0, T_1 .... T_n. (c) and (d) represent the backscattered echo corresponding to the scatterer locations shown in (a) and (b) respectively

The local temperature change T_i results in a change in the round-trip travel time of an ultrasound transmit pulse to the scatterer and is denoted by Δt_i. This travel time change includes the effect of sound speed change and also thermal expansion. The travel time change is mapped into an *equivalent* displacement of the scatterer given by the equation $\Delta d_i = (c\Delta t_i)/2$, where c represents the nominal sound speed in the medium. The new location of the scatterers is shown in panel (b). The local acoustic travel time changes, (Δt_i), result in cumulative shifts in the backscattered echo as illustrated in panel (d). The echo shift at a given depth (Δt_1, $\Delta t_1 + \Delta t_2$, $\Delta t_1 + \Delta t_2 + ... + \Delta t_n$ for the scatterers shown) is thus the cumulative sum of the local travel time changes from depths shallower to it. This

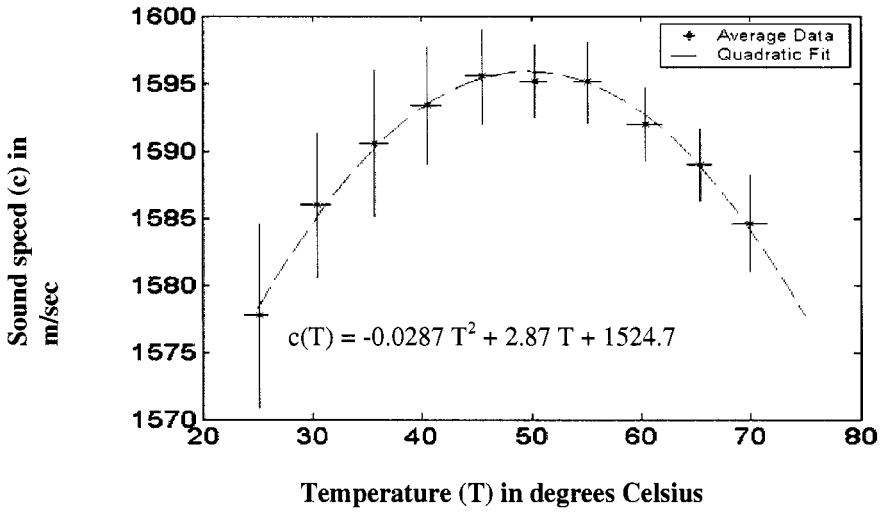

Figure 3.2 Sound speed versus Temperature measured in Ex-vivo Pork Liver. The data is fitted with a second order polynomial (Bloch, S. MS Degree Thesis, University of Washington, Seattle)

cumulative shift is what is observed in the backscattered echo signal. To compute the local acoustic travel time change, the derivative along the depth direction is computed.

Experimentally measured sound speed versus temperature (*c(T)*) curves, typically represented by a second order polynomial [92] for water-based tissue media have been reported in the literature [49, 55, 72]. Specific trends can be noted in the *c(T)* curve for biological tissue with low fat content. Typically, for temperatures near body temperature, the speed of sound increases rapidly with temperature. The sound speed commonly peaks at temperatures between 50 and 70 degrees C, depending on tissue type, and then decreases with further increase in temperature. Figure 3.2 shows the *c(T)* data for ex-vivo pork liver over the therapeutic range fitted by a second order polynomial with the error bars representing variation in estimates from different samples. Data for the thermal expansion coefficient (expressed in /°C) in soft tissue is available for a limited temperature range upto 50°C [92, 93]. In this temperature range, it has been shown that the time shifts caused by thermal expansion are significantly less than that due to the local sound speed changes [72, 94] and can be neglected [73]. From Figure 3.2, it can be seen that the sensitivity of the sound speed versus temperature relationship decreases as the temperature is raised from room temperature close to the coagulation threshold and this complicates the direct mapping of observed echo shits to temperature. In this chapter,

we focus on methods to extract the cumulative echo shifts from the ultrasound backscatter during HIFU exposures. Mapping of this information to temperature is the subject of chapters 4 and 5.

3.3. Mathematical model describing effect of temperature on ultrasound backscatter

In this section, a mathematical formalism relating the echo shifts observed on the backscattered ultrasound signals to temperature change is described. The model assumes that the effect of thermal expansion is negligible, the relation between sound speed and temperature is spatially invariant and that the initial baseline temperature is constant throughout the medium before heating commences. The formalism below closely follows that reported by Miller et. al. [72] but with the addition that the relation between temperature and the *local acoustic travel time change* (due to the sound speed change) is explicitly derived. The mapping between sound speed change and temperature is assumed to be linear in this analysis.

Consider a 2-D arrangement of discrete acoustic scatterers. The sound propagates through the medium along y. The ultrasound echo signal received after propagation through the medium and reflected back is sampled at a regular spacing, Δy. The ultrasound imaging transducer that sends out the sound pulses and detects the echoes is located at $y = 0$. For a uniform sound speed at the baseline temperature of T_0 °C, c_0, the round-trip travel time, t_i, to the i^{th} element in depth is,

$$t_i = \frac{2i\Delta y}{c_0} \tag{3.1}$$

The new round-trip travel time to a depth location i due to the temperature induced change in sound speed is,

$$t_i' = \sum_{k=0}^{k=i} \frac{2\Delta y}{c_k} \tag{3.2}$$

where c_k is the sound speed value for the k^{th} sample volume in the intervening acoustic path between the transducer and the region of tissue under consideration. Therefore, the

travel time change (δt_i) of the i^{th} tissue sample volume in the heated tissue relative to the unheated tissue is,

$$\delta t_i = t_i' - t_i = 2\Delta y \left[\sum_{k=0}^{k=i} \frac{1}{c_k} - \frac{i}{c_0} \right] \tag{3.3}$$

For an imaging system that displays echo information assuming that distance is linearly related to propagation time *via* an assumed uniform sound speed, c_{system}, this travel time change due to local changes in sound speed manifests as an apparent location shift in the backscattered echo given by,

$$\delta y_i = \frac{c_{system}\delta t_i}{2} = t_i' - t_i = c_{system}\Delta y \left[\sum_{k=0}^{k=i} \frac{1}{c_k} - \frac{i}{c_0} \right] \tag{3.4}$$

This equation illustrates how changes in the local sound speed of the medium caused by local temperature rise results in shifts in the echo location in the backscattered ultrasound signal. It may be noted from equation (3.4) that merely estimating the echo shift (δy_i) *at a given location* does not provide unique information related to the local sound speed change *at that location*. This nonuniqueness is illustrated schematically in Figure 3.3 using a pair of simulated sound speed profiles. The variation of sound speed as a function of depth is shown in Figure 3.3(a) for two profiles, *Profile 1* in which the sound speed change is localized to a narrow spatial region in depth and *Profile 2* where the sound speed change is nonzero over a wider region. The baseline sound speed c_0 is 1500 m/s. The magnitude of the sound speed change relative to the baseline is lower for *Profile I* compared to *Profile 2*. Applying equation (3.4) to both the profiles assuming c_{system} = 1540 m/s and Δy= 32 μm, δy_i is computed and plotted in Figure 3.3(b). It can seen from this figure that although the underlying local sound speed change for both the profiles at depths of 0.026 and 0.037 m (marked by the red and green dots on the respective plots) are different, the δy_i values are identical at these points. This is a consequence of the fact that the δy_i values are obtained by accumulating the local sound speed change values. In order to extract local changes in sound speed that could be

directly related to local change in temperature, the derivative along the depth direction must be computed.

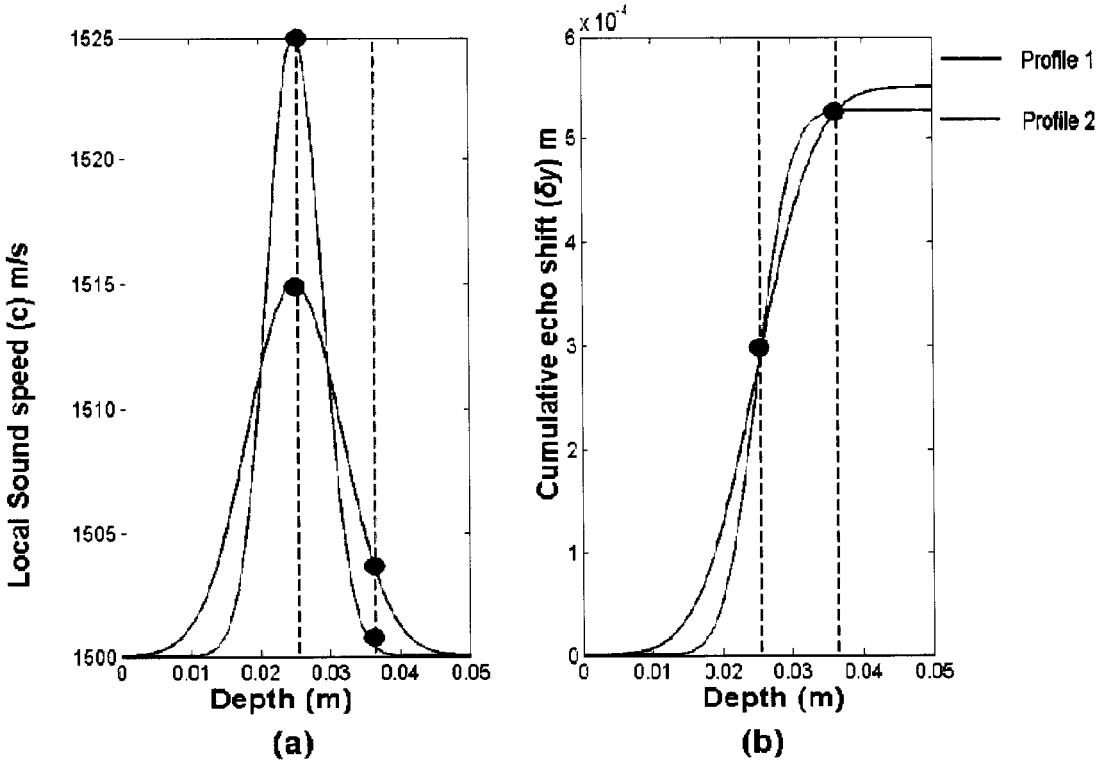

Figure 3.3 (**a**) Local Sound speed change profiles (**b**) Cumulative echo shift profiles corresponding to the sound speed change profiles in (a). The red and green dots on the plots represent locations where *different* local sound speed change values result in the same echo shift value *(Δy)*.

The simplest approach is to compute the difference between adjacent echo shift values Δy_i along depth as per the following equation,

$$\varepsilon_i = \frac{\delta y_{i+1} - \delta y_i}{\Delta y} = c_{system}\left(\frac{1}{c_{i+1}} - \frac{1}{c_0}\right) \tag{3.5}$$

In the above equation, ε_i is defined as *strain* since it is the derivative of echo shifts. In the context of the temperature estimation problem, it is also referred to as *temperature induced strain*. This terminology is used throughout the rest of this document. The operation performed in equation (3.5) to compute the strain is referred to as the *gradient operation*. However, it must be noted that estimation errors in the echo shifts are amplified in the presence of noise through the gradient operator. A commonly used signal

processing approach to overcome this problem is to apply a *least squares strain estimator* on the estimated echo values [95]. The main goal of the least squares strain estimator is to reduce noise amplification due to the gradient operation. This is achieved by performing a piecewise linear curve fit to the estimated echo shift values.

The sound speed c_i at any temperature T_i can be expressed in terms of the change in sound speed relative to the baseline value c_0 (at temperature T_0) as,

$$c_{i+1} = c_0 + \delta c_{i+1} \tag{3.6}$$

Since $\delta c_{i+1} << c_0$, equation (3.5) becomes,

$$\varepsilon_{i+1} = c_{system}\left(\frac{\delta c_{i+1}}{c_0^{\,2}}\right) \tag{3.7}$$

For a linear change in sound speed as a function of temperature (valid in the range from room temperature to about 50° C), the sound speed (c_{i+1}) at temperature T can be expressed in terms of the initial sound speed c_0 as,

$$\delta c_{i+1} = c_{i+1} - c_0 = \beta \delta T_{i+1} \tag{3.8}$$

where β is the temperature coefficient for sound speed and δT is the change in temperature relative to the initial temperature T_0.

Combining equation (3.7) and (3.8) we see that the temperature induced strain (ε) is directly proportional to the induced temperature change,

$$\varepsilon_{i+1} = c_{system}\left(\frac{\beta\ \delta T_{i+1}}{c_0^{\,2}}\right) \tag{3.9}$$

The constants c_{system}, β and c_0 are combined together to form a new scalar constant γ. Equation (3.9) can be rewritten as,

$$\varepsilon_{i+1} = \gamma\ \delta T_{i+1} \tag{3.10}$$

The above equation also shows that to convert the temperature induced strain values computed from the backscatter data to quantitative temperature change, accurate knowledge of the scalar constant γ is required. This quantity however is highly tissue dependent since it depends on the relative proportion of tissue constituents such as fat,

collagen and water [72]. If accurate knowledge of this parameter is available, the strain estimates derived by processing the ultrasound backscatter can be mapped to temperature.

3.4. Inter-tissue variability of relationship between strain and temperature

The precision of the temperature estimates derived from ultrasound backscatter data depends on the slope of the curve used to map strain (ε) to temperature (T). This mapping between strain and temperature is denoted by $\varepsilon(T)$. The $\varepsilon(T)$ relationship shows considerable variability amongst tissue types as it is dependent on tissue composition. The $\varepsilon(T)$ mapping for human liver tissue with different fat and water content is illustrated in Figure 3.4. The temperature induced strain increases with temperature in the range 37-50°C for normal human liver (low fat content) (Figure 3.4(a)), but decreases strongly with temperature for liver tissue with high fat content (Figure 3.4(c)). However, for liver tissue with intermediate fat content (Figure 3.4(b)), the slope of the $\varepsilon(T)$ curve is close to zero in the temperature range 37-50°C. Hence, it is important to keep in mind the influence of inter-tissue variability on the shape of the $\varepsilon(T)$ curve, which in turn affects the precision of the ultrasound based temperature estimates for a given clinical scenario.

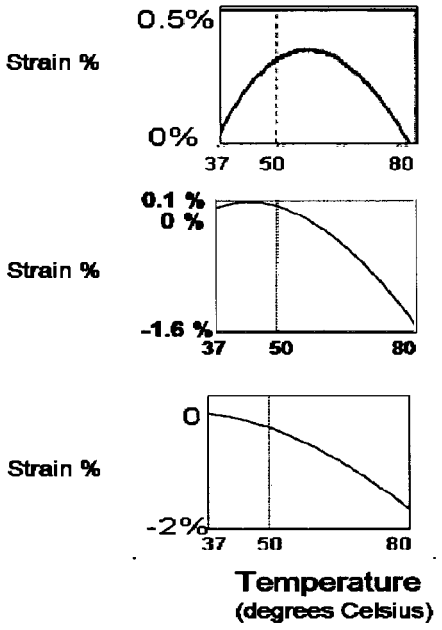

Figure 3.4 Temperature dependence of strain for (a) normal human liver (b) liver with an intermediate fat content (c) marked fatty liver [72].

A detailed survey of the literature on temperature dependence of sound speed (the key contributor to temperature induced strain ε) for mammalian tissues was conducted by Bamber [78] and other authors. Figure 3.5 illustrate measured sound speed versus temperature for a number of different tissue types and pathologies. For almost all of the tissue types shown in the figure, a noticeable change in sound speed as a result of temperature rise is observed for the temperature range reported. Hence, ultrasound temperature estimation in these tissue types should not pose a significant challenge. For the case of liver carcinoma (a potentially important tissue type for HIFU ablation applications), Sehgal reported that the sound speed versus temperature relationship is similar to that of normal healthy liver.

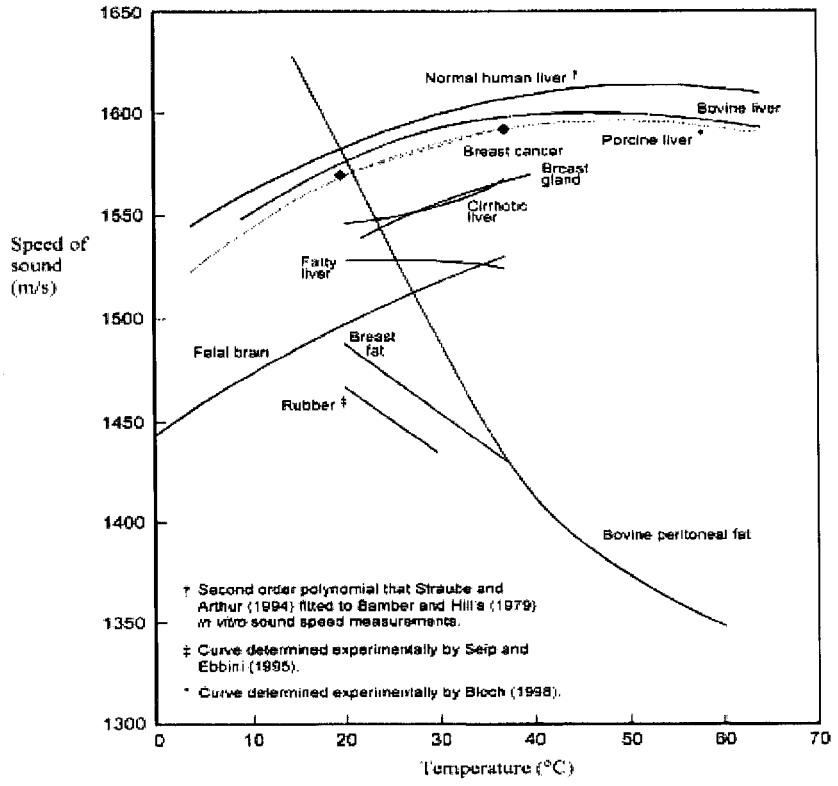

Figure 3.5 Measured temperature dependence of sound speed for different mammalian tissues. The data were reviewed by Bamber (1997) except where noted (Reproduced from Miller and Bamber [72])

3.5. Estimation of temperature induced strain from ultrasound backscatter – Algorithm description

To estimate the echo shifts and the temperature induced strain (ε) from backscattered ultrasound data collected during HIFU therapy, a time domain cross-correlation based algorithm originally developed for elastography [41] was adapted to the current problem. The algorithm operates on pairs of RF data frames acquired sequentially during the HIFU exposure experiment using the HDI 1000 ultrasound scanner. The organization of the RF data set is illustrated in Figure 3.6. The orientation of the imaging transducer is shown in Figure 3.6(a). The vertical direction downward is depth into the sample being imaged and the horizontal direction is the lateral distance. In ultrasound literature, the depth direction is typically referred to as "fast time". A single RF frame comprises of a set of ultrasound scan lines (typically 128), each of which is obtained at a single lateral location by firing a pulse into the medium and receiving the backscattered echoes. A number of such 2-D frames can be acquired sequentially over the duration of the experiment (typically referred to as "slow time" in the ultrasound literature) to obtain a 3-D data set as shown in Figure 3.6(b).

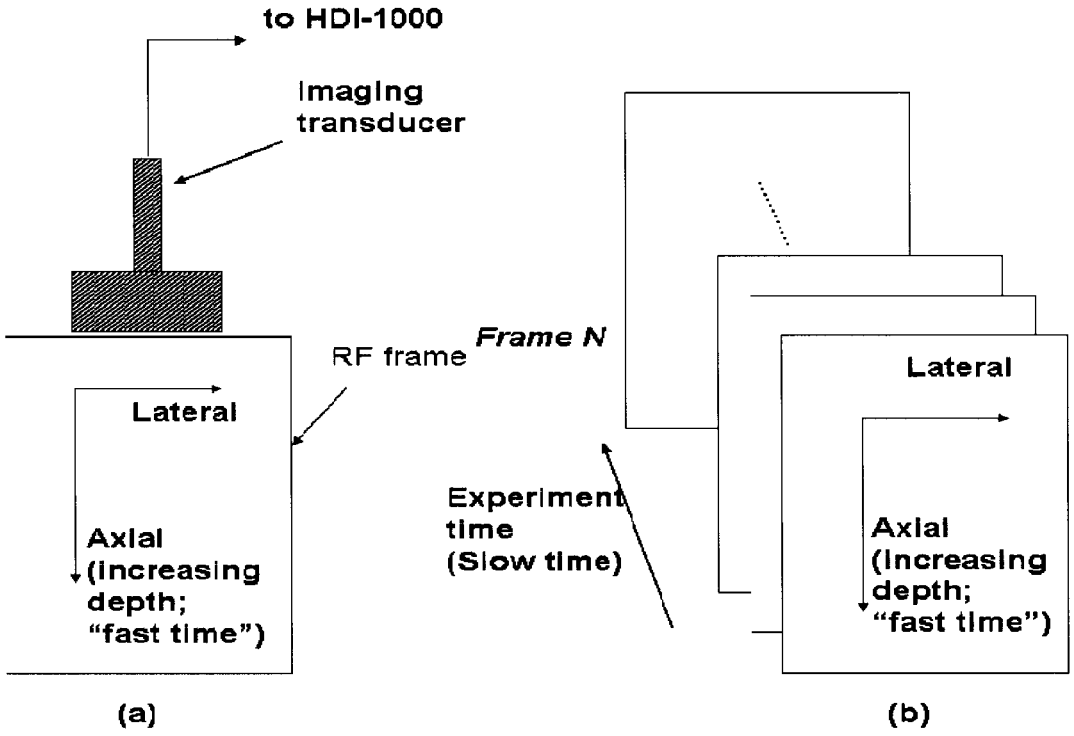

Figure 3.6(a) Orientation of imaging transducer and image acquisition plane **(b)** Organization of the RF data set.

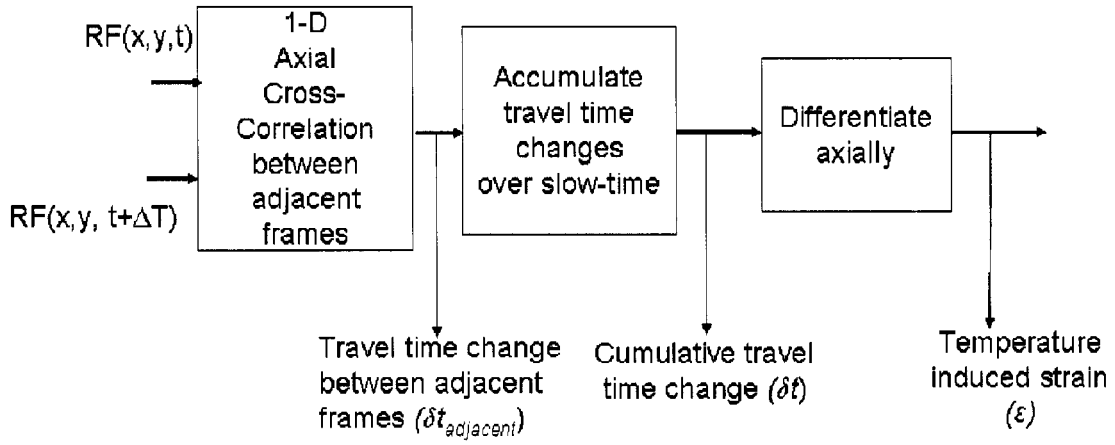

Figure 3.7 Block diagram representation of temperature induced strain estimation algorithm for a pair of RF frames *i* and *i+1* collected at experiment time (slow time) *t* and $t+\Delta T$

A block diagram representation of the RF data processing scheme is shown in Figure 3.7. The RF lines are divided into a set of overlapping segments and the estimation

technique is applied on each of the segments. For a given segment, this operation can be mathematically represented by the following equation,

$$c(j) = \max_{j} \sum_{k=0}^{k=m-1} s_i(k) s_{i+1}(k+j) \qquad -n/2<j<n/2 \tag{3.11}$$

where s_i represents a RF segment on frame i (collected at *slow* time t), s_{i+1} represents a RF segment on frame $i+1$ (collected at *slow* time $t+\Delta T$), j represents the echo shift between s_i and s_{i+1}, m represents the window length, n represents the search range on line $i+1$ and c represents the cross-correlation coefficient. The segments s_{i+1} and s_i are normalized to unit energy. In this case, c represents the normalized cross-correlation coefficient with values ranging from -1 and 1. The various parameters are diagrammed in Figure 3.8.

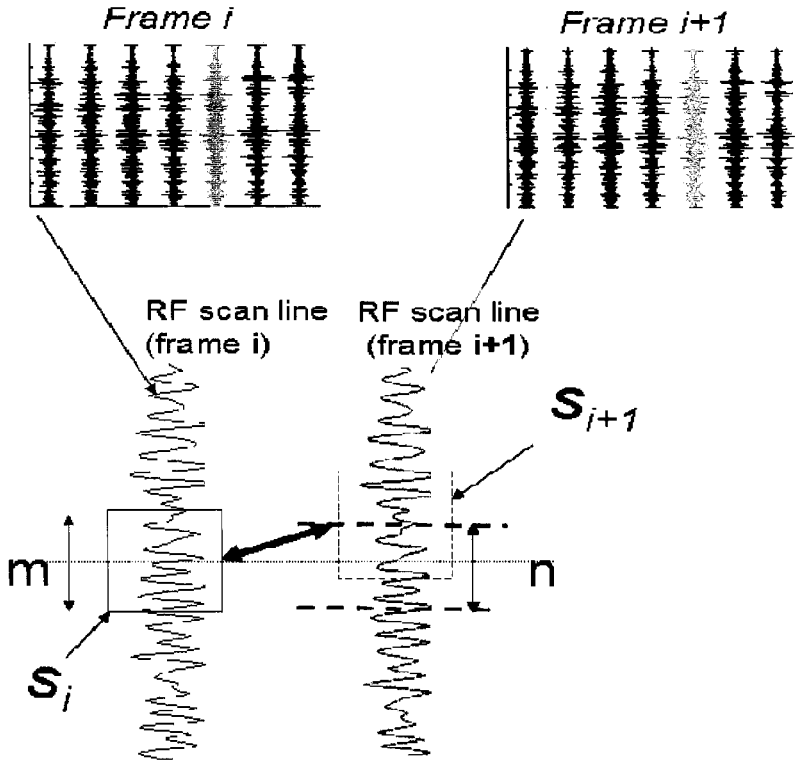

Figure 3.8 Graphical illustration of the various processing parameters used in the algorithm to estimate temperature induced strain

The RF scan lines (typically 128) in each frame are divided into a series of segments of length 1 mm with 20% overlap which gives an effective pixel resolution in the echo

shift image of 0.8 mm. A resolution of 0.8 mm is on the order of the beam widths of the HIFU transducers used in this study and is suitable for visualizing the steep thermal gradients around the HIFU focus. The segment length was chosen such that it contains multiple ultrasonic wavelengths which helps improve the signal-to-noise of the echo shift estimation process. For each segment in a given frame (i), a search region is defined around the same spatial location on a temporally adjacent frame ($i+1$). The segment selected in frame i (say s_i) is multiplied by a window at the top of the search region (s_{i+1}) in frame $i+1$ point-by-point, summed and the value stored in an variable c. This operation is repeated until the end of the search region is reached keeping s_i the same but choosing a new segment s_{i+1} each time that begins one sample below the previous choice of s_{i+1}. The time shift j between s_i and the window choice s_{i+1} that maximizes c is the estimated shift. j is converted to seconds by multiplying by the RF sampling period to obtain the travel time change between adjacent frames $\delta t_{adjacent}$. This operation is repeated for all the overlapping segments defined in frame i to generate a $\delta t_{adjacent}$ 2-D matrix corresponding to frame s_i and then repeated for all the frames taking 2 frames at a time. A 3-D matrix $\delta t_{adjacent}$ of size N-1 (where N is the total number of acquired RF data frames) is thus obtained. A cumulative sum of the time shifts ($\delta t_{adjacent}$) is computed along the temporal direction (slow time) to obtain the cumulative travel time change map (δt) that represents the time shift change with reference to the initial frame before therapy commenced. Computing $\delta t_{adjacent}$ between adjacent frames and then summing them to obtain the cumulative change has been shown to reduce errors due to decorrelation [96]. These estimates of δt are an integrated quantity in that travel time changes detected at a particular depth are influenced by changes along the acoustic path shallower to it. Hence, to obtain the temperature induced strain ε, δt is differentiated axially. The differentiation is performed by fitting a straight line to the δt estimates over a length of 4 mm which corresponds to 5 echo shift estimates spaced 0.8 mm apart. The slope of the fitted line gives ε locally.

The magnitude of the time-shifts $\delta t_{adjacent}$ is typically very small. It varies from $1/10^{th}$ of the RF data sampling interval to a few samples. This necessitates the need for employing accurate sub-sample estimators that are capable of estimating time shifts that are a fraction of a RF sampling period to obtain the desired accuracy. The sub-sample estimator employed in this algorithm is based on the parabolic interpolation technique reported in the literature [97]. The peak of the interpolation function is fitted to a parabola and the maximum point on the parabola is estimated. This enables time-shifts less than a RF sampling period to be estimated. The parabolic interpolation technique does result in biased estimates depending on the true value of the time shift and the bias error function has a characteristic shape of a sine function [97]. The maximum sub-sample estimate error occurs at time shifts 0.25-0.3 samples away from integer shifts while zero bias error occurs at a time shift of 0.5 samples [98]. A number of sub-sample estimators have been proposed in the literature [97, 98]. However, the parabolic estimator is computationally efficient and attractive for use in real-time implementations [97, 99].

3.6. *In vitro* experiments

Experiments were performed in bovine liver and tissue mimicking phantoms to demonstrate that temperature related changes during HIFU therapy can be visualized by tracking the temperature induced strain (ε) measured from the ultrasound backscatter data. Details of these experiments and the results obtained are presented in this section.

3.6.1. Experimental Therapy Protocols

Two clinically applicable experimental therapy protocols were employed. In the first protocol, *point lesions* were created where the HIFU transducer was held stationary while therapy was being delivered. The typical size of the lesion in this case was close to the physical dimensions of the focus of the HIFU therapy transducer (5 mm along HIFU beam propagation, 0.5 mm transverse). The second experimental protocol is referred to as *scanned lesion* protocol. In this approach, the therapy transducer was translated along the circumference of a circle of radius 7.5 mm while it emits the sound beam at a fixed intensity. The lesion extends over the entire circumference of the circle. These protocols

require synchronization between HIFU therapy delivery, the HDI 1000 and the transducer scanning to guarantee HIFU interference free RF data.

3.6.2. Point HIFU lesions in excised bovine liver tissue

3.6.2.1. Experiment Setup

The experimental setup is same as that shown in Fig. 2.8. A 3.5 MHz HIFU therapy transducer (SU-107, Sonic Concepts, Woodinville, WA) with an aperture diameter of 33 mm, and a focal depth of 35 mm was utilized for delivering the HIFU therapy dose. It employed an air-backed, concave, single PZT element. The driving electronics for the HIFU transducer consisted of a signal generator (HP 33120, Hewlett Packard, Palo Alto, CA) driving a power amplifier (A150, ENI, Rochester, NY). The imaging probe used was the ATL CL10-5 (Philips Medical Systems, Bothell, WA) with a frequency range of 5 to 10 MHz. RF data frames were acquired between HIFU exposures, at a rate of about 5 Hz, with the HIFU completely off during the acquisition to avoid interference from the HIFU beam. The RF data acquisition was controlled using the setup described in detail in Chapter 2. Alignment needles mounted at the base of the sample holders were used to ensure that the imaging plane of the ultrasound scanner coincided with the plane of HIFU beam propagation. As part of the experiment setup, before the therapy session commenced, the HIFU transducer was first translated in a 3-D plane until the reflected signal from the near end alignment needle received using a pulse-echo technique was maximized. This ensured that the focus of the HIFU transducer was aligned with the needle. The ultrasound imaging probe was mounted on a specially designed fixture attached to the sample holder so that the imaging plane also coincided with the needles. This was confirmed by ensuring that the needles were visible on the B-mode images. The RF data collected was transferred to the PC at the end of the experiment for offline processing.

Fresh whole beef liver was obtained on the day of the experiment from a local abattoir (Schenk Meat Packing Co., Stanwood, WA) and chilled in phosphate buffered saline (PBS). Pieces of liver were carefully cut to select nearly homogenous tissue by

avoiding large blood vessels. The pieces were sized to fill specially designed tissue holders that allow the imaging and therapy transducers to be registered to the tissue block and oriented such that the longitudinal axis of the therapy beam was in the plane of the imaging probe and perpendicular to it. The liver samples were degassed in PBS and warmed to 37°C in a water tank filled with degassed PBS. The *in situ* therapeutic intensity (I_{SAL}) used was calculated to be 1250 W/cm^2 based on measurements made in water using a radiation force balance and an attenuation coefficient of 0.7 dB/cm/MHz for liver. For the results presented in this section, the total integrated HIFU exposure time (excluding the brief HIFU off times for RF data acquisition) was 2 seconds. The intensity and duration of exposure to HIFU were determined based on comprehensive dosimetry studies conducted in our laboratory to observe the bioeffects under well controlled conditions for a range of experimental parameters [100]. RF frames (Each RF frame is a collect6ion of A-lines over a lateral extent of 2.5 cm with lateral spacing of ~0.2 mm) were collected every 0.2 s during a 0.1 s interruption of HIFU delivery. A single frame was acquired before HIFU therapy commenced to serve as the reference frame. After HIFU exposure, RF data frames were acquired at intervals of 10 seconds for 2 minutes to visualize the cool down period.

3.6.2.2. Results

The results obtained by employing the algorithm described in Section 3.5 on RF data collected from bovine liver are shown in Figure 3.9. The top row represents B-mode images recorded at different time intervals during the experiment. In the middle row, travel time change maps ($\delta t_{adjcent}$) scaled by a nominal value of 1540 m/sec (sound speed assumed on the HDI 1000) are represented as apparent displacement in microns. The HIFU transducer is to the left and the imaging probe is located at the top of the images. The timer represents the temporal location of the current frame with respect to the first frame acquired before HIFU therapy commenced. The color scale is bi-polar where apparent displacement towards and away from the imaging transducer is coded in shades of red and blue respectively. The displacement maps are further modulated by the correlation coefficient (c in equation (3.11)) between RF segments used in the

displacement estimation, with lighter shades of gray representing estimates with lower confidence.

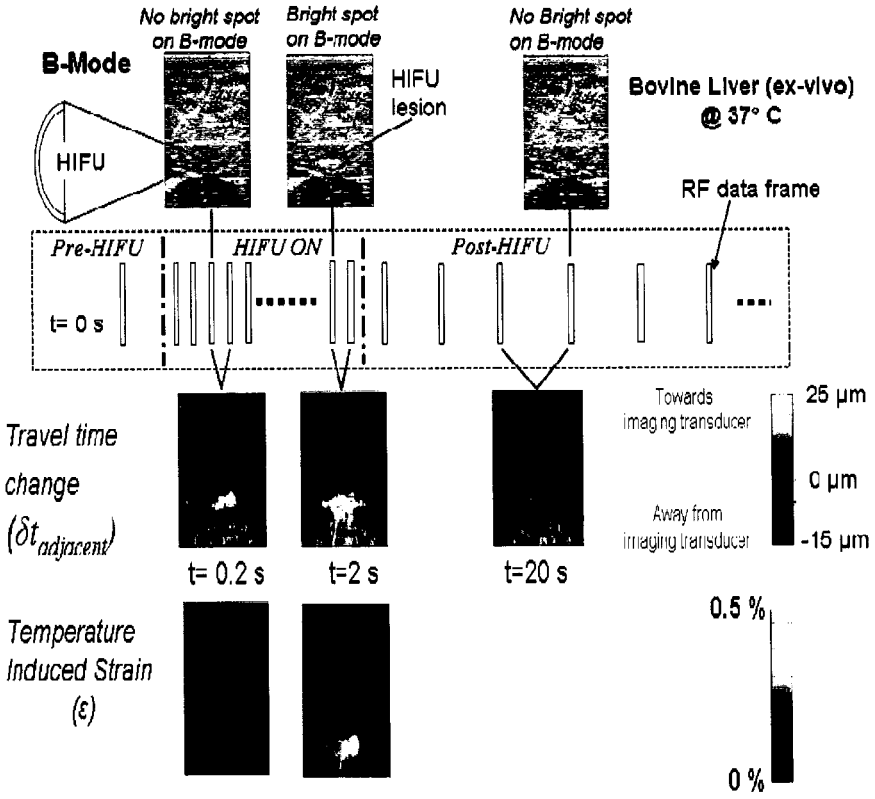

Figure 3.9 Travel time change maps ($\delta t_{adjacent}$) expressed as apparent displacement in microns (middle row) and temperature induced strain maps (bottom row) for in vitro bovine liver experiment. The top row shows the corresponding B-mode images.

It is seen that very soon after the HIFU was turned on ($0 < t < 0.4$ s), apparent motion towards the imaging transducer (located at the top of image) is observed over a large region surrounding the focal zone and appears before any hyperechogenicity appears on the B-mode image. This is related to the rapid increase in temperature in the focal region that results in a decrease in acoustic travel time. Similarly, during the cool-down period (after t=2.2 seconds), apparent motion appears in the opposite direction due to recovery of sound speed values. In the time interval $1.8 < t < 2.2$ *s*, a hyperechogenic spot is seen on the B-mode image while in the corresponding apparent displacement image, the area around the focal spot is delineated by an oval zone with colors indicating maximum positive and negative apparent motions in a random pattern largely masked by

the gray color indicating poor correlation. This is most likely due to the rapid generation of bubbles resulting in de-correlation of the RF data between adjacent frames. The bottom row in Figure 3.9 shows the temperature induced strain (ε) profiles during HIFU therapy delivery, one acquired shortly after HIFU commenced ($t = 0.2$ *s*) and the other at $t=2$ seconds when a hyperechoic spot appears on the B-mode image. Strain change related to the temperature increase at the focal spot can be clearly seen. The decorrelation in the RF data *possibly due to the formation of bubbles* also affects the ε maps in a manner similar to the δt maps as seen from the maps at time $t=2$ *s*.

This experiment demonstrated that estimates of temperature induced strain (δt) computed from the RF data provides useful information for tracking the temperature rise during HIFU therapy. In addition, on a qualitative basis, since changes were seen on the maps before appreciable changes occurred on B-mode images, they provide a method of improved visualization of the lesion location and in guiding the therapy beam.

3.6.3. Scanned HIFU lesion in a tissue mimicking phantom

In arrangements such as those used in the experiment described in section 3.6.2, the HIFU transducer was held stationary during treatment. A disadvantage of such an arrangement in a clinical setting is that the volume of tissue treated by each exposure from a single-element transducer is small, typically 0.15 cm^3 [1]. Hence, treatment of a large tissue volume is time-consuming and requires the creation of an array of point HIFU exposures with adequate cooling time between exposures for the tissues to cool down. To overcome this drawback, alternative approaches aimed at reducing the treatment time while maintaining the efficacy have been proposed. One such alternative approach is to sweep the transducer over the target volume while it is emitting the sound beam. Effective methods of visualizing the region heated during scanning and providing quantitative information on the resulting temperature rise is important for the successful implementation of these protocols. Temperature induced strain (ε) maps were generated using the algorithm described in Section 3.5 applied to data collected during experiments

conducted with this therapy protocol. The methodology and results obtained are presented in this section.

3.6.3.1. Experiment setup

The instrumentation setup is similar to that used for the point lesion experiment protocol (shown in Fig. 2.8). Changes were made to the master control program so that the HIFU transducer attached to a 3-D motion stage could be translated along a circle during the experiment. The imaging transducer was oriented perpendicular to the HIFU beam propagation axis. The relative orientation of the HIFU transducer, imaging transducer and the plane of lesion formation is illustrated in Figure 3.10. The experiments were performed in a tissue mimicking phantom (alginate dental impression material –Jeltrate®, Dentsply International, Milford, DE).

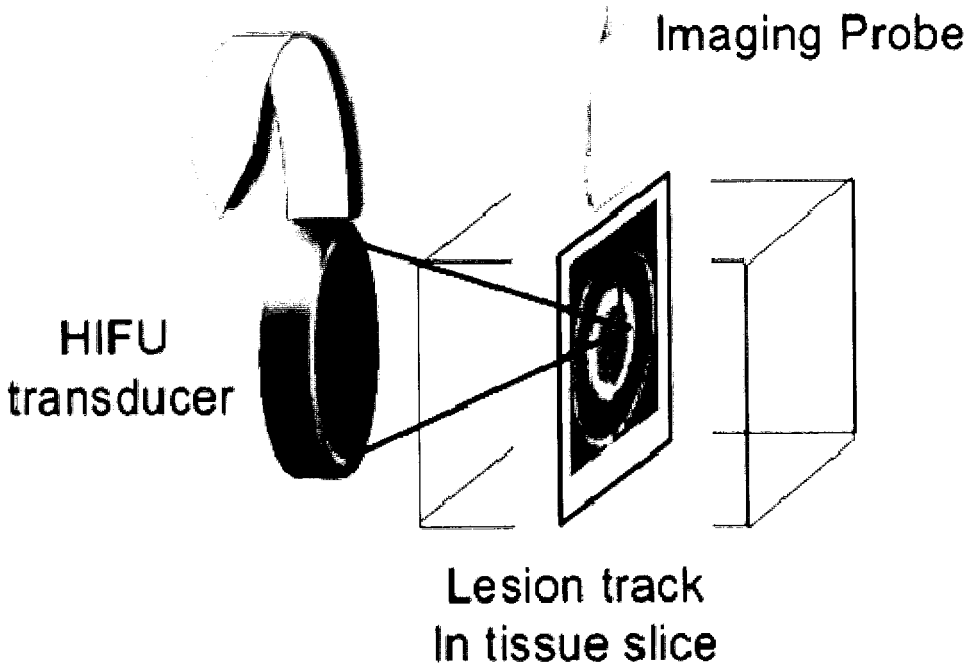

Figure 3.10 Relative orientation of the HIFU transducer, imaging probe and plane of HIFU lesion formation for the scanned lesion formation experiment

The imaging transducer was oriented such that the imaging plane coincides with the plane in which the lesion is formed. The motion stage was programmed to move the HIFU transducer along a circular path of radius 0.75 cm while HIFU was applied to a phantom and RF data was collected during brief interruptions of HIFU delivery and after therapy as well. The therapy lasted 25 seconds and RF data acquisition continued for an additional 50 seconds after HIFU delivery. Maps of temperature induced strain *(ε)* during therapy were generated by analysis of the RF data using the algorithm described in Section 3.5.

3.6.3.2. Results

The ε maps at four different time instants are shown in bottom row of Figure 3.11 while the corresponding B-mode images are shown in the top row. The color scale represents the magnitude of the induced strain towards the imaging transducer positioned above the image. Although no appreciable changes are seen on the B-mode images throughout therapy delivery and cool down, the ε maps clearly show the local temperature change induced by HIFU. As therapy progresses, the ε maps track the temperature rise along the scanning path of the HIFU transducer. These results demonstrate that local temperature changes induced by HIFU can be visualized by tracking changes in ε maps generated from the ultrasound backscatter signals.

To quantify the temperature induced strain over time, the amplitude and width of the strain profiles laterally along the white segment (labeled *R*) in Figure 3.11 were measured by fitting it to a Gaussian function. This location represents the start of the HIFU transducer scanning path. The 1-D strain profiles along segment *R* at five different time instants soon after HIFU therapy commences are shown in Figure 3.. The measured Gaussian radius and amplitude of these profiles are shown in Figure 3.13 and Figure 3.14 respectively. It can be seen that shortly after HIFU therapy commences, the strain amplitude increases consistent with the temperature rise. After a short time, the amplitude begins to decrease since the transducer has moved anti-clockwise away from this location and is no longer depositing the heat at this location causing the temperature to decrease. The Gaussian radius increases with time during the course of HIFU therapy due to

thermal diffusion. *These results demonstrate that the temperature induced strain maps provide an effective means of visualizing the thermal diffusion process. Furthermore, they illustrate the potential to extract quantitative temperature information by relating the strain information to a thermal diffusion model.*

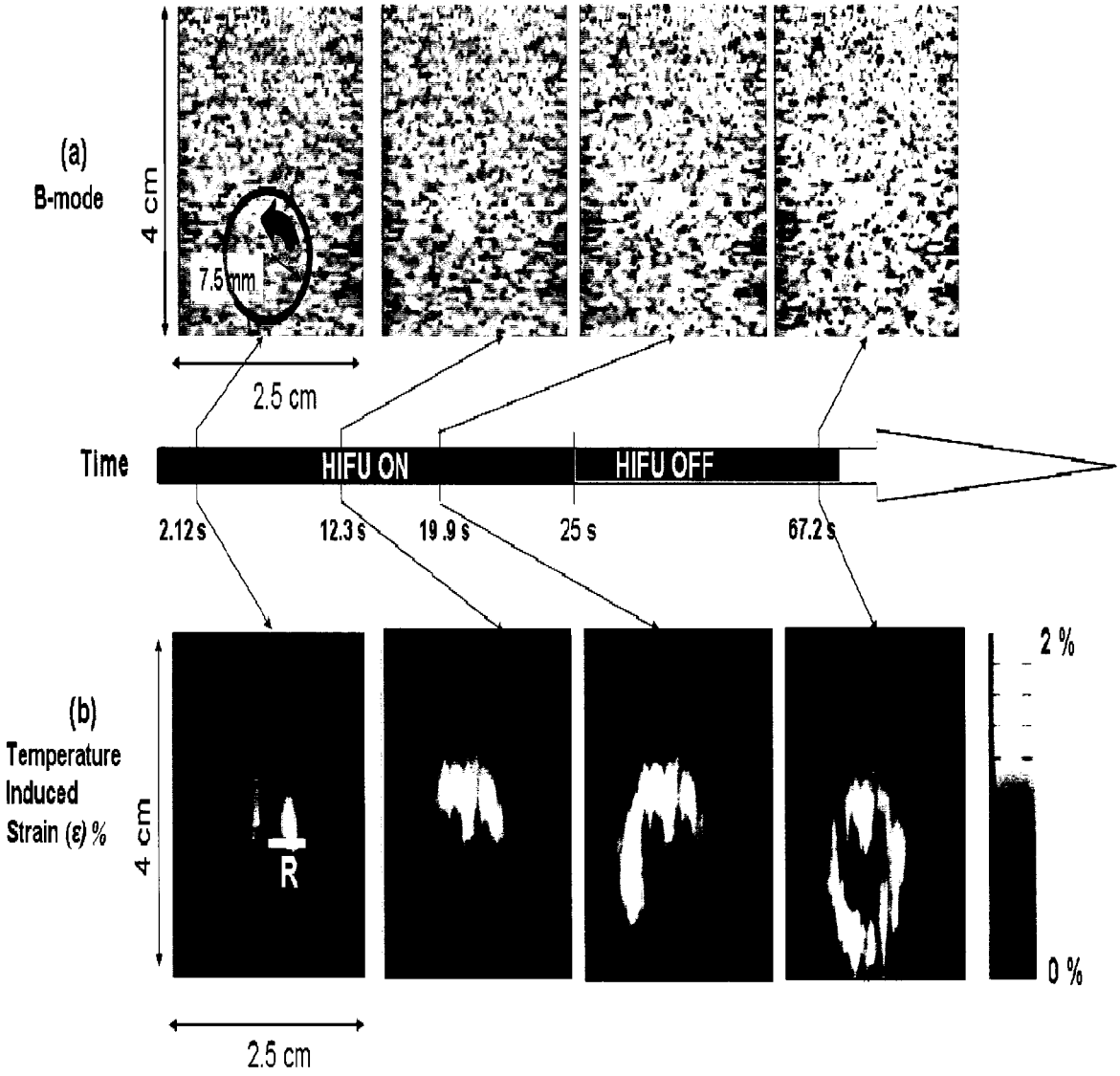

Figure 3.11 Maps of changes in local travel time (bottom row) and corresponding B-mode images (top row) during and shortly after therapy for a circular scanned HIFU therapy protocol in a phantom. The scanning path of the HIFU transducer is shown on the top left B-mode image by the red circle. The strain profiles along the white horizontal line labeled *R* are plotted in Figure 3. below.

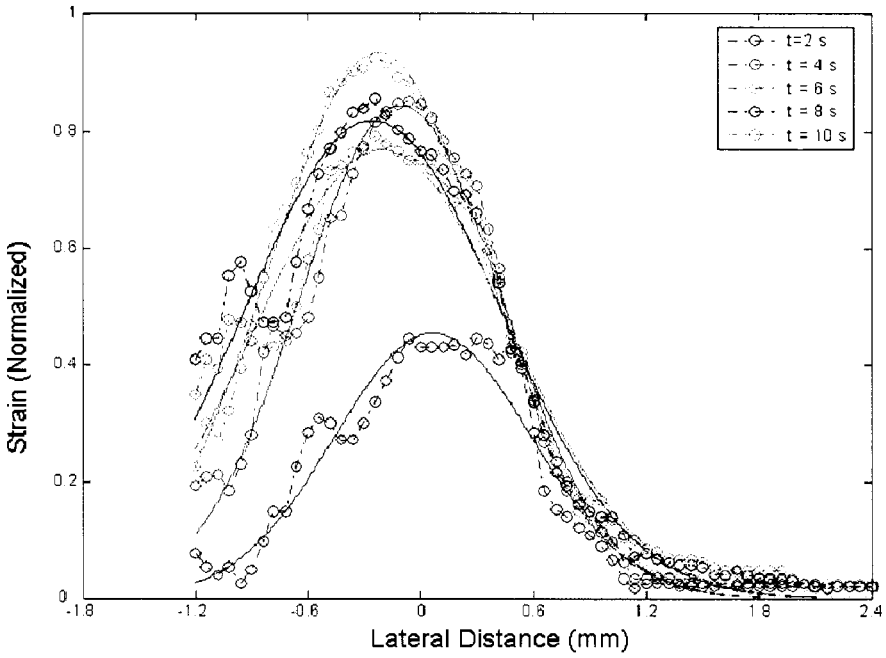

Figure 3.12 1-D lateral strain profiles along *R* in Figure 3.11 at time t=2, 4, 6, 8 and 10 seconds after HIFU therapy commences (-o-) and the corresponding Gaussian fits (—) to each curve.

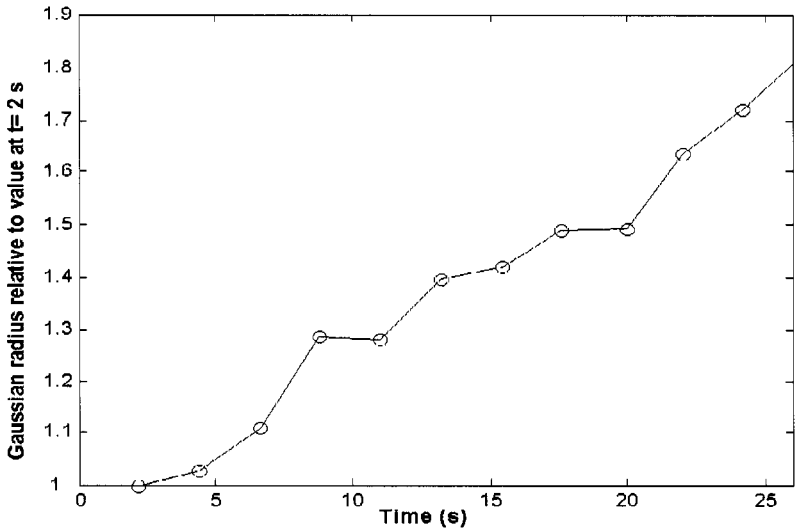

Figure 3.13 Gaussian radius at various times during HIFU heating relative to value at *t*= 2 s for 1-D strain profiles along R in Figure 3.11.

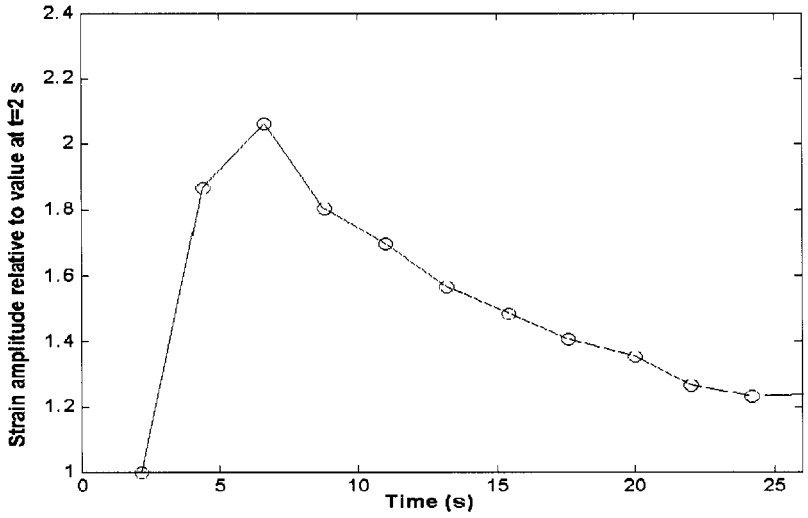

Figure 3.14 Strain amplitude at various times during HIFU heating relative to value at t= 2 s for 1-D strain profiles along R in Figure 3.11.

3.7. Quantitative Temperature Monitoring using Backscattered Ultrasound ("Hotwire" Experiment)

The results of techniques described in section 3.5 showed that analysis of the raw ultrasound backscatter provides improved visualization of lesion evolution by tracking the temperature rise compared to standard B-mode images. However, these techniques are qualitative in nature. In this section, a preliminary experiment to quantitatively compare temperatures estimated from the noninvasive ultrasound based technique with independent measurements made using thermocouples inserted in a tissue mimicking phantom in close proximity to the heat source is described. A phantom was chosen instead of tissue for this preliminary experiment so that the technique could be evaluated in a controlled setting. This experiment also served as a means of validating the strain estimation algorithm (section 3.5). The quantitative comparison was made in the temperature range 23-29°C. For this temperature range, the temperature induced strain is primarily due to the change in the speed of sound with the temperature and the effect of thermal expansion is ignored [73]. To be able to invert the temperature induced strain data to obtain temperature, a separate experiment was performed to explicitly measure

the relation between sound speed and temperature. A detailed description of the experimental setup and the results is provided in this section.

3.7.1. Experiment Setup

An electrical heating element was employed in this experiment instead of an acoustic heat source (HIFU) to induce the temperature rise in a phantom. The main motivation in doing so for this preliminary experiment was to avoid the possibility of bubbles induced by acoustic cavitation from causing de-correlation artifacts in the RF data and focus on demonstrating the feasibility of obtaining quantitative temperature information from the ultrasound backscatter during heating with a controlled heat source. A tissue mimicking gel made with polyacrylamide and loaded with plastic microspheres to ensure scattering was used as the phantom material for this experiment. Pre-gel polyacrylamide solution prepared using the recipe reported in Lafon et.al. [101] was poured into a custom-made sample holder (approximately a cube of side 5 cm edges). A nichrome-chromium heating wire (Omega Engineering Inc., Stamford, CT) with 1.6 Ohm/ft, was pulled taut through the center of the measurement cell. Four needle T-type thermocouples (Omega Engineering Inc., Stamford, CT) were carefully inserted into the gel parallel to the heating wire. The thermocouples were placed at different radial distances from the wire, ranging from 4-11 mm. The exact distances of the thermocouples from the heating wire were measured using the HDI 1000 ultrasound scanner operating in B-mode (HDI 1000, ATL, Bothell, WA). The L11-5 HDI 1000 scanhead was rigidly mounted on the top of the measurement cell to acquire RF data during heating and cooling.

A DC voltage (supplied by "D" cell alkaline batteries, 4 in series supplying ~6 V) was connected to the heating element with a relay switch in series to allow the heating circuit to be turned on and off remotely. The 4 thermocouples were connected to a data acquisition module (HP 34970, Hewlett Packard Inc., Palo Alto, CA) to store the temperature readings in digitized form. The master control program, described in Section 2.3 was modified for this experiment. It controlled the operation of the relay switch, acquisition of temperature readings from the thermocouples using the data acquisition

module and acquisition of the RF data using the HDI 1000. Such a data acquisition scheme ensured time-alignment between the *invasive* thermocouple measurements and *non-invasive ultrasonic* temperature estimation. A schematic representation of the experiment setup is shown in Figure 3.15.

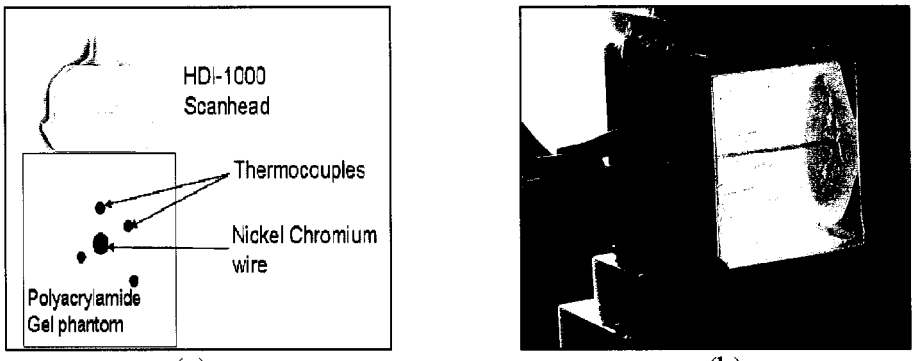

Figure 3.15 (**a**) Schematic representation of the hotwire experiment setup for quantitative temperature estimation. The heating wires and thermocouples are oriented into the page. (**b**) Side view of experimental setup

A reference RF data frame was acquired before heating commenced. The relay switch was closed and the heating circuit was activated. Instantaneously, the data acquisition module was initialized to begin acquisition of readings from the four thermocouples. RF data frames were acquired at an interval of 1 frame/sec during the heating phase. The relay switch was opened after 30 seconds to stop the heating phase. Acquisition of thermocouple readings continued at the same rate during the cooling phase while RF data frames were acquired at a slower rate (frame every 20 seconds) for an additional 2 minutes. The power dissipated in the heating element was constantly monitored by measuring the voltage and current in the circuit. The total power dissipation was approximately 15 W. The RF data was post-processed to obtain estimates of temperature induced strain and mapped to temperature using the independently measured $c(T)$ curves.

3.7.1.1. Independent measurement of c(T) curve

For the processing scheme employed in this experiment, it was necessary to obtain independent estimates of the $c(T)$ curve so that the measured temperature induced strain

could be mapped via *c(T)* to temperature. It may be noted that since thermal expansion is *ignored*, only the sound speed change contributes to the temperature induced strain. Starting from an initial temperature of 22°C, sound speed measurements were made using the sample substitution method [49, 102] for every 10°C rise in temperature. The experimental setup for the measurement is shown in Figure 3.16. A broadband chirp pulse (1-10 MHz) of duration 10 μs was applied to one of a pair of PVDF transducers placed across the sample immersed in a water bath with an electric heater.

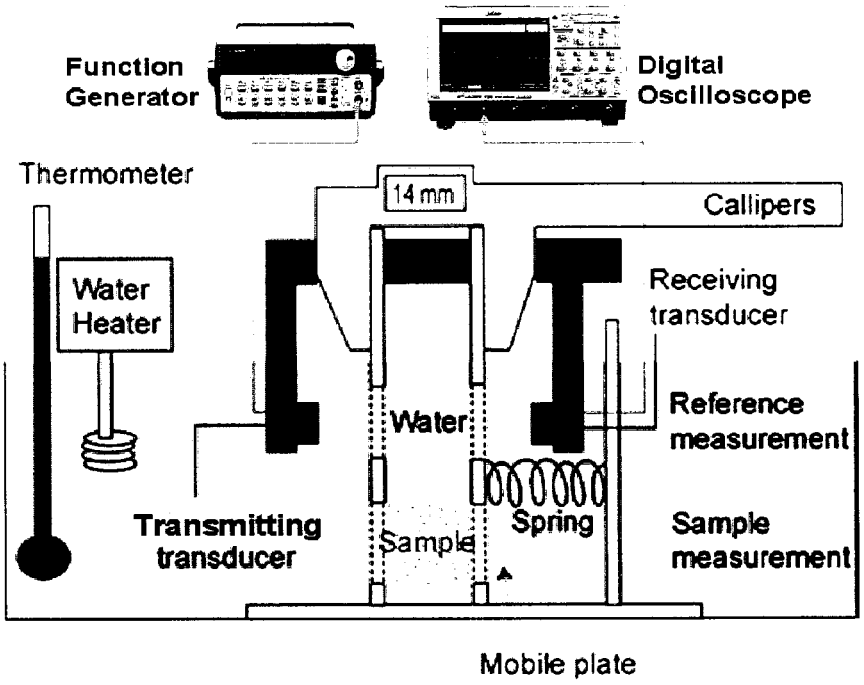

Figure 3.16 Schematic of experiment setup for *c(T)* measurements (*Picture courtesy of Lafon et.al., [101]*)

Thermocouples were placed in the water bath and also embedded in the sample. The spring loaded assembly attached to the calipers ensured that the acoustic propagation distance through the sample was accurately measured throughout the experiment. The signal on the receiving transducer was digitized using an oscilloscope and stored for post-processing. The measurement setup was controlled remotely using custom software developed in LabVIEW™ (National Instruments, Austin, TX). At a given temperature, a measurement was first made in water by placing the transducer pair across the opening marked 'reference measurement' in Figure 3.16. The transducer assembly was then

placed across the sample and a measurement was taken. The attenuation of the sample was computed by analyzing the frequency spectra of the signals received in water and the gel sample using the following equation,

$$Attn(f) = \frac{\left|F_{ref}(f)\right|}{\left|F_{sample}(f)\right|} \tag{3.12}$$

where $F_{ref}(f)$ represents the FFT of the signal in the reference measurement; $F_{sample}(f)$ represents the FFT of the signal in the sample measurement. The attenuation in water is assumed to be negligible.

By estimating the time shift between the signals received in the reference and sample, the sound speed of the sample was calculated using the formula,

$$c_t = \frac{1}{\frac{\Delta t}{d} + c_w} \tag{3.13}$$

where d = width of the sample; c_w = sound speed in water at the temperature of measurement (known from reference data); c_t = sound speed in sample.

Before making a measurement at a given temperature, care was taken to ensure that thermal equilibrium was reached by noting the readings of the thermocouples in the water bath and within the sample. Waveforms acquired during the experiment at a temperature of 39°C are shown in Figure 3.17. The top panel shows the signal received during the reference measurement after propagation through water. The bottom panel shows the signal received after propagation through the sample. The signal received in the phantom is attenuated and shifted towards the origin. Figure 3.18 shows the *c(T)* curve measured for this gel phantom sample.

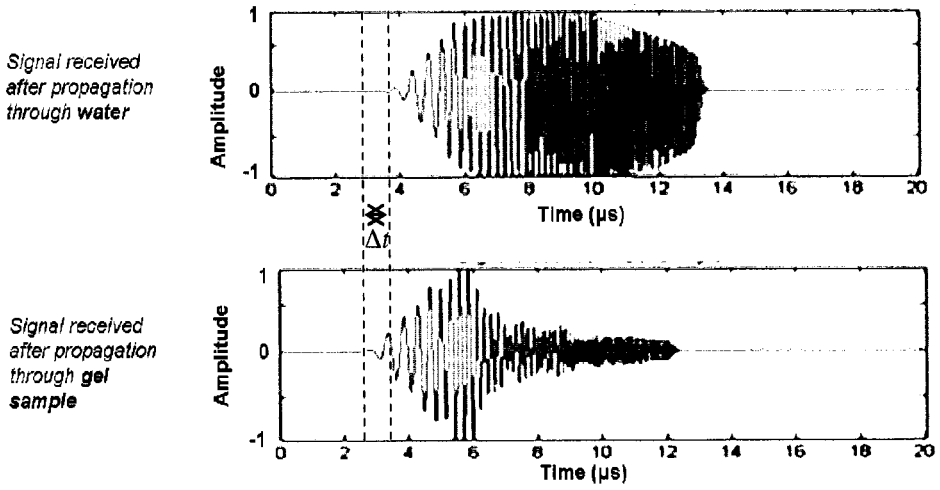

Figure 3.17 Illustration of typical waveforms acquired at the receiver transducer that are used to compute the sound speed of the gel phantom sample. The top plot shows the signal received after propagation through water while the bottom plot shows the signal received after propagation through the gel sample at a temperature of 39° C. The duration of the transmitted chirp pulse is 10 μs with a frequency sweep from 1 to 10 MHz. Note the time shift between the signals received in water and in the sample and the high frequency attenuation in the sample signal. The vertical axis represents the signal amplitude normalized to ± 1. Zero along the x-axis represents an arbitrary time instant along the propagation path between transmit and received transducers and is synchronized on both plots. The time shift Δt between the signals is used in equation (3.13) to compute the sample sound speed.

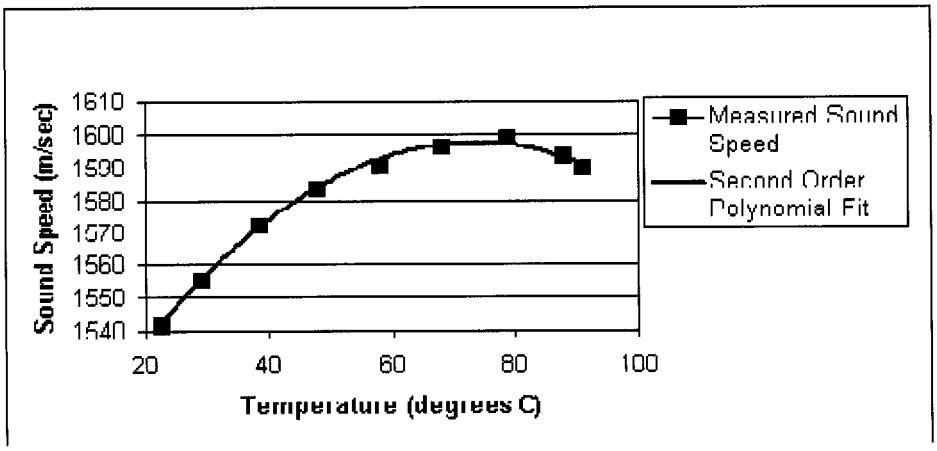

Figure 3.18 Sound speed versus temperature curve for polyacrylamide gel phantom used to invert ultrasound echo shift estimates to temperature

Analysis of the RF data was performed using the algorithm developed in Section 3.5 to compute changes in sound speed. By incorporating the $c(T)$ curve information, temperature maps for the entire experiment were generated. Figure 3.19(a) is a screenshot

of the HDI 1000 ultrasound scanner taken shortly after alignment of the heating wire and thermocouples and shows the relative locations of the thermocouples with respect to the heating wire. Figure 3.19(b) shows the spatial temperature map at time (t = 19.02 seconds). The maximum temperature of about 32° C is seen at the heating wire location with a decrease in temperature away from the location of the wire. Of the four thermocouples situated around the wire, noticeable change (> 0.5°C) was only observed in thermocouple 1 over the time period that the measurements were taken.

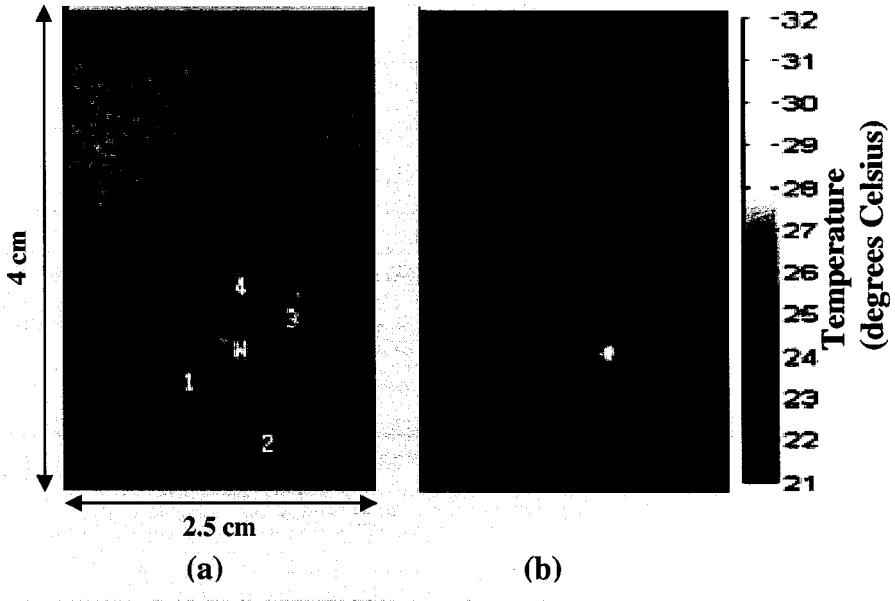

Figure 3.19 (a) A screenshot of the HDI 1000 ultrasound scanner B-mode image showing locations of thermocouples and heating wire (b) Temperatures estimated from sound speed change by processing the RF data incorporating the information from the independently measured c(T) curve at t= 19 seconds.

The B-mode image was spatially registered to the temperature maps derived from the RF data and thermocouple 1 was located on it. The time history of the temperature variation at that location was generated and is shown in Figure 3.20. The temperature readings measured using thermocouples is shown in red on the same figure for comparison. Agreement between the measured values and the non-invasively estimated temperature values is seen with a typical error of 1°C and a maximum absolute error of approximately 2.5° C. Absolute errors of this magnitude would be acceptable over the therapeutic temperature range of interest. Results presented in this section demonstrate

that quantitative temperature changes can be estimated noninvasively by analysis of the RF backscatter. The results show promise for extending the technique to obtain quantitative temperature information—which can be used as a method of monitoring HIFU therapy.

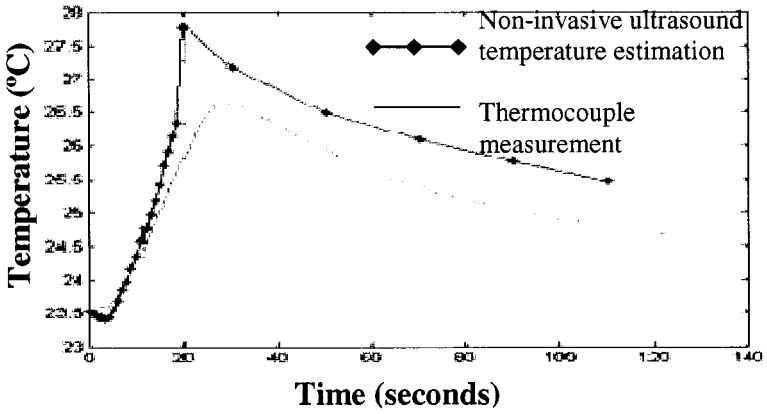

Figure 3.20 Comparison of time profiles of temperature at location of thermocouple 1 in Figure 3.19.

3.8. Tracking Changes in Tissue Scattering Properties during HIFU lesion formation

In this section, a novel signal processing approach based on spectral analysis of the RF data used to detect changes in scattering properties is described. Lesion formation during HIFU therapy is accompanied by changes in local tissue acoustic properties, including increased attenuation due to coagulation [47, 53] and increased backscattering and non-linear effects due to bubbles [24, 103]. Non-invasive acoustic imaging techniques capable of detecting these rapidly evolving changes would be useful for visualizing and monitoring therapy progress. Results from an *in vitro* experiment in which the technique was applied on ultrasound RF signals collected during HIFU exposure is presented in this section. It may be noted that this method, unlike the techniques discussed earlier in this chapter is not directed at temperature estimation. The results obtained show promise for employing this technique in providing clinically useful information directed at monitoring changes in tissue properties during HIFU therapy. Increased harmonic generation at the HIFU focal region is observed soon after HIFU therapy commences. In addition, increased attenuation below the lesion location along

the imaging beam is detected. Tracking the changes in the signature of the ultrasound RF signal provides improved visualization of HIFU lesion formation and can be used to extract information about changes in tissue properties. The algorithm is focused on detecting the *changes* in properties compared to a reference initial frame and hence the effect of the ultrasound system response and local tissue in-homogeneities are removed from consideration in the display.

3.8.1. Description of Algorithm

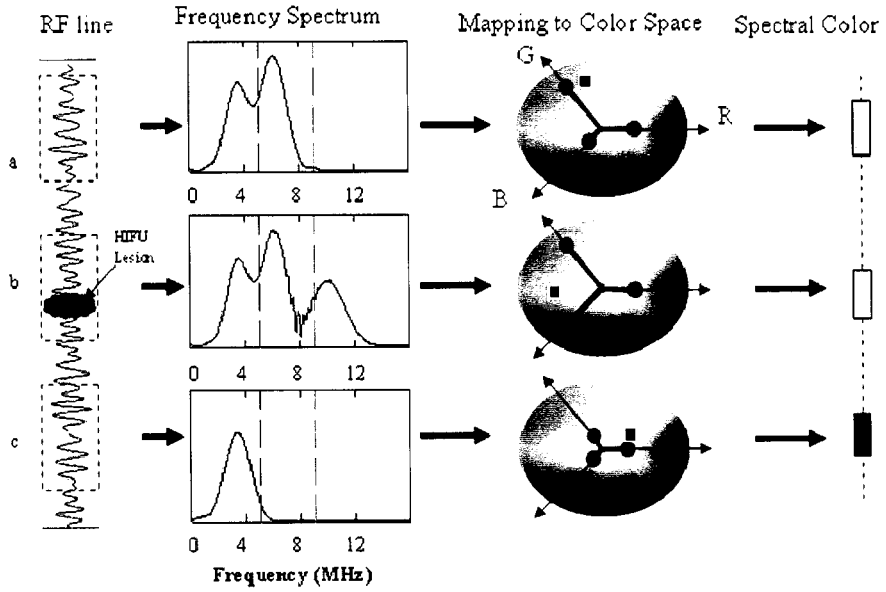

Figure 3.21 Block diagram illustration of algorithm to monitor change in scattering properties. Segments shown on the RF signal by dotted red line represent (**a**) characteristic reference spectrum (**b**) increased harmonic content generation (e.g. bubbles created during HIFU) (**c**) effect of increased attenuation. The red and green dotted lines on the spectrum represent the location of the band edges.

A block diagram representation of the steps involved in this processing scheme is shown in Figure 3.21. A scanline passing through the HIFU lesion in a RF data frame was selected by visual inspection of the corresponding B-mode image consistent with the location of the geometric focus of the HIFU transducer. The chosen scanline was subdivided into segments 8 mm long with 90% overlap, and the Short Time Fourier Transform (STFT) employing a cosine taper window was computed to obtain a local frequency spectrum. Each spectrum was divided into three frequency bands, and the area

within each band was computed to determine the band energy. The three normalized band energies were then assigned to the additive color channels - Red, Green and Blue (R,G,B). The color resulting from these RGB components is referred to as a "spectral color" and was mapped to the screen as a single pixel that occupied $1/10^{th}$ the size of the RF scanline segment due to the 90% overlap. The color mapping is illustrated by the color wheel shown in Figure 3.21 where the component energies are projected onto the RGB axes (basis vectors in this space) and the vector sum gives the resultant color shown by the black dot on the color wheel. Since the goal of this method of display is to visualize the *change* in spectral content over time, the reference frame collected before HIFU therapy commenced was used to normalize the spectrum for each segment. This was done by dividing the component band energies for each segment by the values at the same segment location on the reference frame. Thus, the effects of the ultrasound system response and local tissue in-homogeneities were removed from consideration in the display. Finally, each pixel was scaled to completely saturate the largest among the R,G,B channels; thus, if no change in the spectrum is observed, the pixel appears white. The segments (a), (b) and (c) in Figure 3.21 exhibits different scattering properties. Based on the choice of location of the band edges, increase in energy in the higher frequencies (as might be expected in case of harmonic content generation possibly caused by formation of bubbles) increases the length of the vector projected along the B axis on the color wheel and thus will force the result to have shades of blue (Figure 3.21, segment (b)). On the other hand, a decrease in high frequency content (representative of attenuation) will reduce the length for the vectors projected along the B and G axis compared to R and the resultant color will be shades of red (Figure 3.21, segment (c)).

3.8.2. Results

The results obtained for this processing scheme are illustrated for the data set collected in bovine liver tissue (presented in Section 3.6.2 earlier). Figure 3.22(a) shows a B-mode image with a hyperechogenic spot seen at the lesion location. A scanline passing through the lesion is shown by the red dotted line. The window length (8 mm) and

overlap (90 %) for the FFT line segments are marked on the dotted line. Figure 3.22(b) represents the typical frequency spectrum for a RF line segment indicated by the blue segment on the red dotted scanline in Figure 3.22(a). The spectrum shows a large number of nulls and peaks that are related to the statistics of the scatterer distribution within the particular RF segment. By visual observation of the main peak in the spectrum (around 5 MHz) and the expected location of harmonics, the transition between the red-green band and the green-blue band was selected to be 5 MHz and 9 MHz respectively. In the current implementation, the band edges are selected manually by the user.

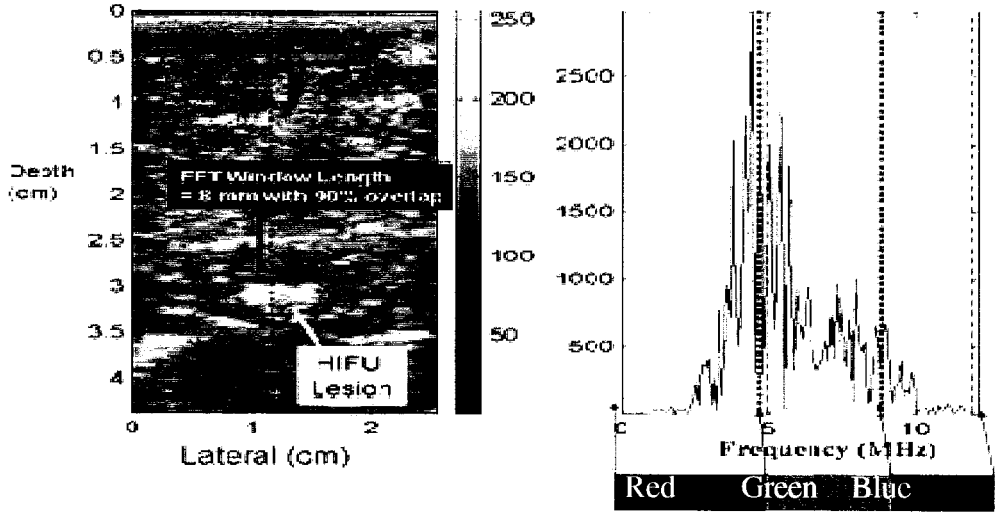

Figure 3.22(a) Illustration of typical parameters used in the algorithm. A scanline (red dotted line) passing through the lesion is selected and the spectrum of overlapping windows with 90% overlap is generated. **(b)** Spectrum of typical RF line segment from bovine liver tissue. The spectrum shows significant variability across the band. The two dotted lines indicate the transition bands Red-Green and Green-Blue.

The final output of the algorithm described in Figure 3.21 is the spectral color image. Figure 3.23(a) shows the conventional M-mode display for a scan line passing through the HIFU lesion. The horizontal axis represents time since the start of RF data acquisition while vertical direction represents depth. Figure 3.23(b) shows the results by applying the above algorithm and is referred to as the spectral color M-mode display. The "spectral-color" M-mode display is inspired by the conventional M-mode commonly used in

ultrasound imaging. The vertical line at the extreme left corresponds to the reference frame used to normalize the entire image and is white throughout. Thus all colors seen are interpreted as changes with respect to the reference frame. At a depth of 3 cm corresponding to the lesion, a bluish cast is observed soon after HIFU therapy commences suggesting harmonic generation. It is hypothesized that the generation of harmonics is due to generation of bubbles produced by out gassing as tissue temperature rises. On the standard M-mode image in Figure 3.23(a), the growth and decay of the hyperechogenic spot in the focal zone is easily observed, but it appears long after HIFU therapy commenced and is very short lived. For $1.8 < t < 2.2$ s, corresponding to the hyperechogenic spot appearing on the B-mode image, a purple color is seen on the "spectral-color" M-mode display resulting from increased backscatter in the fundamental frequency (red band) and harmonic (blue band) due to bubbles.

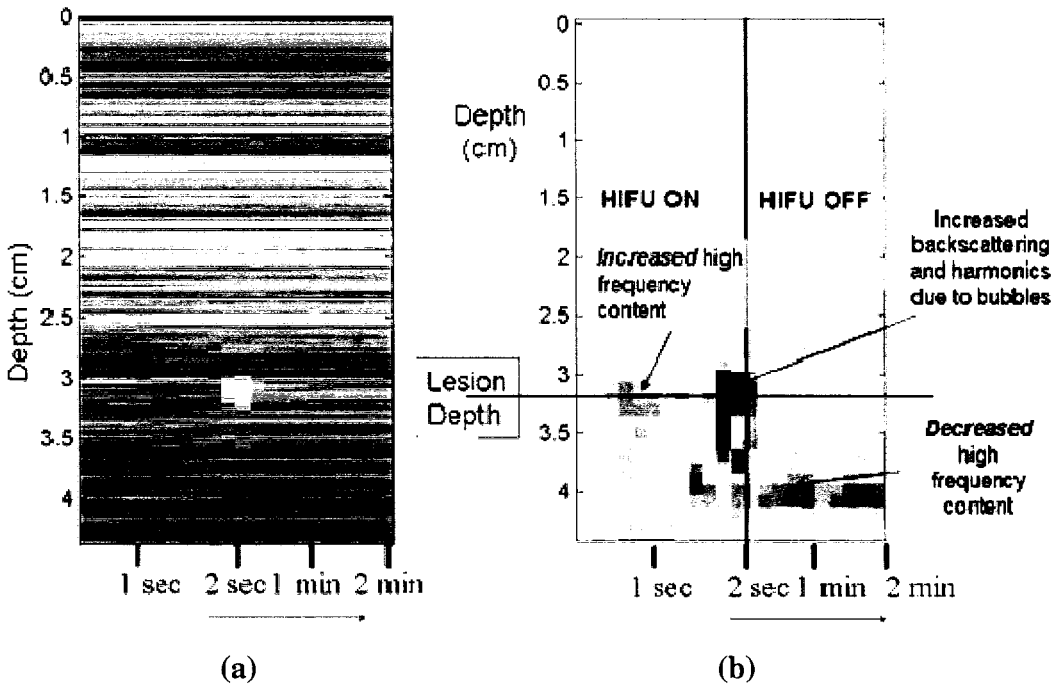

Figure 3.23(a) Standard M-mode display for a scanline passing through the HIFU focal zone (**b**) Spectral color M-mode display for the same line. The time scales are not uniform: during HIFU, the frame rate is about 3 Hz, whereas after HIFU the frame rate is much slower (approx 0.1 Hz) to visualize the diffusion of heat over a 2 minute period.

Below the focal spot in Figure 3.23(b), the spectral M-mode plot turns redder soon after HIFU therapy commenced. The increased attenuation in the focal spot due to the temperature rise results in preferential absorption of high frequency content causing decrease in high frequency backscatter from locations distal to it along the imaging beam (below the focal spot in the image). The effect of increased attenuation in the focal region is thus most pronounced in the backscatter from regions below it. The above results demonstrate potential for the applicability of this qualitative processing scheme for tracking, monitoring and post-treatment visualization of HIFU-induced lesions for ultrasound image guided HIFU therapy.

3.9. Summary and Discussion

A signal processing based approach to estimate *temperature induced strain* from the raw ultrasound backscatter (RF signal) due to temperature change during HIFU therapy was developed and presented in this chapter. This approach was used to analyze the raw ultrasound backscatter data acquired during *in vitro* experiments in freshly excised bovine liver tissue and tissue mimicking phantoms. Local acoustic travel time changes and temperature induced strain derived from the ultrasound backscatter showed information related to the temperature change during and shortly after HIFU exposure. These changes were detected before visible changes were evident on synchronized B-mode images. This technique provides qualitative information about progression of treatment including better visualization of the spatial extent of the heated zone, location of the HIFU focus and enables the underlying heat conduction process to be visualized. However, extracting quantitative temperature information from temperature induced strain measurements requires explicit knowledge of the relation between travel time change and temperature. Quantitative temperature information obtained by inverting the strain data that incorporated independent $c(T)$ measurements compared well with invasive thermocouple measurements as demonstrated in the hotwire experiment (Section 3.7).

The algorithm in section 3.8 demonstrated the ability to detect changes in tissue scattering properties by analyzing changes in the spectral content of the RF data. In the current implementation, the band edges for the sub-bands are set manually by observing

the location of the center frequency and the expected location of the harmonics. An automated technique of estimating these band edges would be beneficial. This could be done adaptively by moving the band edges until the contrast between the fundamental and harmonic energy bands is maximized. The current technique was applied on a single A-line passing through the center of the lesion. Extension of the method to generate 2-D spectral color data would enable better visualization of the treatment region. The evidence of increased attenuation at the site of the lesion in the spectral M-mode display could potentially be of significance as a means of determining the endpoint of thermal therapy. It is however important to confirm whether the attenuation change is as a result of bubbles forming at the lesion site or due to permanent changes in tissue properties due to tissue necrosis. To address this problem, Bailey et. al. [24] showed that overpressure (elevated static pressure) can be used to suppress bubbles in excised tissue. In a related experiment, they also acquired interleaved RF data during HIFU exposure along with the application of overpressure in excised turkey breast muscle tissue. Spectral M-mode images obtained using the spectral analysis technique (Section 3.8) demonstrated that a hyperechoic region and increased harmonic frequencies appeared at the lesion site in the RF echoes of all treatments *without* overpressure and in none *with* overpressure [103]. Lesions were created in all cases. Attenuation of echoes from tissue beyond the lesion was pronounced without overpressure. It was concluded that suppression of the bubbles by overpressure may lead to detection of the permanent change in attenuation solely due to protein denaturation.

3.10. Motivation for bioheat transfer model-based quantitative temperature estimation approach for HIFU therapy monitoring

In this chapter, signal processing based approaches to generate maps of travel time changes (or equivalently temperature induced strain) for extracting temperature related information from the raw ultrasound backscatter data acquired during HIFU therapy were reported. Direct inversion of the RF backscatter data to obtain quantitative temperature information requires explicit knowledge of the relationship between temperature-induced strain (ε) and temperature over the entire temperature range of interest. However, lack of

sensitivity of sound speed change to temperature near the tissue coagulation threshold (55-60 degrees Celsius) makes temperature estimation by direct inversion of the measured travel time shifts a challenging task. A solution to overcoming this problem of lack of sensitivity is to incorporate information about the underlying heat diffusion into the temperature estimation technique. The heat diffusion can be represented mathematically using the bioheat transfer equation [77] parameterized with two constants, heating rate and the thermal diffusivity (for *in vitro* experimental conditions with no perfusion). Such a model-based approach provides two direct advantages compared to a solely signal processing based method relying on direct mapping of temperature induced strain (ε) to temperature (T). First, by estimating the bioheat transfer equation parameters using RF data collected immediately after HIFU therapy is turned on, only the region of high sensitivity in the $\varepsilon(T)$ curve is utilized in the parameter estimation. After the bioheat equation parameters have been estimated, the temperature field throughout therapy can be computed numerically without requiring knowledge of $\varepsilon(T)$. Second, the spatial and temporal constraints imposed by the bioheat equation can be used to regularize the temperature induced strain estimates. This avoids artifacts in the temperature maps due to smoothing and false peaks [70] induced by processing the RF data.

Variability in the $\varepsilon(T)$ relationship between tissue types and possibly between patients further complicates the inversion of temperature induced strain. For example, the sound speed increases as a function of temperature for water-bearing tissues. However, for fatty tissue, the sound speed actually decreases with temperature. It would therefore be desirable to have a noninvasive method of estimating this mapping in the treatment zone for use in clinical situations. Incorporating information about the underlying heat diffusion process using the bioheat transfer equation enables the noninvasive estimation of the $\varepsilon(T)$ relationship. Specifically, the temperature distribution at a calibration point (within the region of interest for HIFU therapy) can be first computed from the bioheat equation using independently measured values for thermal diffusivity and heat source.

The computed temperature distribution at this location can then be compared with the measured RF data to obtain the $\varepsilon(T)$ curve.

Thus, it can be seen that a heat transfer model-based temperature estimation approach can potentially overcome drawbacks associated with the low sensitivity and high variability of the $\varepsilon(T)$ curve in the therapeutic temperature range. The rest of this thesis focuses on the development and implementation of this noninvasive model-based temperature estimation technique. A detailed description of the technique and experimental results obtained in tissue mimicking phantoms are described in Chapter 4 and 5. Application of the methods to excised animal tissue is described in Chapter 6.

4. MODEL-BASED TEMPERATURE ESTIMATION TECHNIQUE FOR HIFU THERAPY MONITORING: PART I

4.1. Introduction

In this chapter, a noninvasive thermal model-based temperature estimation technique for HIFU therapy monitoring is introduced. The technique is based on combining the bioheat equation model with ultrasound backscatter data, measured during HIFU therapy, to derive quantitative temperature information. The chapter begins with a description of the bioheat transfer equation and assumptions regarding the parameters, in Section 4.2. In Section 4.3, a top-level description of the temperature estimation approach is presented. An integral component of this technique is the noninvasive estimation of thermal and acoustic parameters using acoustic sensing methods. This is a calibration step and is performed immediately prior to the therapy in the treatment region. The calibration procedure is described in Section 4.4. The chapter concludes with a discussion of experimental results for the calibration procedure performed in tissue mimicking phantoms. These calibration procedures are then used in Chapter 5 in the temperature estimation step.

4.2. Bioheat Transfer Equation (BHTE)

The basic law that relates the heat flow and the temperature gradient based on experimental observation was derived by Joseph Fourier around 1822. The general differential form of the heat transfer law is,

$$\rho C \frac{\partial T}{\partial t} = \nabla \bullet (k \nabla T) + f \tag{4.1}$$

where ρ is the density, C is the specific heat capacity, k is the thermal conductivity, f represents the distributed heat source term and T is the temperature.

In biological media, equation (4.1) cannot be applied directly due to the complexity and the dynamics of the system. However, f can be expressed as a linear combination of heat sources and heat sinks. The internally generated heat sources that contribute to f, for biological media, include those related to metabolism while the cooling processes are

conduction, advection and convection (also referred to as perfusion in the medical literature). This formulation specifically adapted for biological systems is referred to as the *bioheat transfer equation* [77]. For the *in vitro* experimental procedures performed in this study, the contribution of metabolism as a heat source and convection and advection as heat sinks is ignored [104]. Hence the modified form of the BHTE becomes,

$$\frac{\partial T}{\partial t} = K\nabla^2 T + Q \cdot I(r,z) \tag{4.2}$$

where K is the thermal diffusivity (m^2/sec) given by $K = k/\rho C$, Q (°C/s) represents the local *in situ* heating rate due to ultrasound energy absorption, ρ is the density (kg/m^3), C is the specific heat (J/kg/°C), $I(r,z)$ is the normalized spatial acoustic intensity distribution profile, r represents the axis perpendicular to beam propagation (transverse) and z represents the beam propagation axis (longitudinal). The heating rate Q (°C/s) and the heat source Q_s(W/cm^3) are related by the following equation,

$$Q_s = Q\rho C \tag{4.3}$$

Within the scope of this dissertation, the following assumptions are made regarding the parameters of the BHTE:

- The tissue thermal properties i.e. k, ρ and C are assumed to be spatially and temporally invariant, and isotropic.
- The thermal properties remain constant over the therapeutic temperature range.
- *a priori* knowledge of the normalized spatial beam profile $I(r,z)$ is available. An experimentally measured beam profile or a simulated profile generated using an acoustic wave propagation code could be used.

It may be noted that for a HIFU heat source, Q is a lumped quantity that is influenced by the scattering and attenuation along the beam path, local tissue absorption and non-linear acoustic propagation effects. In this work, as described in the next section the focus is on estimating the lumped quantity, and the individual components are not proposed to be estimated, nor are they necessary to know for our estimation technique.

4.3. Overview of BHTE model-based temperature estimation approach

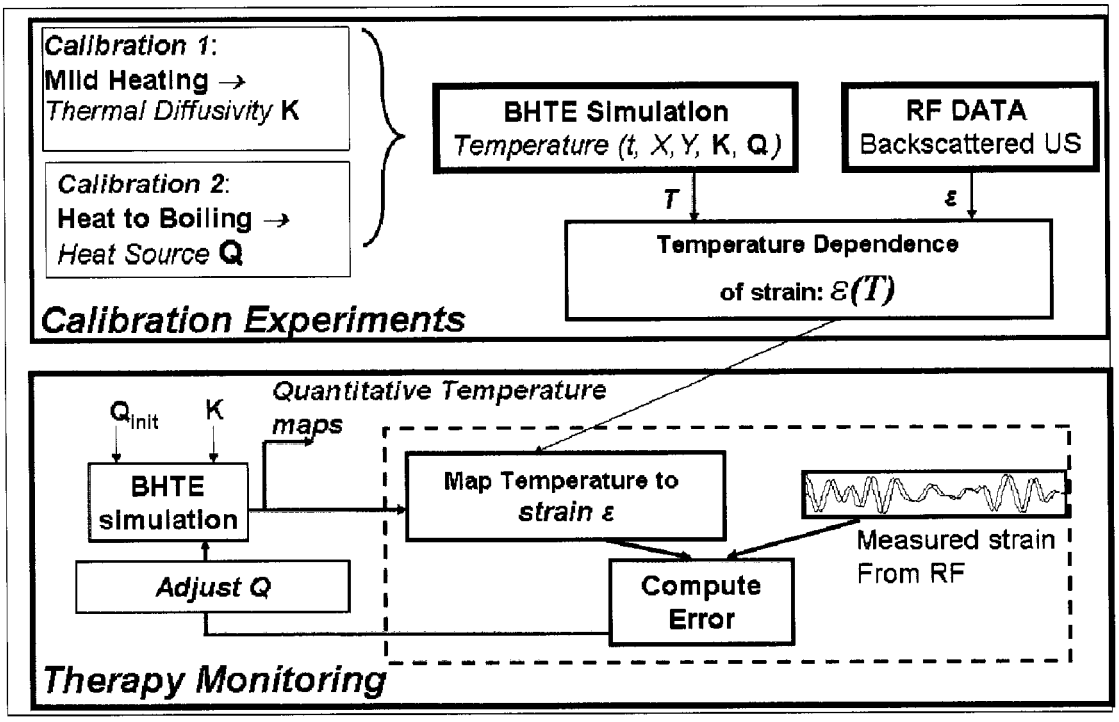

Figure 4.1 Block diagram illustrating model-based temperature estimation approach for monitoring thermal therapy.

The model-based temperature estimation approach for therapy monitoring is outlined in Figure 4.1. Essential to the process are the two pre-therapy "calibration" steps that determine *in situ* values for BHTE parameters K and Q. These two parameters can be measured at single points anywhere in the treatment region of interest, and provide the characterization of local tissue and acoustic path properties necessary for accurate therapy planning and execution. The estimated parameters are used in the BHTE to obtain temperature maps at the current location. The temperature estimates are related to strains estimated from the ultrasound backscatter during the *noninvasive* calibration experiment to obtain the $\varepsilon(T)$ mapping. Once the BHTE parameters have been estimated at a given location using the calibration experiments, the temperature maps for that location can be obtained by computing the BHTE directly. It might thus appear that the estimation of $\varepsilon(T)$ is not required and the ultrasound backscatter information during monitoring is not needed either. But this is applicable only for locations where the BHTE

parameter estimates are accurately known, i.e., where the calibration was performed. Dosimetry studies conducted in our laboratory, that employed scanned transducer protocols, demonstrated *variability* in the observed bioeffect even under *constant exposure conditions* [105]. *The need for monitoring arises because tissue heterogeneities result in local variation in these parameters.* Specifically, in our model, we model the tissue heterogeneity as variations in the parameter Q. The goal of the monitoring step is thus to accurately track these changes in Q.

The lower block diagram in Figure 4.1 illustrates the temperature monitoring step. The parameters estimated in the calibration step, K and $\varepsilon(T)$, are now taken as known. The initial value of Q is also known. The therapy phase begins by following the planned experimental protocol and acquiring interleaved RF frames. These data are processed to compute ε and coupled with the BHTE to estimate the unknown heat source Q as a function of tissue location. As can be clearly seen from the block diagram in Figure 4.1, accurate knowledge of the $\varepsilon(T)$ mapping is required to be able to compare the estimated strain with the predicted strain so that the heat source Q can be adaptively updated. This information can be used to modify the treatment protocol in real-time to optimize safety and efficacy while simultaneously minimizing treatment time.

The set of schematics in Figure 4.2 illustrate how the proposed noninvasive model-based temperature estimation approach can be implemented in a clinical setting for therapy monitoring. First, the calibration experiments are performed at a single representative location within the treatment volume to estimate the local acoustic and thermal parameters of interest (Figure 4.2 *a* and *b*). After the calibration experiments have been completed, the therapy transducer is translated to a new location within the treatment region and the HIFU therapy session commences (Figure 4.2 *c*). In this chapter, the estimation of K and Q is described in detail along with results obtained in tissue mimicking phantoms. The estimation of $\varepsilon(T)$ and the temperature estimation step is presented in Chapter 5.

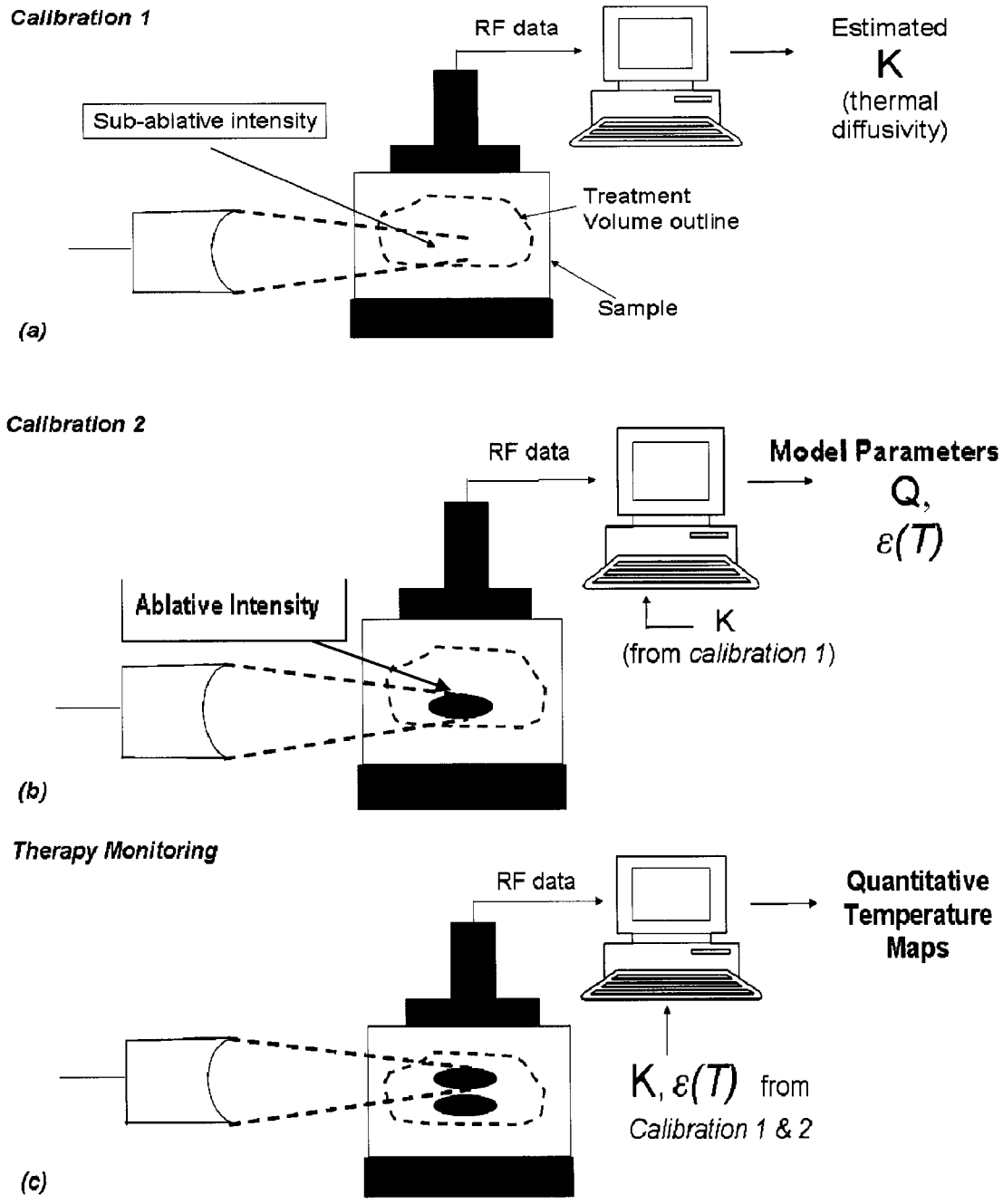

Figure 4.2 Schematics illustrating the experimental protocol for the BHTE model-based noninvasive temperature estimation approach for HIFU therapy monitoring. First, a noninvasive estimate of thermal diffusivity *(K)* is obtained by applying a short HIFU heating pulse and visualizing the cool down period as illustrated in (a). Following this, an ablative HIFU exposure is performed at the same location to estimate the heating rate *(Q)* and temperature dependence of strain $\varepsilon(T)$ as illustrated in (b). After the calibration experiments have been completed, therapy is delivered throughout the treatment volume and continually monitored as illustrated in (c).

4.4. Calibration experiments

4.4.1. Estimation of K

4.4.1.1. Theory

The estimation of thermal diffusivity is based on the principle of thermal clearance [106], Two criteria must be satisfied to effectively use this principle. The first criterion is that a spatial temperature gradient must exist. Second, the heat source must approximate an impulse in both space and time. *The sub-millimeter transverse beam widths of the HIFU beam conveniently satisfies both requirements.*

In this estimation approach, a short HIFU heating pulse is applied and the resulting spatial distribution of temperature is measured. Sub-ablative HIFU intensities are employed to ensure that the maximum temperature rise is no more than 10-15 degrees. The orientation of the HIFU transducer, ultrasound imaging probe and the geometric focus of the HIFU beam is illustrated in Figure 4.3.

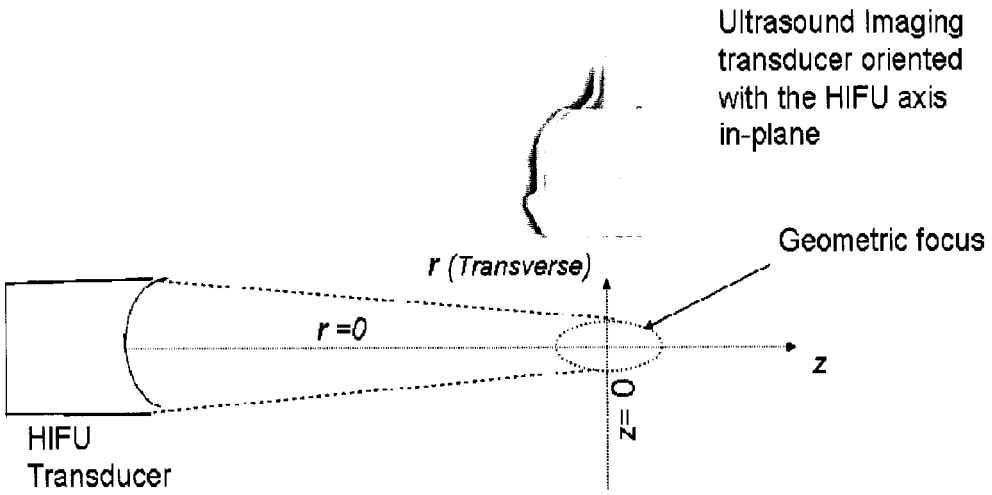

Figure 4.3 Schematic diagram showing the relative orientation of the HIFU transducer, imaging probe and HIFU beam geometric focus

For an impulse HIFU heating pulse applied at time $t=0$, the resulting temperature distribution along the transverse direction r at $z=0$ after the HIFU pulse has been turned off follows the Gaussian profile [106] and can be mathematically represented as,

$$T(r,t)-T_0=\Delta T(r,t)=T_{\max}(t)\,e^{[\frac{-r}{R(t)}]^2}\quad, \tag{4.4}$$

$$\text{where}\,[R(t)]^2\quad=4K(t+\beta) \tag{4.5}$$

In equation (4.4) and (4.5), $T(r,t)$ is the temperature distribution at distance r and time t after the heating pulse was turned off, T_{max} (°C) represents the maximum temperature rise at time t, T_0 is the initial ambient temperature (typically 37°C), $R(t)$ (m^2) is the Gaussian radius, K (m^2/s) is the thermal diffusivity and β (s) represents the diffusion time constant.

Previously, it has been demonstrated [70, 75, 107] that in biological media the temperature-induced strain (ε), directly measured from the ultrasound radio-frequency (RF) backscatter for temperature rises in the range of 10-15 °C above ambient temperature, is directly proportional to the induced temperature change ($\Delta T(r,t)$), i.e.,

$$\Delta T(r,t) = \alpha\,\varepsilon(r,t) \tag{4.6}$$

where α is a scalar constant.

From (4.4) and (4.6), we get,

$$\varepsilon(r,t)=\varepsilon_{\max}(t)e^{-[\frac{r}{R(t)}]^2} \tag{4.7}$$

where $\varepsilon_{\max} = \alpha\,T_{max}$.

Integrating (4.7) along r, the cumulative shift in the ultrasound RF echo locations $s(r,t)$ along the imaging beam has the form of the error function ($erf(x)$),

$$s(r,t)=\int_{u=-\infty}^{u=r}\varepsilon(u,t)du=A_{\max}(t)\int_{u=-\infty}^{u=r}e^{-[\frac{u}{R(t)}]^2}du \tag{4.8}$$

where $A_{max}(t)$ is the peak displacement at time t. From equation (4.8), it can be seen that the parameter $R(t)$ can be measured from the Gaussian width of $s(r,t)$ profiles for all times t. Differentiating equation (4.5) with respect to t, we get,

$$\frac{d([R(t)]^2)}{dt} = 4K \tag{4.9}$$

Equation (4.9) shows that by computing the rate of change of $[R(t)]^2$ versus t, the thermal diffusivity (K) can be estimated. The estimation procedure is noninvasive, and does not depend on the constant α which relates temperature to induced strain. As long as the Signal-to-Noise ratio is high, the value of α does not affect the result. It may be noted from equation (4.8) that errors introduced in the estimation of $s(r,t)$ will affect the estimated $R(t)$ and consequently the thermal diffusivity K. The estimated value of K is used as a "known" quantity in the subsequent estimate of the local heating rate Q described in section 4.4.2.

4.4.1.2. Methodology for estimation of K from ultrasound backscatter

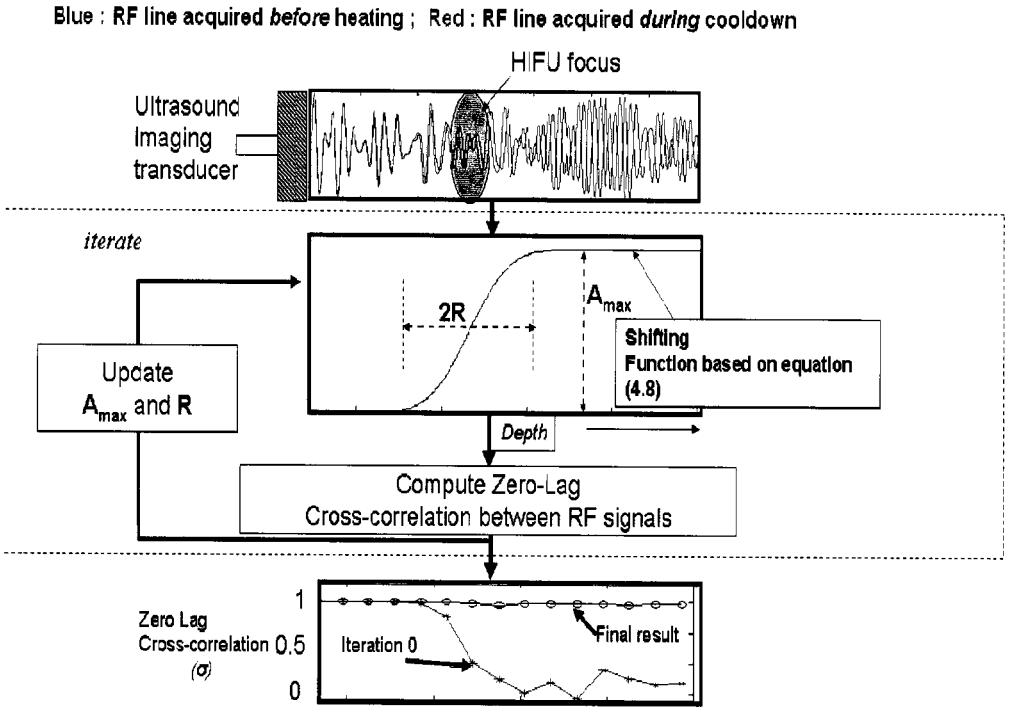

Figure 4.4 Flowchart of iterative minimization based technique to estimate A_{max} and R based on equation (4.8)

In this research, a novel parametric estimation approach has been developed to estimate *strain* using RF backscatter data collected during the HIFU experiment.

Equation (4.8) illustrates that the echo location shifts *s(r,t)* can be represented by a closed functional form and parameterized in terms of A_{max} and R. A schematic representation of the estimation technique is presented in Figure 4.4. Techniques for estimation of temperature-induced ultrasound echo location shifts *s(r,t)* between RF data frames have been previously reported [70, 72, 73]. However, the methods reported by those authors do not incorporate knowledge of the underlying physical heat diffusion mechanism in the estimation procedure. The approach presented here allows direct estimation of thermal parameters by iteratively relating the *temperature change induced* shift in the RF signals with a (physics based) mathematical model describing the thermal diffusion process.

The steps in the algorithm to compute *R(t)* between a pair of RF A-lines passing through the heated region, one acquired before heating commenced ($t=t_0$) and one during cool down ($t=t_{cool}$), are outlined below:

1. *s(r,t)* is mathematically modeled as in equation (4.8) with unknown parameters A_{max} and R at a particular time t. A_{max} and R are set to reasonable initial guess values.
2. The RF line acquired at $t=t_{cool}$ is temporally shifted by the magnitude of *s(r,t)* with values of A_{max} and R set in step 1.
3. The *shifted* RF A-line acquired at $t=t_{cool}$ (from step 2) and RF A-line acquired at $t=t_0$ are both segmented into N non-overlapping segments, and the normalized zero-lag correlation coefficient for each segment i is computed using equation (4.10). A fixed value of N is chosen. For a 1 cm RF line segment, a typical value of N used is 20.

$$\sigma_i = \frac{\sum_{j=1}^{j=m} RF_{preheat}(j,i) * RF_{t=t_0}(j,i)}{\sum_{j=1}^{j=m} [RF_{preheat}(j,i)]^2 * \sum_{j=1}^{j=m} [RF_{t=t_0}(j,i)]^2} \tag{4.10}$$

4. Error function $err = \sum_{i=1}^{i=N} (1-\sigma_i)^2$ is then computed.
5. The parameters $A_{\max}$ and R are updated to minimize *err*

6. Steps 2, 3, 4 and 5 are repeated until *err< (specified tolerance).*

The values of A_{max} and R obtained after convergence are the "best fit" parameters. Typical plots of the zero-lag cross-correlation before and after convergence are shown in the bottom panel of Figure 4.4. At iteration 0, before any processing is applied, the zero-lag correlation drops significantly below unity beyond the HIFU focus due to the echo shifts caused by the temperature change. After convergence, the correlation coefficient uniformly improves to unity throughout the depth direction.

This procedure is repeated for all the RF frames collected during the cool down phase (after HIFU has been turned off) to obtain *R(t)* for each frame. The estimated values of *R(t)* are then fitted to a straight line to obtain the local thermal diffusivity *K,* which is the thermal parameter of interest. The optimization algorithm was implemented using the MATLAB (The Mathworks Inc., Natick, MA) function *fminsearch*, which is based on the Nelder-Mead Simplex search technique [108]. Other optimization techniques such as the Levenberg-Marquardt algorithm [109] could also be employed. The simplex method belongs to the class of direct search optimization methods, and was preferred since it relies *only* on the evaluation of the minimization function. The Levenberg-Marquardt technique, on the other hand, also requires the Jacobian matrix at each iteration and it has to be provided as an analytical expression or calculated using finite differences.

4.4.1.3. Experiments

Experiments to validate the thermal diffusivity estimation algorithm were performed in a tissue mimicking phantom made of alginate based hydrogel containing 95% water by weight. The phantom was prepared by dissolving 16 gm of Jeltrate Dental Impression Material (Dentsply Caulk Inc., Milford, DE) in 300 ml water while stirring continuously to ensure a homogenous mix. The solution was degassed under vacuum and allowed to settle for 20 minutes in specially designed sample holders of size 5×5×6.5 cm in which the solution solidified. The sound speed and acoustic attenuation of the phantom at 25 °C measured using the sample replacement technique [49, 110] was 1483 m/s and 0.35

dB/cm/MHz respectively. The schematic diagram of the experimental setup is shown in Figure 4.5.

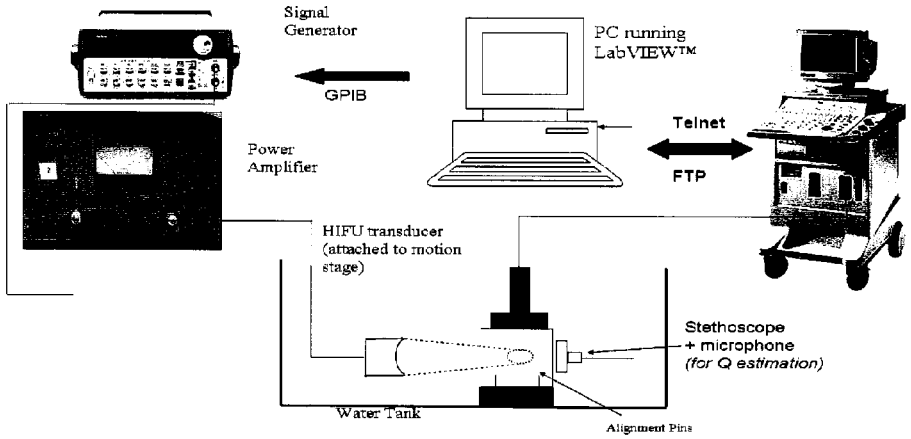

Figure 4.5 Schematic of experimental setup for noninvasive K estimation. The setup is similar to that shown in Figure 2.8. The stethoscope and microphone assembly are used for Q estimation described in Section 4.4.2.

A 5 MHz single element HIFU therapy transducer (SU-104, Sonic Concepts, Woodinville, WA) with an aperture diameter of 16 mm and a focal depth of 35 mm was utilized for delivering the HIFU heating pulse. The HIFU transducer was rigidly attached to a 3-D translation stage. The driving electronics for the HIFU transducer consisted of a signal generator (HP 33120, Hewlett Packard, Palo Alto, CA) driving a power amplifier (A150, ENI, Rochester, NY). The imaging probe used was the ATL CL10-5 (Philips Medical Systems, Bothell, WA) with a bandwidth of 5 to 10 MHz. Vertical alignment pins affixed to the base of the sample holder (Figure 4.5) were used to co-register the HIFU beam propagation plane with the imaging plane. Specifically, before the experiment commenced, the HIFU transducer was operated in pulse-echo mode and translated using the motion stage until the received echo amplitude from the proximal alignment pin was maximum thereby ensuring that the pins were in the HIFU focal plane. The imaging transducer was mounted on the sample holder such that alignment pins were visible on B-mode images as vertical straight lines thus confirming that the imaging plane intersected the HIFU focal zone. RF data frames time-synchronized with the HIFU therapy delivery generation circuitry were acquired using an ATL HDI 1000 ultrasound

scanner during the brief HIFU heating phase lasting 5 seconds and cool down phase lasting 20 seconds. The RF data frames were acquired at a frame rate of 1 frame per second. A personal computer running a software program developed in Labview™ (National Instruments, Austin, TX) controlled the operation of the entire system [91, 111]. The RF data were transferred to the PC at the end of the experiment for offline data analysis. HIFU acoustic intensities were chosen such that the maximum temperature rise induced was approximately 10 °C. The RF data sets were analyzed using the algorithm described in 4.4.1.2 to compute $R(t)$ and a least square fitting was performed to estimate the thermal diffusivity K using equation (4.9). The estimation procedure was tested on 5 phantom samples prepared using the same recipe.

The thermal diffusivity (K) was also independently measured for the phantom samples using the *transient hot-wire technique* [112, 113], a standard method reported in the heat transfer literature for measuring the thermal properties of solids. The estimates obtained by this method were compared with those obtained using the noninvasive ultrasound-based estimation procedure. A schematic representation of the transient hot-wire experiment setup is shown in Figure 4.6. The setup is similar to that used in the preliminary quantitative temperature estimation experiment reported in section 3.6.1 except that the alginate phantom was used in these experiments and the wire was heated by connecting it to a programmable switching power supply (PSP-2010, Goodwill Instek Ltd, Chino, CA) instead of D-type alkaline batteries.

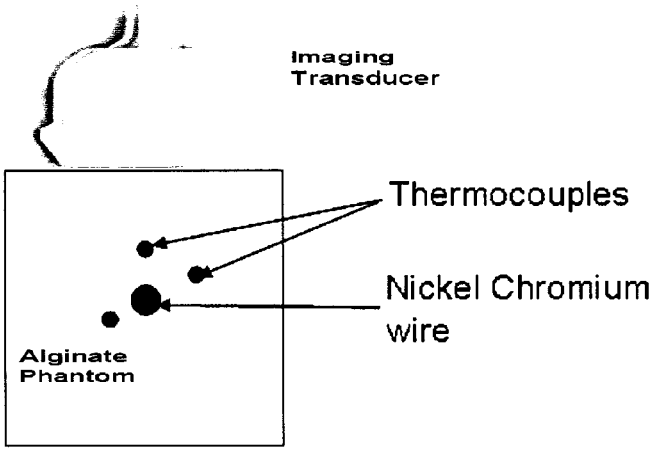

Figure 4.6 Schematic of experimental setup for transient hot-wire technique

A nickel-chromium (Ni-Cr) heating wire was pulled taut through the center of the phantom sample placed in a custom designed aluminum holder of dimensions 5 cm × 5 cm × 6.5 cm. Three 0.2-mm diameter, T-type, thermocouples with copper-constantan junctions (HYP0-33-1-T-G-60-SMPW-M, Omega Engineering Inc., Stamford, CT) were inserted into the phantom (after it has polymerized) under ultrasound B-mode guidance to ensure that the thermocouple stayed parallel to the heating wire along its length. An alternate approach would be to mount the thermocouples and heating wire in place in the sample holder, and then pour the alginate solution. However, with our approach, the hardened sample (after polymerization) provided support to hold the wires in place as they were inserted parallel to the heating wire. The thermocouples were placed at different radial distances from the wire, ranging from 2 to 5 mm. The distances from the tip of the thermocouples to the heating wire were measured using the distance measurement feature on a clinical ultrasound scanner (HDI 1000; Philips/ATL, Bothell, WA). The resolution of these distance measurements is ±0.1 mm. The programmable DC power supply was connected to the heating wire with a relay switch in series to turn the heating circuit on and off remotely.

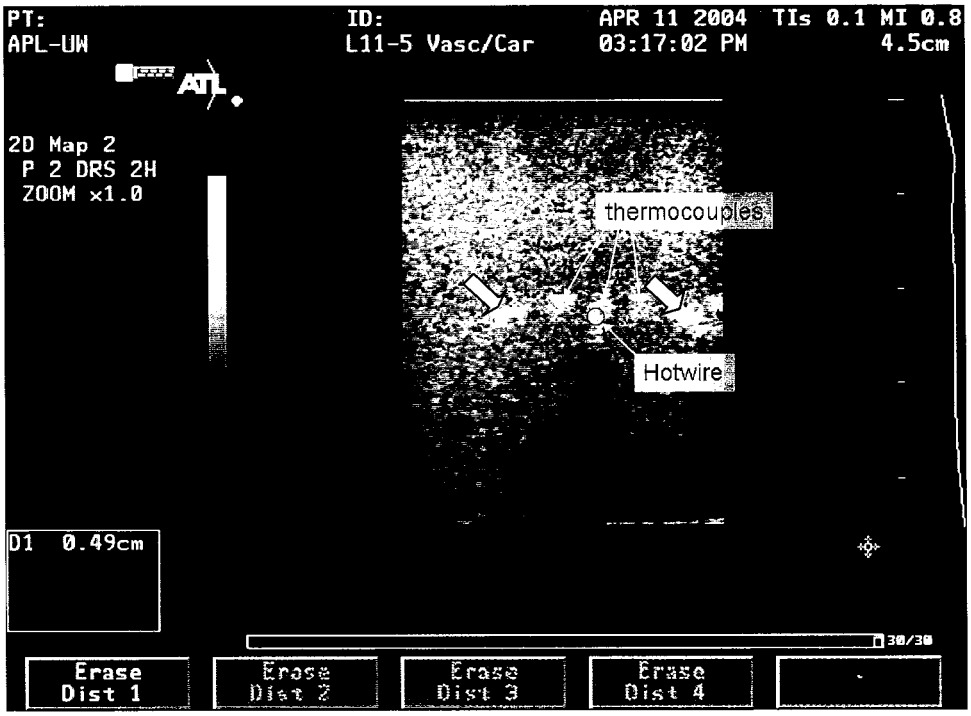

Figure 4.7 B-mode image along a cross-section illustrating the experimental setup for the transient hotwire method. The nichrome wire and the three thermocouples can be seen in the image. Observe the sidelobe artifacts from the wire at locations marked with the solid white arrow.

The thermocouple terminals were connected to a data acquisition module (HP 34970, Hewlett Packard Inc., Palo Alto, CA) to store the temperature readings in digitized form. A software-based control program developed in LabVIEW™ (National Instruments, Austin, TX) controlled the delivery of electrical power to the heating wire and the thermocouple data acquisition. The voltage drop and current through the wire, monitored with a multimeter throughout the experiment, was 2 V and 7 A respectively. The total heating time was 90 seconds and thermocouple data was acquired at a frame rate of 1 Hz throughout this interval. The maximum temperature rise was no greater than 10-15 °C to prevent irreversible changes to the sample under test. The experiments were performed in 4 samples prepared using the same recipe with 3 data sets acquired in each sample.

The spatiotemporal temperature distribution radially outward from the heating wire for the hotwire setup is described by the following equations [112],

$$T(r,t) = -A\,Ei\left(-\frac{r^2}{4Kt}\right) \tag{4.11}$$

$$\text{where } A=\frac{q}{4\pi k}, \qquad Ei(-x)=-\int_{x}^{\infty}\frac{e^{-u}}{u}du \tag{4.12}$$

where q represents the power (W) delivered per unit length of the wire, k represents the thermal conductivity ($W/m/^{o}C$), K is the thermal diffusivity (m^2/s), r represents the radial distance away from the wire (m) and t represents the time (s) after heating commenced. This equation assumes that the heat source is infinitely long with negligible diameter and is surrounded by an infinite solid. The exponential integral, $Ei(x)$ in Equation (4.11) was evaluated using the built-in function *"expint"* in MATLAB (The Mathworks Inc, Natick, MA). The thermocouple data was fitted to equation (4.11) and the thermal diffusivity K was estimated.

4.4.1.4. Experimental results

Figure 4.8 illustrates simulated $s(r,t)$ and $\varepsilon(r,t)$ profiles at various times after the HIFU heating pulse has been turned off for a RF data set acquired in the alginate phantom. The HIFU focus is located at depth of 0.021 m. $\varepsilon(r,t)$ follows the Gaussian shape given by equation (4.7) and $s(r,t)$ has the form of a "erf" function. It can be clearly seen that the radius R increases while the amplitude decreases, as time progresses after HIFU therapy was turned off. This is consistent with the temperature induced echo-shift model represented by equation (4.8). Figure 4.9 illustrates the zero-lag cross-correlation σ_i as a function of depth. At iteration 0 of the iterative algorithm, the zero lag cross-correlation is consistently below unity around the HIFU focus and also distal to it due to the echo shifts induced by the temperature change. After final convergence of the iterative strain estimation procedure, σ_i is uniformly close to unity along depth thus giving confidence in the model used to shift the post-heated RF lines.

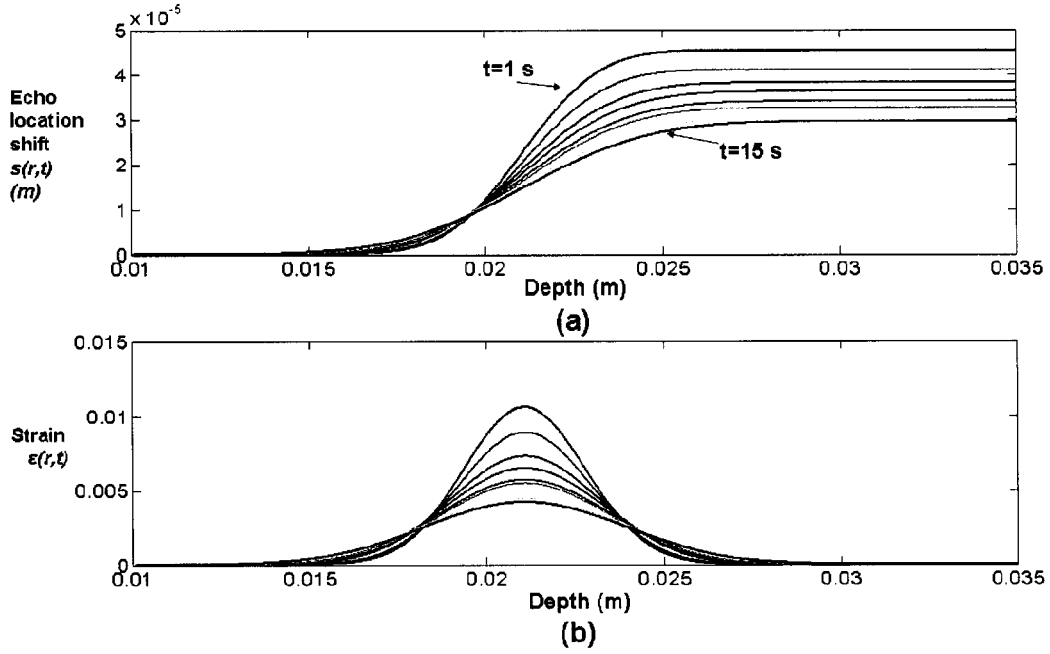

Figure 4.8(a) $s(r,t)$ and **(b)** $\varepsilon(r,t)$ at times t=1 s through 15 s (after HIFU heating pulse was turned off) at intervals of 2 seconds for an A-line passing through center of HIFU focal region. The HIFU focus is located at a depth of 0.021 m along the horizontal axis.

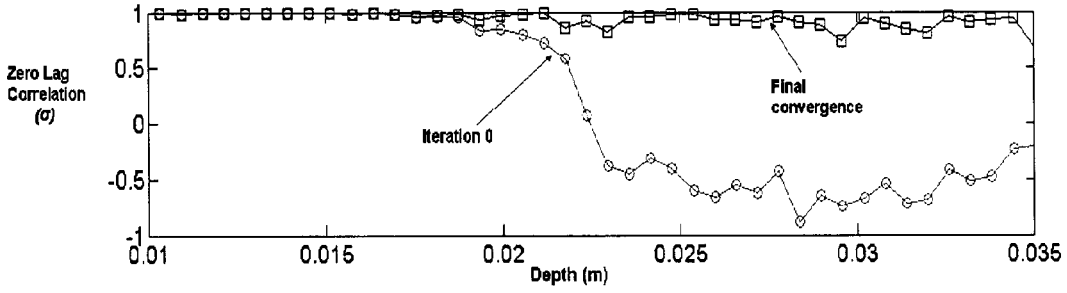

Figure 4.9 Zero-lag cross-correlation σ_i versus depth at iteration 0 (o) and at final convergence (□) of the BHTE model-based strain estimation algorithm (Section 4.4.1.2) for a pair of RF A-lines, one acquired before heating and the other acquired 1 s after the HIFU exposure was turned off. The HIFU focus is located at a depth of 0.021 m along the horizontal axis.

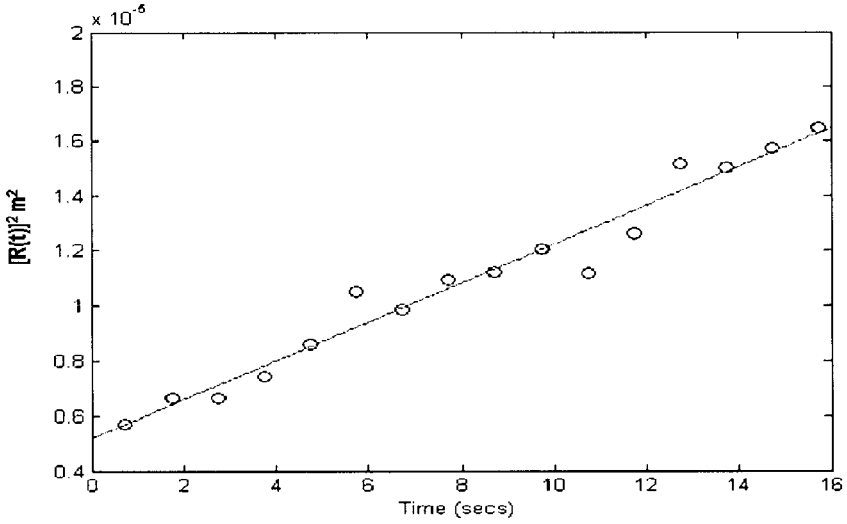

Figure 4.10 Plot of Gaussian radius $R(t)^2$ versus time t estimated from a RF data set acquired in the alginate phantom. The straight line represents a least squares linear fit to the data points and the slope is directly related to the thermal diffusivity.

The estimated $[R(t)]^2$ values are plotted as a function of time t in Figure 4.10 and a least squares linear fit to the data points based on equation (4.5) is shown. Note the good agreement ($r=0.96$) of the data with the straight line model. K calculated using equation (4.9) was 1.72×10^{-7} m^2/s for this phantom sample. The mean estimate of K obtained noninvasively for the 5 phantom samples analyzed was $(1.7\pm0.07) \times 10^{-7}$ m^2/s.

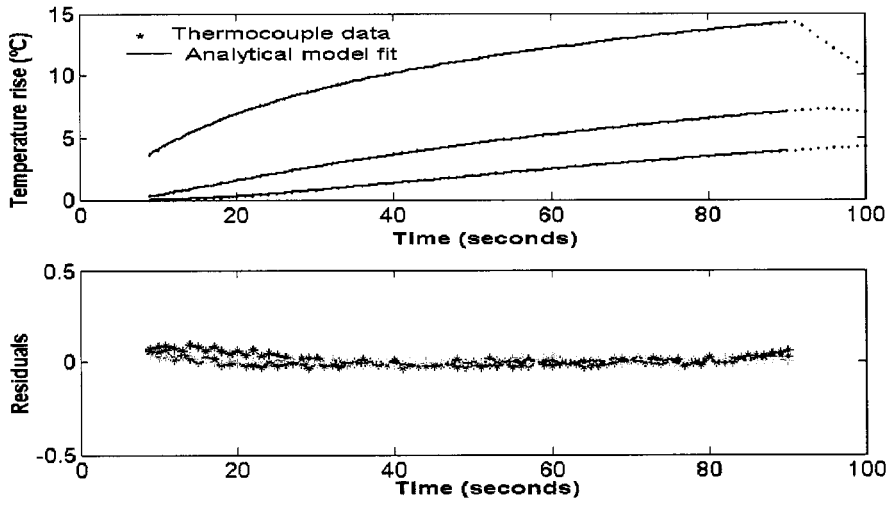

Figure 4.11(a) Temperature profiles measured using thermocouples placed around the nichrome heating wire in the *transient hotwire experiment*. The analytical fit to the data is also shown. The heating was turned off at t=90 s **(b)** Error residuals (in degrees Celsius) between the experimental and analytical model fit in (a). Note the vertical axis limits.

Figure 4.11(a) represents the typical thermocouple profiles obtained during the transient hotwire experiments along with the analytical fit using equation (4.11). Figure 4.11(b) shows the residual error in the fit. The mean value of K estimated using this technique in 4 samples was $(1.44\pm0.2) \times 10^{-7}$ m^2/s. Comparing this value with the noninvasive estimate (mean=$1.7\pm0.07\times 10^{-7}$ m^2/s) derived using the ultrasound based technique, a difference of approximately 15% is seen. A major source of uncertainty in the hotwire method is the exact knowledge of distance between the thermocouples and the heating wire and orientation of the thermocouples. Since $r^2/4K$ appears as a lumped term in equation (4.11), any errors in the measured distance impacts the estimated diffusivity. For example, an error of 0.2 mm in the measured location of a thermocouple placed 2 mm from the wire results in an error of 20% in the estimated diffusivity. In addition, the mathematical equation (4.11) used to fit the thermocouple temperature distribution is based on a set of assumptions. It is assumed that the heating wire is an infinitely long line heat source. In addition, it is assumed that the thermal resistance between the heating wire and the sample at the outer edge of the wire is negligible and that the specific heat capacity of the wire is also negligible [114]. However, in the practical experimental setup employed, a heating wire of finite length was used. As a

result, closer to the walls of the sample holder along the length of the wire, the temperature distribution would not be radial. A thermal insulation layer between the outer boundary of the wire and the sample possibly due to the creation of air cavities could introduce significant thermal resistance thereby reducing the rate at which the heat front propagates radially outward towards the thermocouples from the heating wire. This influences the thermal diffusivity estimate. The finite heat capacity of the heating wire implies that a finite time is required to first heat the wire, only after which the temperature rises in the sample, resulting in a slower rate of temperature rise at the thermocouples. This is not accounted for by equation (4.11) and hence would also bias the diffusivity estimate.

4.4.1.5. Simulations

To validate the ultrasound RF-based technique for the noninvasive estimation of K, simulation experiments were performed by generating RF A-lines during a HIFU heating experiment and applying the iterative estimation technique described in section 4.4.1.2. The procedure outlined by Miller and Bamber [72] was followed to simulate the effect of temperature on backscattered RF data. A detailed illustration of the various steps is provided in Appendix A and described in brief here. A random scatterer distribution was first generated with Gaussian distributed amplitudes while the spacing between the scatterers was derived from a uniform distribution. Twenty scatterers per wavelength were generated to guarantee fully developed speckle. The temperature distribution due to ultrasonic absorption of HIFU energy over a 3 cm × 2 cm 2-D region around the HIFU focus was computed using an axisymmetric finite element representation of the bioheat equation (Equation (4.1)) implemented in FEMLAB™ (Comsol AG, Stockholm, Sweden). A single element transducer with a geometric focal length of 35 mm and active diameter of 16 mm operating at 5 MHz was used as the HIFU therapy device. The normalized beam profile of the transducer simulated under linear acoustic conditions was used to represent the spatial distribution of the heat source. The HIFU therapy ON time was 5 s while the cool down phase was visualized for 15 s. The simulation parameters are listed in Table 1. The HIFU exposure intensity was chosen such that the maximum

temperature reached after heating was not greater than 15 °C above ambient temperature (37 °C). The temperature maps were converted to equivalent sound speed profiles using the mapping in Figure 3.2 [49] for liver tissue which is a primary tissue of interest [115] for HIFU treatment applications. The sound speed profiles along the imaging beam were mapped to apparent displacements and the new locations of the random scatterers were computed. For the ultrasound transmit system, the center frequency was 8 MHz with a fractional bandwidth of 60%. The transmit pulse was convolved with the scatterer profile to generate the RF A-lines. The SNR of the simulated RF signals was set to 20 dB by adding white noise to represent realistic situations. RF frames were generated at a frame rate of 1 frame per second during the entire experiment. Fifty realizations of the simulations were performed to compute first and second order statistics. For the estimation of K, signal analysis was performed along an RF A-line passing through the center of the HIFU focal zone (Figure 4.1). The echo location shifts $s(r,t)$ and the Gaussian radius $R(t)$ were computed for each frame acquired during the cool down phase using the algorithm presented in section 4.4.1.2, and the thermal diffusivity was estimated.

Table 4.1 Acoustic and Thermal parameters used to generate simulated RF lines for validation of ultrasound-based thermal diffusivity *K* estimation algorithm

Parameter	***Value***
Center Frequency (MHz)	8 MHz, 60% bandwidth
Scatterer Density	20 per wavelength
Sound speed (m/s)	1540
Ultrasonic SNR (dB)	20
Sampling Rate (MHz)	32
HIFU ON time (s)	5
HIFU Frequency (MHz)	5
Initial Temperature (°C)	25
Thermal Conductivity (W/m/°C)	0.7
Heat Capacity (J/kg/°C)	4180
Density (kg/m^3)	1000
HIFU transducer geometry	Focal length = 35 mm Aperture = 16 mm
In situ Acoustic Intensity (W/cm^2)	100
Attenuation (dB/cm/MHz)	0.7

The results of the simulations over 50 realizations of random scatterer distributions are plotted in Figure 4.12. The vertical axis represents the ratio of the estimated value of the thermal diffusivity, obtained by applying the ultrasound-based technique, to the true value input into the simulations. The mean value was 0.994 with a standard deviation of 0.089. The mean error between the true value and the estimated result was 0.6%. *These results demonstrate good agreement between the true thermal diffusivity value input into the simulations and the noninvasively estimated values, and validate the performance of the estimation algorithm developed.*

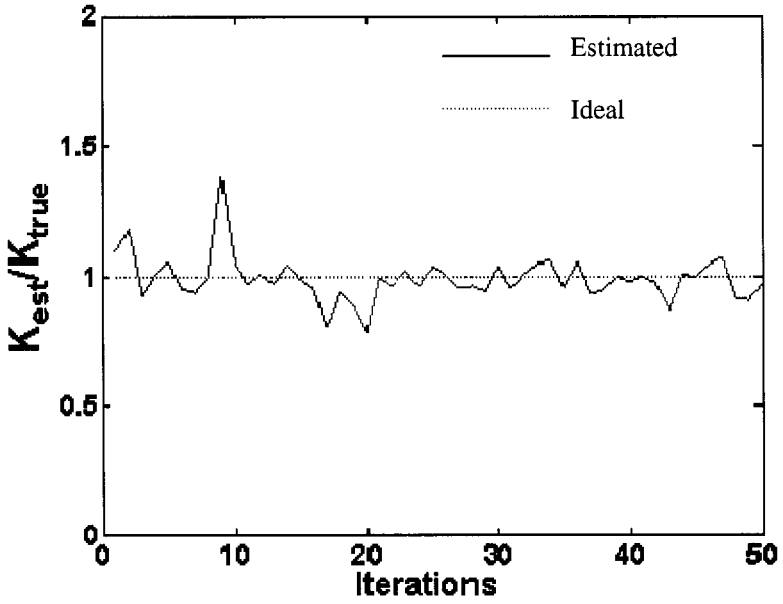

Figure 4.12 Plot of the ratio between *estimated* thermal diffusivity and *true* value input into the simulation over 50 iterations. The ideal value is unity as shown by the red dotted line.

4.4.2. Estimation of Q

4.4.2.1. Methodology

In this section, a novel noninvasive approach of estimating the local *in situ* heating rate Q at the HIFU focus is described. The methodology is motivated by the fact that, typically in HIFU treatments, focal heating rates on the order of 10 °C or more per second are commonly observed [3, 20] and temperatures nearing boiling (100°C at atmospheric pressure) [116-118] have been reported. From equation (4.2), it can be observed that by measuring the *rate of temperature rise at the therapeutic focus from ambient temperature to boiling* (term on left side in equation (4.2)) and accounting for the thermal conduction loss(first term on right side), the heating rate *(Q)* due to ultrasonic absorption can be estimated for a known spatial HIFU beam profile $I(r,z)$. In this work, $I(r,z)$ is computed *a priori* for the experimental HIFU transducer configuration, using a linear acoustic wave propagation tool, and is a constant throughout the procedure. Figure 4.13 illustrates a

typical representative plot of the temperature evolution at the geometric focus of a HIFU transducer.

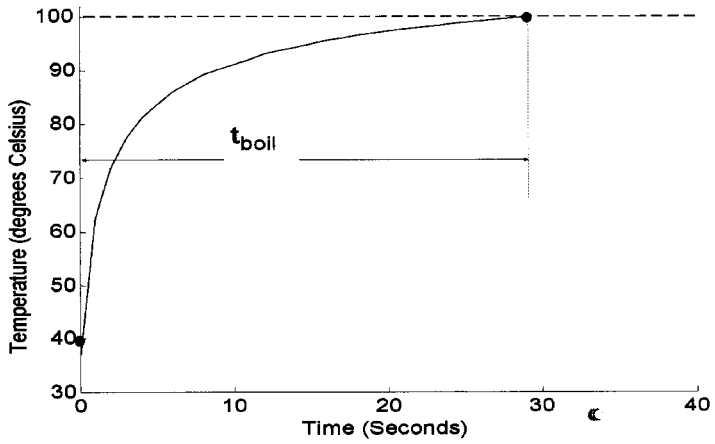

Figure 4.13 Simulated temperature profile at the geometric focus of a HIFU transducer during heating. The horizontal axis represents the time after heating commences. t_{boil} is the time (in seconds) to increase the temperature from ambient to boiling (assumed to be 100°C for aqueous media). t_{boil} is measured experimentally during the HIFU exposure.

For a given known transducer geometry and spatial intensity beam profile, the time t_{boil} required to raise the temperature of the tissue sample from ambient temperature to its boiling point (here assumed to be 100°C for aqueous media) is noninvasively detected using a passive acoustic sensor, sensitive to characteristic acoustic emissions (crackling and popping sounds related to the violent bursting of bubbles) that accompanies boiling. These emissions occur in the audible frequency range (upto 20 KHz). To the best of the author's knowledge, this is the first report of the development of a noninvasive technique to quantitatively estimate the *in situ* heating rate in biological tissue, by measuring the time of onset of boiling. In the approach developed in this thesis, starting with an initial guess value for Q, and using the value of K estimated using the method described in 4.4.1, $T(r,z,t)$ is computed iteratively using a finite element implementation of equation (4.2) to find the best estimate Q such that $T(r=0, z=0, t=t_{boil}) = 100°C$. Here, $(r, z)=(0,0)$ represents the peak of the HIFU focal spot as shown in Figure 4.1.

For independent validation of the estimated *in situ* heating rate, the *in situ* heat source was also calculated using equation (4.13) derived from HIFU parameters for linear acoustic propagation in an attenuating medium [22, 119] as,

$$Q_{cal} = 2\alpha f \; I_{SP} e^{-(2\alpha fx)} \text{ W/cm}^3 \tag{4.13}$$

where α is the acoustic attenuation coefficient (Np/cm/MHz), I_{SP} is the normalized spatial peak temporal average intensity (W/cm^2), f is the HIFU frequency (MHz), and x represents the beam propagation distance (cm). Experimentally measured values for α and I_{sp} were used in the calculation in equation (4.13). It was assumed that the absorption coefficient was equal to the attenuation coefficient and losses due to scattering were negligible [120, 121].

I_{SP} in equation (4.13) was obtained using the following equation [122, 123],

$$I_{SP} = 1.8 \cdot I_{SAL}$$
$$where\ I_{SAL} = \frac{0.683 \cdot W \cdot \eta}{\pi \cdot d^2} \tag{4.14}$$

where I_{SAL} represents the spatial average intensity (linear) (W/cm^2), W represents the electrical power input to the transducer (Watts), d represents the full width half maximum (FWHM) of the transducer measured from the acoustic pressure profile (cm) and η represents the electro-acoustic efficiency of the HIFU transducer. The parameters W, d and η were measured during independent calibration experiments performed before the HIFU therapy experiments and are reported in section 4.4.2.2.

For comparison between Q_{cal} from equation (4.13) and noninvasively estimated heating rate (Q) in the same units (W/cm^3), Q was multiplied by the product of density (ρ) and specific heat (C) to obtain Q_s as in equation (4.3). In practice, it is not necessary to have independent knowledge of Q_s, ρ and C. Only the lumped parameter Q appears in the BHTE of equation (4.2). The estimation procedure is completely noninvasive and only requires measuring t_{boil} experimentally.

4.4.2.2. Experiments

A set of experiments were performed in alginate-based phantoms to assess the utility of the noninvasive technique for estimation of Q by measuring t_{boil}. A commercially

available stethoscope was used as a passive sensor to detect acoustic emissions in the audible frequency range (up to a few KHz) that are characteristic of the onset of boiling. The diaphragm of the stethoscope was attached to a microphone (Figure 4.14) and placed against the alginate sample on the far side from the HIFU transducer as shown in Figure 4.5. The microphone output was sampled using the sound card on the PC at 44.1 KHz and stored for offline processing. The total HIFU ON time was approximately 50 seconds with brief interruption of the HIFU delivery (for 100 ms) every 0.5 s to enable acquisition of interference free B-mode images. The experiments were performed at *in situ* intensities (I_{SAL}) of 406 W/cm^2 and 523 W/cm^2. For each HIFU intensity, exposures were performed at five different spatial locations in a given sample by translating the HIFU transducer along Y and Z directions (Figure 4.5) using the 3-D motion stage. The treatment locations were separated by at least 1 cm to avoid influence from sites already treated. For each of the exposures, the HIFU beam propagation was entirely within the sample. Bulk sound speed and attenuation were measured for each of the samples.

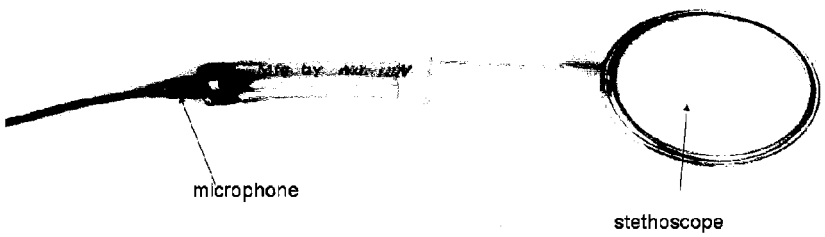

Figure 4.14 Photograph of diaphragm of stethoscope and microphone assembly used for boiling detection.

Prior to the HIFU experiments, the operating characteristics of the HIFU transducer were measured and recorded. The acoustic pressure field of the HIFU transducer was mapped with a needle hydrophone (Specialty Engineering Associates, San Jose, CA) having an active element of 0.15 mm in diameter, and mounted on a 3-D motion stage. For this measurement, the HIFU transducer and the hydrophone were immersed in a water tank containing degassed water. The hydrophone scanned the region around the

focal plane of the HIFU transducer along the longitudinal and transverse directions. The transducer under test was driven by a function generator (HP 33120, Hewlett Packard, Palo Alto, CA) with a maximum peak output voltage of 10 V. The hydrophone output was routed through a pre-amplifier to an oscilloscope (LC9304AM, Lecroy Corp, NY). A Labview™ program recorded the peak-to-peak voltage output of the hydrophone over 50 timebase sweeps of the oscilloscope at each spatial location and also controlled the motion of the 3-D stage. 1-D beam profiles were first obtained transverse to (along r at z=0 in Figure 4.3) and then along the beam propagation axis (along z at $r=0$). 2-D maps were also obtained by scanning the transducer in the vertical plane along the beam propagation axis $(r=0)$ and also transverse to it $(z=0)$. The experimentally measured 2-D normalized pressure distribution is shown in Figure 4.15. The 1-D transverse beam profile through the center of the focal region is shown in Figure 4.16. The full width half maximum (FWHM) distance (d) was calculated from the plots to be approximately 0.91 mm. The electro-acoustic efficiency of the HIFU transducer was measured using a radiation force balance setup. The measurement procedure has been extensively reported in the literature [124]. The plot of output acoustic power versus input electrical power (W) is shown in Figure 4.16. The electro-acoustic efficiency (η) estimated from the slope of this graph was 72.2 %.

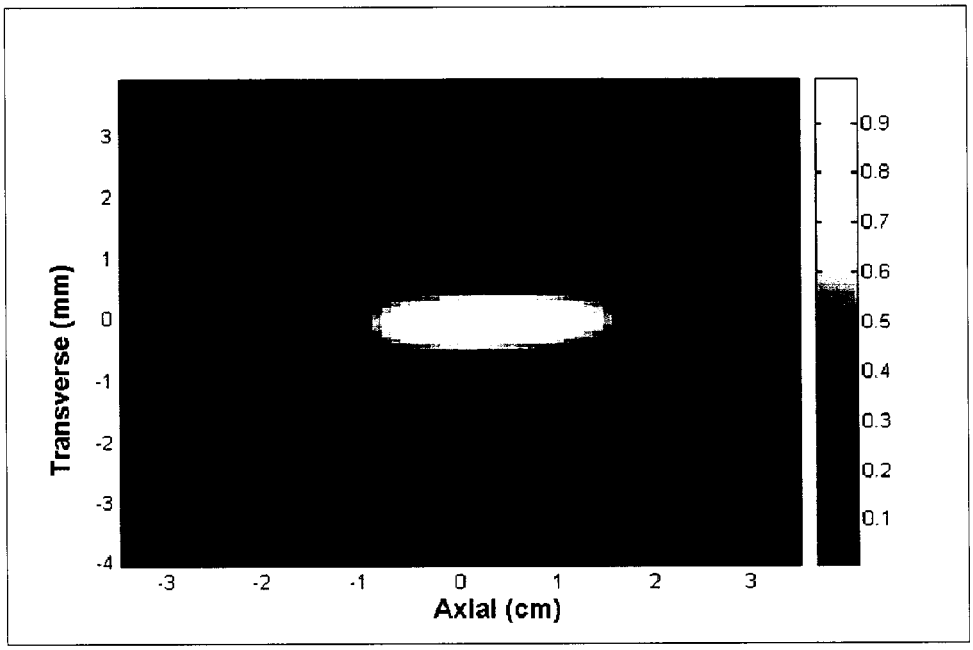

Figure 4.15 Normalized experimentally measured 2-D acoustic pressure profile of HIFU transducer. Zero along the horizontal and vertical axis represents an arbitrary point near the geometric focus of the transducer.

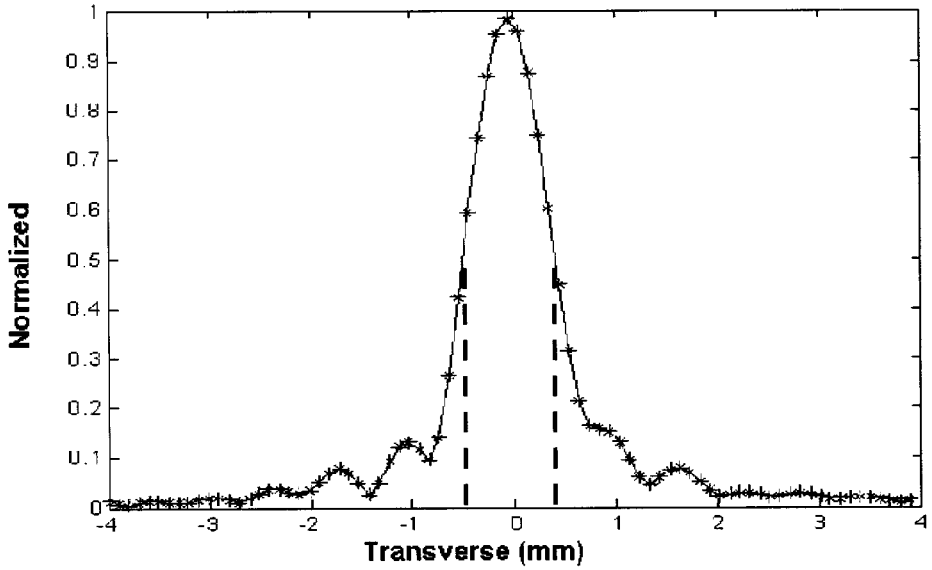

Figure 4.16 Normalized 1-D transverse profile of acoustic pressure distribution for the HIFU transducer. The full-width half maximum (FWHM) is the distance between the two vertical dotted lines in the figure.

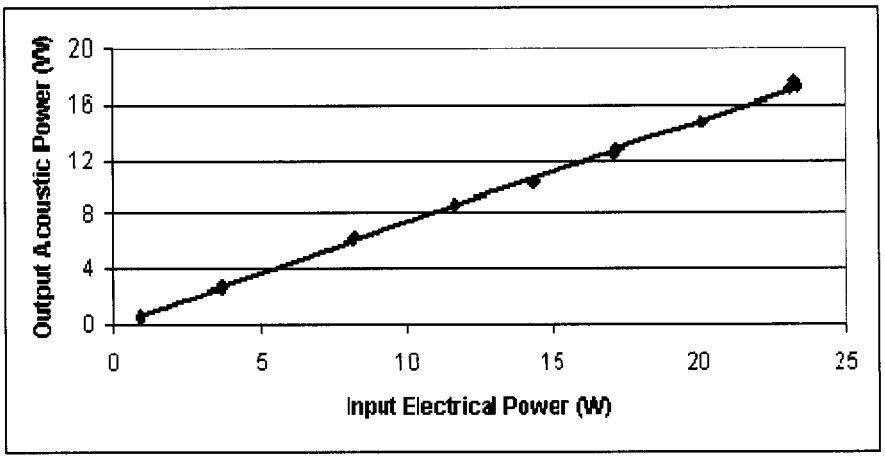

Figure 4.17 Plot showing relation between input electrical power and output acoustic power for the HIFU transducer used in the experiments for noninvasive estimation of Q. The straight line represents a least square fit to the experiment data values.

4.4.2.3. Results

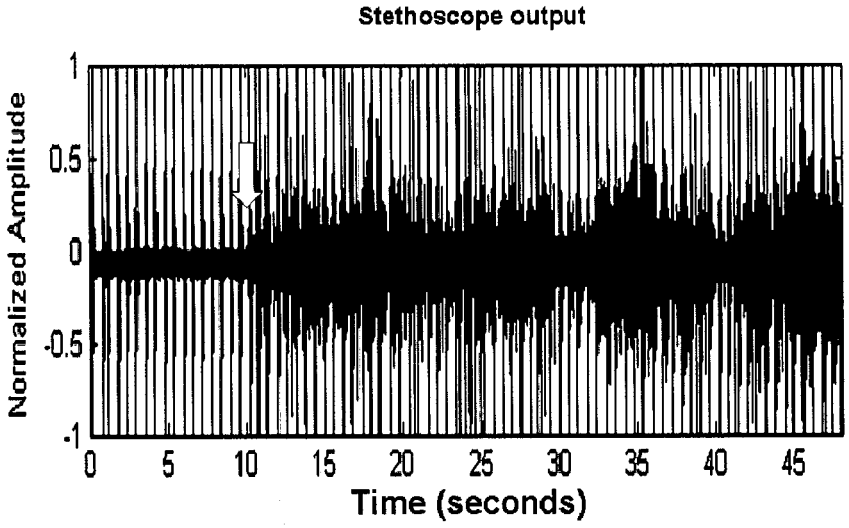

Figure 4.18 Time domain output of stethoscope recorded during a HIFU exposure lasting 50 seconds. The white arrow on the figure represents the onset of boiling.

Figure 4.18 shows a typical time domain output of the stethoscope recorded during the HIFU exposure. At approximately t=10 s after the HIFU is turned on, a marked increase in the amplitude of the stethoscope output signal due to acoustic emissions associated with the formation, and collapse of bubbles related to boiling is seen. The periodic spikes every 2 seconds throughout the HIFU exposure are consistent with the

HIFU beam turned OFF and then ON after 100 ms to capture RF data frames. This is likely due to an acoustic radiation force induced emission. The frequency domain representation (spectrogram) of the 700 Hz high-pass filtered time domain signal, computed using the short time Fourier transform (STFT) is shown in Figure 4.19(b). The occurrence of strong broad band signatures starting at t=30 s, extending in frequency up to 1.5 KHz, corresponds to the onset of boiling. The power computed from the spectrum of Figure 4.19(b) by summing along the vertical axis at each time instant is illustrated in Figure 4.19(c). The sharp increase in the power at the onset of boiling is clearly seen at t=10 s. This information can be used in an automated boiling detector to determine t_{boil}.

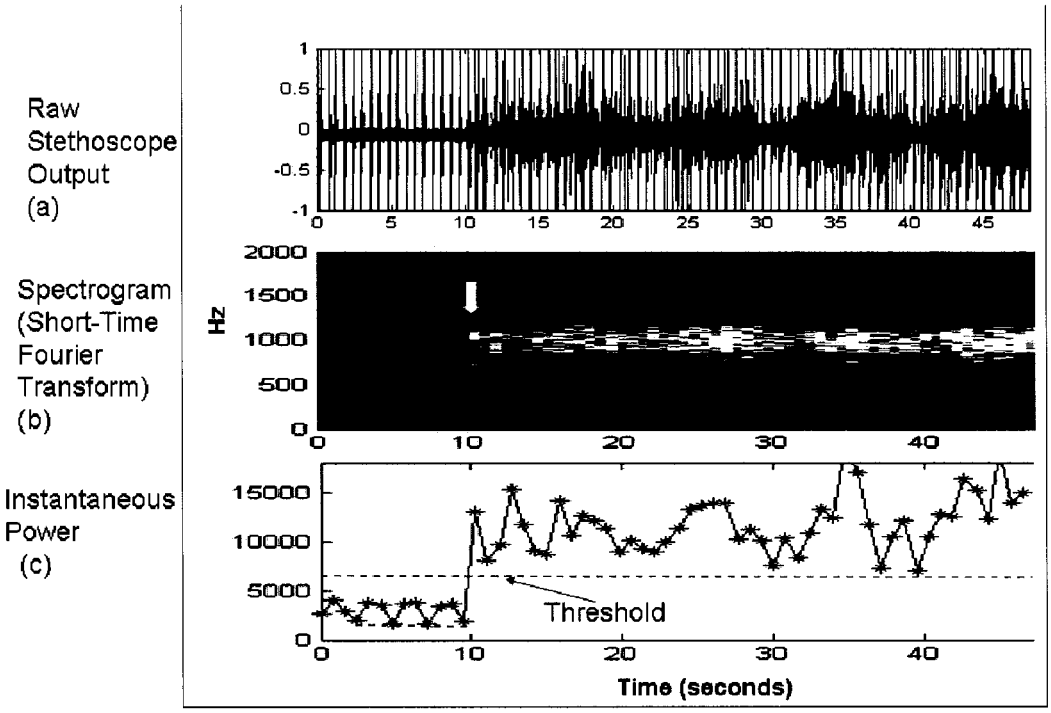

Figure 4.19(a) Typical time domain output of stethoscope recorded during a HIFU exposure lasting approximately 50 seconds as in Figure 4.18. (**b**) Spectrogram of the time domain signal shown in (a) computed using the Short Time Fourier Transform (STFT). White arrow indicates the onset of broad band signatures corresponding to boiling (**c**) Instantaneous Power as function of time. The marked increase at t=10 s represents the onset of boiling

Figure 4.20 shows the estimated boiling onset times for five independent exposures at two *in situ* HIFU intensities of 406±80 W/cm^2 and 523±104 W/cm^2. Good reproducibility in the boiling times for each of these intensities is observed in this homogenous phantom sample. From the experimentally measured boiling times, Q_s (W/cm^3) was estimated using the procedure described in Section 4.4.2.1. In Table 4.2, the noninvasive estimate of the heat source, along with the calculated value obtained using equation (4.13), is presented. A maximum difference of 20 percent is seen between Q_s and Q_{cal} with the calculated value higher at both intensities. This could be explained by the similar range of uncertainty in Q_{cal}, since it is dependent on the experimentally measured bulk acoustic attenuation of the sample and the measured transducer characteristics such as input electric power, electro-acoustic conversion efficiency and the transducer beam profile. The standard deviation in the Q_{cal} estimates reported in Table 4.2 were calculated using (4.13), for a 5% uncertainty in these experimentally measured parameters.

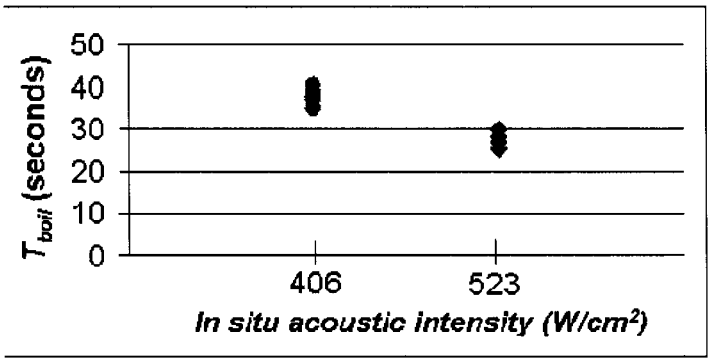

Figure 4.20 Noninvasively detected boiling times for five exposures at two HIFU intensities in the alginate phantom

Table 4.2 Comparison between noninvasively estimated *in situ* heat source (Q_s) and calculated heat source (Q_{cal})

Intensity (I_{SAL}) (W/cm^2)	Estimated *In-situ* Q (W/cm^3) (Q_s)	Calculated *In-situ* Q (W/cm^3) (Q_{cal})	% Difference between means $(Q_{cal}-Q_s)\times 100/Q_{cal}$
406±80	292±2.6	325.8±58.5	10.5
523±104	308.7±3.7	389.7±70.2	20.8

4.5. Summary and Discussion

Novel noninvasive acoustic methods of estimating the *in situ* local thermal diffusivity *(K)* and the *in situ* heating rate were reported in this chapter. To the best of the author's knowledge, this is the first report of the use of noninvasive acoustical techniques for the estimation of local tissue thermal properties. In the analysis presented in this chapter, the medium was considered to be spatially homogenous and isotropic. In heterogeneous media, spatial variations in the thermal properties can be expected. To account for these spatial variations, measurements of K and Q at a number of spatial locations within the region of interest can be repeated, and a spatial map of the thermal properties could be constructed. The methods are designed so that the same transducer used for delivering the therapy dose could be used to determine the thermal parameters noninvasively. The estimation techniques were applied to homogenous tissue mimicking phantoms to demonstrate the proof of principle. These techniques were then applied to biological tissue and these results are presented in Chapter 6.

For the estimation of K, the first criterion is that a spatial temperature gradient must exist. Second, the heat source must approximate an impulse in both space and time. *The sub-millimeter transverse beam widths of the HIFU beam conveniently satisfies both requirements.* In our experiment setup, the imaging scanlines are oriented transverse to the HIFU beam. It is advantageous to image the temperature evolution in this direction since the thermal gradients are greater and hence greater sensitivity exists in the ultrasound backscatter data to thermal diffusion.

Simulation results demonstrated that under realistic signal-to-noise conditions, K can be estimated with a variation of less than 10% using the estimator developed. The estimates of K independently obtained using the invasive transient hot-wire method and the noninvasive method showed a difference of approximately 15%. A major source of uncertainty in the hotwire method is the distance between the thermocouples and the heating wire and orientation of the thermocouples. In addition, as described earlier in section 4.4.1, equation (4.11) includes a number of assumptions regarding the geometry of the heat source and sample, thermal properties of the heating wire, and heat transfer between the heating wire and the sample being tested. Based on a detailed error analysis incorporating model errors and experimental measurement errors, Hammerschmidt [114] showed that the expected uncertainty in the thermal diffusivity can on the order of 30%. Moreover, in this study, the signal processing parameters such as RF data sampling rate, cross-correlation window length (N in equation (4.10)) and thresholds in the optimization routines were manually selected based on *a priori* knowledge and published literature values for similar signal analysis. A detailed error analysis would be necessary in a future study to understand how choice of these parameters affects the $s(r,t)$ estimates and consequently K. Nevertheless, the results of this study clearly demonstrate that the local thermal diffusivity can be noninvasively estimated from the RF data acquired during brief HIFU exposures at sub-ablative intensities.

An A-line based RF processing scheme was adopted in this paper to estimate K with imaging transducer oriented parallel to the HIFU beam propagation direction, and the imaging beam propagation direction perpendicular to the HIFU beam propagation axis. A-lines passing through the center of the HIFU focal region were used in the analysis. This is consistent with the orientation recommended by Simon and Ebbini [70] to minimize the acoustic thermal lens effect (decorrelation in the RF signal due to refraction and refocusing of the US beam during heating) because the thermal gradients within the imaging beam width are smaller at the center of the HIFU focal zone as compared to its edges. Extension of the A-line (1-D) based approach to a 2-D estimation technique performed over multiple adjacent scan lines in the heated region might benefit from

incorporating the thermal lens effect in an appropriate numerical model [125] to minimize model inconsistencies.

The estimation of the heating rate Q was based on first experimentally measuring the time required to raise the temperature of the focal point from ambient to boiling (assumed to be 100°C in aqueous media), and then applying the BHTE iteratively to compute the heating rate. The time series output of the stethoscope and the corresponding power spectrum in Figure 4.18 illustrates that the t_{boil} can be clearly detected. The boiling times measured within a given sample showed good reproducibility for both levels of acoustic intensities. This is consistent with the fact that the samples are prepared to be spatially homogeneous. Q_s obtained using the noninvasive technique and Q_{cal} (equation (4.13)) shows a maximum difference of 20 percent with the calculated value higher than the estimated in both cases. This difference is on the order of the uncertainties observed in the measured values of attenuation (α) and spatial peak intensity (I_{SP}) in equation (4.13). Uncertainties in I_{SP} result from measurements of the input electrical power, electro-acoustic efficiency and the 6 dB beam width of the incident pressure field. The calculation also assumes that the attenuation coefficient is equal to the absorption coefficient, while in reality this may not be true due to scattering losses.

In this work, a linear acoustic propagation model was employed to compute the *in situ* beam profile $I(r,z)$ used in equation (4.2) and Q_{cal} in equation (4.13). However, presence of acoustic nonlinearities has been previously reported for the intensity levels typically used in HIFU [104]. The influence of the nonlinearities on magnitude of the local heating rate and its spatial intensity profile depends not only on the applied acoustic intensity, but also the intervening path attenuation. If the effect of nonlinearities were to only influence the magnitude of the heating rate, while still maintaining the spatial profile close to the linear approximation, the estimated Q_s would include this effect since it is a free parameter in the fitting process. If the effect of nonlinearities were strong enough to modify the local heat source spatial profile due to increased absorption of higher harmonics, Q_s would be biased since the estimation would be performed using an incorrect spatial heat source distribution profile. The effect of nonlinearities can be

explicitly included by employing a nonlinear acoustic wave propagation model to compute the spatial intensity profile $I(r,z)$ instead of a linear propagation model employed in the current work.

Although the motivation for developing noninvasive methods to estimate the thermal diffusivity and the heat source was to be able to uniquely estimate the mapping between temperature and temperature-induced strain (ε) (refer Figure 4.1), the methods developed in this paper can also be used in therapy planning applications to predict the applied thermal dose at the treatment site and accordingly decide on the treatment protocol. *Current therapy planning procedures typically use values derived from the literature or assumed standard values for the thermal diffusivity and local heating rate.* However, these properties are tissue composition dependent and patient dependent [106]. *The availability of noninvasive in situ estimates at the treatment locations can reduce the uncertainty in the knowledge of these parameters and thus improve the accuracy of the predicted results. The techniques developed in this chapter are a way of "remotely" estimating these parameters.*

4.6. Conclusions

A noninvasive technique of estimating the thermal diffusivity and the local heating rate during thermal therapy such as HIFU has been developed and presented in this chapter. Within the limits of experimental uncertainties and model induced errors, the results from *in vitro* experiments performed in tissue mimicking phantoms show good agreement between the *noninvasive* estimation techniques and independent *established* validation procedures. The applicability of these techniques can be extended to assess the heterogeneity of biological tissue and construct spatial maps of the variation of tissue specific thermal parameters. The techniques developed in this chapter have applications in therapeutic dosimetry planning, quantitative temperature imaging and potentially as a tissue characterization tool.

In the next chapter, the ultrasound-based therapy monitoring approach based on noninvasive temperature estimation using the BHTE is discussed and validated in the alginate phantoms. The noninvasive estimation of tissue thermal properties is an essential

step of the monitoring approach, and relies on the estimation techniques presented in this chapter.

5. MODEL-BASED TEMPERATURE ESTIMATION TECHNIQUE FOR HIFU THERAPY MONITORING: PART II

5.1. Introduction

In Chapter 4, the two step model-based temperature estimation approach for HIFU therapy monitoring technique was introduced. In the first step, local tissue thermal properties are estimated locally during calibration experiments, performed at a single location in the treatment region of interest. These calibration experiments were described in detail in Chapter 4 along with results from experiments performed in tissue mimicking phantoms. After the thermal properties (K and Q) have been estimated, as illustrated in Figure 4.1, temperature maps obtained by simulating the BHTE are related to the temperature induced strain ε measured from the ultrasound backscatter, to *noninvasively* obtain the mapping between strain and temperature referred to as $\varepsilon(T)$. In the second step, using the estimated $\varepsilon(T)$ mapping as a known quantity, temperature estimation is performed as illustrated in the block diagram in the lower half of Figure 4.1. *This chapter focuses on the noninvasive estimation of $\varepsilon(T)$ and the temperature estimation step.* The estimation methodology and results from tissue mimicking alginate phantoms are presented. Unless mentioned otherwise, in this chapter it is assumed that K and Q have been already estimated and are *a priori* known quantities.

5.2. *In situ* Estimation of $\varepsilon(T)$

5.2.1. Estimation methodology

The relation between temperature induced strain (ε) and temperature (T) incorporates the effect of change of sound speed versus temperature $c(T)$ and thermal expansion. In the estimation procedure described here, only the lumped quantity $\varepsilon(T)$ is estimated. The goal is not to separate the contribution due to the sound speed change and thermal expansion. As mentioned earlier in Chapter 3, the $\varepsilon(T)$ relation is non-monotonic with temperature and can be represented by a second order polynomial of the form,

$$\varepsilon(T) = bT^2 + aT \tag{5.1}$$

where a,b represent scalar coefficients and T represents the temperature rise above the ambient value (typically 37 degrees C). However, for a relatively small temperature rise of up to 10-15 degrees from ambient temperature, equation (5.1) can be well approximated by a linear relation of the form,

$$\varepsilon(T) = aT \tag{5.2}$$

A detailed simulation analysis showing the resulting strain profiles for the representations in equations (5.1) and (5.2) is provided in Appendix B. The simulations provide insight as to how the strains vary locally depending on the mapping between strain and temperature. In our approach, $\varepsilon(T)$ is represented by equation (5.2) because the parameter estimation for therapy monitoring is performed immediately (typically within 1 s) after HIFU therapy commences, while the maximum temperature rise is less than 15 degrees Celsius. Hence the focus during the $\varepsilon(T)$ estimation step is only on estimating the slope of the linear fit (parameter a). This parameter is determined by relating the echo shift between the first two RF frames acquired immediately after therapy commences with simulated temperature maps at that location obtained using the BHTE. The flowchart in Figure 5.1 illustrates the implementation of the $\varepsilon(T)$ estimation algorithm. The estimation is performed using RF data collected during the calibration experiment.

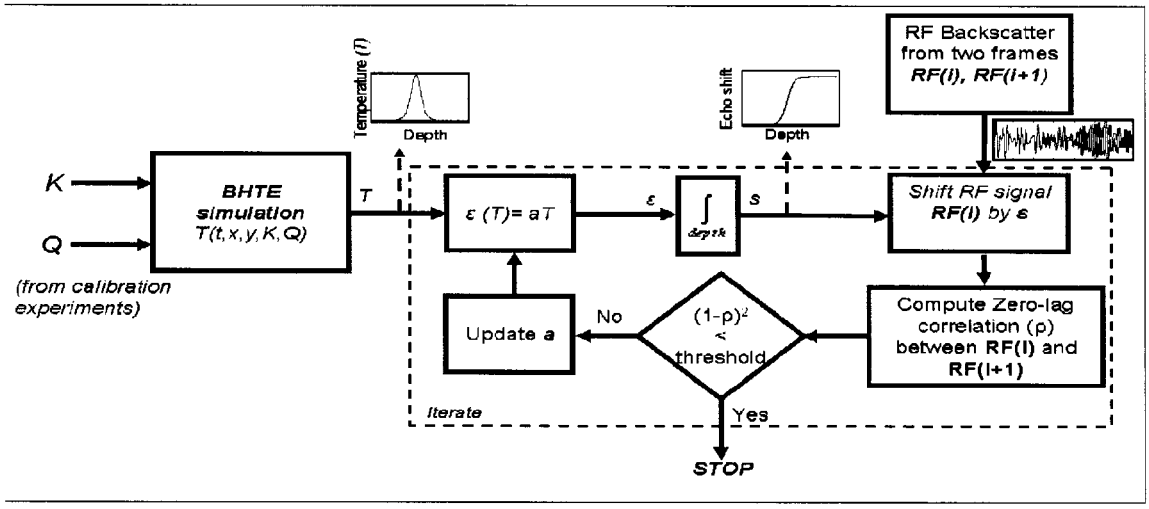

Figure 5.1 Flowchart illustrating the iterative optimization technique for noninvasive estimation of $\varepsilon(T)$. The estimation is performed on RF data collected during the calibration exposure.

The technique is implemented as an iterative optimization problem with the goal being to estimate the optimum value of parameter a for the given RF data set. An initial guess value for parameter a is first selected. The BHTE equation is then evaluated using the values of K and Q estimated from the calibration experiments. This gives the predicted temperature profiles for that particular location. The predicted temperature profiles are mapped into strain using $\varepsilon(T)$ and then integrated along the depth direction to obtain the predicted echo shift. These echo shift estimates are then used to shift the samples of RF line *RF(i)*. The *shifted* RF line *RF(i)* and *RF(i+1)* are divided into a number of nonoverlapping segments (typically each segment is 0.75 mm in length). The zero lag correlation ρ between corresponding segments on these RF lines is then computed following the approach presented in section 4.4.1.2. The minimization function is computed as $(1-\rho)^2$ for each of the segments and then summed to obtain the cumulative error estimate. Parameter a is updated after each iteration until the cumulative error estimate is below a pre-defined threshold.

It may be noted that although the temperature profiles for the current location can be directly evaluated based on knowledge of K and Q without the need for explicit estimation of $\varepsilon(T)$, this would not provide the ability to adaptively track changes in Q during the therapy monitoring step. In order to be able to relate the BHTE predicted temperature maps with the RF backscatter data collected during therapy, $\varepsilon(T)$ must be estimated and hence the need to go through the steps outlined in Figure 5.1. It is assumed that $\varepsilon(T)$ *is spatially constant* and hence the value estimated during the calibration step is used as a constant known parameter during therapy monitoring.

The experimental data acquisition to validate the techniques for independent estimation of $\varepsilon(T)$ was performed as part of the boiling onset detection step presented in section 4.4.2. It may also be noted that the RF data collected during the boiling onset detection experiments was solely for use in the estimation of $\varepsilon(T)$. Only the stethoscope data was used for boiling onset detection.

5.2.2. Experimental data acquisition and analysis

RF data was acquired and processed offline based on the flowchart illustrated in Figure 5.1. The heat source *(Q)* and the thermal diffusivity *(K)* estimated during the calibration experiments were input into the BHTE to compute the predicted temperature profiles. The value of Q was 291.72 W/cm^3 while K was 1.7×10^{-7} m^2/s. These values were estimated during the calibration experiments. The BHTE equation was implemented using the finite element technique in FEMLAB (Comsol AG, Stockholm, Sweden). Sample plots showing the finite element mesh, acoustic beam profile (normalized) and simulated temperature distribution are presented in Figure 5.2. For more detailed information on the FEMLAB implementation, the reader is referred to Appendix A in this document. The iterative algorithm in Figure 5.1 was implemented using the MATLAB function *fminsearch*, which is an implementation of the Nelder-Mead simplex optimization technique. The analysis was performed on 10 adjacent RF A-lines passing through the center of the HIFU focal zone. The measurements were repeated at different test locations within two different phantom samples. The noninvasive estimates of $\varepsilon(T)$ thus obtained were compared with invasive measurements of $\varepsilon(T)$ independently obtained using the setup described in Section 5.2.3.

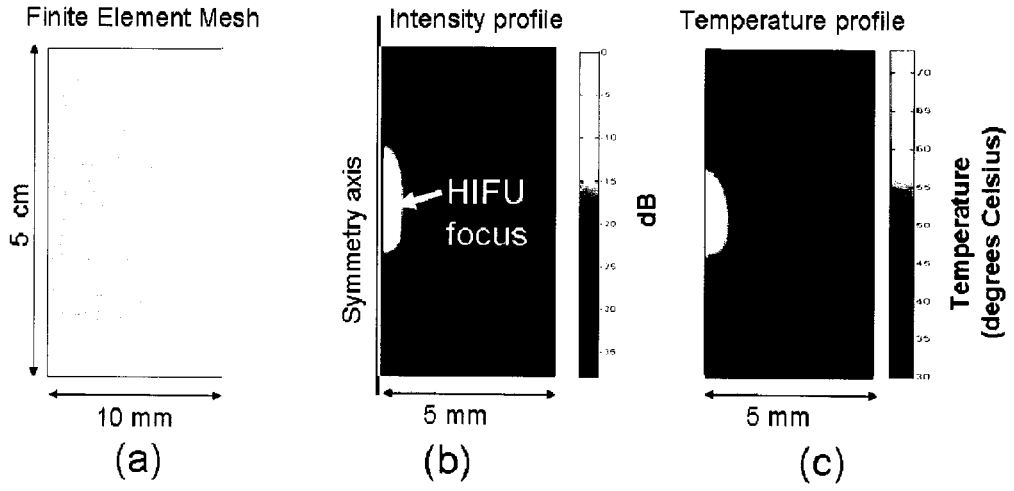

Figure 5.2(a) Finite element mesh (**b**) Normalized acoustic intensity profile in dB scale and (c) Spatial temperature distribution obtained using the multiphysics finite element modeling tool—FEMLAB™. A high density of mesh elements is used around the HIFU focus to capture the steep thermal gradients. Note the difference in scale between the horizontal and vertical axis in the plots. The HIFU transducer is situated at the bottom of these figures and the beam propagates vertically upward.

5.2.3. Invasive measurement of $\varepsilon(T)$—ground truth measurements

For independent validation of $\varepsilon(T)$, the relationship was also measured using an invasive technique widely reported in the literature [70, 75]. The invasive estimates are considered the ground truth measurements. These measurements are performed by tracking the echo shifts in the backscattered ultrasound when a sample is uniformly heated over the temperature range of interest, and $\varepsilon(T)$ is computed from these echo shift estimates.

A temperature controlled water bath heating experiment was performed in order to uniformly characterize the $\varepsilon(T)$ relationship of the alginate phantom sample. A photograph of the experimental setup is shown in Figure 5.3. The sample was placed in a temperature controlled water bath with one thermocouple inserted into the phantom and another immersed in the water bath. An electric heater with an inbuilt thermostat and circulator (VWR Scientific Products, West Chester, PA) was immersed in the water bath to uniformly heat the water bath and the sample. A commercial ultrasound imaging probe (L11-5, Philips Medical Systems, Bothell, WA) was immersed in the water bath and placed such that it images a cross-section of the sample. Care was taken to ensure that the

imaging probe was not rigidly placed against the sample, thus allowing the sample to freely expand. The water bath was heated in increments of approximately 10 degrees Celsius, and the thermostat turned the heater off automatically when a given preset temperature was reached. An RF data frame was collected using the HDI 1000 scanner at each temperature increment after ensuring that difference in the temperature readings between the two thermocouples was no greater than ±0.2 degrees Celsius.

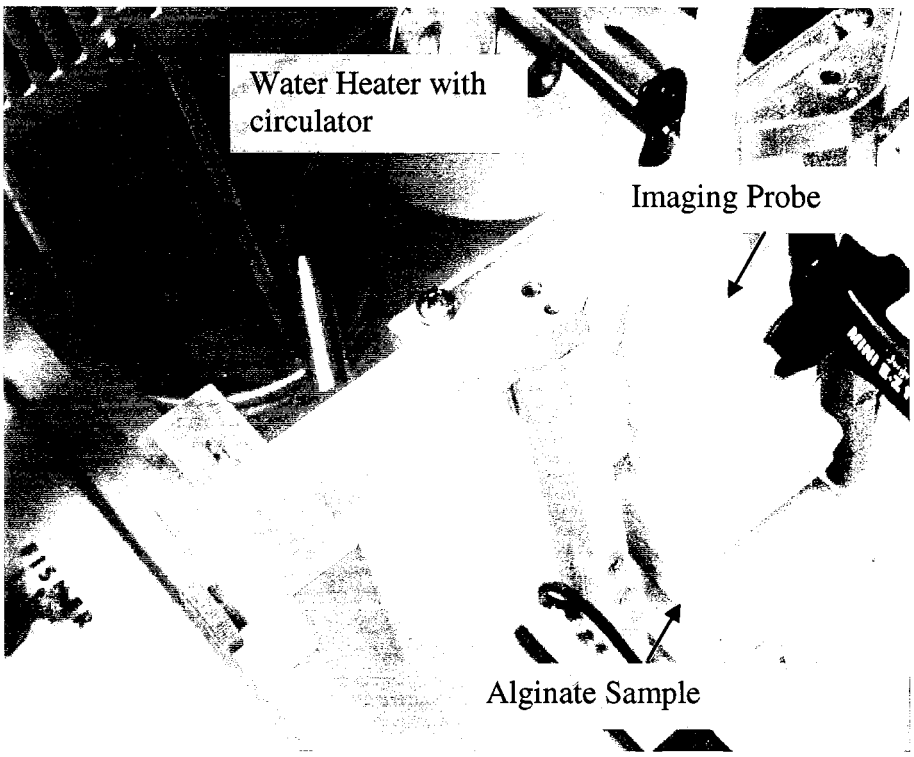

Figure 5.3 Photograph of experimental setup for invasive measurement of ε(T) using water bath setup

A B-mode image of the sample reconstructed from the RF data collected during the water bath heating experiment is displayed in Figure 5.4(a). The backscattered echoes for an A-line passing through the sample at the different temperatures are shown in Figure 5.4(b). The reflection at the interface between the sample and the base of the holder can be clearly seen in the echo signal. As the temperature rises, the echoes shift towards the imaging transducer placed at the top of the B-mode image. Figure 5.4(b) clearly shows that the sensitivity of the temperature induced strain to temperature is greatest for temperatures close to ambient temperature. As the temperature rises above 50°C, the

sensitivity of the echo shifts to temperature change reduces and reaches a plateau close to 70°C. Beyond 70°C, the echo shifts occur in the opposite direction with the echoes moving away from the imaging transducer as the temperature rises. Hence, the best sensitivity for the estimation of parameters from the RF data is in the temperature range between 25-55 °C. From the echo shifts, the temperature induced strain was computed and the mapping, $(\varepsilon(T))$, that relates strain to temperature, is plotted in Figure 5.5.

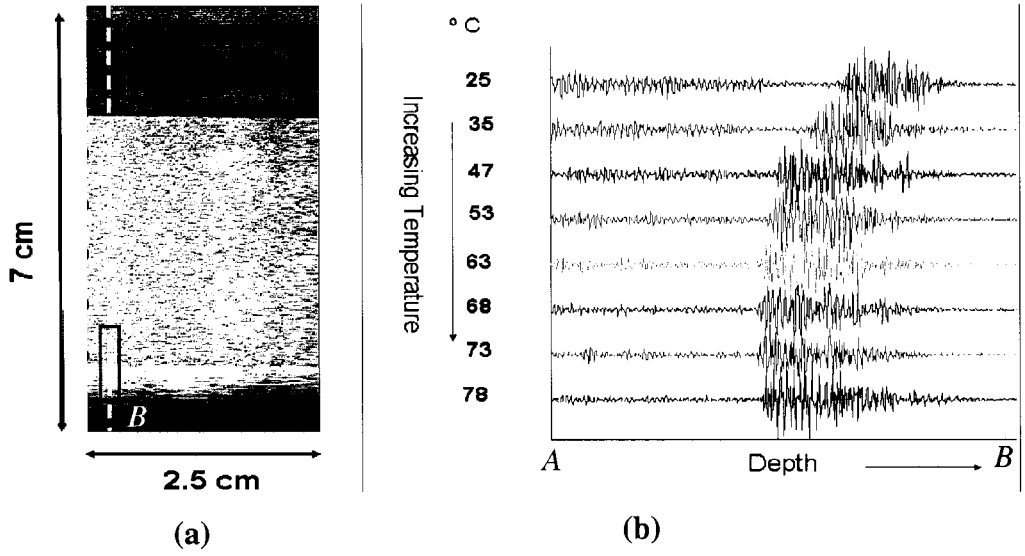

Figure 5.4 (**a**) B-mode image of sample immersed in water tank during heating. (**b**) RF echoes over the axial distance represented by the rectangular segment (A-B) in (a) for the scanline shown by the dotted line.

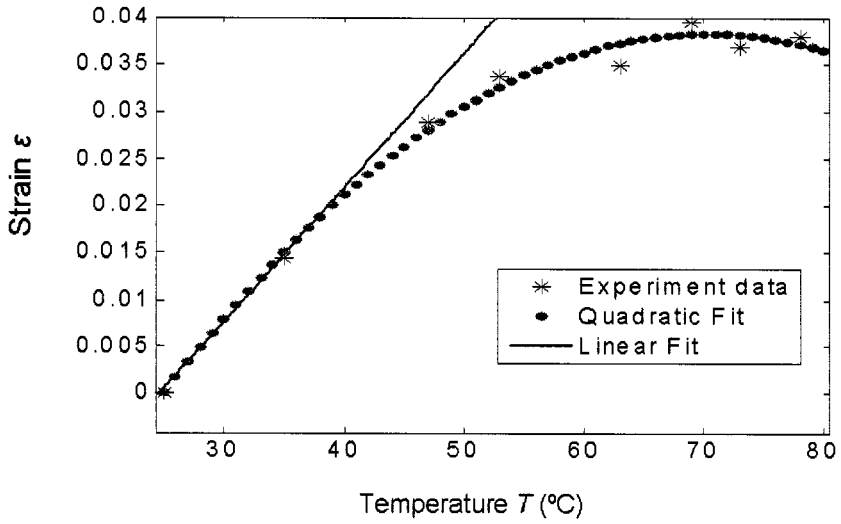

Figure 5.5 Plot of experimentally measured temperature induced strain ε as a function of temperature and polynomial fits to the data

5.2.4. Comparison between invasive and noninvasive ε(T) results

Figure 5.6 shows a comparison between the slope of the noninvasive $\varepsilon(T)$ mapping (parameter a), obtained using the technique described in section 5.2.1, and the independently obtained invasive ground truth measurements of section 5.2.3. The error bars for the noninvasive measurement are generated from measurements using 10 adjacent RF A-lines around the center of the HIFU geometric focus. For the ground truth measurements, the slope of the linear fit to the $\varepsilon(T)$ mapping (shown in Figure 5.5) was also calculated and is plotted in Figure 5.6. The error bars on the invasive estimate represents the 95% confidence interval to the linear fit.

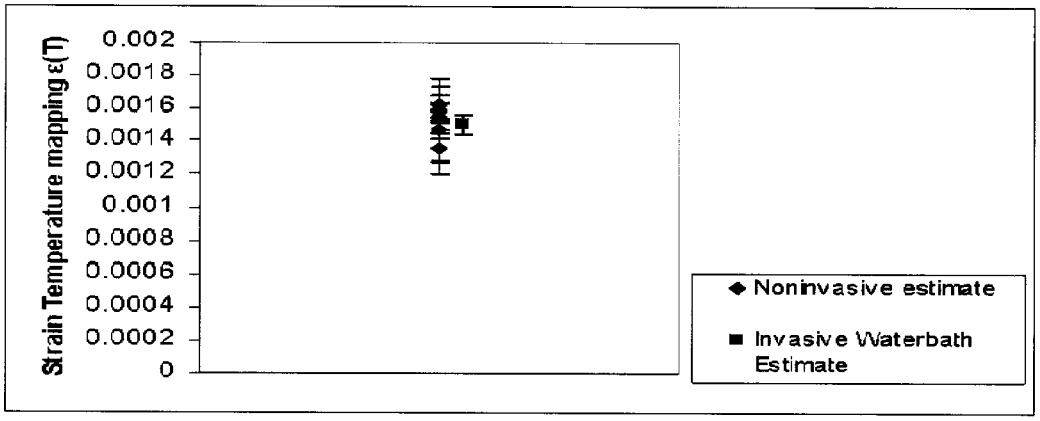

Figure 5.6 Comparison between noninvasive and invasive (water bath) estimates of $\varepsilon(T)$

5.3. Noninvasive Temperature estimation

5.3.1. Description of noninvasive temperature estimation technique

The temperature estimation technique based on noninvasive estimation of BHTE parameters is presented in this section. The noninvasive estimates of $\varepsilon(T)$ obtained in section 5.2.4 are used as a known quantity in this step. A block diagram representation of the estimation technique is presented in Figure 5.7. It may be noted that the mapping between temperature and strain is modeled as a linear function in this estimation technique. This is because the iterations to estimate temperature, by first estimating the BHTE parameter Q, are only performed on the initial frames (typically frames acquired within the first second after HIFU heating commences), and a linear model for $\varepsilon(T)$ is valid in this range. Once Q has been estimated using the initial set of frames, the BHTE is used to compute temperature throughout the exposure. *This approach thus overcomes the limitations imposed by the low sensitivity of $\varepsilon(T)$ over parts of the therapeutic temperature range of interest.*

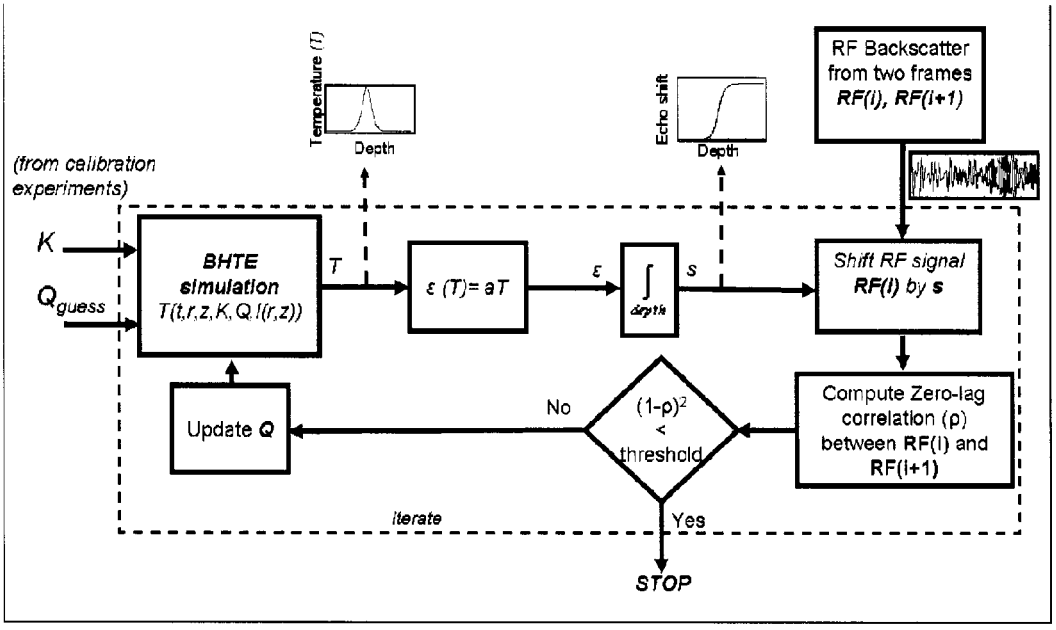

Figure 5.7 Block diagram representation of iterative optimization based technique for noninvasive temperature estimation

The technique is implemented as an iterative optimization problem as illustrated in Figure 5.7 with the goal being to estimate the optimum value of the parameter Q. The approach is conceptually similar to that employed to estimate the parameter a in section 5.2.1. An initial guess value for parameter Q is first selected (usually obtained in prior calibration experiments). The BHTE equation is then evaluated using the values of K and Q estimated from the calibration experiments. This gives the predicted temperature profiles for that particular location. The predicted temperature profiles are mapped to strain using the estimated parameter a and then integrated along the depth direction to obtain the predicted echo shift. These echo shift estimates are then applied to shift the samples of RF line *RF(i)*. The *shifted* RF line *RF(i)* and *RF(i+1)* are each divided into a number of non-overlapping segments, and then the zero lag correlation ρ between the corresponding segments is computed. Parameter Q is updated after each iteration until the minimization function is below a pre-defined threshold. The estimated value of Q at convergence is then input into the BHTE to compute temperature maps at the site of

treatment. The BHTE simulation for a region treated using scanned HIFU protocols can use the spatially varying estimates of Q to develop a simulation of HIFU treatment.

5.3.2. In vitro experiments for noninvasive temperature estimation

The noninvasive temperature estimation technique was tested during *in vitro* experiments performed in the alginate tissue-mimicking phantom. Independent validation of the technique was performed by comparing the *noninvasive* temperature estimates with thermocouple (HYP0-33-1-T-G-60-SMP-M, Omega Engineering Inc., Stamford, Connecticut) readings inserted into the phantom. A special mechanical fixture with through holes to insert thermocouples was designed and built. A schematic drawing of the fixture, developed using a computer-aided design program (SolidWorks, Concord, MA), is shown in Figure 5.8. The fixture was attached to the HIFU transducer assembly and oriented such that the thermocouples could be positioned around the geometric focus of the HIFU transducer. The fixture also contained micropositioners so that the locations of the thermocouples could be precisely adjusted. The micropositioners are used to adjust the thermocouple position precisely with respect to the geometric focus of the HIFU transducer. A digital photograph of the experiment setup with the fixture used to hold the thermocouples during an HIFU exposure is shown in Figure 5.9.

As part of a pre-alignment step performed before the experiment commences, the thermocouples are precisely positioned with respect to the HIFU focus in water (before the thermocouples have been immersed in the sample). This is done after the HIFU transducer has been aligned with respect to the needles affixed to the base of the sample holders (see Figure 4.5). For aligning the HIFU transducer with the thermocouples, the HIFU transducer is set up in pulse-echo mode and connected to a function generator (HP 33120, Palo Alto, CA) operating in burst mode at a repetition rate of 100 Hz. Each burst consists of 10 cycles of a 5 MHz sine wave with 10 V_{pp} amplitude. The HIFU transducer is connected to an oscilloscope to visually observe transmitted and received signals. The micropositioners on the thermocouple assembly are adjusted in all three directions (X,Y, Z) until a reflection from one of the thermocouples (thermocouple 1 in Figure 5.10) is

visible on the oscilloscope. This ensures that the thermocouple is within the focal region of the HIFU transducer. The micropositioners are then adjusted in all three directions until the received signal amplitude is maximized, thus ensuring that the thermocouple is now at the focal peak. The thermocouple fixture is then translated transverse to the HIFU beam propagation axis until it lies outside the first side lobe of the HIFU beam. This alignment procedure ensures that the thermocouples are located around the HIFU beam where the temperature rises are significant but yet not within the HIFU main lobe. This minimizes the influence of viscous heating effects [126, 127], commonly referred to as the *thermocouple artifact* [128], on the temperature readings. After the alignment procedure is complete, the thermocouples are inserted into the sample. With this arrangement, the thermocouples are typically at transverse distances of 1, 3 and 4 mm from the HIFU beam propagation axis. A B-mode image of the phantom with thermocouples placed around the HIFU focus is shown in Figure 5.10.

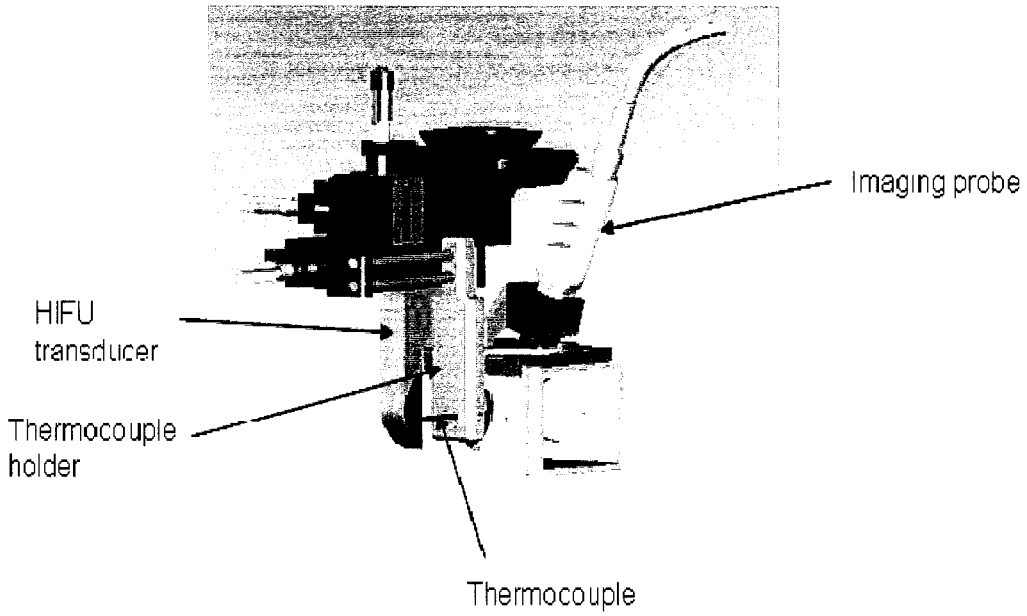

Figure 5.8 Schematic diagram of thermocouple holder used to position thermocouples around the geometric focus of the HIFU transducer. *Drawing courtesy of Andy Proctor*

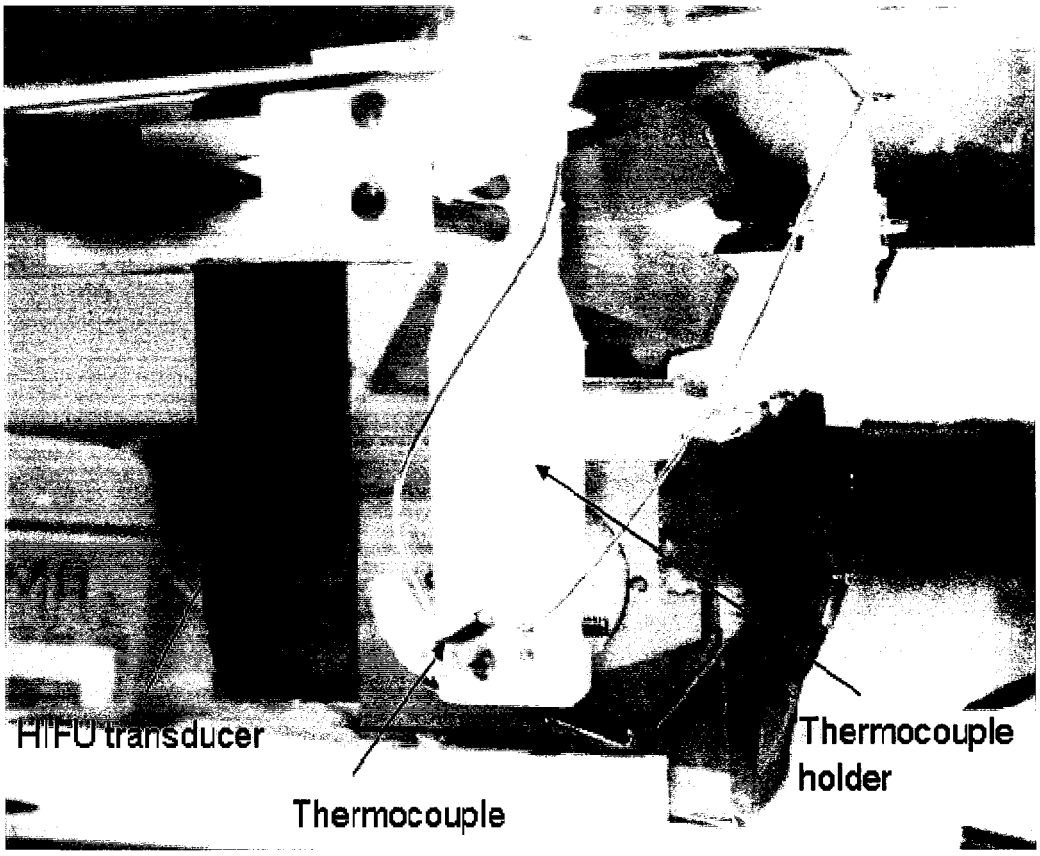

Figure 5.9 Photograph of experimental setup for noninvasive temperature estimation and validation using thermocouples. The thermocouple holder is rigidly attached to the HIFU transducer assembly. The thermocouples are inserted through the holes on the holder and their position in the sample is confirmed on the B-mode image.

The master control program previously developed to collect RF data from the HDI 1000 commercial ultrasound scanner during HIFU therapy was modified so that the thermocouple readings could also be acquired simultaneously during the HIFU heating experiment. The thermocouples were connected to separate analog input channels on a computer controlled data acquisition unit (HP 34970, Hewlett Packard, Palo Alto, CA). The sampling rate on each of the analog input channels was set to 10 Hz. Acquisition of thermocouple data was initiated at the start of HIFU therapy delivery, and continued for approximately 30 s into the cool down period after HIFU delivery had been turned off. The total HIFU therapy delivery time was 7 seconds, with brief interruptions every 500 ms for acquiring RF data as in previous HIFU therapy experiments reported in Chapter 4.

The *in situ* HIFU intensity for the exposures was 265±52 W/cm^2. The first two RF frames acquired immediately after therapy commenced (within the first 1 second) were used in the iterative estimation algorithm to determine the parameter Q. The estimated values of Q were then input in the BHTE to obtain the temperature maps. The experiments were performed starting at an initial baseline temperature of 29°C.

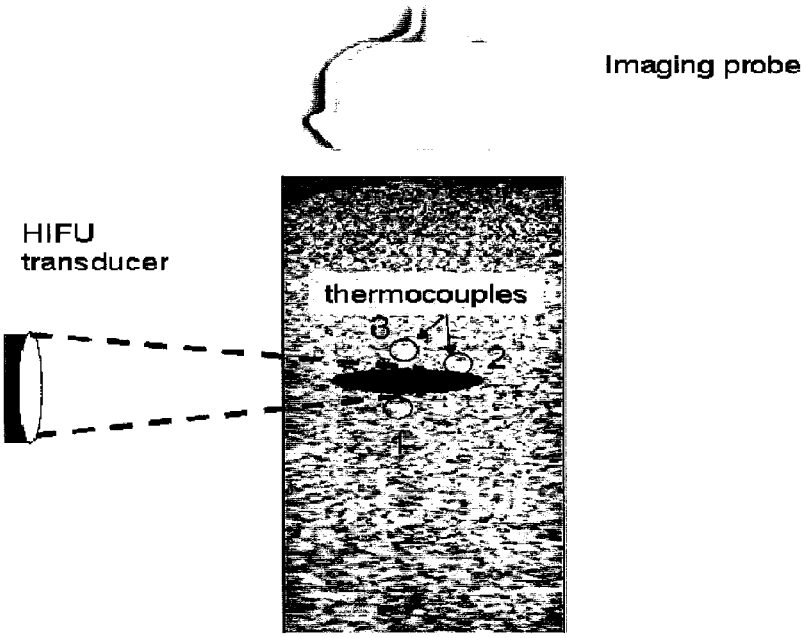

Figure 5.10 B-mode image showing the location of the three thermocouples, HIFU transducer and imaging probe

5.3.3. Results

The intermediate results obtained after 1, 3, 5 and 10 iterations of the estimation technique (Figure 5.7) are presented in the four different panels of Figure 5.11. The topmost plot in each of the panels shows the "raw" RF signals before any processing is applied. The blue trace represents the signal before heating commences while the red trace represents the signal obtained during heating. The third plot in each of the panels shows the model predicted echo shift, s, for a given value of Q. The HIFU focus location is shown by the ellipse in this plot. The second plot shows the RF lines after the pre-heated RF line (blue) has been shifted by the model-predicted echo shift profile s. The fourth plot shows the zero-lag cross-correlation between the signals at iteration 0

before any processing (*red* line) and at the current iteration (*blue* line). Proximal to the HIFU focus location and closer to imaging transducer, the zero-lag correlation is close to unity consistently. This is expected since no heating has occurred in this zone. Distal to the HIFU focus, the zero-lag correlation coefficient before any processing is applied however decreases to 0.8. As the iterations proceed, the zero-lag cross-correlation increases from close to 0.8 distal to the heated zone to almost unity at iteration 10. Accordingly, it can be seen that the signals in the second plot start to overlap each other. The temperature estimates are then obtained by solving the BHTE with the updated value of Q obtained at convergence. A comparison of the noninvasively estimated temperatures at the thermocouple locations (1, 3 and 4 mm from the HIFU beam propagation axis) and the corresponding thermocouple estimates is provided in Figure 5.12. Note the good agreement between the noninvasively estimated temperatures and the thermocouple estimates over the entire duration of the experiment. The predicted temperature rise at the focal point of the HIFU transducer derived from the BHTE model is also shown in the figure. This plot shows that the maximum temperature recorded during the HIFU exposure is approximately 57 degrees Celsius. Spatial maps of the temperature evolution around the HIFU focus were also computed. These maps are presented in Figure 5.13 for different times after HIFU therapy commenced. This result demonstrates the ability of the algorithm to estimate temperatures in the therapeutic temperature range. The delivered thermal dose at the location of the maximum temperature rise for this case was 433 dose equivalent minutes which exceeds the threshold for tissue necrosis of 120-240 minutes referenced to 43°C [60]. *Furthermore, these results demonstrate that although the temperature induced strain lacks sensitivity over parts of the therapeutic temperature range, by combining information from the backscatter data with the BHTE this lack of sensitivity can be overcome.*

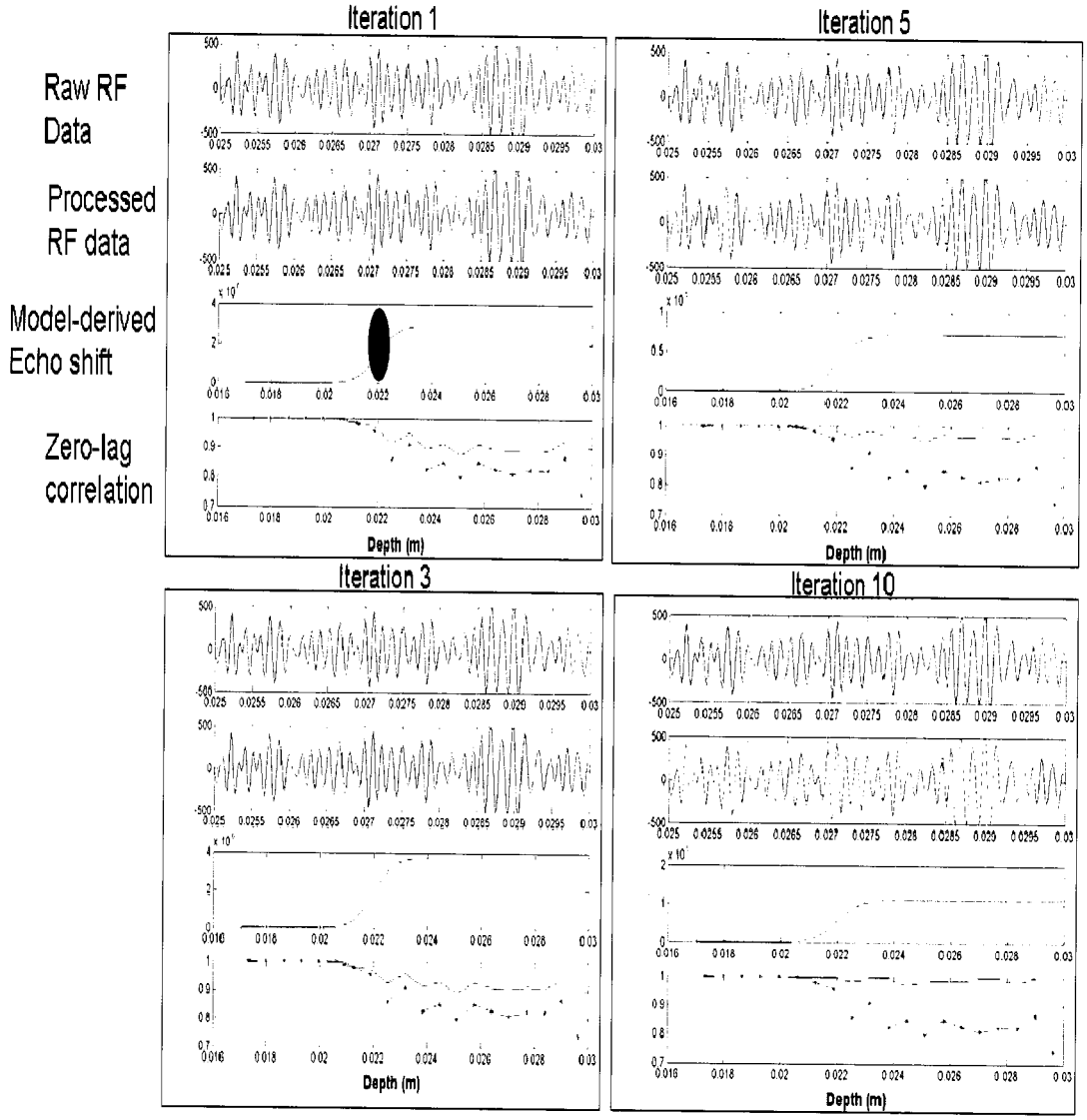

Figure 5.11 Illustration of the technique for noninvasive temperature estimation at iterations 1, 3, 5 and 10. The location of the HIFU geometric focus is shown by the ellipse in panel 3 of Iteration 1. Note that the horizontal axis in plots 1 and 2 for each of the four iteration panels ranges from 2.5 cm to 3 cm. The range for plots 3 and 4 is from 1.5 cm to 3 cm.

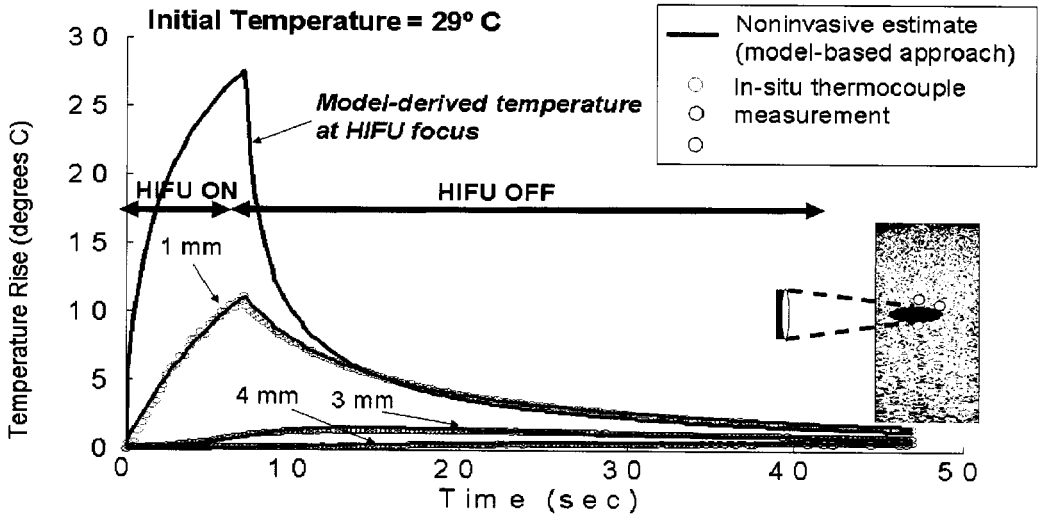

Figure 5.12 Comparison between noninvasive temperature estimates and readings from in situ thermocouples placed at transverse distances of 1, 3 and 4 mm from the HIFU focus. The location of the thermocouples is shown on the B-mode image on the right.

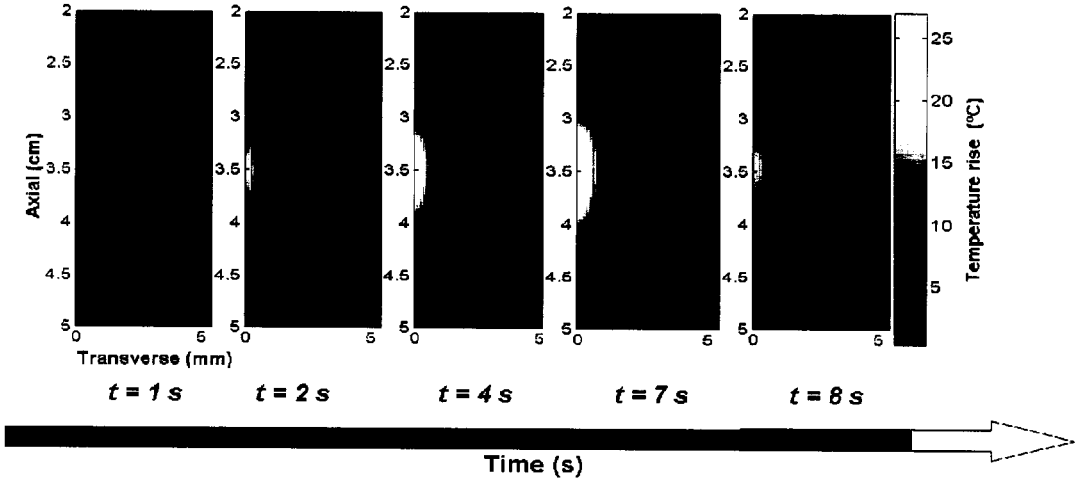

Figure 5.13 Spatial profiles showing the temperature evolution around the HIFU focus at times t=1, 2, 4, 7 and 8 s after the HIFU therapy delivery started. The HIFU therapy delivery was turned off at t=7.2 s. The color bar represents the temperature rise in degrees Celsius above the ambient temperature. The HIFU transducer is at the top of these figures and the beam propagates vertically downward. The figures represent simulated temperature fields using BHTE parameters estimated from ultrasonic measurements, and confirmed by thermocouple readings.

5.4. Discussion

A quantitative temperature estimation technique designed for HIFU therapy monitoring was reported in this chapter. The methods developed provide the ability to estimate temperatures throughout the therapeutic range and is thus a departure from

previously reported techniques [70, 79, 94], that were applicable to the hyperthermia range where the temperature rise is only a few degrees above ambient temperature. A key difference between the current approach and previously reported methods is the coupling of the BHTE with echo shift information from the RF backscatter to obtain the temperature information *noninvasively*. This provides the ability to estimate temperatures in regions of low sensitivity of the $\varepsilon(T)$ curve. Previously reported methods relied on direct inversion of ε via the $\varepsilon(T)$ mapping to obtain temperature. However, since the $\varepsilon(T)$ does not provide high sensitivity throughout the therapeutic temperature range, these methods were only applicable in the low temperature range where the sensitivity of the $\varepsilon(T)$ curve was high. In the current approach, the initial high sensitivity linear region of the $\varepsilon(T)$ curve was used to noninvasively estimate the BHTE parameters. Once the BHTE parameters have been estimated, the BHTE was used to compute the temperature information throughout the HIFU exposure.

This estimation technique assumes that the local *in situ* heat source Q does not change as a function of temperature and that the value estimated at the beginning of treatment is valid throughout the exposure. The close agreement between the thermocouple measurements and the noninvasive ultrasonic temperature estimates appear to confirm the validity of this assumption. From Figure 5.12, it can be seen that the thermocouple placed 1 mm from the focus matches the noninvasive temperature estimates, both during heating and post-HIFU during cool down. If the effect of local absorption change had been significant at the focus, one would expect to see an inflection point in this thermocouple reading since it is placed close to the focus. The local *in situ* heat source Q is a function of the local ultrasonic absorption coefficient and the intervening path attenuation. Temperature induced changes in the ultrasonic attenuation coefficient have been previously reported in the literature [47, 49, 129, 130]. However, the study by Techavipoo et. al. [130] claimed that attenuation changes were dominant only after the sample that was exposed to thermal ablation cooled down to room temperature (a process that typically takes a couple of minutes). They reported that no significant attenuation change was observed in measurements taken at the elevated

temperatures. They conclude based on these results that the attenuation increase is predominantly due to tissue necrosis or coagulation and not the temperature elevation. It is possible to determine through modeling, if the increase in attenuation in the intervening path counteracts the increase in local tissue absorption, effectively resulting in no net change in the local heating rate. However, we did not test this hypothesis in this thesis. If change in absorption is important for certain tissue types, it would need to be incorporated into the BHTE model.

An integral part of the temperature estimation technique developed in this chapter was the noninvasive estimation of the mapping between temperature induced strain ε and temperature T. In previous studies [70, 79, 94], this mapping parameter was *invasively* determined prior to treatment. Such an invasive approach would not be effective in an *in vivo* clinical setting. Moreover, due to large scale variability in this parameter as a function of tissue type [72, 73], it would be useful to estimate it for a given region of interest in the patient before the treatment commences. The noninvasive method proposed in this chapter could be used for this purpose.

5.5. Conclusions

A noninvasive ultrasound-based temperature estimation technique for HIFU therapy monitoring has been developed in this chapter. The techniques were developed and validated on tissue mimicking phantoms. Good agreement was observed between noninvasive temperature estimates and independent thermocouple readings obtained close to but not at the HIFU focus. In the next chapter, results obtained by applying the methods developed in Chapter 4 and 5 on freshly excised turkey muscle tissue are presented.

6. *IN VITRO* TISSUE EXPERIMENTS

6.1. Introduction

The noninvasive temperature estimation algorithm developed in Chapter 4 and 5 was tested on excised turkey breast muscle tissue. Details of these experiments and the results obtained are presented in this chapter. The chapter begins with a description of the tissue preparation in section 6.2. The experiment protocol and setup is discussed in section 6.3. The noninvasive temperature estimation results are presented in section 6.4.

6.2. Tissue preparation

In vitro experiments on turkey breast muscle (Foster Farms, Kelso, WA) were performed using the experiment system previously described in Chapter 5. Prior to the experiments, the samples were cut into convenient sizes so that they could be placed in the sample holders of dimensions 5×5×6.5 cm. The samples were then immersed in de-ionized water and degassed under vacuum. The degassing process continued until no visible outgassing from the sample was evident. This process typically lasted 30-40 minutes. A photograph of the sample placed in the degassing tank is shown in Figure 6.1. Care was taken to ensure that the samples were arranged in the holder, such that the direction of propagation of the ultrasound therapy and imaging beam was perpendicular to the fiber orientation. This is important to consider because of the anisotropy of muscle fibers. In muscle, the attenuation along the fibers exceeds that across the fibers by a factor of 2 or 3 [92]. After degassing, the tissue sample was placed near the center of the holder and suspended vertically on a clamp with the aid of a needle and sewing thread as shown in Figure 6.2. With the sample held in this position, alginate gel was poured into the holder to encase the tissue sample. This arrangement ensured that the tissue sample was positioned in the center of the holder allowing easy insertion of thermocouples into the tissue. It also ensured that the ultrasound therapy beam enters through a relatively flat front surface. Not doing so may lead to significant refraction, and misalignment of the imaging and therapy beams. The propagation distance through the gel was approximately 1 cm. The attenuation and sound speed was measured using the sample replacement

technique for each of the samples in the experiment. The average sound speed and attenuation measured over 4 samples was 1567.8±12.4 m/s and 1.24±0.18 dB/cm/MHz respectively. These attenuation measurements were performed with the muscle fibers oriented perpendicular to the beam propagation direction. The attenuation values measured with the fibers oriented parallel to the beam propagation direction was 2.1±0.16 dB/cm/MHz. The reported values for attenuation in muscle, perpendicular and parallel to the fibers are in the range of 0.9-1.4 dB/cm/MHz and 1.6-2.8 dB/cm/MHz, respectively [92]. The attenuation of the alginate gel phantom was also independently measured to be 0.34±0.032 dB/cm/MHz.

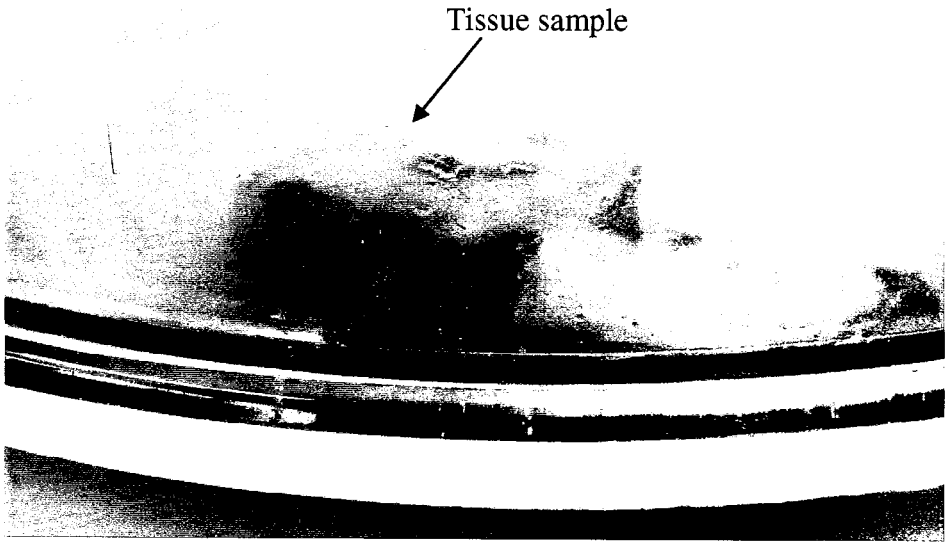

Figure 6.1 Photograph of turkey breast muscle tissue sample placed in the degassing chamber

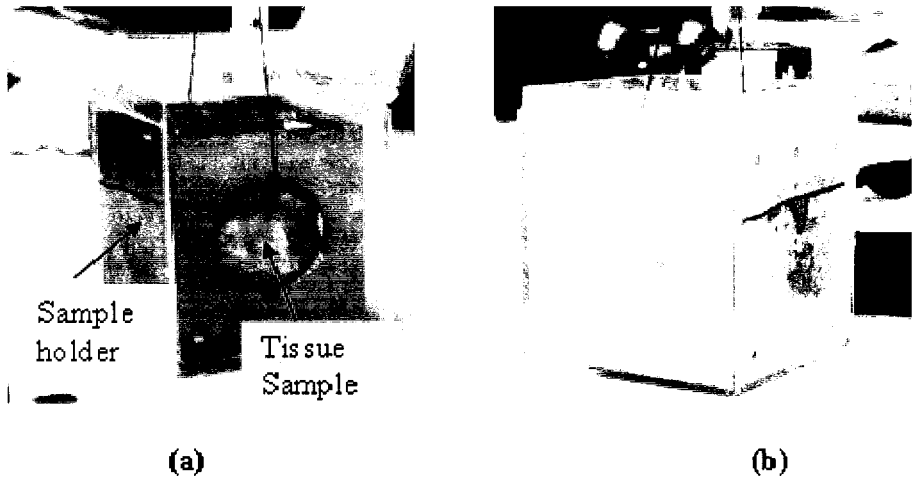

Figure 6.2 (a) Tissue sample suspended by a sewing thread from a clamp and held in place near the center of the sample holder (b) Alginate gel is poured to encase the tissue

6.3. Experiment setup

The therapy experiments were performed using the same instrumentation setup as that employed for the phantom experiments earlier reported in Chapters 4 and 5. A 5 MHz HIFU transducer was mounted on a 3-D motion stage and manually translated to create lesions at different locations within the tissue sample. The separation between adjacent exposure locations was greater than 1 cm to avoid any interaction between the lesion sites. A total of 4 independent samples were analyzed. For each of the samples, calibration experiments to extract the thermal parameters were first performed. A brief HIFU exposure at an *in situ* HIFU intensity of about 30 W/cm^2 was applied to estimate the thermal diffusivity *(K)*. These exposures were typically 5 seconds in duration and the diffusivity parameter was extracted during the cool down period. Following this, HIFU exposure at an *in situ* intensity of 173±50 W/cm^2 was performed to raise the focal temperature of tissue to boiling to noninvasively estimate the heating rate Q. The exposures were repeated at different locations in each sample to evaluate the uniformity of results. The thermal parameters estimated during these experiments were then input into the BHTE and combined with RF data simultaneously acquired during the calibration exposure to noninvasively estimate the temperature to strain mapping, referred to as $\varepsilon(T)$. After the calibration experiments were completed, the therapy

transducer was translated to a previously untreated location and HIFU was applied at an *in situ* intensity of 350±104 W/cm^2 for 5-10 s to induce tissue necrosis. The model-derived noninvasive ultrasonic temperature estimates were compared with independent thermocouple measurements obtained at three different locations around the HIFU focus.

Independent of the noninvasive methods described in the previous paragraph, the "invasive" ground truth estimate of $\varepsilon(T)$ using the water bath setup was also obtained. The experimental procedure was identical to that employed for the phantom sample. This experiment was performed on a different tissue sample from that used for the therapy monitoring experiments. The sample was heated over the temperature range 22 to 56 degrees Celsius since this was range of the $\varepsilon(T)$ curve used in the temperature monitoring step.

6.4. Results and Discussion

The results obtained in the *in vitro* turkey muscle experiments are presented in this section. The calibration results are presented first followed by results from the temperature estimation step.

6.4.1. Estimation of thermal diffusivity (K)

A plot of Gaussian radius as a function of time during cool down (after HIFU therapy has been turned off) is shown in Figure 6.3 for one of the samples tested. The slope of the linear fit to the data points is related to the thermal diffusivity and was measured to be 1.42×10^{-7} m^2/s for this sample. The uncertainty in this estimate at the 95% confidence level was 0.3×10^{-7} m^2/s. The thermal diffusivity estimates obtained from the remaining samples tested were 1.18×10^{-7}, 1.3×10^{-7} and 1.55×10^{-7} m^2/s. The variation in the diffusivity values is possibly due to the local heterogeneities and inter-sample variability that would be expected between independent tissue samples. For comparison, the reported range of values for thermal diffusivity in the literature for muscle is 1.25-1.54×10^{-7} m^2/s [92].

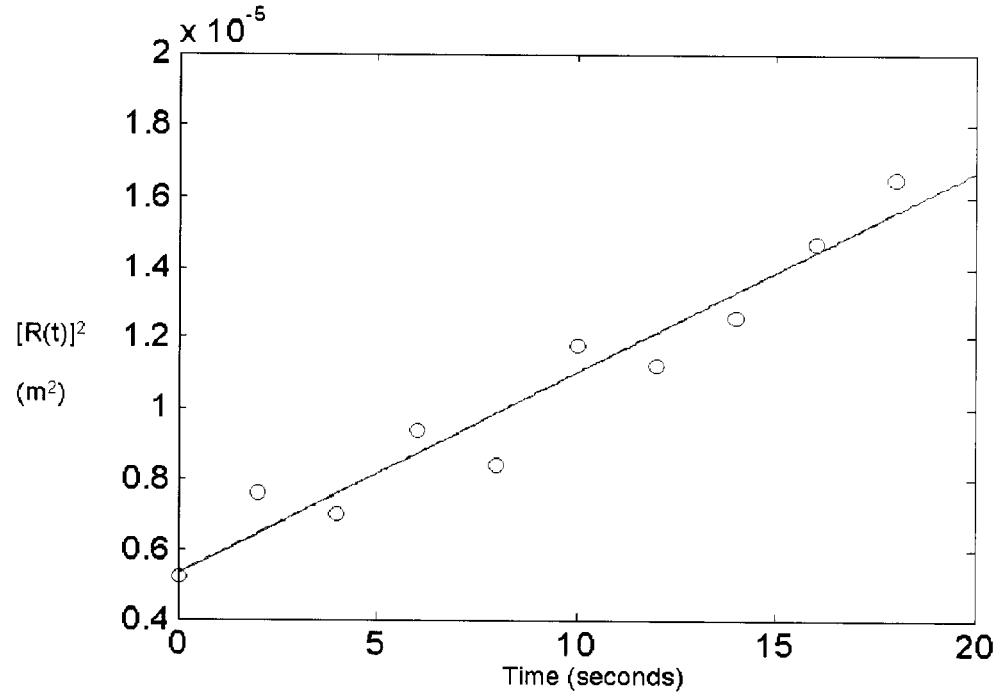

Figure 6.3 Plot of square of Gaussian radius *R(t)* versus time after the HIFU heating pulse was turned off. The dots represent the values estimated by analysis of the RF data and the straight line represents the linear least squares fit to the data points.

6.4.2. Noninvasive detection of boiling onset and in situ heating rate

A sample time series output of the stethoscope during a HIFU exposure in turkey breast muscle tissue is shown in Figure 6.4(a) along with the spectrogram in Figure 6.4(b). It can be seen from the spectrogram plot that the onset of boiling can be clearly detected, and this spectral information can also be used for automated boiling detection. The ability to noninvasively detect the onset of boiling was tested at a number of sample locations within each sample. Results from these different samples are shown in Figure 6.5.

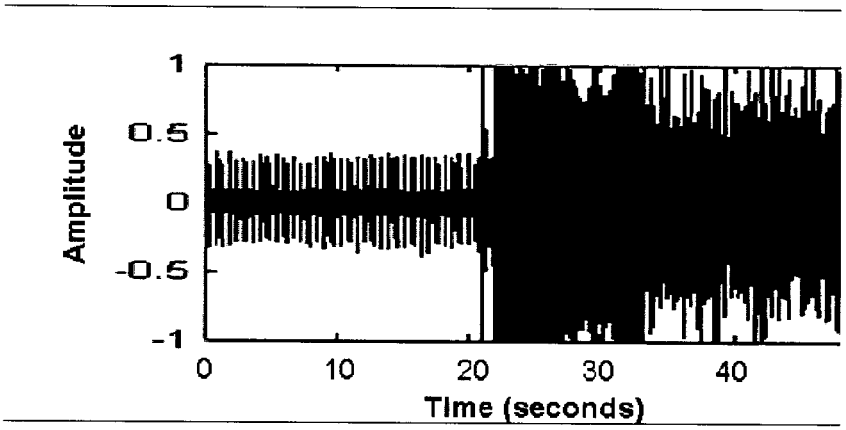

(a)

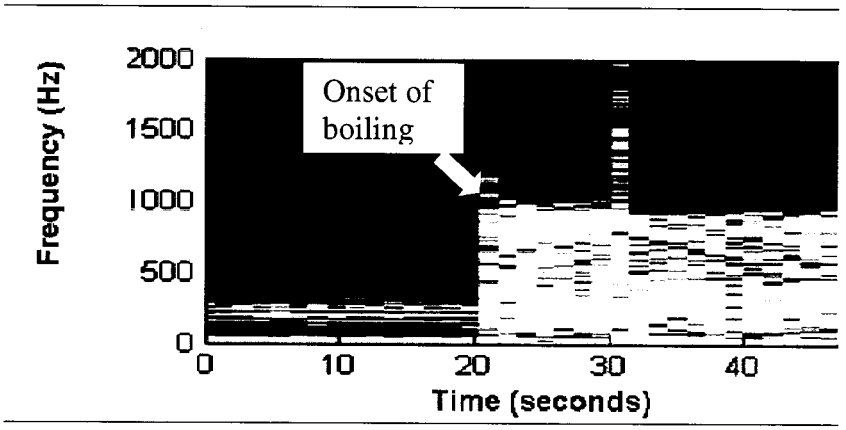

(b)

Figure 6.4(a) Plot showing output of stethoscope during HIFU therapy delivery (**b**) Spectrogram of stethoscope output shown in (a)

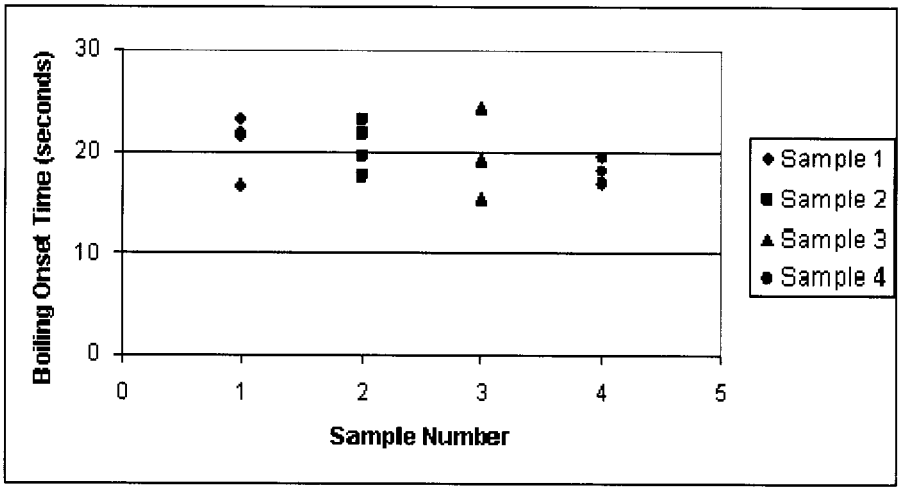

Figure 6.5 Plot illustrating detected boiling onset times for four different turkey breast muscle samples

The boiling time estimates were used with the BHTE to estimate the local heating rate. Table 6.1 shows a comparison between the noninvasive heating rates, derived from the boiling times, and the calculated values obtained using the formulas relating the applied electrical power and heating rate, presented earlier in Chapter 4. The intervening attenuation loss along the ultrasonic propagation path, resulting from the 1 cm alginate gel and muscle tissue, was accounted. The difference of approximately 18 percent between the calculated and estimated values can be explained by the similar range of uncertainties in the measured values of attenuation, electromechanical transducer efficiency and applied electrical power, and the possibility of HIFU beam distortion. The net uncertainty in the calculated heat source resulting from an uncertainty of 5% in each of these measured parameters was calculated to be approximately 25%.

Table 6.1 Comparison between estimated heat source and calculated heat source

In situ Intensity (W/cm^2)	Estimated Heat Source (W/cm^3)	Calculated Heat Source (W/cm^3)	Difference (%)
173±50	203.7±7.03	240±57.6	17.65±10.9

6.4.3. Estimation of $\varepsilon(T)$

A plot of temperature induced strain ε as a function of temperature T derived from the water bath experiment is presented in Figure 6.6. Also shown is a polynomial fit to the experimentally measured values. From the plot, it can be seen that $\varepsilon(T)$ varies nearly linearly as a function of temperature while the temperature is below 40 degrees Celsius. Closer to 50 degrees Celsius, the slope of the strain versus temperature relationship decreases and becomes flat at 50 degrees Celsius. The linear fit to the $\varepsilon(T)$ relationship is shown in Figure 6.7. The slope of this linear fit was used as the ground truth $\varepsilon(T)$ value to compare with the noninvasive estimate derived from the calibration experiments.

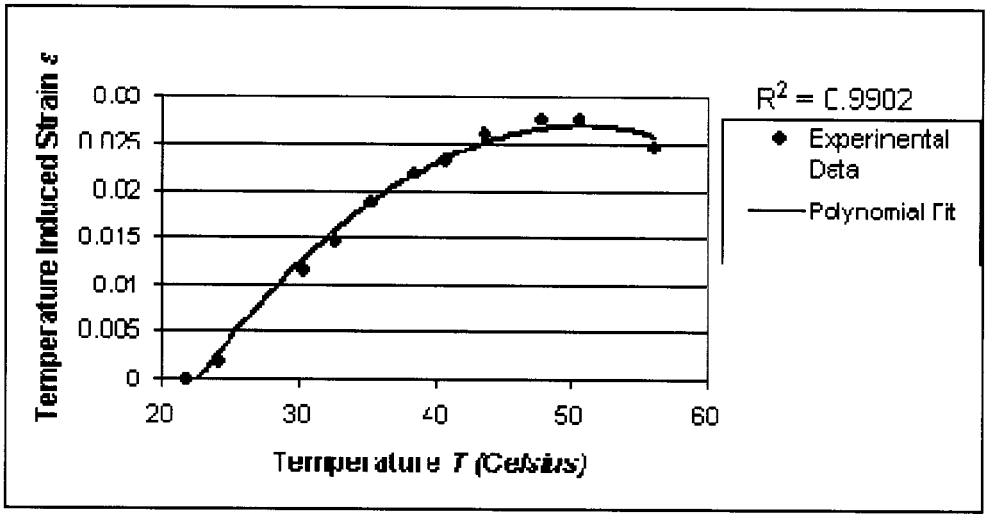

Figure 6.6 Plot of temperature induced strain (ε) versus temperature (T) measured using the waterbath experiment setup. The dots represent the measured experimental data and the curve represents a polynomial least squares fit to the data points.

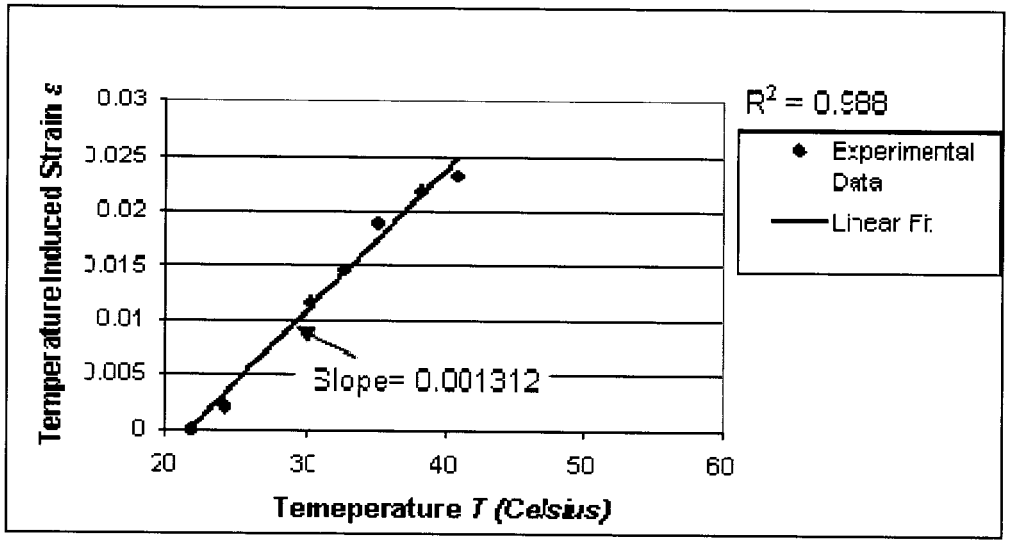

Figure 6.7 Linear least squares fit to $\varepsilon(T)$ mapping in the temperature range between 22 to 40 degrees.

The estimates of the slope of the $\varepsilon(T)$ mapping derived noninvasively from the calibration experiments are illustrated in Figure 6.8 for the four different samples analyzed. In each of the samples, the estimation was performed at multiple locations. Each dot represents the mean estimate (over for 10 adjacent RF scanlines) at a single location in the sample. The standard deviation for each data point is approximately 11% of the estimated value. Also overlaid on the same graph are the estimates of slope of $\varepsilon(T)$ derived from the water bath measurement. The results demonstrate agreement between the noninvasive estimate and the invasive water bath estimate. In most cases, the invasive water bath estimate is slightly higher than the noninvasive estimate. This could be explained by the fact that if the imaging plane does not pass through the hottest zone of the HIFU focal region due to refraction of the therapeutic beam, the observed strain would be smaller than the actual maximum value. Previously, Miller et. al. [73] reported that the resulting decrease in observed strain could be approximately 25%. The effect of this artifact would be greater with a smaller HIFU focal beam width due to larger thermal gradients.

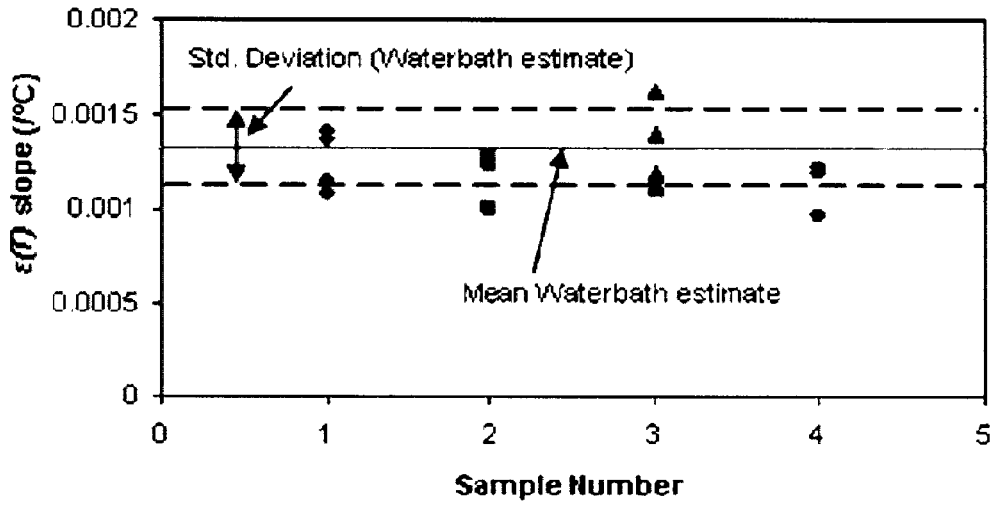

Figure 6.8 Comparison between noninvasively estimated $\varepsilon(T)$ slope values and ground truth measurements obtained using the water bath setup. The data points represent experimental measurements in four independent tissue samples. The water bath estimate is shown as the solid horizontal line and the dotted lines represent the corresponding estimated standard deviation.

6.4.4. Noninvasive temperature estimation

The iterative estimation algorithm described in detail in Chapter 5 was used to compute temperature estimates for the tissue experiments. Alignment procedures were performed before the experiment to ensure that the location of the thermocouples around the focus was accurately known. The thermocouples were arranged so that the thermocouples were placed close to but not within the HIFU focus. A B-mode image showing the arrangement of the thermocouples in the tissue sample is presented in Figure 6.9. The thermocouples were placed at radial distances (perpendicular to the axis of beam propagation) of 1 mm, 3 mm and 4 mm away from the focus.

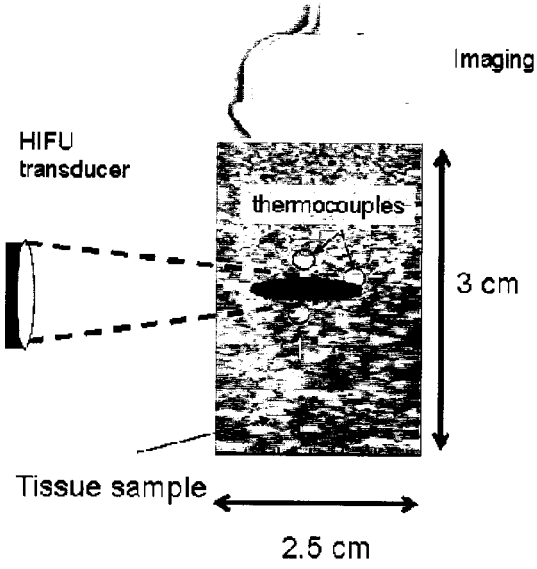

Figure 6.9 B-mode image showing thermocouples inserted in the turkey breast tissue sample. The thermocouples are located 1, 3 and 4 mm radial distances away from the HIFU beam axis.

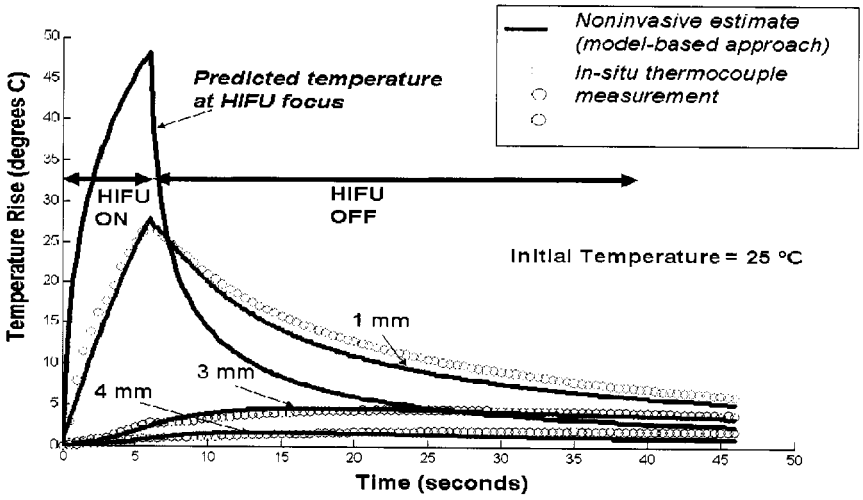

Figure 6.10 Comparison between thermocouple readings and noninvasive temperature estimates at 1, 3 and 4 mm radial distances away from the axis of the HIFU transducer.

Plots of the noninvasive temperature estimates and the corresponding thermocouple data are illustrated in Figure 6.10. These temperature profiles were obtained for an *in situ* HIFU intensity of 350 W/cm^2. The noninvasive estimates were obtained from the solution of the BHTE at the location of the thermocouples. The plots show good agreement between the thermocouple data and the noninvasive temperature estimates.

The predicted temperature profile at the HIFU focus derived from the BHTE model is also plotted in the figure. This plot shows that the maximum temperature rise was approximately 50°C starting from an initial ambient temperature of 25°C. Spatial maps of the temperature profiles were also generated during and after HIFU therapy delivery. These are presented in Figure 6.11.

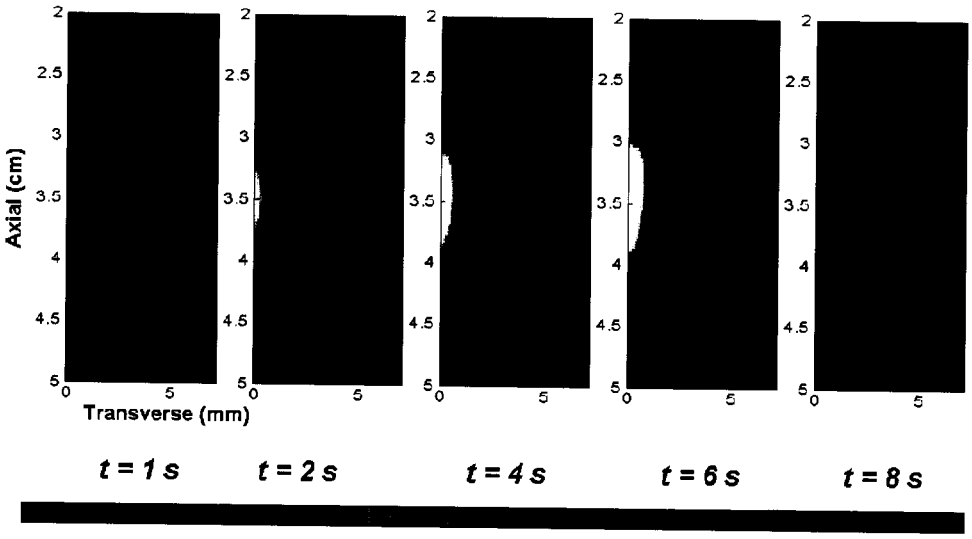

Figure 6.11 Spatial maps illustrating the temperature evolution around the HIFU focus at various times during and after HIFU therapy delivery. The HIFU transducer is located at the top of the figure and the beam propagates vertically downward. The geometric focus of the HIFU transducer is at 3.5 cm. The total therapy ON time for this experiment was 6 s.

6.5. Temperature dependence of thermal diffusivity

For the *in vitro* experimental scenarios considered in this thesis, the thermal diffusivity (K) was assumed to be a numerical constant over the entire therapeutic temperature range of interest. This assumption has also been made by a number of previous authors who developed simulation programs to predict the temperature rise during HIFU [104, 120]. They showed good agreement between the simulated temperature profiles and measured temperature estimates using thermocouples. Furthermore, the close agreement between the thermocouple profiles and the noninvasive ultrasound-based temperature estimates obtained using the model-based temperature estimation technique (developed in this thesis) illustrated in Figure 6.10 suggests that this assumption is possibly valid over the duration of HIFU therapy employed in the

experiment. One of the salient features of HIFU therapy is that the desired therapeutic effect at the treatment location can be achieved within a few seconds [20]. Over this short treatment duration, the heat loss due to thermal diffusion can be considered to have a minimal influence on the resulting spatial temperature distribution. All of these considerations suggest that the error in the temperature estimates due to the assumption of constant thermal diffusivity is not likely to be significant.

Previous studies by various authors have reported on the temperature dependence of tissue thermal diffusivity. These studies were especially of great interest for hyperthermia applications, where the treatment times were considerably longer and the heat transfer process is influenced by thermal diffusion. The question of whether the temperature dependence of tissue thermal diffusivity is important for HIFU applications needs to be investigated further. To the best of the author's knowledge, no study has reported on the temperature dependence of tissue thermal diffusivity specifically for HIFU applications, where the treatment time scales are much shorter than that in hyperthermia applications. Duck [92] summarized the results obtained by different authors for measured values of temperature dependence of tissue thermal diffusivity in the temperature range 3-45°C. The temperature coefficient of tissue thermal diffusivity for kidney, liver, muscle and spleen was reported to be in the range of 0.1-0.43 %/°C.

A preliminary study was conducted to verify if the influence of temperature dependence of thermal diffusivity is important in the muscle tissue samples used in the experiments reported in this thesis. Since the thermal diffusion mechanism is most dominant for longer heating times compared to shorter heating times, the heating times were at least 15 seconds for this study. Temperature estimates computed using the BHTE with a constant thermal diffusivity (no temperature dependence) were compared with *in situ* measured thermocouple temperature profiles for a 45 second HIFU exposure, and the result is plotted in Figure 6.12. Good agreement between the measured thermocouple temperature profiles and the computed estimates can be seen throughout the heating phase and the cool down phase.

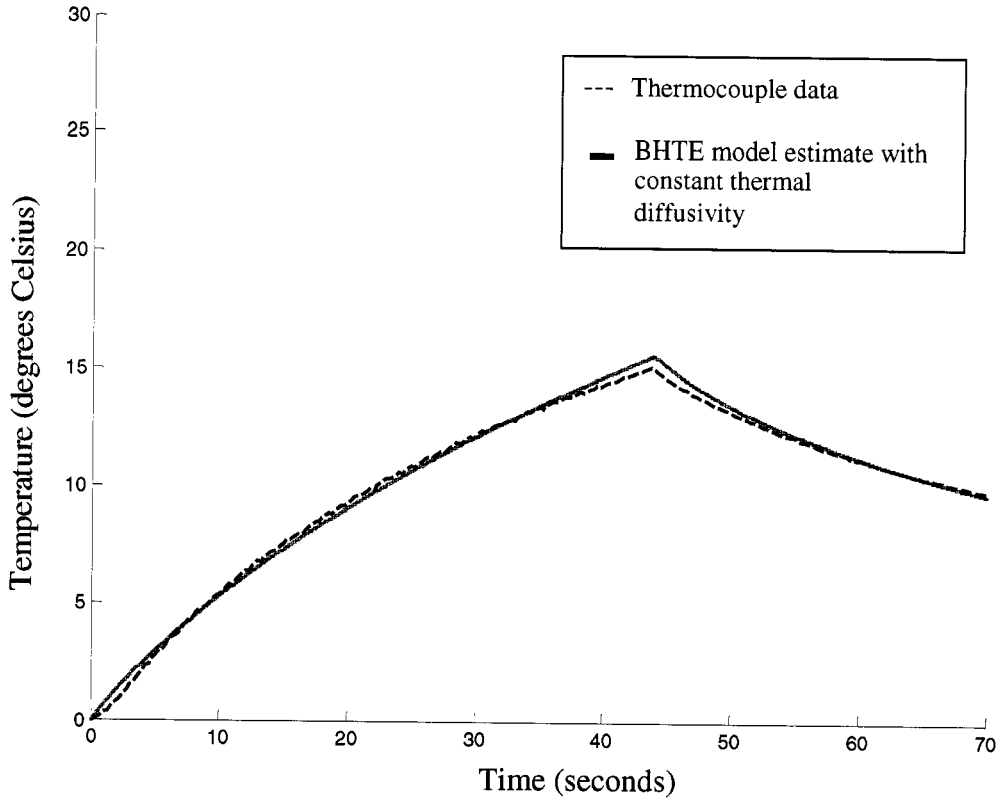

Figure 6.12 Comparison between BHTE computed temperature profiles and measured thermocouple profiles for a 45 second HIFU exposure.

6.6. Conclusion

The noninvasive temperature algorithm for HIFU therapy monitoring developed in Chapters 4 and 5 was tested on excised samples of turkey breast muscle. The results showed good agreement between the noninvasive *in situ* estimates and corresponding profiles from thermocouples inserted in the tissue medium. These results demonstrate potential for the applicability of ultrasound based temperature estimation techniques for HIFU therapy monitoring and could serve as a viable alternative to MRI based techniques, which are the gold standard for noninvasive thermometry during thermal ablation therapy in clinical use today.

7. CONCLUSIONS AND FUTURE WORK

7.1. Conclusions

This dissertation addressed the problem of developing an ultrasound based technique for noninvasive thermometry to monitor the progress of HIFU therapy. A major hindrance in the widespread clinical acceptance of noninvasive ablative therapies such as HIFU has been the lack of adequate quantitative methods for targeting, monitoring treatment progress, evaluating treatment efficacy, and determining the endpoint of therapy. Quantitative estimates of the *in situ* temperature distribution during therapy provide information about the thermal dose, which is a clinically useful indicator of the endpoint of therapy. Moreover, since the therapy modality is ultrasound based, it is useful to have the accompanying monitoring modality also be an ultrasound based technique. Previous methods of ultrasound based temperature estimation were designed mainly for use at sub-ablative temperatures typically encountered in hyperthermia applications and hence find limited applicability in ablative treatment modalities such as HIFU and Radio Frequency Ablation with target temperatures typically in the range of 60 to 100 degrees Celsius. The focus of this thesis was specifically on the development of noninvasive ultrasound based temperature estimation techniques, applicable in the therapeutic temperature range and obtained using ultrasound backscatter data.

The work in this dissertation comprised three parts. The *first* part focused on the development of a software-based data acquisition system to collect unprocessed ultrasound backscatter data, from a commercial ultrasound scanner (ATL HDI 1000). The system provides the ability to externally control the operation of the HDI 1000 ultrasound scanner, and the capability to synchronize RF data acquisition with additional devices and instruments (e.g. motion controllers, temperature measurement devices, therapy delivery modules) that are part of the experiment setup. Although the primary application for this system in our research is acquisition of RF data during HIFU experiments, the system can be easily adapted to meet the data acquisition needs for other emerging ultrasound-based imaging modalities requiring access to RF data.

In the *second* part, the emphasis was on demonstrating that improved visualization of lesion evolution can be obtained by processing the raw ultrasound backscatter compared to the demodulated envelope detected data. Two signal processing based approaches were applied. In the first approach, it was shown that by tracking the echo shifts in the backscattered ultrasound signals (caused by sound speed change and local thermal expansion), local temperature change information can be clearly visualized. The changes were visible not only during heating but also during the cool down after therapy delivery concluded where the recovery of sound speed values and contraction of tissue resulted in echo shifts in the opposite direction relative to the heating phase. *These results showed that the ultrasound backscatter contains information that could be used to extract quantitative temperature estimates. This served as a motivation for part three of the thesis where the goal was specifically to derive quantitative temperature information.* The second signal processing based approach developed was directed at detecting changes in tissue scattering properties by analysis of the spectral content of the ultrasound backscatter data. Compared to M-mode data that showed the appearance of a hyperechoic spot some time after therapy commenced, visible changes due to increased harmonic frequency generation were seen on the spectral display very shortly after therapy commenced. Corresponding to the onset of the hyperechogenic spot on the B-mode data, evidence of increased backscattering *possibly* due to bubbles was seen on the spectral maps. Furthermore, decreased high frequency content in the ultrasound backscatter from locations distal to the lesion along the imaging beam gave evidence of increased attenuation at the lesion location. These results showed compelling potential for the use of advanced signal processing techniques to achieve the goal of image-guided HIFU therapy.

In part three of the dissertation, the focus was on the development of a quantitative temperature estimation technique that would be applicable for HIFU therapy monitoring. A key contribution of this thesis in this regard is the development of a model-based approach that relates the underlying heat diffusion process with ultrasound echo shift information derived from the measured backscatter to obtain temperature estimates. It

was shown in this work that the use of the BHTE equation to constrain the inversion of ultrasound backscatter data enables the estimation of temperature even in regions where the $\varepsilon(T)$ curve becomes insensitive to temperature changes. This is of critical importance in HIFU therapy monitoring since for most soft tissues, the $\varepsilon(T)$ curve flattens out near the coagulation threshold (approximately 50-60°C) which complicates the inversion process. Temperature estimates obtained noninvasively with the model-based approach were in close agreement with invasive thermocouple measurements with accuracy of approximately 1°C. *This method of temperature estimation is a departure from previously reported techniques that relied on direct inversion of the echo shift information from the backscatter data.*

Another key contribution of this thesis is the *development of novel noninvasive methods of estimating acoustic and thermal parameters needed for temperature estimation.* All of the methods were designed so that they could be performed before the therapy session commences at a representative location within the treatment region of interest and are therefore referred to as calibration measurements. With regard to the temperature dependent strain mapping, $\varepsilon(T)$, there exists variation between tissues types, and inter-patient variability can also be expected. For example, the initial slope of the curve is positive for tissues with high water content and negative for tissue with high lipid content [54, 72]. The noninvasive technique of estimating the $\varepsilon(T)$ curve developed in this thesis reduces the uncertainty in the knowledge of this important parameter required for temperature estimation. The techniques for estimation of thermal parameters such as thermal diffusivity and local heating rate are also novel noninvasive methods, and rely solely on the processing of acoustic signals.

A key development in this thesis was the application of physical model based signal processing approaches for analyzing the ultrasound backscatter data. In this approach, underlying information about the thermal diffusion provided by the BHTE was coupled with the RF backscatter data to estimate the parameters of interest such as thermal diffusivity, heating rate, $\varepsilon(T)$ and temperature. Such an approach avoided the need to explicitly first estimate the temperature induced strain using signal processing methods,

which typically requires empirical choice of signal processing parameters such as cross-correlation window length and spatial filters. Previously, Simon et. al. [70] had reported with reference to cross-correlation based methods that making an arbitrary choice of processing parameters can result in signal processing induced artifacts, and requires careful interpretation of the results. With the model-based signal analysis approach adopted in this thesis, the spatial filter parameters are inherently determined by the thermal constants used in the model. The use of the iterative optimization approach to estimate the parameters also provides an added measure of confidence that the data does satisfy the assumptions in the model when the error residuals are below an acceptable level.

In summary, the work presented in this thesis demonstrated the feasibility of an ultrasound based temperature estimation technique specifically designed for applications in thermal therapy monitoring. Although the work was directed towards HIFU therapy monitoring applications which is the main focus of our research group, the underlying framework and paradigm of the approach can be adapted for use in other thermal therapies such as Radio Frequency Ablation and microwave therapies.

7.2. Suggestions for future work

7.2.1. Applicability in *in vivo* conditions

This thesis focused on demonstrating the feasibility of the temperature estimation algorithm in *in vitro* conditions. The effect of tissue perfusion as a heat transport mechanism was therefore not considered in this analysis, and likewise external motion was not considered. The next step in the research would be to extend the applicability of the methods to *in vivo* conditions. The potential complications that need to be accounted for include the effect of patient breathing, bulk motion of transducer assembly (especially for freehand scanning) and tissue perfusion. Given the short treatment times typically used in HIFU therapy, it can be expected that the effect of perfusion would not be very significant over the treatment duration. In cases where the effect is deemed to be significant enough (especially for highly perfused organs such as the liver), quantitative

knowledge of the perfusion rate might have to be incorporated into the heat diffusion model via the BHTE and determined during the calibration step. A noninvasive technique for determining the perfusion rate has been recently proposed in the MRI imaging literature [106]. This approach can be extended to ultrasound data and used to estimate the perfusion rate as part of the calibration step. Potential techniques that could be applied for effective motion compensation are presented in section 7.2.4. It may be possible to lump perfusion loss in with the thermal diffusivity, but highly advective cooling would require substantial modification of the algorithm.

7.2.2. Two dimensional estimation algorithm

The processing methods adopted in this thesis were based on one dimensional analysis of the RF data. The echo shifts and temperature induced strain estimates were computed by processing a pair of RF lines from adjacent frames acquired at the same line of sight (scanline). For model fitting, only the computed temperature estimates along a single axial scan line passing through the HIFU focal region were used. The techniques developed can be extended to two dimensional processing. Two dimensional temperature maps obtained from the BHTE could be related to RF echo shifts determined using a 2-D cross-correlation algorithm [70] to estimate the thermal and acoustic parameters. If the two dimensional data is properly pre-conditioned and filtered, such an approach would result in robust estimates of the parameters, since more independent data are used in the estimation procedure. However, care must be taken to ensure that the effect of acoustic beamforming in the imaging system is properly accounted for. Beamforming errors could occur due to local thermal gradients within the width of the imaging beam that could introduce artifacts distal to the heating zone and cause decorrelation effects in the RF signals. This effect, which depends on the local thermal gradients induced by HIFU, is most severe at the extremities of the focal zone along the HIFU beam propagation direction and less severe around the center of the heated region [70, 72]. Methods for correcting the thermal lens artifact have been proposed and these could be incorporated in the heat transfer model [125].

7.2.3. Estimation of $\varepsilon(T)$ parameters over the entire therapeutic range

In this dissertation, estimation of thermal and acoustic parameters were performed only over the initial portion of the $\varepsilon(T)$ curve, that could represented by a linear relation ($\varepsilon=aT$). These estimates were then used with the BHTE to compute the temperature maps. The limitation of such an approach is that the model does not permit the thermal parameters to change over time. Rather, once the thermal parameters have been estimated during the initial heating phase, they are assumed to be constant throughout the treatment. By modeling the $\varepsilon(T)$ curve as a second order polynomial ($\varepsilon=aT^2+bT$), information from the ultrasound backscatter can be related to the BHTE throughout the exposure, and the therapy parameters can be updated throughout as well. This requires that all coefficients of the second order polynomial of the $\varepsilon(T)$ curve be estimated accurately during the calibration step. For a single point lesion, only the region around the focal peak can be used to resolve the parameter a since the higher temperatures only occur around a small spatial region around the focus. This introduces uncertainty in the estimates of a. If instead of a point lesion, a scanned lesion protocol were adopted where the transducer is mechanically translated across the treatment region while it is emitting the therapy beam, the spatial extent of the temperature change would be greater and would provide more spatial data to estimate a thus improving its accuracy. This requires modification of the HIFU experimental protocol used in this work. However, the motivation to create scanned lesions in clinical HIFU practice is manifold since treatment throughput is greater and more cost effective. Modification of the estimation techniques to incorporate these changes could result in valuable improvement in the applicability of this noninvasive temperature estimation technique.

7.2.4. Motion compensation

In clinical scenarios, bulk motion due to respiration and movement of the transducer during therapy especially with freehand scanning, can influence the performance of time shift estimation and cross-correlation techniques used to estimate the echo shifts and the

temperature induced strain. These motion effects typically include bulk translation, deformation and rotation of tissue over regions much greater than the spatial extent of the heated zone. A possible method of separating the artifacts would be to approach it as a two step motion tracking problem. In the first step, block matching algorithms [131] could be employed over regions of an RF image to compensate for the motion effects. An appropriate signal deformation model would need to be employed in this step. After the global bulk motion has been compensated, the BHTE model-based approach can be employed to estimate the temperature induced echo shifts and inversely estimate the temperature. The advantage of using a BHTE model-based approach in such a scenario is that if bulk motion artifacts were not properly compensated, the iterative optimization step would not converge; residuals of the minimization function would remain significantly higher, and they could be used as an indication of uncertainty in the derived estimates.

7.2.5. Homogeneity of thermal and acoustic parameters

In this dissertation, it was assumed that the thermal and acoustic parameters are locally homogenous and isotropic. Hence K, Q in the BHTE equation and $\varepsilon(T)$ were scalar quantities. It was further assumed that once K and $\varepsilon(T)$ has been estimated during the calibration step, they can be assumed to be constant throughout the entire treatment region. The values estimated in the calibration step were kept constant during the monitoring step. In regions of large scale heterogeneity, as might be encountered in tissue regions with dense vasculature, it might be necessary to perform the calibration experiments at a number of different regions within the treatment volume to generate a *spatial map* of the variation in K and $\varepsilon(T)$. This spatial map could then be fed into the BHTE during the therapy monitoring step to obtain the noninvasive temperature information.

7.2.6. Optimization of therapy and real-time dosimetry control

From the *in situ* measured temperature estimates during therapy, the applied thermal dose can be computed. This provides the ability to evaluate therapy progress and efficacy

during the treatment, since the thermal dose has been shown to be a clinically effective indicator of the endpoint of ablative thermal therapy. The quantitative thermal dose estimates can be used to adaptively update the therapy delivery parameters so that treatment efficacy is maximized. A feedback controller can be designed to update the applied heating rate using information from the therapy monitoring system. Such control mechanisms have been previously applied for MRI thermometry based dose optimization techniques [62, 132]. With the advent of ultrasound based temperature estimation techniques, these adaptive control mechanisms can be applied to temperature information derived from ultrasound. Since the ultrasound data is typically acquired in real-time, it could provide the capability for improved therapeutic dose control at much higher update rates compared to MRI.

7.2.7. Validation studies with MRI thermometry

A gold standard temperature mapping tool in current clinical HIFU practice is MR based thermometry. A logical next step in demonstrating the ability of ultrasound based methods to successfully compete with MR-based methods would be to demonstrate its ability to provide temperature information at a comparable level of accuracy and higher temporal resolution in multi-modality validation studies. Such validation studies would provide the impetus to bring the technique proposed in this dissertation closer to clinical use.

REFERENCES

[1] G. ter Haar, "Acoustic Surgery," *Physics Today*, vol. 54, pp. 29, 2001.

[2] L. A. Crum and K. Hynynen, "Sound Therapy," in *Physics World*, August 1996.

[3] S. Vaezy, M. Andrew, P. Kaczkowski, and L. Crum, "Image-guided acoustic therapy," *Annu Rev Biomed Eng*, vol. 3, pp. 375-90., 2001.

[4] C. T. Moonen, B. Quesson, R. Salomir, F. C. Vimeux, J. A. de Zwart, J. J. van Vaals, N. Grenier, and J. Palussiere, "Thermal therapies in interventional MR imaging. Focused ultrasound," *Neuroimaging Clin N Am*, vol. 11, pp. 737-47, xi, 2001.

[5] J. Palussiere, R. Salomir, B. Le Bail, R. Fawaz, B. Quesson, N. Grenier, and C. T. Moonen, "Feasibility of MR-guided focused ultrasound with real-time temperature mapping and continuous sonication for ablation of VX2 carcinoma in rabbit thigh," *Magn Reson Med*, vol. 49, pp. 89-98, 2003.

[6] F. Wu, Z. B. Wang, W. Z. Chen, J. Z. Zou, J. Bai, H. Zhu, K. Q. Li, F. L. Xie, C. B. Jin, H. B. Su, and G. W. Gao, "Extracorporeal focused ultrasound surgery for treatment of human solid carcinomas: early Chinese clinical experience," *Ultrasound Med Biol*, vol. 30, pp. 245-60, 2004.

[7] D. B. Zippel and M. Z. Papa, "The Use of MR Imaging Guided Focused Ultrasound in Breast Cancer Patients; a Preliminary Phase One Study and Review," *Breast Cancer*, vol. 12, pp. 32-8, 2005.

[8] F. Wu, W.-Z. Chen, J. Bai, J.-Z. Zou, Z.-L. Wang, H. Zhu, and Z.-B. Wang, "Pathological changes in human malignant carcinoma treated with high-intensity focused ultrasound," *Ultrasound in Medicine & Biology*, vol. 27, pp. 1099-1106, 2001.

[9] F. Wu, W.-Z. Chen, J. Bai, J.-Z. Zou, Z.-L. Wang, H. Zhu, and Z.-B. Wang, "Tumor vessel destruction resulting from high-intensity focused ultrasound in patients with solid malignancies," *Ultrasound in Medicine & Biology*, vol. 28, pp. 535-542, 2002.

[10] N. T. Sanghvi, R. S. Foster, R. Bihrle, R. Casey, T. Uchida, M. H. Phillips, J. Syrus, A. V. Zaitsev, K. W. Marich, and F. J. Fry, "Noninvasive surgery of prostate tissue by high intensity focused ultrasound: an updated report," *European Journal of Ultrasound*, vol. 9, pp. 19-29, 1999.

[11] S. Vaezy, R. Martin, P. Kaczkowski, G. Keilman, B. Goldman, H. Yaziji, S. Carter, M. Caps, and L. Crum, "Use of high-intensity focused ultrasound to control bleeding," *J Vasc Surg*, vol. 29, pp. 533-42., 1999.

[12] S. Vaezy, R. Martin, G. Keilman, P. Kaczkowski, E. Chi, E. Yazaji, M. Caps, S. Poliachik, S. Carter, S. Sharar, C. Cornejo, and L. Crum, "Control of splenic bleeding by using high intensity ultrasound," *J Trauma*, vol. 47, pp. 521-5., 1999.

[13] S. Vaezy, R. Martin, U. Schmiedl, M. Caps, S. Taylor, K. Beach, S. Carter, P. Kaczkowski, G. Keilman, S. Helton, W. Chandler, P. Mourad, M. Rice, R. Roy, and L. Crum, "Liver hemostasis using high-intensity focused ultrasound," *Ultrasound Med Biol*, vol. 23, pp. 1413-20., 1997.

[14] T. Livraghi, "Treatment of hepatocellular carcinoma by interventional methods," *Eur Radiol*, vol. 11, pp. 2207-19, 2001.

[15] J. R. Leyendecker and G. D. Dodd, 3rd, "Minimally invasive techniques for the treatment of liver tumors," *Semin Liver Dis*, vol. 21, pp. 283-91, 2001.

[16] G. S. Gazelle, S. N. Goldberg, L. Solbiati, and T. Livraghi, "Tumor ablation with radio-frequency energy," *Radiology*, vol. 217, pp. 633-46, 2000.

[17] J. R. Stewart and F. A. Gibbs, Jr., "Hyperthermia in the treatment of cancer. Perspectives on its promise and its problems," *Cancer*, vol. 54, pp. 2823-30., 1984.

[18] F. K. Storm, D. L. Morton, L. R. Kaiser, W. H. Harrison, R. S. Elliott, T. H. Weisenburger, R. G. Parker, and C. M. Haskell, "Clinical radiofrequency hyperthermia: a review," *Natl Cancer Inst Monogr*, vol. 61, pp. 343-50., 1982.

[19] G. ter Haar and J. W. Hand, "Heating techniques in hyperthermia. III. Ultrasound," *Br J Radiol*, vol. 54, pp. 459-66., 1981.

[20] S. Vaezy, R. Martin, and L. Crum, "High intensity focused ultrasound: a method of hemostasis," *Echocardiography*, vol. 18, pp. 309-15., 2001.

[21] M. M. Madersbacher S, "Tissue ablation by high-intensity focused ultrasound in benign prostatic hypertrophy," *J Urol (Paris)*, vol. 99, pp. 349-355, 1993.

[22] T. G. Leighton, *The Acoustic Bubble*. London: Academic Press, 1994.

[23] N. A. Watkin, G. R. ter Haar, and I. Rivens, "The intensity dependence of the site of maximal energy deposition in focused ultrasound surgery," vol. 22, pp. 483, 1996.

[24] M. R. Bailey, L. N. Couret, O. A. Sapozhnikov, V. A. Khokhlova, G. ter Haar, S. Vaezy, X. Shi, R. Martin, and L. A. Crum, "Use of overpressure to assess the role of bubbles in focused ultrasound lesion shape in vitro," *Ultrasound Med Biol*, vol. 27, pp. 695-708., 2001.

[25] W. J. Fry, "Ultrasound in neurology," *Neurology*, vol. 6, pp. 693-704, 1956.

[26] N. T. Sanghvi and R. H. Hawes, "High-intensity focused ultrasound," *Gastrointest Endosc Clin N Am*, vol. 4, pp. 383-95, 1994.

[27] R. J. Siegel, S. Atar, M. C. Fishbein, A. V. Brasch, T. M. Peterson, T. Nagai, D. Pal, T. Nishioka, J.-S. Chae, Y. Birnbaum, C. Zanelli, and H. Luo, "Noninvasive, Transthoracic, Low-Frequency Ultrasound Augments Thrombolysis in a Canine Model of Acute Myocardial Infarction," *Circulation*, vol. 101, pp. 2026-2029, 2000.

[28] H. E. Cline, K. Hynynen, R. D. Watkins, W. J. Adams, J. F. Schenck, R. H. Ettinger, W. R. Freund, J. P. Vetro, and F. A. Jolesz, "Focused US system for MR imaging-guided tumor ablation," *Radiology*, vol. 194, pp. 731-7., 1995.

[29] C. Bohris, W. G. Schreiber, J. u. u. Jenne, I. Simiantonakis, R. Rastert, H.-J. Zabel, P. Huber, R. Bader, and G. Brix, "Quantitative MR temperature monitoring of high-intensity focused ultrasound therapy," *Magnetic Resonance Imaging*, vol. 17, pp. 603-610, 1999.

[30] F. Kallel, R. J. Stafford, R. E. Price, R. Righetti, J. Ophir, and J. D. Hazle, "The feasibility of elastographic visualization of HIFU-induced thermal lesions in soft tissues," *Ultrasound in Medicine & Biology*, vol. 25, pp. 641-647, 1999.

[31] N. McDannold, R. L. King, F. A. Jolesz, and K. Hynynen, "The use of quantitative temperature images to predict the optimal power for focused ultrasound surgery: in vivo verification in rabbit muscle and brain," *Med Phys*, vol. 29, pp. 356-65, 2002.

[32] K. Hynynen, O. Pomeroy, D. N. Smith, P. E. Huber, N. J. McDannold, J. Kettenbach, J. Baum, S. Singer, and F. A. Jolesz, "MR imaging-guided focused ultrasound surgery of fibroadenomas in the breast: a feasibility study," *Radiology*, vol. 219, pp. 176-85, 2001.

[33] N. T. Zervas and A. Kuwayama, "Pathological characteristics of experimental thermal lesions. Comparison of induction heating and radiofrequency electrocoagulation," vol. 37, pp. 418, 1972.

[34] T. Wu, J. P. Felmlee, J. F. Greenleaf, S. J. Riederer, and R. L. Ehman, "Assessment of thermal tissue ablation with MR elastography," vol. 45, pp. 80, 2001.

[35] R. Yang, C. R. Reilly, F. J. Rescorla, P. R. Faught, N. T. Sanghvi, F. J. Fry, T. D. Franklin, Jr., L. Lumeng, and J. L. Grosfeld, "High-intensity focused ultrasound in the treatment of experimental liver cancer," *Arch Surg*, vol. 126, pp. 1002-9; discussion 1009-10, 1991.

[36] L. Chen, I. Rivens, G. ter Haar, S. Riddler, C. R. Hill, and J. P. Bensted, "Histological changes in rat liver tumours treated with high-intensity focused ultrasound," *Ultrasound Med Biol*, vol. 19, pp. 67-74, 1993.

[37] R. Righetti, F. Kallel, R. J. Stafford, R. E. Price, T. A. Krouskop, J. D. Hazle, and J. Ophir, "Elastographic characterization of HIFU-induced lesions in canine livers," *Ultrasound Med Biol*, vol. 25, pp. 1099-113., 1999.

[38] T. Varghese, J. A. Zagzebski, and J. Lee, F. T., "Elastographic imaging of thermal lesions in the liver in vivo following radiofrequency ablation: preliminary results," *Ultrasound in Medicine & Biology*, vol. 28, pp. 1467-1473, 2002.

[39] T. Varghese, U. Techavipoo, W. Liu, J. A. Zagzebski, Q. Chen, G. Frank, and F. T. Lee, Jr., "Elastographic measurement of the area and volume of thermal lesions resulting from radiofrequency ablation: pathologic correlation," *AJR Am J Roentgenol*, vol. 181, pp. 701-7, 2003.

[40] X. Shi, R. W. Martin, D. Rouseff, S. Vaezy, and L. A. Crum, "Detection of high-intensity focused ultrasound liver lesions using dynamic elastometry," *Ultrason Imaging*, vol. 21, pp. 107-26., 1999.

[41] J. Ophir, I. Cespedes, H. Ponnekanti, Y. Yazdi, and X. Li, "Elastography: a quantitative method for imaging the elasticity of biological tissues," *Ultrason Imaging*, vol. 13, pp. 111-34., 1991.

[42] M. Fatemi and J. F. Greenleaf, "Ultrasound-Stimulated Vibro-Acoustic Spectrography," *Science*, vol. 280, pp. 82-85, 1998.

[43] E. Konofagou, J. Thierman, and K. Hynynen, "The use of ultrasound-stimulated acoustic emission in the monitoring of modulus changes with temperature," *Ultrasonics*, vol. 41, pp. 337-345, 2003.

[44] K. Nightingale, M. S. Soo, R. Nightingale, and G. Trahey, "Acoustic radiation force impulse imaging: in vivo demonstration of clinical feasibility," *Ultrasound Med Biol*, vol. 28, pp. 227-35, 2002.

[45] B. J. Fahey, K. R. Nightingale, D. L. Stutz, and G. E. Trahey, "Acoustic radiation force impulse imaging of thermally- and chemically-induced lesions in soft tissues: preliminary ex vivo results," *Ultrasound Med Biol*, vol. 30, pp. 321-8, 2004.

[46] F. L. Lizzi, R. Muratore, C. X. Deng, J. A. Ketterling, S. K. Alam, S. Mikaelian, and A. Kalisz, "Radiation-force technique to monitor lesions during ultrasonic therapy," *Ultrasound Med Biol*, vol. 29, pp. 1593-605, 2003.

[47] C. A. Damianou, N. T. Sanghvi, F. J. Fry, and R. Maass-Moreno, "Dependence of ultrasonic attenuation and absorption in dog soft tissues on temperature and thermal dose," *J Acoust Soc Am*, vol. 102, pp. 628-34., 1997.

[48] W. L. Straube and R. M. Arthur, "Theoretical estimation of the temperature dependence of backscattered ultrasonic power for noninvasive thermometry," *Ultrasound Med Biol*, vol. 20, pp. 915-22., 1994.

[49] S. H. Bloch, M. R. Bailey, L. A. Crum, P. J. Kaczkowski, G. W. Keilman, and P. D. Mourad, "Measurements of sound speed in excised tissue over temperatures expected under high-intensity focused ultrasound conditions," *Journal of Acoustical Society of America*, vol. 103, pp. 2868, 1998.

[50] N. L. Bush, I. Rivens, G. R. ter Haar, and J. C. Bamber, "Acoustic properties of lesions generated with an ultrasound therapy system," *Ultrasound Med Biol*, vol. 19, pp. 789-801, 1993.

[51] S. Vaezy, X. Shi, R. W. Martin, E. Chi, P. I. Nelson, M. R. Bailey, and L. A. Crum, "Real-time visualization of high-intensity focused ultrasound treatment using ultrasound imaging," *Ultrasound Med Biol*, vol. 27, pp. 33-42., 2001.

[52] A. Sibille, F. Prat, J. Y. Chapelon, F. Abou el Fadil, L. Henry, Y. Theillere, T. Ponchon, and D. Cathignol, "Extracorporeal ablation of liver tissue by high-intensity focused ultrasound," *Oncology*, vol. 50, pp. 375-9., 1993.

[53] M. Ribault, J. Y. Chapelon, D. Cathignol, and A. Gelet, "Differential attenuation imaging for the characterization of high intensity focused ultrasound lesions," *Ultrason Imaging*, vol. 20, pp. 160-77., 1998.

[54] J. C. Bamber and C. R. Hill, "Ultrasonic attenuation and propagation speed in mammalian tissues as a function of temperature," *Ultrasound Med Biol*, vol. 5, pp. 149-57., 1979.

[55] R. L. Nasoni, T. Bowen, W. G. Connor, and R. R. Sholes, "In vivo temperature dependence of ultrasound speed in tissue and its application to noninvasive temperature monitoring," *Ultrason Imaging*, vol. 1, pp. 34-43., 1979.

[56] S. A. Johnson, D. A. Christensen, C. C. Johnson, J. F. Greenleaf, and B. Rajagopalan, "Non-instrusive measurement of microwave and ultrasound-induced hyperthermia by acoustic temperature tomography," presented at Proceedings of IEEE Symposium on Ultrasonics, 1977.

[57] C. Weidensteiner, B. Quesson, B. Caire-Gana, N. Kerioui, A. Rullier, H. Trillaud, and C. T. Moonen, "Real-time MR temperature mapping of rabbit liver in vivo during thermal ablation," *Magn Reson Med*, vol. 50, pp. 322-30., 2003.

[58] G. Ter Haar, "HIFUS Treatments: Dosimetric Considerations," presented at 2nd International Symposium on Therapeutic Ultrasound, Seattle, Washington, USA, 2002.

[59] C. A. H. Damianou, K.; Xiaobing Fan, "Evaluation of accuracy of a theoretical model for predicting the necrosed tissue volume during focused ultrasound surgery," *Ultrasonics, Ferroelectrics and Frequency Control, IEEE Transactions on*, vol. 42, pp. 182-187, 1995.

[60] S. A. Sapareto and W. C. Dewey, "Thermal dose determination in cancer therapy," *Int J Radiat Oncol Biol Phys*, vol. 10, pp. 787-800., 1984.

[61] C. Damianou and K. Hynynen, "The effect of various physical parameters on the size and shape of necrosed tissue volume during ultrasound surgery," *J Acoust Soc Am*, vol. 95, pp. 1641-9, 1994.

[62] M. B. Kowalski, B.; Webb, A.G.; Jian-Ming Jin, "Optimization of electromagnetic phased-arrays for hyperthermia via magnetic resonance temperature estimation," *Biomedical Engineering, IEEE Transactions on*, vol. 49, pp. 1229-1241, 2002.

[63] L. C. Curiel, F.; Souchon, R.; Birer, A.; Chapelon, J.Y., "1.5-D high intensity focused ultrasound array for non-invasive prostate cancer surgery," *Ultrasonics, Ferroelectrics and Frequency Control, IEEE Transactions on*, vol. 49, pp. 231-242, 2002.

[64] C. T. Moonen, B. Quesson, R. Salomir, F. C. Vimeux, J. A. de Zwart, J. J. van Vaals, N. Grenier, and J. Palussiere, "Thermal therapies in interventional MR imaging. Focused ultrasound," *Neuroimaging Clin N Am*, vol. 11, pp. 737-47, xi., 2001.

[65] S. T. S. Clegg, T.V.; Murphy, K.A.; Rosner, G.L.; Dewhirst, M.W., "Inverse techniques in hyperthermia: a sensitivity study," *Biomedical Engineering, IEEE Transactions on*, vol. 41, pp. 373-382, 1994.

[66] R. M. Arthur, W. L. Straube, J. D. Starman, and E. G. Moros, "Noninvasive temperature estimation based on the energy of backscattered ultrasound," *Med Phys*, vol. 30, pp. 1021-9., 2003.

[67] P. E. Huber, J. W. Jenne, R. Rastert, I. Simiantonakis, H.-P. Sinn, H.-J. Strittmatter, D. von Fournier, M. F. Wannenmacher, and J. Debus, "A New Noninvasive Approach in Breast Cancer Therapy Using Magnetic Resonance Imaging-guided Focused Ultrasound Surgery," *Cancer Res*, vol. 61, pp. 8441-8447, 2001.

[68] E. A. Stewart, W. M. W. Gedroyc, C. M. C. Tempany, B. J. Quade, Y. Inbar, T. Ehrenstein, A. Shushan, J. T. Hindley, R. D. Goldin, and M. David, "Focused ultrasound treatment of uterine fibroid tumors: Safety and feasibility of a noninvasive thermoablative technique," *American Journal of Obstetrics and Gynecology*, vol. 189, pp. 48-54, 2003.

[69] O. Rouvière, D. Lyonnet, A. Raudrant, C. Colin-Pangaud, J. Y. Chapelon, R. Bouvier, J. M. Dubernard, and A. Gelet, "MRI Appearance of Prostate following Transrectal HIFU Ablation of Localized Cancer," *European Urology*, vol. 40, pp. 265-274, 2001.

[70] C. Simon, P. VanBaren, and E. S. Ebbini, "Two-dimensional temperature estimation using diagnostic ultrasound," *Ultrasonics, Ferroelectrics and Frequency Control, IEEE Transactions on*, vol. 45, pp. 1088-1099, 1998.

[71] C. S. Simon, J.; Seip, R.; Ebbini, E.S., "A robust and computationally efficient algorithm for mean scatterer spacing estimation," *Ultrasonics, Ferroelectrics and Frequency Control, IEEE Transactions on*, vol. 44, pp. 882-894, 1997.

[72] N. R. Miller, J. C. Bamber, and P. M. Meaney, "Fundamental limitations of noninvasive temperature imaging by means of ultrasound echo strain estimation," *Ultrasound Med Biol*, vol. 28, pp. 1319-33, 2002.

[73] N. R. Miller, J. C. Bamber, and G. R. ter Haar, "Imaging of temperature-induced echo strain: preliminary in vitro study to assess feasibility for guiding focused ultrasound surgery," *Ultrasound Med Biol*, vol. 30, pp. 345-56, 2004.

[74] H. K. Chiang, C.-K. Liao, Y.-H. Chou, T.-T. Pan, and S.-C. Pan, "In-vitro ultrasound temperature monitoring in bovine liver during RF ablation therapy using autocorrelation," presented at Ultrasonics Symposium, 2002. Proceedings. 2002 IEEE, 2002.

[75] T. Varghese, J. A. Zagzebski, Q. Chen, U. Techavipoo, G. Frank, C. Johnson, A. Wright, and J. Lee, F. T., "Ultrasound monitoring of temperature change during

radiofrequency ablation: preliminary in-vivo results," *Ultrasound in Medicine & Biology*, vol. 28, pp. 321-329, 2002.

[76] S. K. Huang, "Radio-frequency catheter ablation of cardiac arrhythmias: appraisal of an evolving therapeutic modality," *Am Heart J*, vol. 118, pp. 1317-23, 1989.

[77] H. H. Pennes, "Analysis of Tissue and Arterial Blood Temperatures in the Resting Human Forearm, vol.1, pp. 93-122.," *J. Appl. Physiol.*, vol. vol.1, pp. 93±122, 1948.

[78] J. Bamber, P. M. Meaney, M. Doyley, R. Clarke, and G. Ter Haar, "Non-invasive temperature imaging using ultrasound echo strain: Preliminary simulations," *Acoustical Imaging*, vol. 23, pp. 25-33, 1997.

[79] R. Seip and E. S. Ebbini, "Noninvasive estimation of tissue temperature response to heating fields using diagnostic ultrasound," *IEEE Trans Biomed Eng*, vol. 42, pp. 828-39., 1995.

[80] R. E. Daigle, "Ultrasonic diagnostic imaging system with personal computer architecture." USA: Atlantis Diagnostics International, 1998.

[81] J. G. Abbott and F. L. Thurstone, "Acoustic speckle: Theory and experimental analysis," *Ultrasonic Imaging*, vol. 1, pp. 303-324, 1979.

[82] J. W. Goodman, "Some fundamental properties of speckle," *J. Opt. Soc. Amer.*, vol. 66, pp. 1145-1150, 1976.

[83] M. Lubinski, S. Emelianov, and M. O'Donnell, "Speckle tracking methods for ultrasonic elasticity imaging using short-time correlation," *IEEE Transactions On Ultrasonics Ferroelectrics And Frequency Control*, vol. 46, pp. 82-96, 1999.

[84] M. O'Donnell, A. R. Skovoroda, B. M. Shapo, and S. Y. Emelianov, "Internal displacement and strain imaging using ultrasonic speckle tracking," *IEEE Ultrasonics, Ferroelectrics and Frequency Control, IEEE Transactions on*, vol. 41, pp. 314-325, 1994.

[85] J. C. Kucewicz, L. Huang, and K. W. Beach, "Plethysmographic arterial waveform strain discrimination by Fisher's method," *Ultrasound Med Biol*, vol. 30, pp. 773-82, 2004.

[86] W. F. T. Walker, G.E., "A fundamental limit on delay estimation using partially correlated speckle signals," *Ultrasonics, Ferroelectrics and Frequency Control, IEEE Transactions on*, vol. 42, pp. 301-308, 1995.

[87] K. W. Beach, "Tissue Pulsatility Imaging for the Detection of Solid Tumors," *Dept. of Surgery Annual Report*, 2001-2002.

[88] T. X. Misaridis, K. Gammelmark, C. H. Jorgensen, N. Lindberg, A. H. Thomsen, M. H. Pedersen, and J. A. Jensen, "Potential of coded excitation in medical ultrasound imaging," *Ultrasonics*, vol. 38, pp. 183-9, 2000.

[89] J. J. Mai and M. F. Insana, "Strain imaging of internal deformation," *Ultrasound Med Biol*, vol. 28, pp. 1475-84, 2002.

[90] R. Entrekin, P. Jackson, J. R. Jago, and B. A. Porter, "Real time spatial compound imaging in breast ultrasound: Technology and early clinical experience," *Medica Mundi*, vol. 43, pp. 35–43, 1999.

[91] A. Anand, P. J. Kaczkowski, R. Daigle, L. Huang, and L. A. Crum, "Using the ATL HDI-1000 Ultrasound Scanner for monitoring HIFU-induced lesion formation," presented at SPIE Medical Imaging, San Diego, CA, 2003.

[92] F. Duck, *Physical Properties of Tissue: A Comprehensive Reference Work*: Elsevier Science & Technology Books.

[93] R. Souchon, G. Bouchoux, E. Maciejko, C. Lafon, D. Cathignol, M. Bertrand, and J. Y. Chapelon, "Monitoring the formation of thermal lesions with heat-induced echo-strain imaging: A feasibility study," *Ultrasound Med Biol*, vol. 31, pp. 251-9, 2005.

[94] R. Maass-Moreno, C. A. Damianou, and N. T. Sanghvi, "Noninvasive temperature estimation in tissue via ultrasound echo-shifts. Part II. In vitro study," *J Acoust Soc Am*, vol. 100, pp. 2522-30, 1996.

[95] Kallel, "Least Squares Strain Estimator for Elastography," *UMB*, 1997.

[96] T. Varghese, J. Ophir, and I. Cespedes, "Noise reduction in elastograms using temporal stretching with multicompression averaging," *Ultrasound in Medicine & Biology*, vol. 22, pp. 1043-1052, 1996.

[97] I. Cespedes, Y. Huang, J. Ophir, and S. Spratt, "Methods for estimation of subsample time delays of digitized echo signals," *Ultrason Imaging*, vol. 17, pp. 142-71., 1995.

[98] F. Viola and W. Walker, "A comparison of the performance of time-delay estimators in medical ultrasound," *IEEE TRANSACTIONS ON ULTRASONICS FERROELECTRICS AND FREQUENCY CONTROL*, vol. 50, pp. 392-401, 2003.

[99] F. Viola and W. Walker, "A spline-based algorithm for continuous time-delay estimation using sampled data," *IEEE Trans Ultrason Ferroelectr Freq Control*, vol. 52, pp. 80-93, 2005.

[100] M. Andrew, C. Lafon, P. Kaczkowski, B. Cunitz, A. Anand, and L. Crum, "Experimental apparatus and method for in vitro HIFU dosimetry studies," presented at International Symposium on Therapeutic Ultrasound, Seattle, WA, 2002.

[101] C. K. Lafon, P.J.; Vaezy, S.; Noble, M.; Sapozhnikov, O.A., "Development and characterization of an innovative synthetic tissue-mimicking material for high intensity focused ultrasound (HIFU) exposures," presented at Ultrasonics Symposium, 2001 IEEE, 2001.

[102] R. J. Miller, L. A. Frizzell, J. F. Zachary, and W. D. O'Brien, Jr., "Attenuation coefficient and propagation speed estimates of intercostal tissue as a function of pig age," *IEEE Trans Ultrason Ferroelectr Freq Control*, vol. 49, pp. 1421-9, 2002.

[103] M. Bailey, Justin Reed, Ajay Anand, P. Kaczkowski, Wayne Kreider, Shahram Vaezy, Lawrence A. Crum, Ralf Seip, Jahangir Tavakkoli, and N. T. Sanghvi, "Cavitation detection and suppression in HIFU," presented at International Symposium on Therapeutic Ultrasound, Lyon, France, 2003.

[104] F. Curra, "Medical ultrasound algorithm for noninvasive high intensity ultrasound applications," in *Bioengineering*. Seattle: University of Washington, 2001, pp. 108.

[105] P. Kaczkowski, M. Andrew, A. Brayman, S. Kargl, B. Cunitz, C. Lafon, V. Khoklova, and L. Crum, "In Vitro Examination of Non-Linear Heat Deposition in HIFU Lesion Formation," presented at 2nd International Symposium on Therapeutic Ultrasound, Seattle, WA, 2002.

[106] H.-L. M. Cheng and D. B. Plewes, "Tissue Thermal Conductivity by Magnetic Resonance thermometry and focused ultrasound heating," *Journal of Magnetic Resonance Imaging*, vol. 16, pp. 598-609, 2002.

[107] M. Pernot, M. Tanter, J. Bercoff, K. R. Waters, and M. Fink, "Temperature estimation using ultrasonic spatial compound imaging," *IEEE Trans Ultrason Ferroelectr Freq Control*, vol. 51, pp. 606-15, 2004.

[108] J. A. Nelder and R. Mead, "A Simplex Method for Function Minimization," *Comput. J.*, pp. 308-313, 1965.

[109] D. Marquardt, "An Algorithm for Least-Squares Estimation of Nonlinear Parameters," *SIAM J. Appl. Math.*, vol. 11, pp. 431-441, 1963.

[110] E. L. Madsen, F. Dong, G. R. Frank, B. S. Garra, K. A. Wear, T. Wilson, J. A. Zagzebski, H. L. Miller, K. K. Shung, S. H. Wang, E. J. Feleppa, T. Liu, W. D. O'Brien, Jr, K. A. Topp, N. T. Sanghvi, A. V. Zaitsev, T. J. Hall, J. B. Fowlkes, O. D. Kripfgans, and J. G. Miller, "Interlaboratory comparison of ultrasonic backscatter, attenuation, and speed measurements," *J Ultrasound Med*, vol. 18, pp. 615-631, 1999.

[111] A. Anand and P. J. Kaczkowski, "Monitoring formation of high intensity focused ultrasound (HIFU) induced lesions using backscattered ultrasound," *Acoustics Research Letters Online*, vol. 5, pp. 88-94, 2004.

[112] H. S. Carslaw and J. C. Jaeger, *Conduction of heat in solids*, 2d ed. Oxford: Clarendon Press, 1959.

[113] A. F. Prokop, S. Vaezy, M. L. Noble, P. J. Kaczkowski, R. W. Martin, and L. A. Crum, "Polyacrylamide gel as an acoustic coupling medium for focused ultrasound therapy," *Ultrasound in Medicine & Biology*, vol. 29, pp. 1351-1358, 2003.

[114] U. Hammerschmidt and W. Sabuga, "Transient hot wire (THW) method: Uncertainty assessment," *International Journal Of Thermophysics*, vol. 21, pp. 1255-1278, 2000.

[115] G. ter Haar, D. Sinnett, and I. Rivens, "High intensity focused ultrasound--a surgical technique for the treatment of discrete liver tumours," vol. 34, pp. 1743, 1989.

[116] R. L. Clarke and G. R. ter Haar, "Temperature rise recorded during lesion formation by high-intensity focused ultrasound," *Ultrasound Med Biol*, vol. 23, pp. 299-306, 1997.

[117] P. P. Lele, "Effects of ultrasound on "solid" mammalian tissues and tumors in vivo. Ultrasound: Medical applications, biological effects and hazard potential.," 1986.

[118] A. L. Malcolm and G. R. ter Haar, "Ablation of tissue volumes using high intensity focused ultrasound," *Ultrasound Med Biol*, vol. 22, pp. 659-69, 1996.

[119] D. T. Blackstock, *Fundamentals of physical acoustics*. New York: Wiley, 2000.

[120] P. M. Meaney, R. L. Clarke, G. R. ter Haar, and I. H. Rivens, "A 3-D finite-element model for computation of temperature profiles and regions of thermal

damage during focused ultrasound surgery exposures," *Ultrasound Med Biol*, vol. 24, pp. 1489-99, 1998.

[121] C. R. Hill, *Physical principles of medical ultrasound*. London: John Wiley & Sons, 1986.

[122] C. R. Hill, I. Rivens, M. G. Vaughan, and G. R. ter Haar, "Lesion development in focused ultrasound surgery: a general model," *Ultrasound Med Biol*, vol. 20, pp. 259-69, 1994.

[123] C. Damianou, "In vitro and in vivo ablation of porcine renal tissues using high-intensity focused ultrasound," *Ultrasound Med Biol*, vol. 29, pp. 1321-30, 2003.

[124] P. A. Lewin, N. Barrie-Smith, M. Ide, K. Hynynen, and M. Macdonald, "Interlaboratory acoustic power measurement," *J Ultrasound Med*, vol. 22, pp. 207-13, 2003.

[125] A. Alaniz, F. Kallel, E. Hungerford, and J. Ophir, "Variational method for estimating the effects of continuously varying lenses in HIFU, sonography, and sonography-based cross-correlation methods," *J Acoust Soc Am*, vol. 111, pp. 468-74, 2002.

[126] W. J. Fry and R. B. Fry, "Determination of absolute sound levels and acoustic absorption coefficients by thermocouple probes- Theory," *J Acoust Soc Am*, vol. 26, pp. 294-310, 1954.

[127] W. J. Fry and R. B. Fry, "Determination of absolute sound levels and acoustic absorption coefficients by thermocouple probes-- experiment," *J Acoust Soc Am*, vol. 26, pp. 311-317, 1954.

[128] F. M. Waterman, M. W. Dewhirst, P. Fessenden, T. V. Samulski, P. Stauffer, B. Emami, P. Corry, S. D. Prionas, M. Sapozink, T. Herman, and et al., "RTOG quality assurance guidelines for clinical trials using hyperthermia administered by ultrasound," *Int J Radiat Oncol Biol Phys*, vol. 20, pp. 1099-107, 1991.

[129] V. Zderic, A. Keshavarzi, M. Andrew, S. Vaezy, and R. Martin, "Attenuation of porcine tissues in vivo after high-intensity ultrasound treatment," *Ultrasound Med Biol*, vol. 30, pp. 61-66, 2004.

[130] U. Techavipoo, T. Varghese, Q. Chen, T. A. Stiles, J. A. Zagzebski, and G. R. Frank, "Temperature dependence of ultrasonic propagation speed and attenuation in excised canine liver tissue measured using transmitted and reflected pulses," *J Acoust Soc Am*, vol. 115, pp. 2859-65, 2004.

[131] Y. Zhu and T. J. Hall, "A modified block matching method for real-time freehand strain imaging," *Ultrason Imaging*, vol. 24, pp. 161-76, 2002.

[132] M. Malinen, T. Huttunen, K. Hynynen, and J. Kaipio, "Simulation study for thermal dose optimization in ultrasound surgery of the breast," *MEDICAL PHYSICS*, vol. 31, pp. 1296-1307, 2004.

[133] T.Varghese, J., "Enhancement of echo-signal correlation in elastography using temporal stretching," *Ultrasonics, Ferroelectrics and Frequency Control, IEEE Transactions on*, vol. 44, pp. 173-180, 1997.

[134] R. M. Lerner, S. R. Huang, and K. J. Parker, ""Sonoelasticity" images derived from ultrasound signals in mechanically vibrated tissues," *Ultrasound Med Biol*, vol. 16, pp. 231-9., 1990.

APPENDIX A: GENERATION OF SIMULATED RF DATA

The methodology for generating RF data sets via computer simulations for a given scatterer distribution and 2-D temperature distribution, during a HIFU treatment exposure is presented in this section. These simulated data sets were used at different points in the thesis to validate algorithms, test data analysis software programs, and perform controlled noise-free experiments. The flowchart of the simulation technique is presented in Figure A.1. Spatial and temporal homogeneity of the various tissue specific thermal and acoustic parameters was assumed. The effect of thermal expansion was ignored. Only the effect of sound speed change was included. The sound speed change results in an *apparent change* in the location of the scatterers.

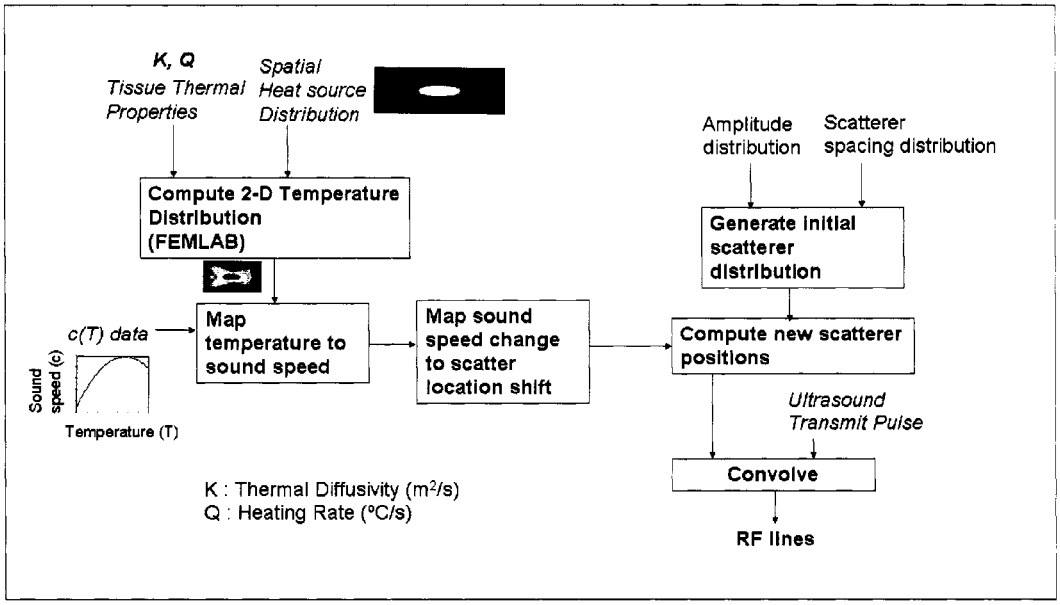

Figure A.1 Flowchart of simulated RF data generation scheme. The temperature distribution is generated first using the finite element implementation of the bioheat equation. A known *c(T)* relationship is used to map the temperature estimates to sound speed, and then to scatterer location shift. *These scatterer shifts are apparent shifts.* These scatterer shift values are used to displace an independently generated random scatterer distribution. The RF lines are generated by convolving the scatterer distribution with the ultrasound transmit pulse.

The various steps in the process are as follows:

Step 1:

The finite element software, FEMLAB™ (Comsol Inc, Stockholm, Sweden) is used to generate the temperature distribution for conditions representative of a HIFU heating experiment. The spatial profile of the acoustic heat source due to ultrasonic absorption in the medium is assumed to be known *a priori* (from computations of a linear acoustic propagation code), and read into the FEMLAB environment from an archived MATLAB data file. FEMLAB employs the finite element method for solving the heat transfer equation. The first step in the simulation is to setup the geometry and the finite element mesh. 2-D axisymmetry of the HIFU beam profile is employed in the simulations to reduce the computation time. A screenshot of the FEMLAB interface showing the axisymmetric axis and the finite element mesh is shown in Figure A.2. Values for thermal diffusivity, heating rate due to ultrasonic absorption, and initial conditions are input through the various visual interface dialog boxes in the FEMLAB software environment. A sample temperature distribution for a HIFU heating experiment is shown in Figure A.3. Typically, temperature maps at a number of discrete time instants during the HIFU exposure is simulated, and used in the subsequent steps.

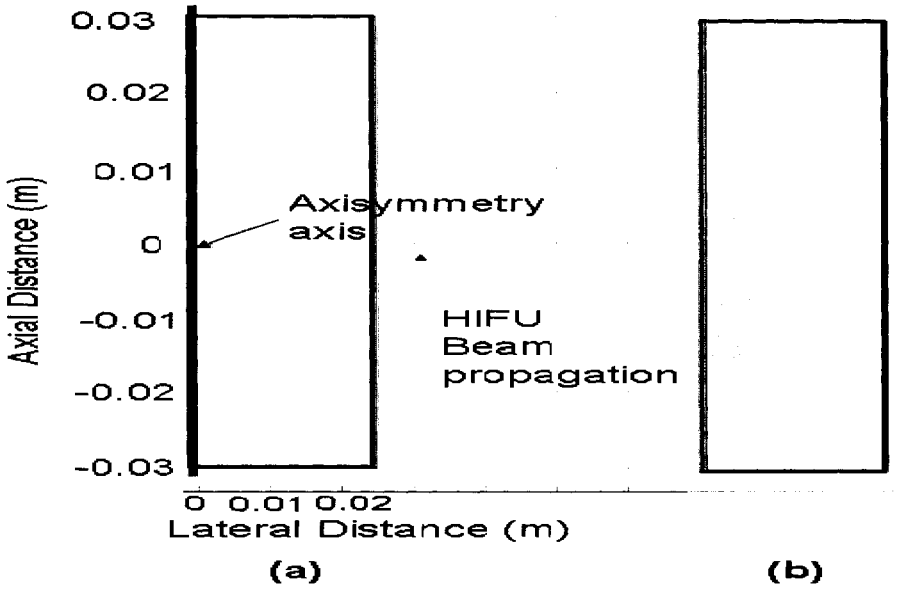

Figure A.2 (**a**) Simulation geometry with axisymmetry along the HIFU beam propagation axis (**b**) Finite element mesh with higher mesh element density near the focal zone of the HIFU transducer. The geometric focus of the HIFU transducer is located at (0, 0).

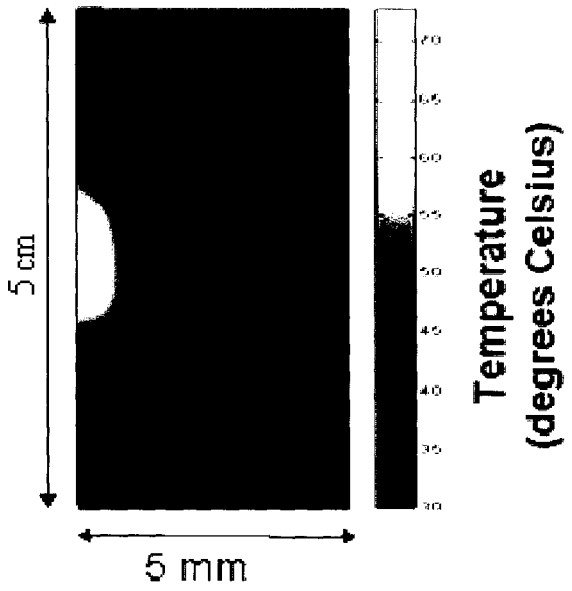

Figure A.3 Temperature profile computed using the finite element implementation of the BHTE. The leftmost vertical edge represents the axisymmetry axis. The HIFU beam propagates upward.

It may be noted that within the geometry, the temperature field is evaluated at the nodes of the FEMLAB finite element mesh. This mesh is typically non-uniform with arbitrary spacing between the nodes. However, when working in the ultrasound RF data space, typically a standard rectilinear grid with uniform spacing is employed. The spacing along the depth direction is determined by the sampling rate of the ultrasound system. Hence, to map temperatures from the non-uniformly spaced FEMLAB mesh to the rectangular grid, a set of MATLAB routines have been developed. These are built using the FEMLAB interpolation functions provided through the MATLAB interface. The temperature field is re-sampled at the location of the ultrasound scatterers, and at each scatterer position a temperature estimate is obtained.

Step 2:

In this step, the simulated temperature maps are mapped into sound speed using a known mapping between sound speed and temperature. Figure 3.2 represents such a mapping for porcine liver tissue. From these maps, the change in sound speed at each time instant with respect the initial sound speed is calculated, and the effective shift in the scatterer location is computed using equation 3.4.

Step 3:

A 2-D scatterer distribution was independently generated in MATLAB. The scatterer amplitudes were derived from a Gaussian distribution, and the scatterers were uniform distributed. A sample scatterer distribution along a RF A-line with 40 scatterers per wavelength is shown in Figure A.4.

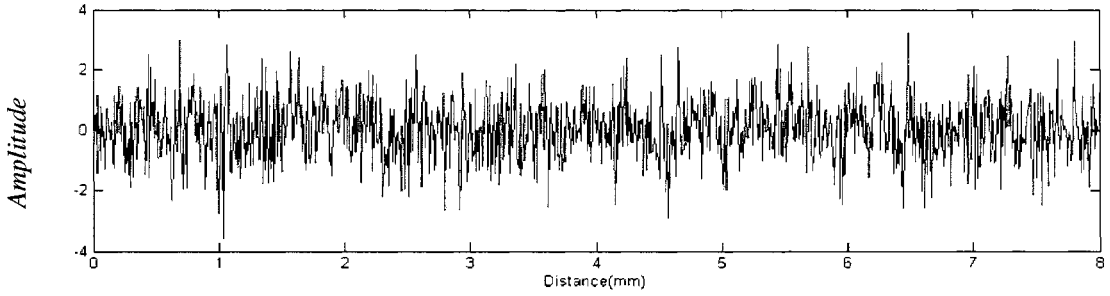

Figure A.4 Scatterer distribution along a RF A-line. The vertical axis represents the scattering strength and the horizontal axis is along the depth direction. Negative values for scattering strength are used to represent 180 degree phase shifts in the reflected signal.

The ultrasound system parameters were chosen to closely represent a standard ultrasound scanner. An example of a broadband ultrasound pulse with a 5 MHz center frequency with 60% spectral bandwidth is shown in Figure A.5.

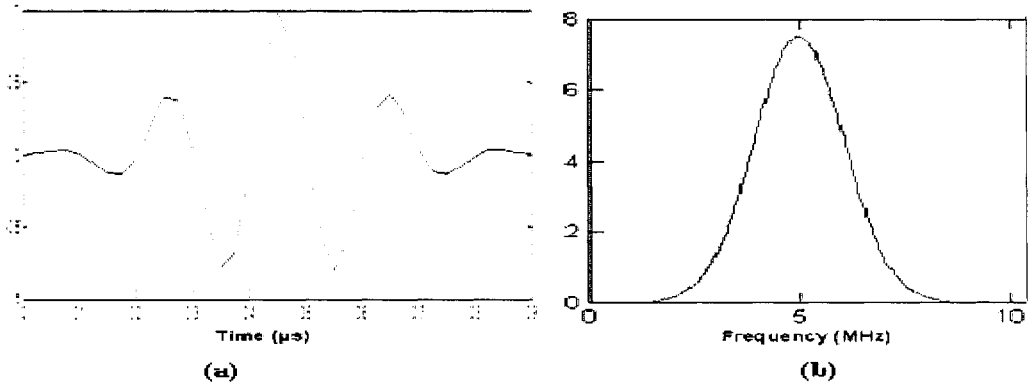

Figure A.5 (**a**) Ultrasound transmit pulse used in the simulations with center frequency of 5MHz and bandwidth of 50%. (**b**) Frequency spectrum for the pulse shown in (a).

Step 4:

The scatterer shift profiles generated in Step 2 are used to translate the scatterer field independently generated in step 3, to produce the shifted scatterer distribution. The

magnitude of the scatterer location shift would depend on the temperature rise and magnitude of the *c(T)* mapping. The transmit pulse is then convolved with the scatterer distribution to obtain the simulated RF lines. A convolutional model with only single scattering is assumed for this purpose. The simulated RF signals are input into the various data analysis programs developed in this dissertation, and were used to validate the accuracy of time shift estimators, compare between different classes of estimators and test the performance of different algorithms. A typical scatterer shift profile along an A-line passing through the HIFU heating zone is shown in Figure A.6. Figure A.7 shows a pair of RF lines for two frames, one acquired before heating commenced and the other during heating.

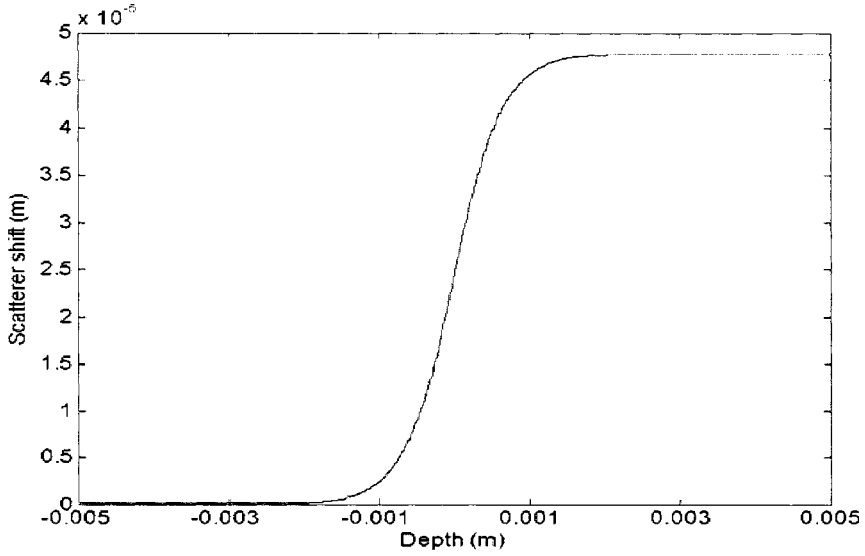

Figure A.6 Scatterer shift along the depth direction. The focus of the HIFU transducer is located at the origin along the horizontal axis. Note the steep gradient in scatterer shift around the HIFU focus.

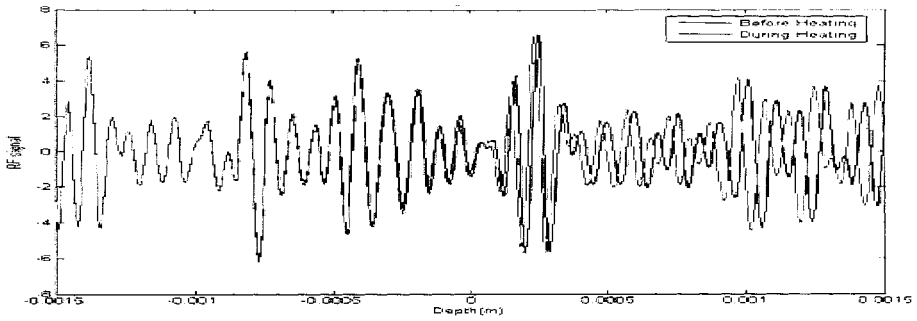

Figure A.7 Simulated RF signals generated before therapy commenced and during heating. The origin along the horizontal axis represents the location of the geometric focus of the HIFU transducer.

APPENDIX B: RELATION BETWEEN TEMPERATURE INDUCED STRAIN *(ε)* AND TEMPERATURE *(T)*

When a region of tissue is heated, the backscattered ultrasound signals (RF) from the region experience shifts in the echo locations. These shifts are due to a combination of two effects, changes in the *local sound speed of the medium* with temperature and *tissue thermal expansion*. Spatial derivatives of the shifts taken along the depth direction are referred to as temperature induced strain ε. The sound speed varies non-monotonically as a function of temperature over the therapeutic range of interest and can be represented by a quadratic polynomial for tissues with high water content. The echo shift due to thermal expansion would either be in the same direction as the sound speed change or would oppose it. This depends on the boundary conditions employed and the geometry of the sample. For the sake of discussion in this section, only the cumulative strain obtained after adding the two effects is considered. In this section, typical plots of ε for different temperature ranges are presented. These plots illustrate the influence of the non-monotonic sound speed versus temperature relationship on the observed strain profiles. For comparison, differences in the strain profiles between a monotonic and non-monotonic $\varepsilon(T)$ relationship is presented. The monotonic $\varepsilon(T)$ relation is represented by a linear polynomial of the form $\varepsilon = a*T + c$, and the non-monotonic relation is represented by a quadratic polynomial as $\varepsilon = b*T^2 + a*T + c$, where a, b and c are numerical constants that are typically tissue type and sample specific. It can be seen from the results that differences in the echo shift profiles for these two cases are subtle, and this makes the estimation of the second order term b for the non-monotonic $\varepsilon(T)$ relation challenging.

Consider a simulated 2-D axisymmetric temperature field around the focus of a HIFU transducer. The 1-D temperature profile along a scan line passing through the focus of the HIFU transducer is shown in Figure B.1. The HIFU transducer is located at the left of the image. The line plots in the figure represent different times during HIFU heating. These temperature estimates were mapped to strain using two model $\varepsilon(T)$ curves – one

assuming a linear relation and the other assuming a quadratic polynomial relation. Figure B.2 shows plot of the linear and quadratic relationship as a function of temperature.

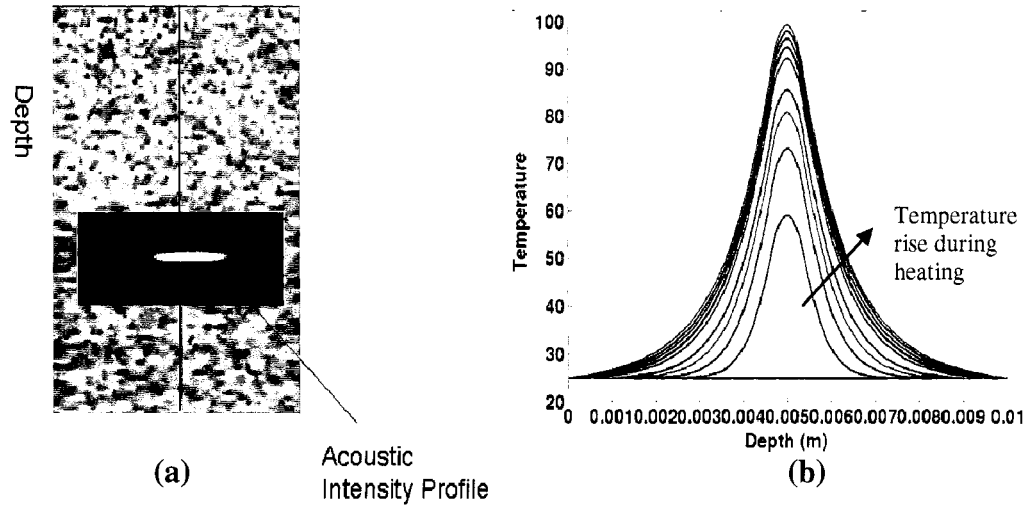

Figure B.1(a) B-mode image showing the location of the HIFU focus. The HIFU transducer is placed at the left of the image. **(b)** Temperature distribution in and around the HIFU focus in degrees Celsius along the *red* vertical line in (a).

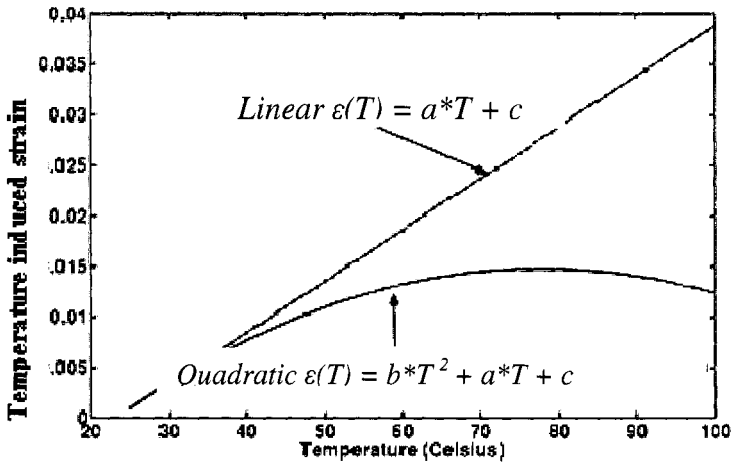

Figure B.2 Linear and quadratic $\varepsilon(T)$ profiles

The strain profiles along the depth direction for the linear and quadratic polynomial cases are shown in Figure B.3(a) and (b). It can be observed that soon after HIFU heating commences, the green plots in both figures have similar shapes. This is expected because at this early time, the maximum temperature is around 60°C and hence the polynomial ε(T) can be approximately by a linear relation in this temperature range. The key

difference between the green plots in the two figures is that the peak is broader for the quadratic relationship since the $\varepsilon(T)$ starts to flatten out near 60°C.

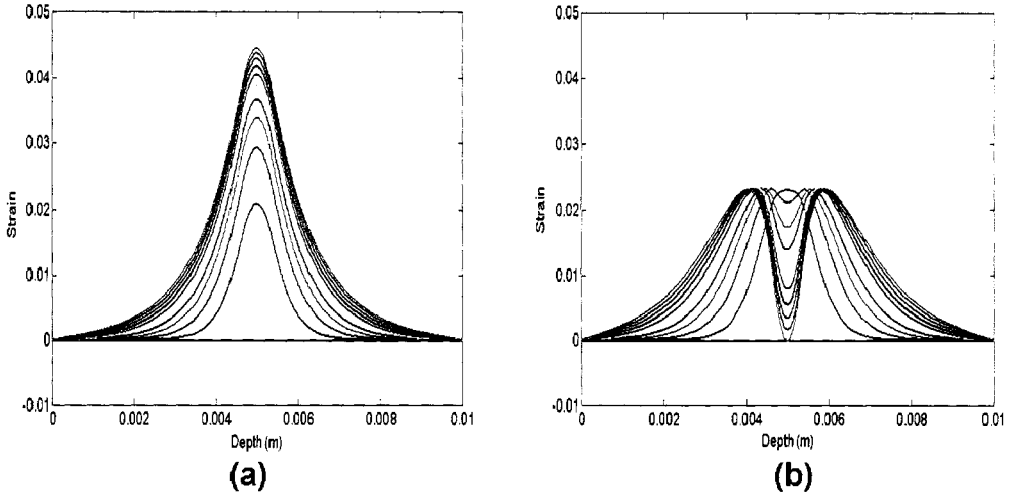

Figure B.3 Simulated strain (ε) profiles for **(a)** Linear and **(b)** Quadratic $\varepsilon(T)$ relationship

At later times, the strain profiles generated from the quadratic relation show a dip near the geometric focus of the HIFU transducer. Moreover, for typical HIFU focal spot dimensions (1 mm) such as that used in this simulation, the dip in the strain occurs over a very small spatial region and must be accurately resolved to be able to estimate the strains accurately. Figure B.4 shows the cumulative echo shift obtained by summing the strain maps along the depth direction. Note the subtle difference between the linear and quadratic case. The difference is limited to the small spatial region around the focus with the overall shape of the profiles remaining the same for most part of the curve. This result shows that the influence of the quadratic term b is localized to a small region around the HIFU focus. The ability to resolve the dip relies on the ability of the strain estimation algorithms to compute these rapidly varying local strains, and imposes limitations on the length of the cross-correlation windows and filter lengths applied. A large correlation window, although preferred for improving the local signal to noise ratio, could smear the rapidly varying local echo shifts.

The steep thermal gradients around the HIFU focus result in localized strain changes over a narrow spatial region. This is further complicated by the quadratic relation

between temperature and strain which reduces the sensitivity of strain to temperature change. If the echo shifts vary significantly across a cross-correlation window, it results in biased estimates [133] since the cross-correlation estimators are based on the assumption that the shift is constant within the entire window.

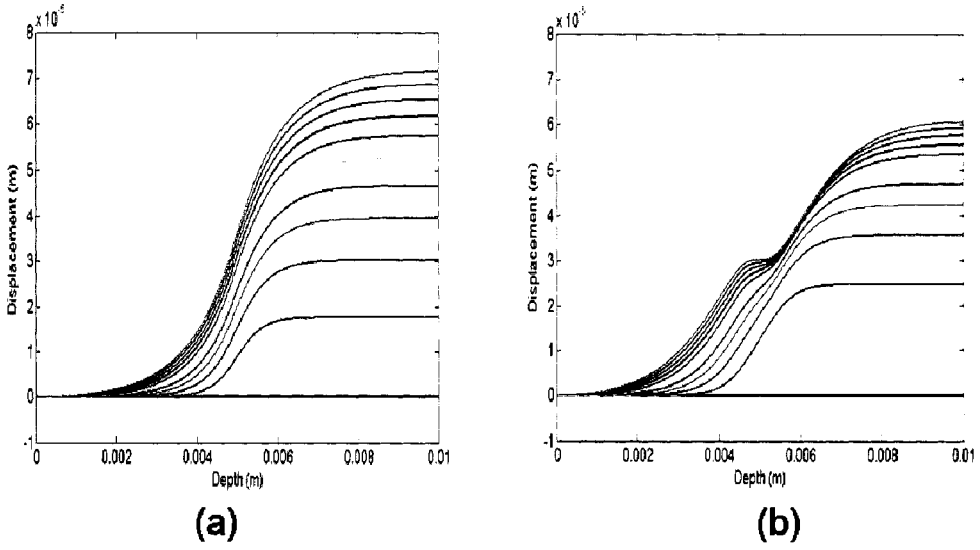

Figure B.4 Scatterer location shift profiles for the (**a**) Linear and (**b**) Quadratic $\varepsilon(T)$ relationship corresponding to the strain profiles in Figure B.3.

To improve the signal to noise ratio, larger correlation window lengths are usually preferred. However, this is at the cost of spatial resolution. A possible solution is to increase the extent of the heated zone by defocusing the HIFU beam, so that the strains corresponding to higher temperatures occur over a larger region and can be more easily resolved. This is especially essential for estimating the terms in the quadratic $\varepsilon(T)$ relationship noninvasively with high accuracy. The second order term b especially can be estimated with greater accuracy if high temperatures occur over a larger spatial region.

APPENDIX C: RF DATA ANALYSIS PROGRAMS AND GRAPHICAL USER INTERFACES

Software programs to implement the algorithms developed in Chapters 3, 4 and 5 on RF data, acquired from the HDI 1000 ultrasound scanner, were developed using MATLAB™. The implementation details of these programs are presented in this section. To enhance the usability of the programs, graphical user interfaces (GUI) were developed using the built-in tool MATLAB GUIDE. The details of the programs and their features are presented below. The programs can be divided into the following categories based on their functions:

C.1. HDI 1000 RF data analysis GUI

This program parses the data file containing RF frames, collected using the HDI 1000 during the HIFU experiment. The user interface allows visualization of desired portions of the data as A-lines or B-mode images, and calls other routines that compute temperature induced strain, thermal diffusivity and acoustic parameters. The MATLAB interface with FEMLAB, used to compute simulated temperature profiles for use in the model-based temperature estimation algorithm, is also implemented within this GUI-based program. A screen shot of the GUI is shown in Figure C.1. The RF data file is first read in. The sub-routines in the GUI then parse the data, and generate matrices that hold the B-mode image data and the RF data for all the frames in the sequence. The various buttons and edit boxes shown on the GUI are used to set the processing parameters and control options. All buttons required to provide a particular functionality are grouped together. The button group marked *A* on the figure is used to select subsets of RF frames that need to be processed in the current data set. The start frame and end frame can be selected and the spacing between frames can be chosen. After the desired frames have been loaded, the set of sliders marked *B* allow the user to scroll through the data in time, and view the B-mode images and RF data series from a desired region of interest. These are displayed in the corresponding panels on the GUI. For a given frame, the set of lines to be processed is selected by button group *C*. This is especially useful for A-line

based RF processing algorithms where only a few selected RF lines are to be processed. The buttons in group *D* can be used to select parts of the RF A-line for processing. This is especially useful for data sets collected during HIFU heating, where the changes are localized over a small region in space. The parameters for the processing algorithms are selected using the buttons in group *E* and *F*. The cross-correlation algorithm parameters such as window length and window overlap are selected in *E*. These parameters are expressed in terms of RF sampling points. The button group *F* sets the signal processing parameters for sub sample interpolation and the numerical methods applied for the estimation of thermal diffusivity. The push buttons in group *G* are then used to select the processing to be applied on the RF data set. The various processing algorithms are implemented as sub-functions of this main GUI.

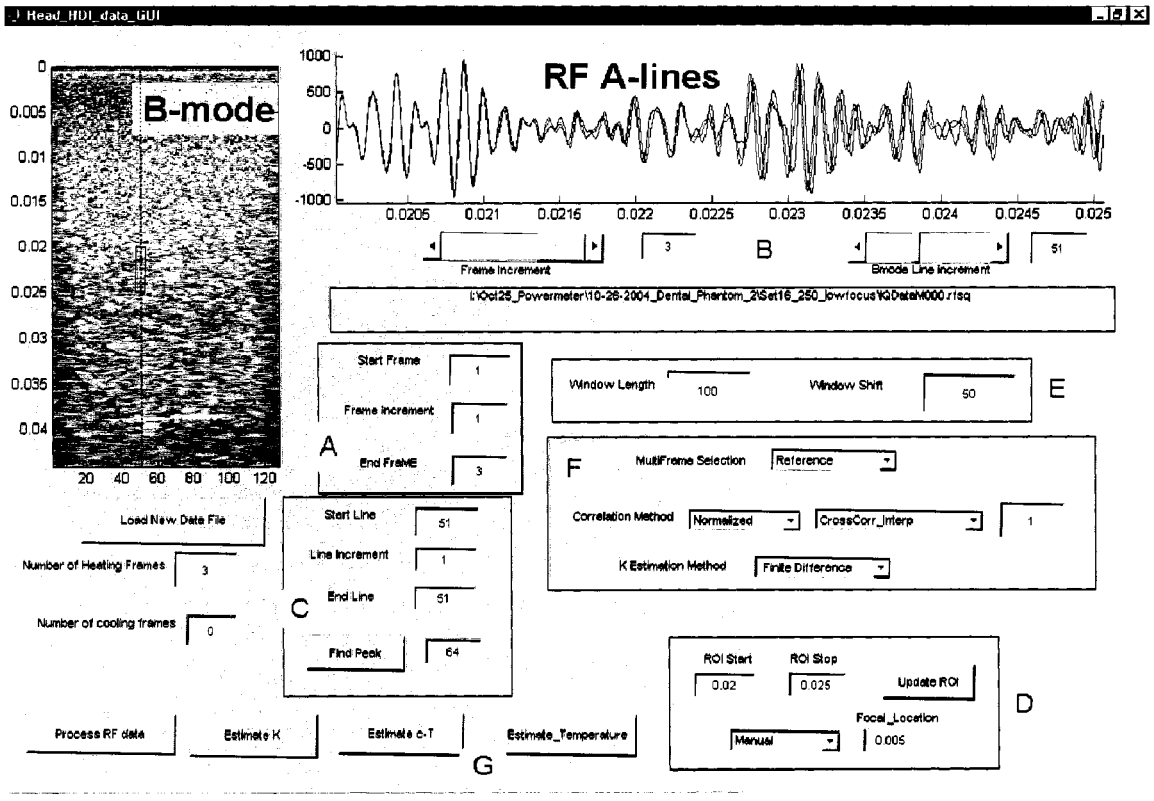

Figure C.1 Screen shot of graphical user interface developed for analysis of RF data acquired from the HDI 1000 ultrasound scanner.

C.2.Heat Source Estimation GUI

This GUI was developed to implement the noninvasive heat source *(Q)* estimation algorithm presented in Chapter 4. FEMLAB simulations for a given acoustic heat source *(Q)* are simulated in the background and the temperature information is output to this GUI. Measured acoustic and thermal parameters are input in the GUI and used to compute the calculated heat source for comparison. A screenshot of the GUI is shown in Figure C.2. The various buttons are grouped by function as shown in the figure. For a heat source value entered in button group *A*, the bioheat equation is solved using FEMLAB (via the MATLAB command line interface) to compute the 2-D temperature maps. The temperature profiles at selected points in the 2-D map are then plotted in the figure. The heat source is iteratively modified until the focus temperature reaches boiling. For computing the calculated *in situ* value to compare with the estimated value, the long list of buttons in group *B* are used to enter the various acoustic and thermal parameters required for the calculation. The difference between the calculated and estimated values is shown in the indicator marked *C*.

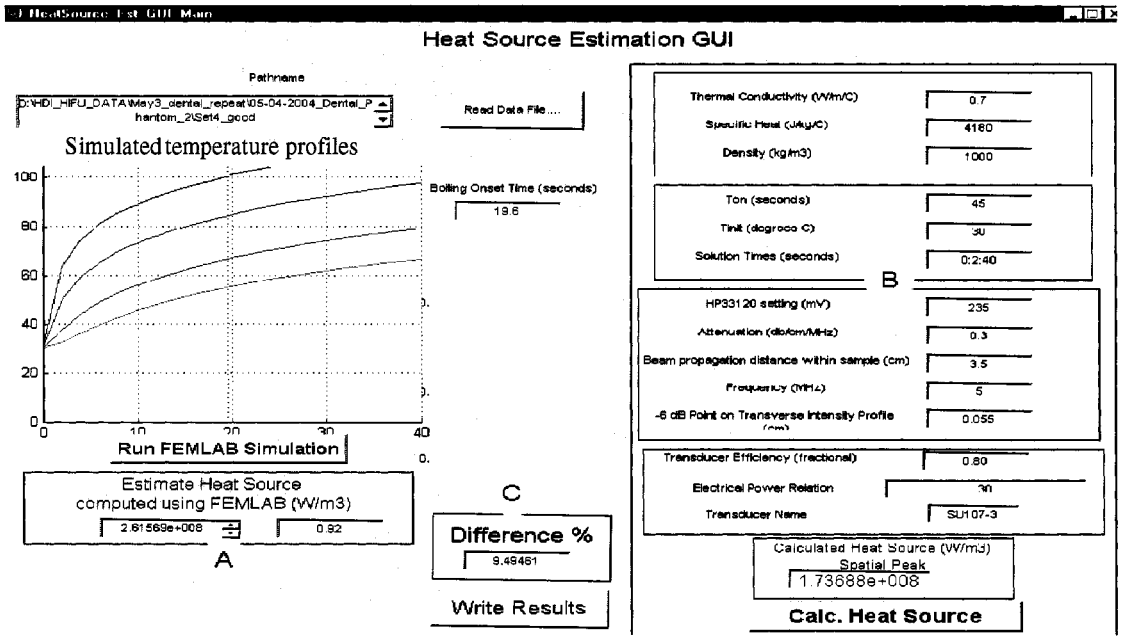

Figure C.2 Screen shot of graphic user interface designed to implement the noninvasive heat source estimation technique

C.3. Boiling Onset Detection GUI

This GUI allows the user to read in an audio file collected with the stethoscope during HIFU exposure and perform spectral analysis on the data to detect the time instant corresponding to the onset of boiling. Various spectral analysis parameters such as window length, overlap and the number of points in the FFT computation can be set from this GUI. A screen shot of the GUI is shown in Figure C.3. The stethoscope data and thermocouple temperature output are shown in the corresponding panel on the GUI. The button group *A* allows the user to enter the processing parameters for computing the spectrogram. The spectrogram is shown in a separate plot on the right side of the GUI. The lower right plot shows the instantaneous power in the signal. The vertical red slider can be stepped through this plot to locate the time instant when boiling was initiated. The buttons marked *B* are used to load the data files and activate the spectral analysis routines to compute the spectrogram. The results of this boiling detection GUI are typically used in the heat source estimation GUI to noninvasively estimate the *in situ* heat source.

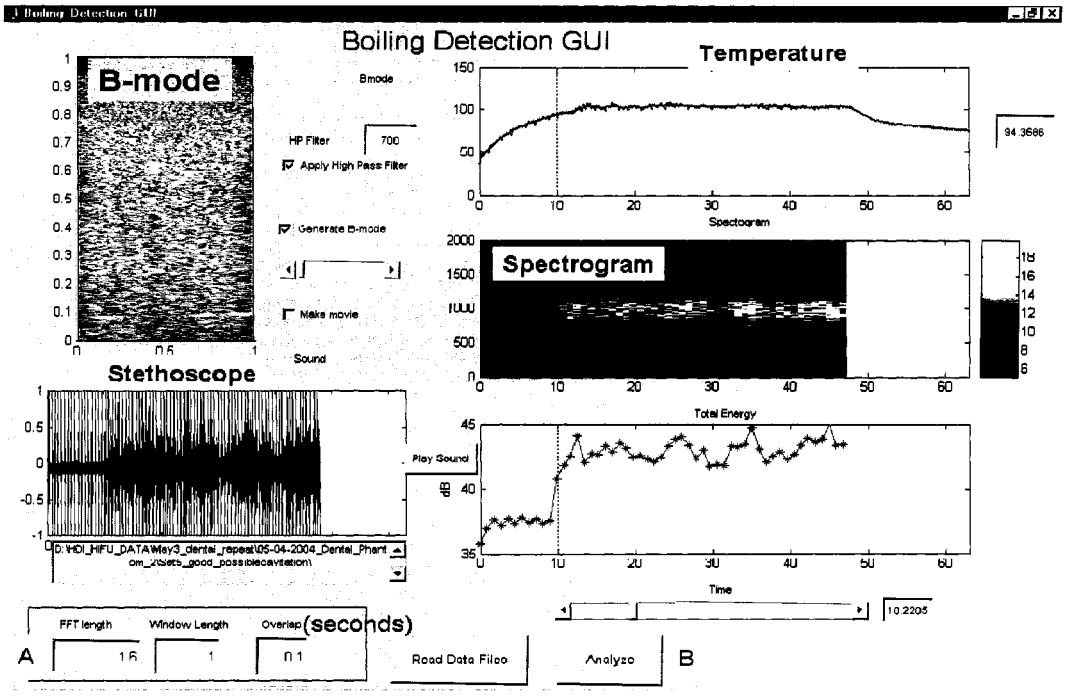

Figure C.3 Screen shot of the graphical user interface developed to implement the noninvasive boiling onset detection technique.

VITA

Ajay Anand was born in Madras (Chennai), India in 1977. He received his Bachelor's degree in Electronics Engineering from the University of Bombay, India in June 1998. Immediately thereafter, he moved to the United States to pursue his graduate studies. He earned the Master of Science degree in Biomedical Engineering from the University of Texas Southwestern Medical Center, Dallas in June 2000, and the Master of Science in Electrical Engineering from the University of Washington, Seattle in June 2003. While at the University of Texas, he was awarded the President's award for academic excellence. He is currently pursuing his doctoral degree in Electrical Engineering at the University of Washington. Ajay has presented his doctoral research work at international conferences and symposia, including the IEEE Ultrasonics Symposium and the Acoustical Society of America (ASA). He recently received the best student paper award at the ASA meeting in Nashville, TN.